Evidence For Muon Neutrino Oscillation In An Accelerator-based Experiment

Hirokazu Maesaka

Department of Physics,
Faculty of Science,
Kyoto University

July, 2005

Abstract

We present the evidence for muon neutrino oscillation based on the measurement of the KEK-to-Kamioka long baseline experiment. The data corresponding to 8.9×10^{19} protons on target is analyzed in this thesis. At the middle of the run, the far detector, Super-Kamiokande, was damaged by an accident, and rebuilt with about a half of the PMT density. In addition, a fully-active scintillator detector, SciBar, was newly constructed at the near site. This is the first time to present the results with SciBar and the second phase of Super-Kamiokande. We study neutrino oscillation by using both the distortion of the neutrino energy spectrum and the reduction in the number of events. The neutrino energy spectrum at the near site is measured by a near detector complex, and it is used to estimate the neutrino energy spectrum at the far site. The neutrino event rate at the near site is also measured, and the number of events in Super-Kamiokande is predicted. In total, 107 neutrino events have been observed by Super-Kamiokande, while the expectation from the near detector without oscillation is $150.9^{+11.5}_{-10.1}$ events. The reconstructed neutrino energy of 57 single-muon events are compared with the expected spectrum from the near detector. The two-flavor neutrino oscillation model is examined by using the above results. The best fit oscillation parameters are obtained to be

$$(\Delta m^2,\ \sin^2 2\theta) = (2.8 \times 10^{-3}[\mathrm{eV}^2],\ 1.0).$$

The 90% confidence interval of Δm^2 at $\sin^2 2\theta = 1$ is estimated to be

$$1.9 \times 10^{-3} \leq \Delta m^2 \leq 3.6 \times 10^{-3}\ [\mathrm{eV}^2].$$

These results are consistent with atmospheric neutrino experiments. The null oscillation hypothesis is excluded with 99.995% probability, corresponding to 4.0 standard deviations.

Acknowledgments

First of all, I would like to express my great appreciation to my supervisor Prof. Koichiro Nishikawa, for introducing me to the K2K experiment and supporting me throughout my graduate career. He has instructed me in many things: interestingness of high energy physics, techniques of physics experiments, and skills in data analysis.

I would also like to thank Prof. Tsuyoshi Nakaya. He has been giving me a lot of useful advise, and he has provided a strong leadership in the development and construction of the SciBar detector. My thanks go to Dr. Atsuko K. Ichikawa for a number of instructions in the structural design and construction of SciBar. I am also thankful to Dr. Masashi Yokoyama for his helpful suggestions concerning construction, operation and analysis of SciBar.

The SciBar detector has been realized by hard work of all the group members. Dr. M. Yoshida, Dr. K. Nitta, Mr. M. Hasegawa, Mr. S. Yamamoto, Mr. Y. Takubo, Mr. T. Sasaki and Mr. T. Morita have devoted considerable efforts to the design, construction, operation, and analysis of the SciBar detector. Dr. I. Kato gave us many pieces of advice on the overall situation. Dr. A. Pla-dalmau in Fermilab developed and mass-produced scintillator strips. Prof. S. Aoki gave us many good suggestions on how to handle the plastic fiber. Prof. R. J. Wilkes and Mr. H. G. Berns furnished us with the polish machine of the fiber assembly. Dr. M. Tanaka and Mr. T. Murakami created the readout electronics with sophisticated technology. Prof. S. B. Kim, Dr. K. K. Joo, Dr. E. J. Jeon, and Ms. M. J. Lee manufactured and tested the electronics. Dr. Y. Hayato cooperated closely with us in preparing the online data handling program and in doing the neutrino interaction simulation. Prof. L. Ludovici, Prof. P. Loverre, Prof. U. Dore, and Mr. C. Mariani brought the electro-magnetic calorimeter from CERN. Dr. F. Sanchez developed the elegant track finding algorithm. Dr. K. Kobayashi created the nice slow monitor system. Dr. A. Suzuki, Dr. M. Iinuma, Mr. S. Nawang, Mr. K. Hayashi, Mr. S. Ueda, Mr. K. Hiraide, Mr. J. Kubota, Mr. D. Kerr, Mr. R. Terri, Mr. Eric J., Mr. P. Rovegno, Ms. M. Tuchscher, Mr. K. Shiraishi, Prof. I. T. Lim, Mr. S. S. Choi, Prof. M. Khabibullin, and Mr. M. Oleg kindly helped us to install the SciBar detector. Prof. T. Takahashi dispatched students to KEK, and they assisted us voluntarily in the construction. Analysis contributions have been provided by Ms. E. Aliu, Mr. X. Espinal, Ms. A. Rodriguez, Ms. S. Andringa, Ms. A. M. Tornero-Lopez, and Mr. G. V. Sitjes. Mr. M. Taino and Mr. N. Tanaka in KEK, Mr. H. Sukegawa and Mr. M. Odakura from Nikka Setsubi Engineering Company, and all the people of Wachi Kensetsu Company, Hokuto Company, Futaba Kogyo Company, Suzuno Giken Company, CI Kogyo Company, and Rin'ei Seiki Company exerted energetic efforts to construct the structure and the hardware of the SciBar detector. Kuraray Company produced wavelength shifting fibers, and Hamamatsu Photonics Company manufactured multi-anode PMTs. IDEAS Company produced readout ASICs, and Meisei Electric Company assembled electronics components. I am deeply grateful to all the people who has worked together for the SciBar detector.

In addition, my study is supported by all the K2K collaborators. Prof. Y. Totsuka, Prof. K. Nakamura, Prof. Y. Suzuki, Prof. C. K. Jung, and Prof. R. J. Wilkes have administrated the K2K experiment with best efforts. The beamline monitors have been supported by Dr. T. Hasegawa, Dr. T. Maruyama, and the other beamline group members. The 1KT detector has

been maintained and analyzed by the 1KT group, especially by Prof. Y. Itow, Prof. M. Shiozawa Dr. M. Miura, Dr. J. Kameda, and Dr. I. Kato. The SciFi detector has been supported and studied by Prof. M. Sakuda, Dr. T. Ishida, Dr. R. Gran, Dr. T. Iwashita, and Dr. H. Yokoyama, and the other SciFi group people. Prof. T. Kobayashi and Dr. M. Yoshida have controlled the LG detector. Dr. T. Ishii, Dr. T. Inagaki, and Mr. J. H. Choi have worked hard to take care of the MRD detector. The Super-Kamiokande data have been provided by Prof. K. Kaneyuki, Dr. Y. Obayashi, and Dr. S. Yamada. The oscillation analysis has been significantly contributed by Dr. T. Nakadaira. I would like to convey my warm appreciation to all the K2K collaborators. I also gratefully acknowledge all the people of the KEK 12GeV PS group, the beam channel group, the Super-Kamiokande collaboration, and Kamioka Mining and Smelting Company, for the generous cooperation to carry out the K2K experiment.

I would like to thank all the members in the high energy physics group of Kyoto University. Prof. N. Sasao, Prof. H. Sakamoto, Dr. R. Kikuchi, and Dr. T. Nomura, have advised and encouraged me in various occasions. I have enjoyed the laboratory life with Mr. M. Suehiro, Dr. Y. Ushiroda, Dr. H. R. Sakai, Mr. T. Fujiwara, Dr. S. Nishida, Mr. H. Yokoyama, Mr. K. Mizouchi, Ms. K. Uchida, Mr. T. Sumida, Mr. S. Tsuji, Mr. T. Shirai, Ms. N. Taniguchi, and Ms. K. Takezawa. I have been firmly supported by Ms. A. Nakao and the other secretaries. I had a very pleasant time throughout the graduate school period.

Finally, I want to thank my family for supporting me to complete the graduate course.

Hirokazu Maesaka
Kyoto, Japan
July, 2005

Contents

Chapter 1

Introduction

Neutrinos are elementary particles with spin 1/2 and no electric charge. They interact through only the weak interaction. There are three neutrino types found so far: ν_e, ν_μ, and ν_τ, associating with the three charged leptons. Although the neutrino masses have been directly searched for as listed in Table 1.1, no finite mass has ever been found.

The evidence for finite neutrino masses has been found, however, through neutrino oscillations observed by atmospheric[5], solar[6, 7], reactor[8], and accelerator-based[9] neutrino experiments. Neutrino oscillation is the phenomenon that neutrino flavor changes periodically with its time evolution. It is caused by the mixing between the flavor eigenstates and the mass eigenstates, when neutrinos have non-degenerate masses. In the two-neutrino case, the probability that a neutrino type ν_α with energy E [GeV] transforms to the other type ν_β after traveling L [km] in vacuum is

$$P(\nu_\alpha \to \nu_\beta) = \sin^2 2\theta \cdot \sin^2 \left(1.27 \cdot \Delta m^2\,[\mathrm{eV}^2] \cdot \frac{L\,[\mathrm{km}]}{E\,[\mathrm{GeV}]} \right), \tag{1.1}$$

where θ is the mixing angle, and Δm^2 ($\equiv m_2^2 - m_1^2$) is the difference between the squares of the mass eigenvalues (m_1, m_2), as derived in Section 1.1. Thus, the discovery of neutrino oscillation is the evidence for finite neutrino masses and mixings.

The flavor eigenstate of a neutrino, ν_α ($\alpha = e, \mu, \tau$), is expressed by mass eigenstates, ν_i ($i = 1, 2, 3$):

$$\nu_\alpha = \sum_i U_{\alpha i}^* \nu_i, \tag{1.2}$$

where $U_{\alpha i}$ is an element of the 3×3 unitary matrix of neutrino mixing called "MNS[1] matrix", which is an analogue of CKM matrix in the quark sector. There are four degrees of freedom in the MNS matrix: three of them are mixing angles and the other is a CP phase. There are two Δm^2's on the assumption of three neutrinos. The present knowledge of these parameters is still poor, compared to the quark sector, as summarized later in Section 1.3.

Nonzero neutrino masses raise possibilities of new neutrino features: for example, the neutrinos can be either Majorana or Dirac fermions, massive neutrinos can have nonzero magnetic moments, the heavier neutrinos can decay into lighter ones, and neutrinos may be a sizable fraction of dark matter. Neutrino mixing opens the possibility of CP violation by analogy with the quark sector. Therefore, the establishment of the finite neutrino mass and mixing and the measurement these parameters make a strong impact on the particle physics.

In the following sections, we describe basic knowledge of neutrino oscillation, the present status of oscillation measurements, and the outline of this thesis.

[1] Initials of Z. Maki, M. Nakagawa, and S. Sakata, who first proposed neutrino mixing[10].

Table 1.1: Present limit of neutrino mass evaluated by Particle Data Group[1].

Neutrino	Mass limit	Experiment
ν_e	< 3 eV/c^2 (95% C.L.)	^{3}H β decay[2]
ν_μ	< 0.17 MeV/c^2 (90% C.L.)	pion decay[3]
ν_τ	< 18.2 MeV/c^2 (95% C.L.)	tau decay[4]

1.1 Neutrino oscillation

We briefly summarize the phenomenology of neutrino oscillation. In the two-neutrino case, the flavor eigenstates, ν_α and ν_β, is written by

$$\begin{pmatrix}\nu_\alpha \\ \nu_\beta\end{pmatrix} = \begin{pmatrix}\cos\theta & \sin\theta \\ -\sin\theta & \cos\theta\end{pmatrix}\begin{pmatrix}\nu_1 \\ \nu_2\end{pmatrix} \equiv U\begin{pmatrix}\nu_1 \\ \nu_2\end{pmatrix}, \tag{1.3}$$

where ν_1 and ν_2 are the mass eigenstates and θ is the mixing angle. While a neutrino is generated as a flavor eigenstate via weak interaction, the time evolution of its state is described in terms of the mass eigenstates. Since the states ν_i have common momentum p according to the momentum conservation law, the time evolution is expressed by

$$\begin{pmatrix}\nu_1(t) \\ \nu_2(t)\end{pmatrix} = \begin{pmatrix}e^{-iE_1 t} & 0 \\ 0 & e^{-iE_2 t}\end{pmatrix}\begin{pmatrix}\nu_1(0) \\ \nu_2(0)\end{pmatrix}, \tag{1.4}$$

where E_i $(= \sqrt{p^2 + m_i^2})$ are energy eigenvalues. Thus, the time evolution of the flavor eigenstates is solved as

$$\begin{pmatrix}\nu_\alpha(t) \\ \nu_\beta(t)\end{pmatrix} = U\begin{pmatrix}e^{-iE_1 t} & 0 \\ 0 & e^{-iE_2 t}\end{pmatrix}U^{-1}\begin{pmatrix}\nu_\alpha(0) \\ \nu_\beta(0)\end{pmatrix}. \tag{1.5}$$

Suppose a neutrino is generated as ν_α (*i.e.* $\nu_\alpha(0) = 1$ and $\nu_\beta(0) = 0$), its surviving probability after traveling a distance L is obtained as

$$\begin{aligned} P(\nu_\alpha \to \nu_\alpha) = |\nu_\alpha(t)|^2 &= 1 - \sin^2 2\theta \cdot \sin^2\left(\frac{\Delta m^2 L}{4p}\right) \\ &= 1 - \sin^2 2\theta \cdot \sin^2\left(1.27 \cdot \Delta m^2\,[\mathrm{eV}^2] \cdot \frac{L\,[\mathrm{km}]}{E\,[\mathrm{GeV}]}\right), \end{aligned} \tag{1.6}$$

where $\Delta m^2 \equiv m_2^2 - m_1^2$ and relativistic approximation $E_i \simeq p + m_i^2/2p$ are used. Thus, the oscillation probability is expressed as a function of L/E.

1.2 Key issues for neutrino oscillation experiment

We discuss the experimental sensitivity to neutrino oscillation and key issues for the design of a neutrino oscillation experiment. The sensitivity to the neutrino oscillation parameters, $\sin^2 2\theta$ and Δm^2, depends on the choice of L/E for each experiment according to Equation (1.6). The experimental precision of $\sin^2 2\theta$ is dominated by the statistics around the oscillation maximum $(1.27 \cdot \Delta m^2 \cdot L/E \sim \pi/2)$. The precision of Δm^2 depends on the measurement accuracy of L/E, since Δm^2 is multiplied by L/E in Equation (1.6). In summary, key issues for the design of a neutrino oscillation experiment are: (1) choice of L/E, (2) statistics at the oscillation maximum, and (3) L/E reconstruction resolution.

1.3 Present knowledge about neutrino oscillation

We review the present knowledge about neutrino oscillation. Neutrino oscillation experiments are classified into three sectors: atmospheric, solar, and reactor neutrino sectors corresponding to the three mixing angles in the MNS matrix. We describe the current status of each sector.

1.3.1 Atmospheric neutrino sector

Atmospheric neutrinos are produced by decays of pions and kaons which are generated by the collision of primary cosmic rays with the upper atmosphere. The most frequent decay chain of these mesons is

$$\begin{aligned} \pi^{\pm}\ (K^{\pm}) &\rightarrow \mu^{\pm} + \overset{(-)}{\nu}_{\mu} \\ &\downarrow \\ \mu^{\pm} &\rightarrow e^{\pm} + \overset{(-)}{\nu}_{\mu} + \overset{(-)}{\nu}_{e}. \end{aligned} \tag{1.7}$$

The energy spectrum of these neutrinos peaks at approximately 1 GeV, and extends to the order of 100 GeV. The flight length runs from 10 km, for neutrinos coming from the zenith, to 13000 km, for those coming from the nadir. Therefore, the L/E of atmospheric neutrinos stretches from 1 to 10000. The L/E of each neutrino event is approximated by the energy and the direction of the lepton produced by neutrino interaction.

Although atmospheric neutrinos are composed of both muon and electron neutrinos, it has been found that only muon neutrinos oscillate into other neutrinos ($\nu_{\mu} \rightarrow \nu_{x}$ oscillation). At present, the 90% C.L. intervals of the oscillation parameters in the atmospheric neutrino sector, $\Delta m^2_{\rm atm}$ and $\theta_{\rm atm}$, are

$$\begin{aligned} 1.9\times10^{-3} < \Delta m^2_{\rm atm} < 3.1\times10^{-3}\ [{\rm eV}^2], \\ \sin^2 2\theta_{\rm atm} > 0.90, \end{aligned} \tag{1.8}$$

according to Super-Kamiokande results[11]. The allowed region of these parameters is shown in Figure 1.1. In this sector, ν_x's are likely to be ν_{τ}'s.

Several accelerator-based experiments are investigating this parameter region. By using pion decay in flight ($\pi^+ \rightarrow \nu_{\mu} + \mu^+$), muon neutrino beam is produced, and it is detected after a certain length of flight. Neutrino oscillation is examined by comparing the measured beam property with the expected one. The K2K experiment[12], which is the subject of this thesis, is one of the accelerator-based experiments, and the indication of neutrino oscillation has been obtained[9]. The advantage of an accelerator-based experiment is described in Section 1.4.

1.3.2 Solar neutrino sector

Solar neutrinos are created by nuclear fusion reactions at the center of the Sun. Only electron neutrinos are produced. Therefore, solar neutrino experiments are sensitive to $\nu_e \rightarrow \nu_x$ oscillation. The neutrino energy spectrum distributes from 0 to 15 MeV. Since the distance between the Sun and the Earth is 1.5×10^8 km, the sensitivity to Δm^2 reaches down to 10^{-11} eV^2 in case of vacuum oscillation[2]. Solar neutrino experiments can measure Δm^2 up to 10^{-3} eV^2, if we take "MSW[3] effect[13]" into account. Here, the MSW effect is the phenomenon that the effective mass eigenvalue is shifted when neutrinos travel through matter.

Recent solar neutrino experiments, such as Super-Kamiokande[6] and SNO[7], report that the electron neutrino flux from the Sun is significantly smaller than the expected flux while

[2] Vacuum oscillation is defined as neutrino oscillation following Equation (1.6) in contrast to MSW oscillation.
[3] The initials of Mikheyev, Smirnov, and Wolfenstein.

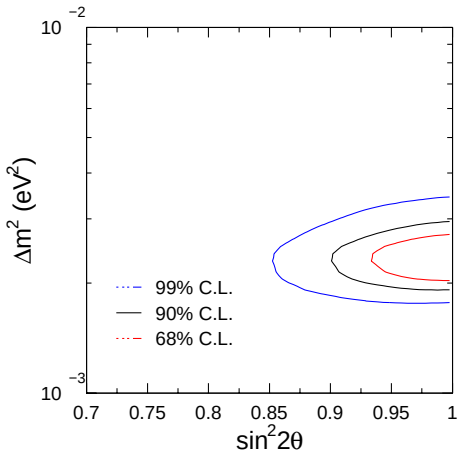

Figure 1.1: Allowed region of the oscillation parameters for the atmospheric neutrino sector.

the total neutrino flux is consistent with the expectation. These results are consistent with neutrino oscillation. The mass square difference and the mixing angle are measured to be $\Delta m^2_{\odot} \simeq 7 \times 10^{-5}$ eV^2 and $\tan^2\theta_{\odot} \simeq 0.4$, respectively. The allowed region of these parameters are shown in Figure 1.2 (lines of the left)[14].

The neutrino oscillation in this sector has been studied by a reactor neutrino experiment, KamLAND[14][4]. This experiment observes electron anti-neutrinos produced by β-decays of nuclear fission products. The energy spectrum of observable neutrinos spreads from 2 MeV to 8 MeV. The baseline length is approximately 180 km. Therefore, the L/E is roughly 4×10^4 km/GeV, which matches to solar neutrino oscillation.

KamLAND has observed smaller neutrino flux than the expected one. This result is a strong support of solar neutrino oscillation. The allowed region of the oscillation parameters from the KamLAND data is shown in Figure 1.2 (hatched areas of the left). The combined analysis[14] of both solar and reactor experiments shows that the allowed intervals of the oscillation parameters are

$$\begin{aligned} \Delta m^2_{\odot} &= 7.9^{+0.6}_{-0.5} \times 10^{-5}\ [\mathrm{eV}^2], \\ \tan^2\theta_{\odot} &= 0.40^{+0.10}_{-0.07}. \end{aligned} \tag{1.9}$$

The allowed region of the oscillation parameters from this analysis is shown in Figure 1.2 (right).

We briefly discuss the difference in the shape of the allowed region between solar neutrino experiments and KamLAND. For solar neutrino experiments, the sensitivity to $\theta_{\odot}$ is better than KamLAND thanks to the MSW effect in the Sun. However, the MSW effect makes the oscillation probability almost independent of neutrino energy (E_ν) in the energy region of $E_\nu > 5$ MeV, where Super-Kamiokande and SNO are sensitive. For KamLAND, the oscillation probability follows Equation (1.1), which is a sinusoidal function of L/E. Therefore, the $\Delta m^2_{\odot}$ sensitivity of KamLAND is significantly better than that of solar neutrino experiments. Thus, the combined result of solar and KamLAND experiments restricts the oscillation parameters within a very small region. Consequently, the neutrino oscillation in this sector has been established by using two neutrino sources with different systematics.

[4] Although we describe other reactor neutrino experiments in Section 1.3.3, they are sensitive to another mixing angle because their L/E are much shorter. Therefore, KamLAND is exceptionally classified into the solar neutrino sector.

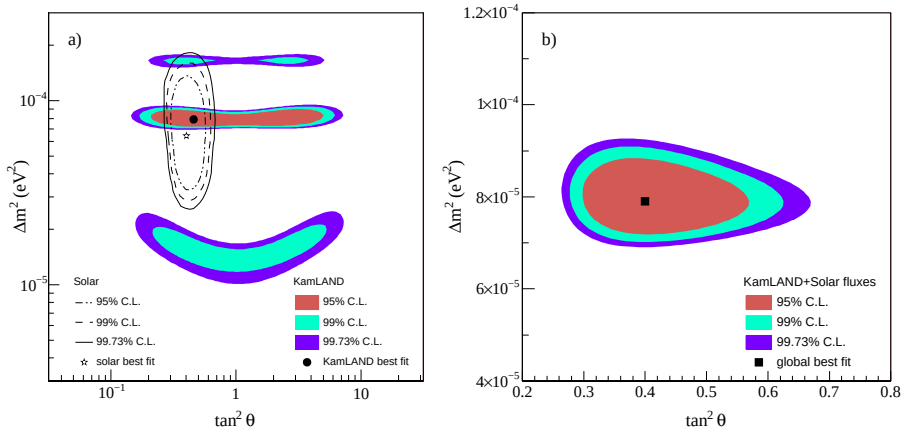

Figure 1.2: Allowed region of the oscillation parameters for the solar neutrino sector. The left figure shows the results from solar neutrino experiments (lines) and KamLAND (shaded areas) separately. The right figure shows the combined result of them.

1.3.3 Reactor neutrino sector

The other mixing angle is investigated by studying $\nu_e \to \nu_x$ oscillation at $\Delta m^2_{\rm atm}$, corresponding to $L/E \sim 400$. This channel has been searched for by some reactor experiments[15] with baseline length of approximately 1 km. No evidence has ever been found. The 90% C.L. upper limit on the mixing angle is

$$\sin^2 2\theta < 0.1 \ , \tag{1.10}$$

when $\Delta m^2 > 3 \times 10^{-3}$ eV^2.

This sector is also studied by an accelerator-based experiment. The neutrino oscillation in this sector transforms a part of muon neutrinos into electron neutrinos ($\nu_\mu \to \nu_e$ oscillation). In other words, the appearance of electron neutrinos is the evidence for the finite mixing angle in this sector. This channel has been studied by the K2K experiment[16]. The signal of $\nu_\mu \to \nu_e$ oscillation has not been observed so far.

1.4 Necessity for accelerator-based experiment

Neutrino oscillation in the atmospheric neutrino sector has been observed only by atmospheric neutrino experiments before the K2K experiment. To establish this phenomenon further more, another experiment with different systematics is needed. As mentioned in Section 1.3.1, an accelerator-based experiment is able to investigate this region. One of the advantages of an accelerator-based experiment is that the neutrino flight length L is constant. Furthermore, since the neutrino beam direction is known, the neutrino energy E is precisely reconstructed by using kinematical conditions.

In case of atmospheric neutrino experiments, both the direction and the energy of a neutrino are approximated from the scattered particles from neutrino interaction. Therefore, the precision of L/E is not very good. In the Super-Kamiokande analysis[11], for instance, the precision of L/E is typically 70%. For accelerator-based experiments, the precision is 10% level. Therefore, accelerator-based experiments have a great advantage in measuring Δm^2. In addition, an accelerator-based experiment measures the neutrino beam properties before oscillation by putting a neutrino detector near the production point. Comparison between near and far detectors considerably reduces uncertainties in neutrino flux, neutrino energy spectrum, and neutrino interaction.

To utilize these advantages, the KEK-to-Kamioka long baseline neutrino oscillation experiment (KEK-PS-E362), named "K2K", was proposed[12] and has been carried out[9, 17]. K2K is the first long baseline experiment sensitive to atmospheric neutrino oscillation.

1.5 Outline of this thesis

This thesis is dedicated to obtain the evidence for the disappearance of ν_μ and to measure the oscillation parameters in the atmospheric neutrino sector. We analyze the data from the K2K experiment. Since a new detector, called SciBar, was installed in the middle of the K2K experiment, the design, construction, and analysis of SciBar are presented in detail.

The outline of the thesis is as follows. The K2K experiment is introduced in Chapter 2. The experimental setup of K2K is described in Chapter 3. The SciBar detector is subsequently explained in detail in Chapter 4. The MC simulation for each physics process and each experimental component are described in Chapter 5. The analysis of the SciBar detector is described in Chapter 6. The overview of the neutrino oscillation analysis is provided in Chapter 7. The analysis of each detector is described in Chapter 8 – 11, and the neutrino oscillation analysis is performed in Chapter 12. Finally, the conclusion is summarized in Chapter 13.

Chapter 2

Overview of K2K Experiment

We introduce the K2K experiment in this chapter. We give an outline of the experiment, and summarize the analysis strategy. On the basis of the strategy, we describe the design concept of the experimental setup. Finally, we present the history of the K2K experiment.

2.1 Outline

The K2K experiment is proposed to confirm atmospheric neutrino oscillation and to measure the oscillation parameters. An almost pure muon neutrino (ν_μ) beam produced by a 12 GeV proton beam at KEK[1]. The ν_μ beam is detected by Super-Kamiokande (SK), a 50kt water Cherenkov detector, after 250 km flight. The locations of KEK and SK are shown in Figure 2.1. In addition to the SK measurement, a near detector complex (ND) at KEK measures ν_μ beam properties just after the ν_μ production. By comparing the results between ND and SK, we examine neutrino oscillation in the atmospheric sector and measure the oscillation parameters.

The ν_μ beam energy is widely spread around the mean energy 1.3 GeV. Therefore, the K2K experiment is sensitive to the range of $\Delta m^2 \sim 10^{-3} - 10^{-2}$ [eV^2], which covers atmospheric neutrino oscillation ($\Delta m^2 \sim 3 \times 10^{-3}$ [eV^2] and $\sin^2 2\theta \sim 1$). Figure 2.2 shows the oscillation probability as a function of neutrino energy (E_ν) and the ν_μ energy spectra at SK with and without neutrino oscillation. A typical parameter set suggested by atmospheric neutrino experiments is chosen in this figure.

The oscillation signal of the K2K experiment has two features: the distortion of the ν_μ energy spectrum and the deficit of the number of SK events. In case of $\nu_\mu \to \nu_\tau$ oscillation, ν_τ does not have the scattering amplitude for charged current interaction, because E_ν is below the tau production threshold (~ 3.5 GeV). Therefore, the ν_μ energy spectrum at SK shows a characteristic oscillation pattern (Figure 2.2), and the number of SK events becomes smaller than the extrapolation from ND. We use both information for the neutrino oscillation analysis.

The K2K experiment is also investigating $\nu_\mu \to \nu_e$ oscillation by searching for electron neutrino events in SK. In this thesis, we do not analyze this channel.

2.2 Analysis strategy

We describe the analysis strategy for the comparison of the energy spectra and the the number of events between ND and SK.

[1] High Energy Accelerator Research Organization in Tsukuba.

Figure 2.1: Overview of the K2K experiment. The ν_μ beam produced at KEK is detected by Super-Kamiokande after 250 km flight.

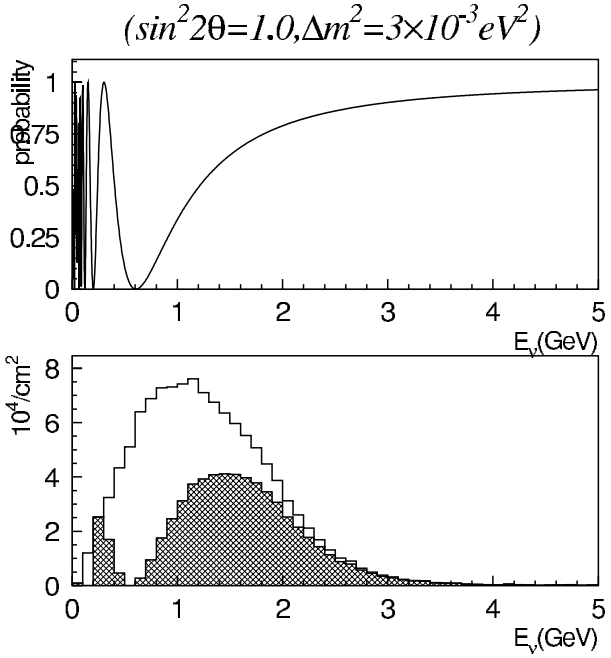

Figure 2.2: Oscillation probability as a function of E_ν (top) and E_ν spectra with and without neutrino oscillation (bottom). The oscillation parameters are chosen to be $(\Delta m^2, \sin^2 2\theta) = (3\times10^{-3}\ [\mathrm{eV}^2], 1.0)$.

2.2.1 Comparison of the energy spectra between ND and SK

We compare the energy spectra between ND and SK by following three steps.

1. Reconstruct the E_ν spectrum at ND, $\Phi_{\rm ND}(E_\nu)$.
2. Obtain the expected E_ν spectrum at SK, $\Phi_{\rm SK}(E_\nu)$, by extrapolating from $\Phi_{\rm ND}(E_\nu)$.
3. Compare the reconstructed E_ν spectrum with $\Phi_{\rm SK}(E_\nu)$.

Strictly speaking, $\Phi_{\rm XX}(E_\nu)$ is defined as the neutrino flux at XX (ND or SK) as a function of E_ν. When we compare the energy spectra, we consider only the spectrum shape and do not care the flux itself. When we study the number of events, on the other hand, we take the flux into account.

We reconstruct the neutrino energy spectrum by using charged-current quasi-elastic (CC-QE) interaction:

$$\nu_\mu + n \to \mu^- + p, \tag{2.1}$$

which is a dominant process in the K2K experiment. Assuming CC-QE interaction, the parent neutrino energy ($E_\nu^{\rm rec}$) is calculated by using the muon momentum (p_μ) and the angle with respect to the beam (θ_μ):

$$E_\nu^{\rm rec} = \frac{m_p^2 - (m_n - V)^2 - m_\mu^2 + 2(m_n - V)E_\mu}{2(m_n - V - E_\mu + p_\mu \cos\theta_\mu)}, \tag{2.2}$$

where m_p, m_n, m_μ, E_μ, and V are the proton mass, the neutron mass, the muon mass, the muon energy ($\sqrt{p_\mu^2+m_\mu^2}$), and nuclear potential energy (27 MeV for ^{16}O), respectively. The Fermi motion of the neutron are neglected in this formula. By using the relationship between $E_\nu^{\rm rec}$ and (p_μ, θ_μ), we reconstruct the E_ν spectrum at ND, $\Phi_{\rm ND}(E_\nu)$.

We extrapolate $\Phi_{\rm SK}(E_\nu)$ from $\Phi_{\rm ND}(E_\nu)$ by multiplying the neutrino flux ratio of the far site to the near site, $R_{F/N}(E_\nu)$, *i.e.* $\Phi_{\rm SK}(E_\nu)$ is expressed by

$$\Phi_{\rm SK}(E_\nu) = R_{F/N}(E_\nu) \cdot \Phi_{\rm ND}(E_\nu). \tag{2.3}$$

Since the shape of $\Phi_{\rm ND}(E_\nu)$ is not the same as that of $\Phi_{\rm SK}(E_\nu)$ in the K2K experiment, $R_{F/N}(E_\nu)$ depends on E_ν. The strategy to obtain $R_{F/N}(E_\nu)$ is described in Section 2.3.3.

The CC-QE candidate events in SK are selected, and the reconstructed E_ν of these events are finally compared with $\Phi_{\rm SK}(E_\nu)$ by using a maximum likelihood method.

2.2.2 Comparison of the number of events between ND and SK

We compare the number of events between ND and SK by following three steps.

1. Count the number of events at ND, $N_{\rm ND}^{\rm obs}$.
2. Obtain the expected number of events at SK, $N_{\rm SK}^{\rm exp}$, by extrapolating from $N_{\rm ND}^{\rm obs}$.
3. Compare the number of observed SK events, $N_{\rm SK}^{\rm obs}$, with $N_{\rm SK}^{\rm exp}$.

In this analysis, all event types are used to maximize the statistical sensitivity.

We introduce the estimation of $N_{\rm SK}^{\rm exp}$. In the null oscillation case, $N_{\rm SK}^{\rm exp}$ is written by

$$\begin{aligned} N_{\rm SK}^{\rm exp} &= \frac{\int dE_\nu \cdot \Phi_{\rm SK} \cdot \sigma_{\rm SK} \cdot \epsilon_{\rm SK}}{\int dE_\nu \cdot \Phi_{\rm ND} \cdot \sigma_{\rm ND} \cdot \epsilon_{\rm ND}} \cdot \frac{M_{\rm SK}}{M_{\rm ND}} \cdot N_{\rm ND}^{\rm obs} \\ &= \frac{\int dE_\nu \cdot \Phi_{\rm ND} \cdot R_{F/N} \cdot \sigma_{\rm SK} \cdot \epsilon_{\rm SK}}{\int dE_\nu \cdot \Phi_{\rm ND} \cdot \sigma_{\rm ND} \cdot \epsilon_{\rm ND}} \cdot \frac{M_{\rm SK}}{M_{\rm ND}} \cdot N_{\rm ND}^{\rm obs}, \end{aligned} \tag{2.4}$$

where $\sigma_{\rm SK}$ ($\sigma_{\rm ND}$) is the neutrino cross-section with the target material of SK (ND), $\epsilon_{\rm SK}$ ($\epsilon_{\rm ND}$) is the detection efficiency of SK (ND), and $M_{\rm SK}$ ($M_{\rm ND}$) is the target mass of SK (ND). Since Φ, σ, and ϵ depend on E_ν, they are integrated by E_ν.

One of the characteristics of this analysis is the error cancellation between ND and SK. In Equation (2.4), for example, $\Phi_{\rm ND}$ are included in both the numerator and the denominator. Even if $\Phi_{\rm ND}$ have ambiguities, their deviations from the true values are identical. As a result, their influence on $N_{\rm SK}^{\rm exp}$ are reduced to be almost negligible. Similarly, if the target material of ND is the same as that of SK (water), *i.e.* $\sigma_{\rm ND} = \sigma_{\rm SK}$, the error on the neutrino-nucleus cross-section is also canceled out. Thus, a near detector with water target is necessary for this analysis.

Finally, we discuss the statistical sensitivity of this analysis. Suppose that the oscillation parameters are, for example, $\Delta m^2 = 3 \times 10^{-3}$ [eV^2] and $\sin^2 2\theta = 1$ (Figure 2.2), the number of SK events is expected to be 65% of the null oscillation case. Therefore, we need at least 100 events (10% statistical error) to exclude the null oscillation hypothesis with three standard deviations (99.7% C.L.) if the systematic error is negligible. This requirement is one of the most important subjects for the design of the K2K experiment.

2.3 Design of the experimental setup

Based on the analysis strategy, we describe the design of each experimental setup. Figure 2.3 shows the schematic view of the K2K setup.

2.3.1 Neutrino beamline

The ν_μ beam is mainly produced by decays of positive pions in flight ($\pi^+ \to \mu^+ + \nu_\mu$). These pions are produced by hitting 12 GeV protons on an aluminum target, and focused by a pair of magnetic horns. The pions decay into ν_μ and μ^+ in a 200m-long decay volume. The ν_μ beam passes through ND located 300m downstream of the target, and flies toward SK. The design of the target, the horns, and the decay volume are optimized to maximize the neutrino flux (Section 3.2.2 and 3.2.3).

2.3.2 Beam monitoring

To confirm that the direction and the yield of the neutrino beam are stable for each beam pulse, we monitor the primary proton beam and the muon from pion decay. Primary proton beam monitors (Section 3.2.1) are installed in the transport line between the accelerator and the production target. The muon from pion decay is measured by the MUMON detector (Section 3.2.4) installed behind the beam dump.

2.3.3 Extrapolation of the neutrino flux from ND to SK

We explain the concept of the flux extrapolation. If the neutrino beam is produced at a point source, the Far/Near flux ratio $R_{F/N}(E_\nu)$ is

$$R_{F/N}(E_\nu) = \frac{L_{\rm ND}^2}{L_{\rm SK}^2}, \tag{2.5}$$

where $L_{\rm ND} = 300$ m ($L_{\rm SK} = 250$km) is the distance between the neutrino source and ND (SK). In other words, the flux follows L^{-2} law, and $R_{F/N}(E_\nu)$ is independent of E_ν. In the K2K experiment, however, $R_{F/N}(E_\nu)$ is different from Equation (2.5) and not independent of E_ν due to the finite size of the pion decay volume.

We evaluate $R_{F/N}(E_\nu)$ by the following procedure.

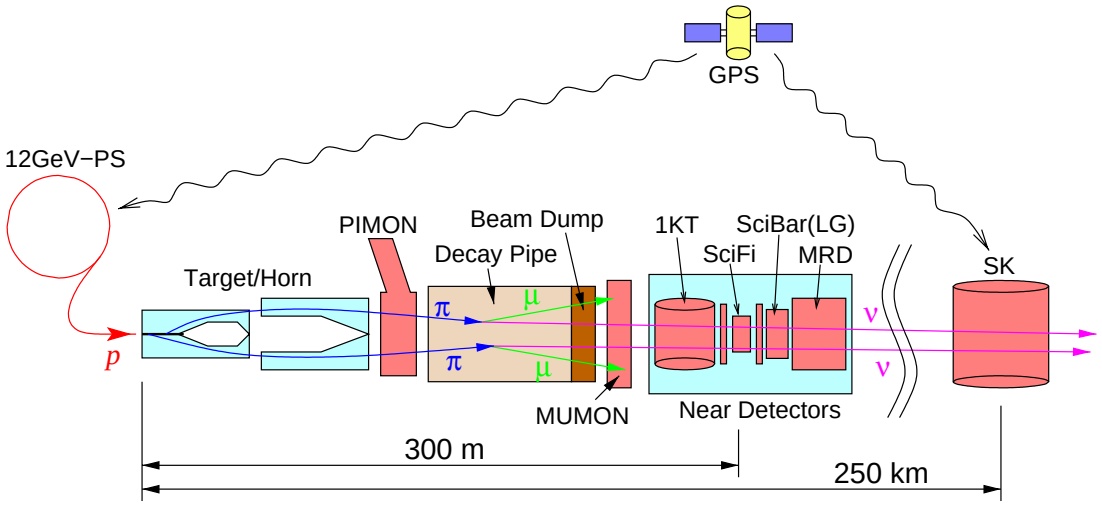

Figure 2.3: Schematic view of the K2K setup.

1. Obtain the property (momentum and direction) of produced pions.
2. Evaluate $\Phi_{\rm ND}(E_\nu)$ and $\Phi_{\rm SK}(E_\nu)$ by using the decay kinematics of a pion and the geometry of the decay volume.
3. Take the ratio between $\Phi_{\rm ND}(E_\nu)$ and $\Phi_{\rm SK}(E_\nu)$.

Since the pion decay kinematics is well-known, the uncertainty in the second step is small. There is no ambiguity in the third step, because we just calculate the ratio. However, the first step has a large uncertainty, according to past pion production measurements (Section 5.1.2). Therefore, we measure the property of the pions just after the horn magnets by using the PIMON detector (Section 3.2.5). The analysis of $R_{F/N}(E_\nu)$ is described in Chapter 10.

2.3.4 Far detector: Super-Kamiokande

We employ Super-Kamiokande (SK) as the far detector of K2K. SK is a 50kt water Cherenkov detector in Kamioka, Gifu prefecture (Section 3.4). The reason why SK is suitable for the far detector is because SK has sufficient mass to accumulate neutrino events. The event rate in SK is expected to be 0.4 event/day without neutrino oscillation. Therefore, the requirements for the statistics (more than 100) is satisfied by the run time of a few hundred days.

Furthermore, SK is able to select CC-QE events for the analysis of neutrino energy spectra. The CC-QE candidate event of SK is the event in which only one muon-like particle is observed, because the associated proton often does not emits Cherenkov light due to its high Cherenkov threshold in water[2] (~ 1.1 GeV/c).

2.3.5 Near detector complex

Purposes of ND are summarized below:

- Measure the E_ν spectrum at ND, $\Phi_{\rm ND}(E_\nu)$, which is used by both the E_ν spectrum analysis and the event rate analysis.
- Measure the number of events in ND, $N_{\rm ND}^{\rm obs}$, to estimate the expected number of events in SK, $N_{\rm SK}^{\rm exp}$.

[2]The Cherenkov threshold of a muon is approximately 0.12 GeV/c.

- Study neutrino interaction to reduce uncertainties in the neutrino cross-section, the kinematics of neutrino scattering, etc.

- Monitor the neutrino beam stability by observing the neutrino itself.

To fulfill these purposes, ND is designed as a combination of a 1kt water Cherenkov detector (1KT) and a Fine-Grained Detector (FGD). FGD is comprised of a scintillating fiber tracker with water target (SciFi), a lead glass calorimeter (LG) until 2001, a fully-active scintillator detector (SciBar) since October 2003, and a muon range detector (MRD).

Detector components of 1KT (Section 3.3.1) are same as those of SK except for the size of the water tank. Therefore, the detector response is almost same as SK. As a result, the error cancellation in Equation (2.4) is maximized by using 1KT. We employ 1KT to obtain $N_{\rm ND}^{\rm obs}$ in this thesis. We also use 1KT to reconstruct the E_ν spectrum.

SciBar (Chapter 4) and SciFi (Section 3.3.2) are tracking detectors designed to detect both the muon and the proton from CC-QE interaction. Therefore, SciBar and SciFi are suitable for the E_ν spectrum measurement. When we study neutrino interaction, we mainly use SciBar data because SciBar has better track finding capability.

MRD (Section 3.3.5) is constructed to measure the energy of a muon from SciBar or SciFi and to monitor the neutrino beam stability. Most part of MRD is made of iron to identify a muon.

LG (Section 3.3.3) is installed to measure the electron neutrino contamination in the beam. In this thesis, we do not use electron neutrino data, but muon energy deposit in LG is into taken into account if a muon passes through LG.

2.3.6 Timing synchronization

Timing synchronization between the accelerator and SK is performed using GPS[3] (Section 3.5). Although SK data has a atmospheric neutrino background ($\sim$ 6 events/day), this background becomes negligible if we select the event synchronized with a beam pulse.

2.4 History of K2K

A brief history of the K2K experiment is summarized in Table 2.1. The neutrino data taking started in June 1999 with the horn current of 200 kA (80% of design value). This period is named "K2K-Ia". In November 1999, the horn current increased to 250 kA (design value), and the data had been accumulated until July 2001 (K2K-Ib). The results from K2K-Ia and K2K-Ib are published in [9] for $\nu_\mu \to \nu_x$ oscillation and in [16] for $\nu_\mu \to \nu_e$ oscillation.

In November 2001, a severe accident happened in Super-Kamiokande, and many PMTs were crashed. After the reconstruction of SK with a half PMT density, the experiment resumed in January 2003, and took data until June 2003 (K2K-IIa). In the K2K-IIa period, there was no lead glass calorimeter. A new near detector, SciBar, was installed in the summer 2003, and the neutrino data was taken again from October 2003 to February 2004 (K2K-IIb). In this thesis, we describe the first result from K2K-IIa, K2K-IIb, and SciBar.

Figure 2.4 shows the number of delivered protons on the target (POT). In total, 1.01×10^{20} POT have been delivered. The POT recorded by SK are 8.9×10^{19}, which are analyzed to examine neutrino oscillation. Since the beam property of K2K-Ia is different from that of the other runs due to smaller horn current, K2K-Ia is separately treated. We use all the runs for the comparison of the number of events between ND and SK. On the other hand, we do not employ K2K-Ia for the comparison of the neutrino energy spectra but K2K-Ib and K2K-II.

[3]Global Positioning System.

Table 2.1: History of K2K.

1995	Proposal was approved at KEK.
1996	Civil construction started.
1999 Jun.	Data taking with the horn current of 200kA. (K2K-Ia)
1999 Nov.– 2001 Jul.	Data taking with the horn current of 250kA. (K2K-Ib)
2001 Nov.	SK accident. Removal of LG.
2003 Jan.– 2003 Jun.	Data taking with a half PMT density of SK. (K2K-IIa)
2003 Jul.– 2003 Sep.	Construction of SciBar.
2003 Oct.– 2004 Feb.	Data taking with SciBar (K2K-IIb)

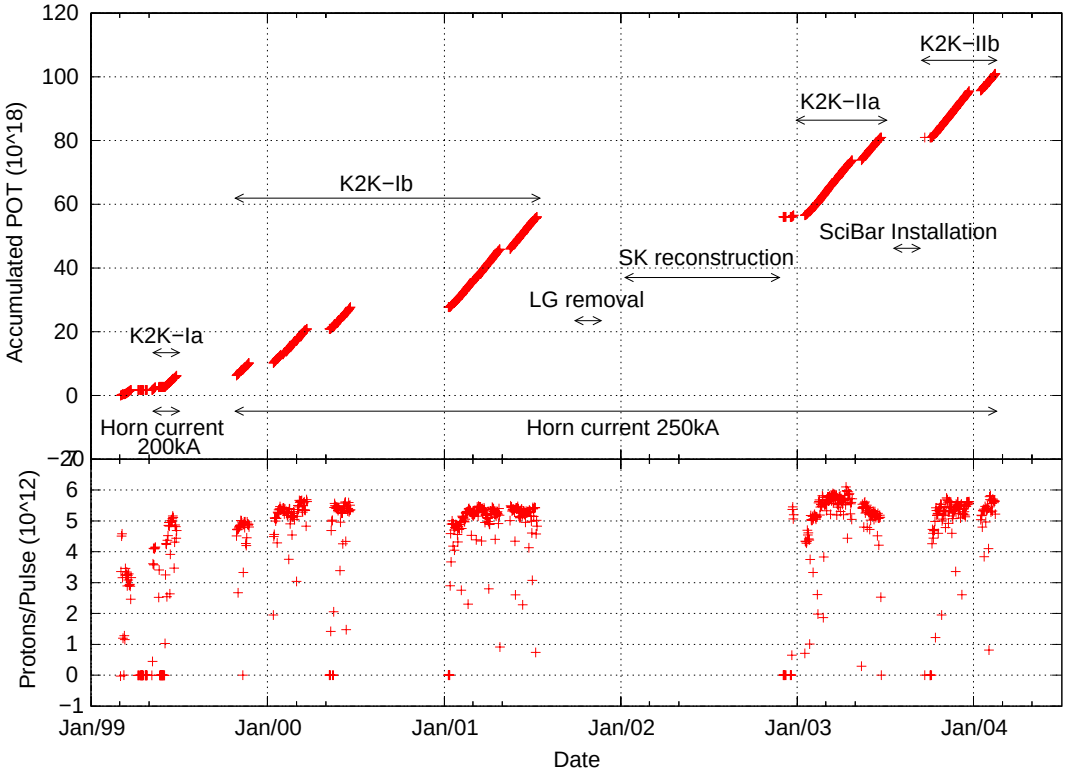

Figure 2.4: The number of protons delivered to the target. The upper figure shows the accumulated number since the beginning of the experiment. The name of each period, horn current, and changes of the detector configuration are also illustrated. The lower figure shows the number of protons per spill.

Chapter 3

Experimental Setup

The setup of the K2K experiment is composed of accelerator, neutrino beamline, near detectors, and a far detector (Super-Kamiokande). In this chapter, we describe each component and the basic performance.

3.1 Primary proton accelerator

The primary proton beam is provided by the 12 GeV proton synchrotron (KEK-PS)[18] at KEK. The specifications of KEK-PS are summarized in Table 3.1. Protons are accelerated by 750 keV Cockcroft-Walton accelerator, 40 MeV drift-tube LINAC, 500 MeV booster synchrotron, and 12 GeV synchrotron (main-ring). Approximately 7×10^{12} protons are accelerated in every repetition cycle of 2.2 seconds. Protons with 12 GeV kinetic energy are extracted in one turn, and transported to the primary proton beamline. This extraction method is called "fast extraction", and each pulse of the extracted proton beam is called "spill". The harmonic number of the main-ring is nine, and hence the extracted beam has nine-bunch time structure. The bunch spacing is 125 nsec, and the duration of the spill is 1.1 μsec.

3.2 Beamline

3.2.1 Primary proton beamline

Figure 3.1 is a schematic view of the beamline. The proton beam is extracted toward the north, and it is bent by about 90 degrees toward Super-Kamiokande in the arc section. The beam is finally focused on the production target. Due to the sphericity of the Earth, the beam is bent downward by 1.075 degrees.

Intensity monitors and profile monitors are ubiquitously installed in the beamline. Current transformers (CT) are used to monitor the beam intensity. CT is a toroidal coil which picks up the induced current from the beam. Figure 3.2 shows a schematic view of CT, and Figure 3.3 shows an oscilloscope image of a typical signal from CT, in which a clear nine-bunch structure is seen. CT is read by a charge-sensitive ADC with spill-by-spill basis. The transportation efficiency of the proton beam is monitored by using the beam intensity of each CT. The CT just before the target ("TGT-CT" in Figure 3.1) measures the number of delivered protons on the target (POT). Since the neutrino beam flux is proportional to POT, we often use POT as a normalization factor for the neutrino event rate[1].

The proton beam profile is measured by a segmented plate ionization chamber (SPIC)[19]. Figure 3.4 shows a schematic view and a typical profile of SPIC. SPIC consists of three copper

[1] Figure 2.4 shows the number of protons measured by TGT-CT.

Table 3.1: Specifications of KEK 12 GeV proton synchrotron (fast extraction).

Kinetic energy	12 GeV
# protons in main-ring	7×10^{12} protons/spill
# bunches	9
Bunch separation	125 nsec
Spill duration	1.1 μsec
Repetition cycle	2.2 sec

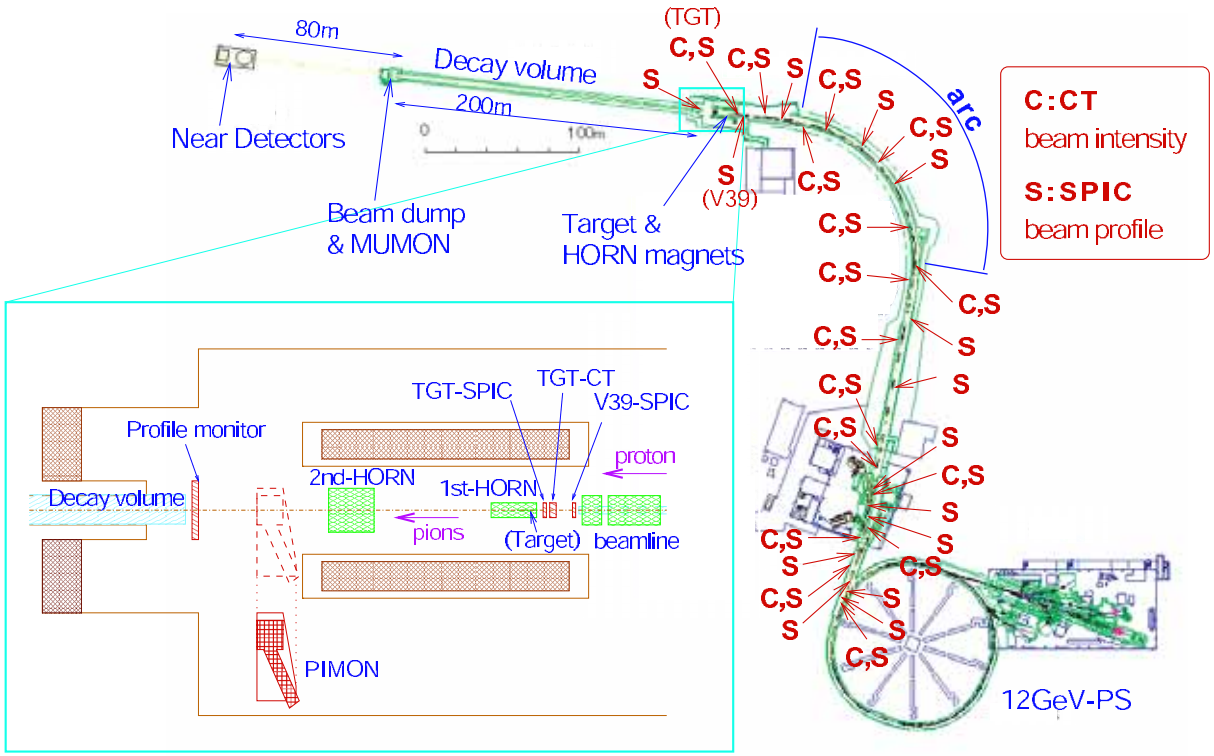

Figure 3.1: Schematic view of the beamline. The characters "C" and "S" indicate the locations of the CTs and the SPICs, respectively. A zoomed view of the target station is also shown.

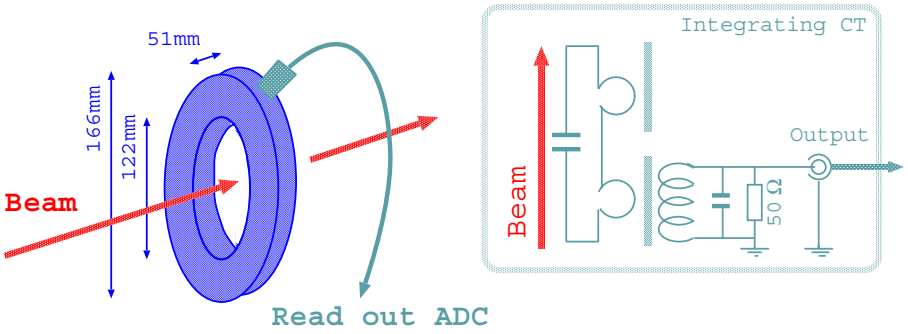

Figure 3.2: Schematic view of CT.

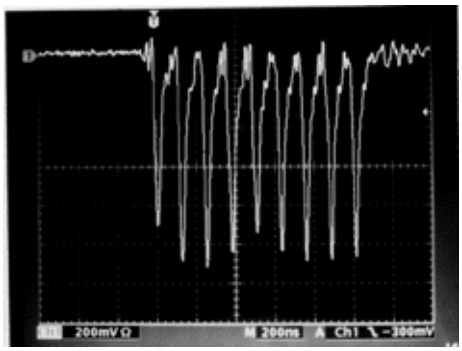

Figure 3.3: Oscilloscope image of CT. Horizontal axis is 200 nsec/div. The nine-bunch structure can be seen clearly.

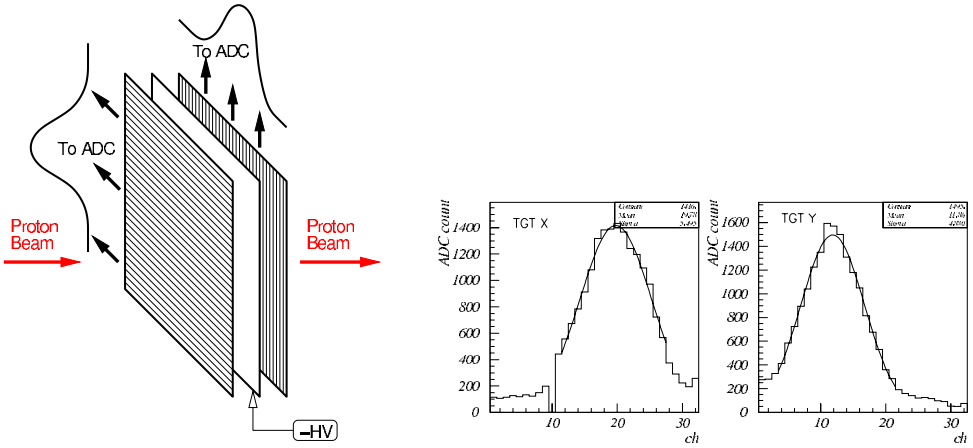

Figure 3.4: Schematic view and typical profile of SPIC. The profile is taken by the SPIC just before the target.

sheets. The central one is for the cathode plane, and the outer ones are for horizontal and vertical readout anode planes which are composed of narrow strips. The SPIC just before the target is segmented every 1.27 mm, and the other ones are divided every 5 mm. The gaps between the electrodes are filled with helium gas. The signal from each strip is recorded by a charge-sensitive ADC.

3.2.2 Production target and magnetic horns

Figure 3.5 shows a schematic view of the production target and the two magnetic horns[20]. Positive pions produced in the target are focused by the horns, and negative ones are defocused. To maximize the focusing effect, the aluminum target rod (66cm-long) is installed inside the first horn, and it also performs as the inner conductor of the horn current. The diameter of the target was 20 mm in June 1999, and it is 30 mm since November 1999. The horns are driven by a pulsed current, whose peak was 200 kA in June 1999, and is 250 kA since November 1999. The maximum magnetic field of 3.3 T is achieved on the surface of the target, when the horn current is 250 kA. The horn current is monitored by CTs installed in the power lines.

Figure 3.6 shows the comparison of neutrino fluxes with and without the horn current using a Monte Carlo simulation. In case of 250 kA operation, the neutrino flux above 0.5 GeV is 22 times as large as that without the horn current.

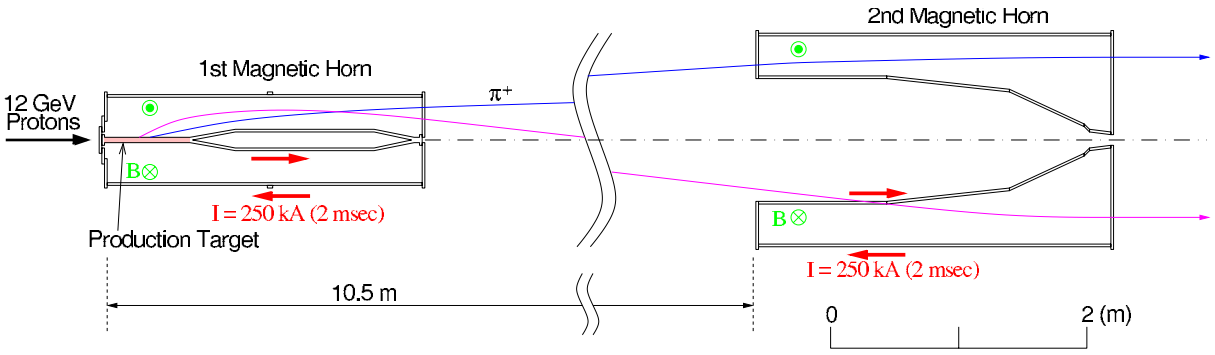

Figure 3.5: Schematic view of the production target and horns.

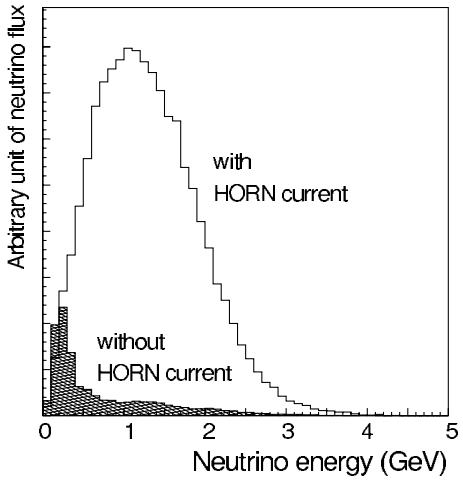

Figure 3.6: The neutrino flux with (solid line) and without (hatched ares) horn current. This is estimated by a Monte Carlo simulation.

3.2.3 Decay tunnel

The positive pions focused by the horns enter a 200m-long decay volume as shown in Figure 3.7. The pions decay to muon neutrinos and positive muons in this volume. The decay volume is a cylindrical pipe with three sections: 1.5m-diameter 10m-long, 2.0m-diameter 90m-long, and 3.0m-diameter 100m-long cylinders. The decay volume is filled with 1 atm. helium gas to reduce hadronic interactions. At the end of the decay volume, there is a beam dump composed of 3.5m-thick iron and 2.0m-thick concrete. The beam dump stops all the particles except for neutrinos and high energy muons.

3.2.4 Muon monitor

A muon monitor (MUMON)[21] is installed behind the beam dump. The purpose of MUMON is to measure the beam direction and the muon yield spill-by-spill basis. Figure 3.8 shows a schematic view of MUMON. MUMON consists of an ionization chamber (ICH) and a silicon pad detector array (SPD). Muons with the momentum above 5.5 GeV/c are observed by MUMON. These muons are finally absorbed by downstream soil.

ICH is a segmented ionization chamber like SPIC. The dimensions are 190 cm (horizontal) $\times$ 175 cm (vertical). The anodes of ICH are segmented into 5cm-pitch strips. The number of

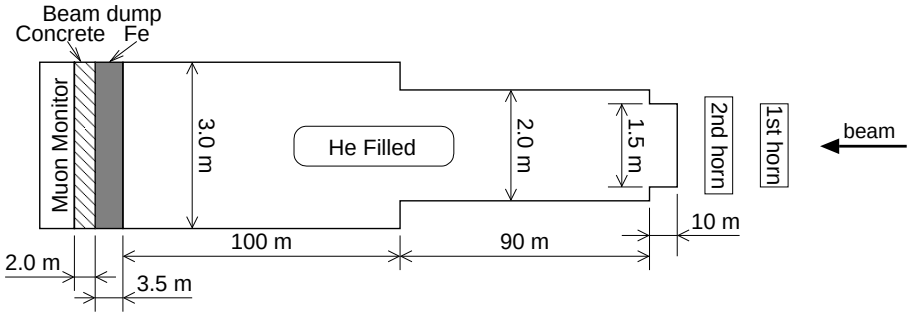

Figure 3.7: Schematic view of the decay tunnel.

readout strips is 36 channels in the horizontal direction and 32 channels in the vertical direction. Because of the difficulty to make a large chamber, ICH consists of six modules with the size of 60×90 cm^2. The corresponding strip lines of adjacent modules are electrically connected to make a long strip. All the modules are inserted into a gas vessel filled with argon gas. A signal of each strip is read by a charge-sensitive ADC. The upper two histograms of Figure 3.9 show a typical profile of ICH. Some insensitive areas in the profile are due to the gaps between the modules.

SPD consists of two types of silicon pad detectors: small-type and large-type. The small-type detector has a sensitive area of 1.0×2.0 cm^2, and 17 pads are arranged along the horizontal and the vertical axes with 35cm-pitch. The large-type detector has a sensitive area of 3.4×3.05 cm^2, and 9 pads are arranged diagonally with 74.2 cm interval. The signal from each pad is read by a charge-sensitive ADC. The lower two plots of Figure 3.9 show a typical profile of SPD (small-type).

ICH data is used for the beam direction measurement, because ICH observes finer profile than SPD. SPD data is employed to monitor the muon yield, because the output of SPD is more stable than ICH. Thus, ICH and SPD are complementary to each other.

3.2.5 Pion monitor

In order to obtain the neutrino energy spectra at near and far sites and the spectrum ratio between them, the property of the secondary pions was measured in some special short runs, by using a gas Cherenkov imaging detector (PIMON). Since the decay kinematics of a pion is well-known, we can predict the neutrino energy spectra at both near and far sites from the momentum and the direction of each pion, and we obtain the spectrum ratio between near and far sites. Therefore, we measured the (p_π, θ_π) two-dimensional distribution just after the horns using a pion monitor (PIMON)[21], where p_π is a pion momentum and θ_π is a pion angle with respect to the beam axis. Since there are some pion production models which are significantly different from each other (Section 5.1.2), it is another purpose of PIMON to choose the best model among them.

Since the target diameter and the horn current is different between the K2K-Ia (June 1999) and the other runs (since November 1999), PIMON data were taken twice in June 1999 (horn current 200 kA) and November 1999 (250 kA).

Figure 3.10 shows a schematic drawing of PIMON. Cherenkov photons emitted from pions are reflected and focused by a fan-shaped spherical mirror. These photons are detected by a PMT array at the focal plane of the mirror. Detector components are put into a gas vessel filled with freon gas R-318 (C_4F_8). Since the fan-shaped mirror focuses the Cherenkov photons from only a small region of the azimuthal angle of pions, Cherenkov rings are aligned along a line, as

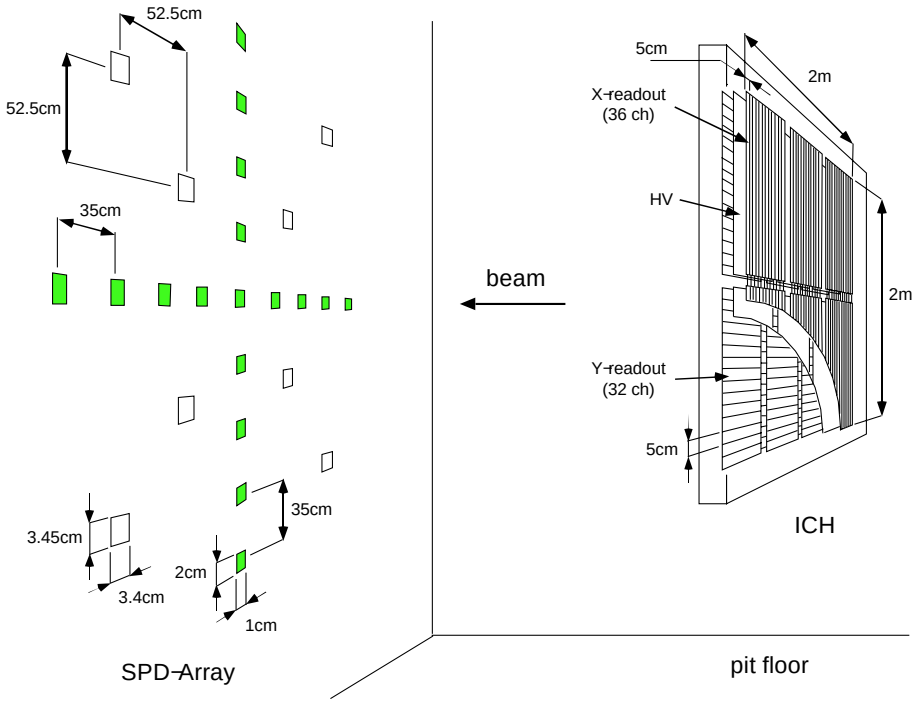

Figure 3.8: Schematic view of MUMON. An ionization chamber (ICH) is located upstream, and silicon pad detectors (SPD) are arranged downstream For SPD, filled boxes show small-type pads, and open boxes show large-type pads.

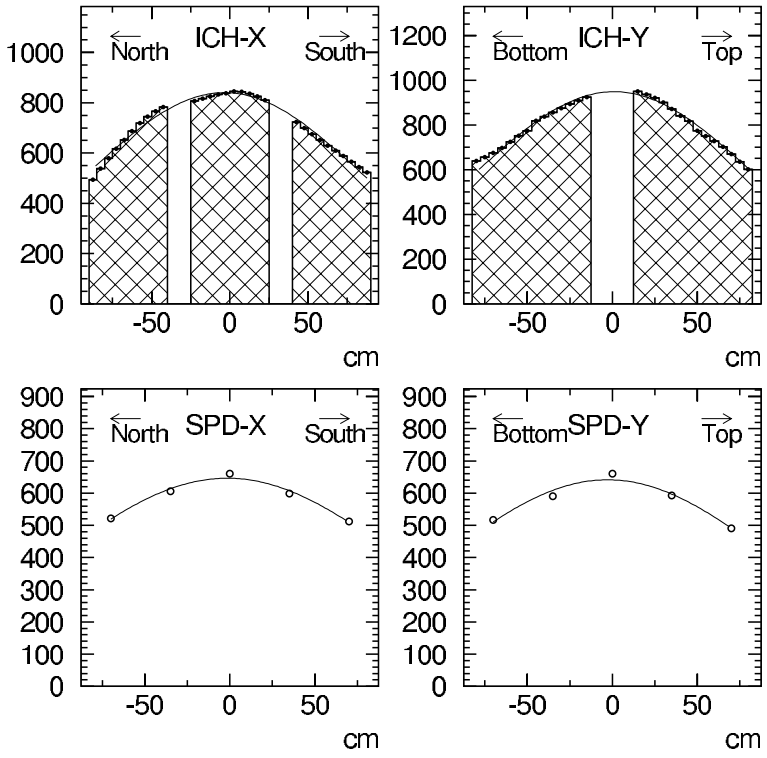

Figure 3.9: A typical profile of MUMON. The upper figures are the profile of ICH, and the lower ones are that of SPD (small-type).

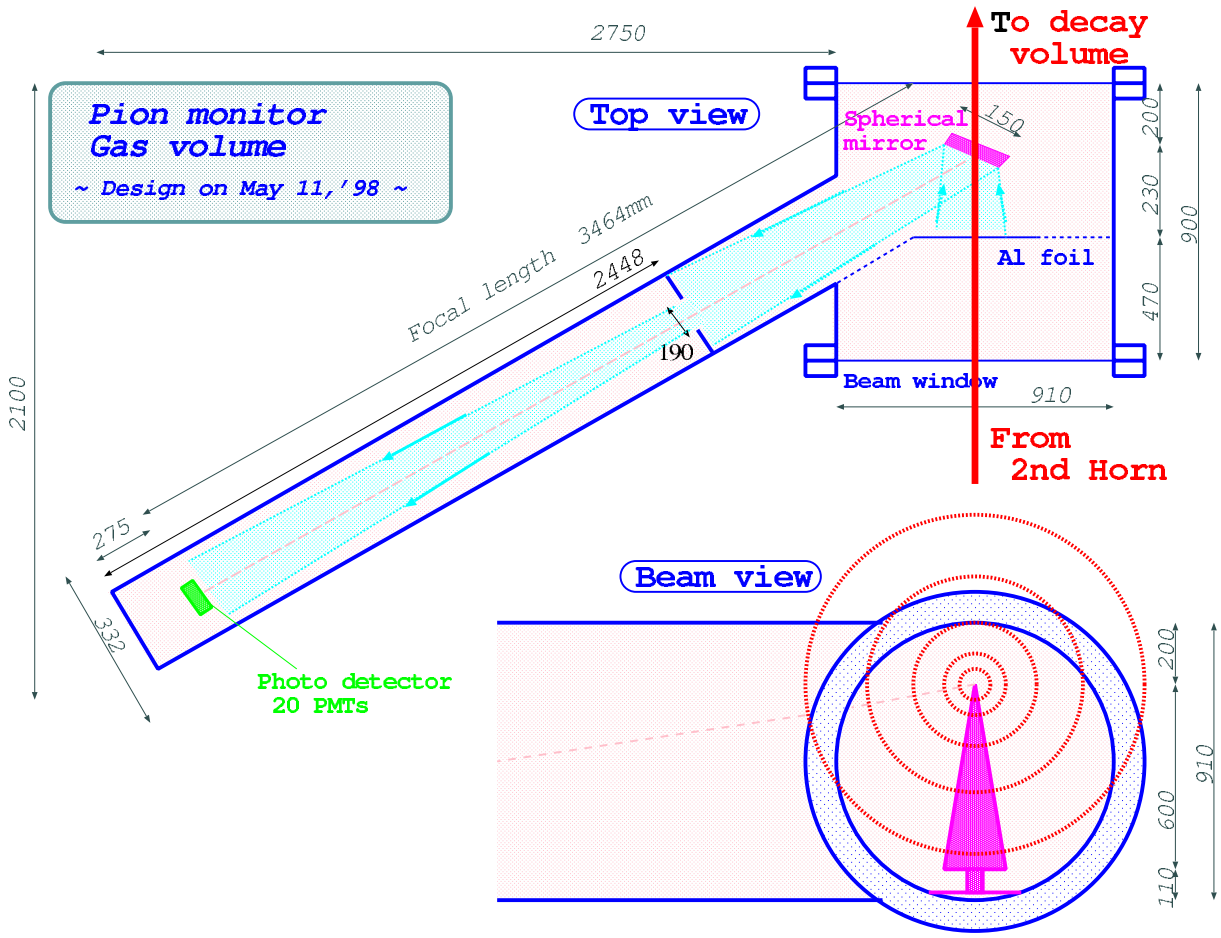

Figure 3.10: Schematic drawing of PIMON.

shown in Figure 3.11. Therefore, pion kinematics are obtained from one-dimensional readout. Pion angle θ_π is reproduced from the position of the ring image.

The refractive index is adjustable by varying the pressure. PIMON data were taken with several different pressure conditions. The pion momentum distribution is extracted from Cherenkov opening angle and the threshold momentum of each condition. To avoid a large background from the primary 12 GeV proton, the refractive index is set lower than the threshold of 12 GeV proton, $n = 1.00264$. Due to this limit, we cannot measure the pion momentum region of $p_\pi < 2$ GeV/c, which corresponds to the neutrino energy region of $E_\nu < 1$GeV.

The PMT array consists of 20 PMTs which are arranged every 3.5 cm. The sensitive region of the PMT is a 8mm-diameter circle. The array is moved vertically by 40mm for calibration and for fine data taking. Since the PMT is exposed to a intense Cherenkov light ($\sim 10^9$ photons instantly), a special photo-cathode (multi-alkali: Sb-Na-K-Cs) is used and the gain is set to be small ($\sim$ 300 in June 1999, 20–50 in November 1999) to keep the response linear.

3.2.6 Data acquisition

The data acquisition (DAQ) system of beamline monitors is triggered by an accelerator signal synchronized with beam spill timing. The data are taken with spill-by-spill basis. Due to the long beamline, there are four DAQ stations and six front-end computers. The data are sent to a

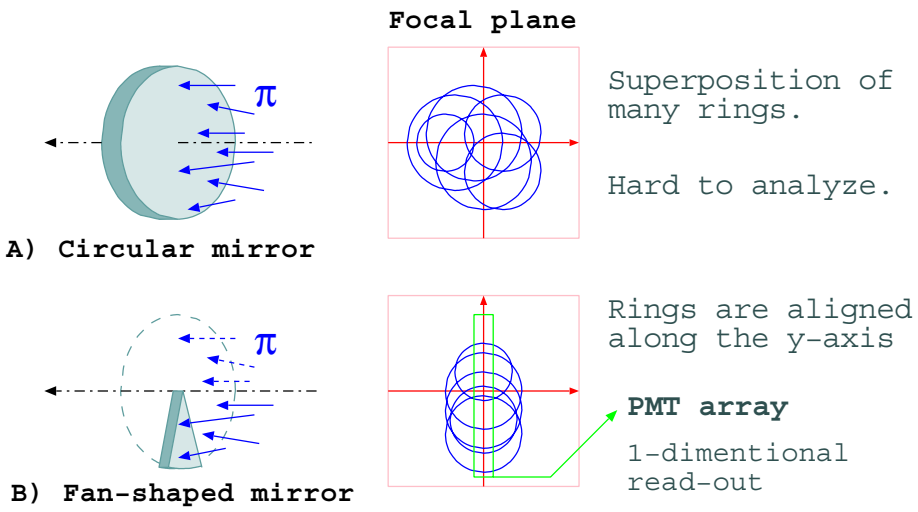

Figure 3.11: The advantage of the fan-shape mirror of PIMON. The upper figure shows ring images of a circular mirror, and the lower figure shows those of a fan-shaped mirror. Cherenkov rings are aligned along a line in the case of a fan-shaped mirror.

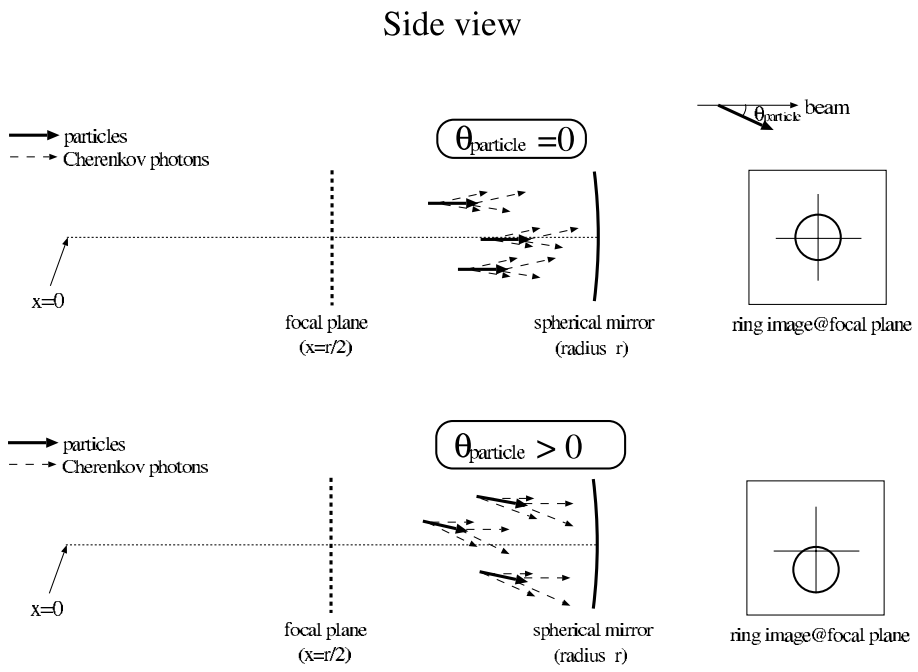

Figure 3.12: Principle of θ_π measurement of PIMON.

host computer via Ethernet and stored to a hard disk drive. In addition to the beam monitors, GPS time stamp for each beam timing is recorded and stored, to synchronize between a beam spill and a Super-Kamiokande event. The detail of GPS is described in Section 3.5.

3.3 Near detector complex

Based on the conceptual design of the near detector (ND) described in Section 2.3.5, ND is constructed as a combination of several neutrino detectors: a 1KT water Cherenkov detector (1KT), a scintillating fiber tracker with water target (SciFi), a lead glass calorimeter (LG) for K2K-Ia and K2K-Ib, a fully-active scintillator detector (SciBar) for K2K-IIb, and a muon range detector (MRD). A schematic view of ND is shown in Figure 3.13. Since the beam center is about 10 m underground, ND is installed in the large cylindrical hole with the dimensions of 16m-deep and 24m-diameter.

3.3.1 1kt water Cherenkov detector

A 1kt ring-imaging water Cherenkov detector (1KT)[22] is installed at the most upstream of the near detector hall. It is a small version of Super-Kamiokande. Figure 3.14 shows a schematic view of 1KT. The water tank is a cylinder with the dimensions of 10.8 m in diameter and 10.8 m in height. Approximately 1 kton of pure water are filled in the tank. The inside of the tank is optically separated into two parts: the inner detector (ID) of the cylindrical volume of 8.6 m in diameter and 8.6 m in height, and the outer detector (OD) surrounding ID. There are 680 20-inch PMTs facing inward on the surrounding frame of ID. The photo-cathode coverage of ID is 40%. The thickness of OD is 1 m for the barrel part and 0.6 m for the bottom part. There are 68 8-inch PMTs facing outward on the support frame: 42 of them are attached to the upstream 1/3 of the barrel part and the rest are attached to the bottom. The purpose of OD is to veto incoming particles induced by neutrinos and to trigger cosmic ray events for calibration. The water is always circulated and cleaned by a purification system. This system removes dusts, bacterias, and metallic ions. The attenuation length of the water has been kept stably longer than 50 m for the whole runs.

The refractive index n of water is 1.33–1.36 depending on the wavelength. The momentum thresholds of Cherenkov radiation for electron, muon, pion, and proton are 0.58, 120, 159, and 1070 MeV/c, respectively. A particle with $\beta = 1$ emits approximately 340 photons per 1 cm in the wavelength 300–600 nm, where a 20 inch PMT is sensitive. The opening angle of Cherenkov radiation is 42 degrees.

Both charge and timing of PMT signals are digitized by a front-end module, called "ATM (analog timing module)"[23]. One ATM processes 12 PMTs. In addition, ATM generates an analog sum of PMT signals (PMTSUM) and a rectangular signal whose pulse height is proportional to the number of hit PMTs (HITSUM). The analog sum of all the PMTSUM signals from ID is recorded by 500 MHz and 100 MHz flash-ADCs. The flash-ADC data is used to count the number of events in a spill by counting the number of peaks in the PMTSUM signal, because ATM cannot separate multiple events within 1.2 μsec. Trigger condition is that the sum of the HITSUM signals from all ATMs is greater than or equal to 40 hits. In 1999, a signal reflection at the input of ATM was found, and it was a cause of fake events. Therefore, buffer amplifiers have been attached to ATM for impedance matching since January 2000.

PMT gain and timing are calibrated by some light sources[22]. The uncertainty in the PMT gain is several % level. The absolute energy scale is checked by cosmic ray muons and neutrino events. There are three kinds of events for cosmic rays: vertically through-going muons, horizontally through-going muons, and stopping muons within ID. For each category, total Cherenkov light yield per unit length is compared with the MC simulation. The fractional difference of

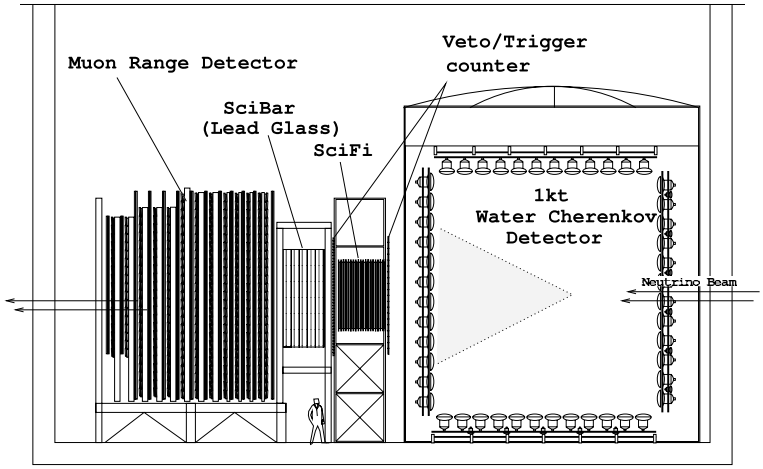

Figure 3.13: Schematic view of the near detector complex.

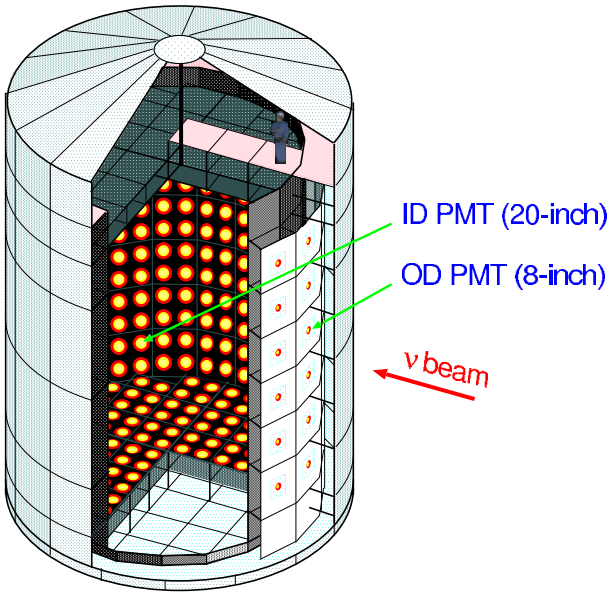

Figure 3.14: Schematic view of 1KT.

this quantity between data and the MC simulation, (MC–DATA)/DATA, is illustrated in Figure 3.15. For the energy scale calibration using neutrino events, we use the invariant mass of neutral pions (π^0) and the total photo-electrons from outgoing muons. The results are shown in Figure 3.15 together with the cosmic ray results. Thus, all the measurements are within +2.0% –3.0%. We assign this value to the systematic error of the energy scale.

3.3.2 Scintillating fiber detector

A scintillating fiber tracker with water target tanks (SciFi)[24] is located downstream of 1KT. Figure 3.16 shows a schematic view of SciFi. SciFi consists of 20 scintillating fiber layers interleaved with 19 aluminum tanks filled with water. The scintillating fiber is made of polystyrene, and its diameter is 0.7 mm. Each tracking layer is composed of two fiber sheets for vertical and horizontal readout. The tracking area has the dimensions of 260×260 cm^2. The water target tank has a size of $240 \times 240 \times 6$ cm^3, and it is comprised of 15 rectangular pipes with 16×6 cm^2 cross-section and 1.8mm-thick aluminum wall. The weight of the target water is 6 tons in total.

The scintillating fibers are connected to image-intensifier tubes read out by CCD cameras (IIT-CCD). A hit fiber is seen as a cluster of CCD pixels. The gate width of the IIT-CCD is 100 μsec, which is much wider than the beam duration (1.1μsec). Therefore, fine timing information of a track is provided by an associating hit of a trigger/veto counter (TGC).

TGC is a plastic scintillator hodoscope installed upstream and downstream of SciFi. The upstream hodoscope consists of 20 scintillators with the size of $466 \times 20 \times 4$ cm^3, covering 466×400 cm^2 area. The downstream one is comprised of 40 scintillators with the dimensions of $466 \times 10 \times 4$ cm^3, covering the same area. Figure 3.17 shows a schematic view of the scintillator of TGC. The both ends of each scintillator are viewed by 2 inch PMTs. The timing and charge from each counter are recorded.

The hit finding efficiency of SciFi is measured by using cosmic rays. Figure 3.18(left) shows the hit finding efficiency for each IIT-CCD. The efficiency is approximately 95%[25]. The track finding efficiency is also estimated by using cosmic ray events. Figure 3.18(right) shows the efficiency as a function of the number of fiber sheets that a particle passes through. More than 90% of tracks are reconstructed if they penetrate more than five layers.

3.3.3 Lead glass calorimeter

A lead glass Cherenkov calorimeter (LG)[26] was located downstream of SciFi until 2001. The purpose is to distinguish electrons from muons for the measurement of the electron neutrino contamination in the beam. Figure 3.19 shows a schematic view of LG and the drawing of an LG cell. LG covers the area of 2.4 (vertical) $\times$ 3.0 (horizontal) m^2. The dimensions of the cell are approximately $12 \times 12 \times 34$ cm^3. A 3 inch PMT is attached to each cell. LG was once used in the TOPAZ experiment[27] at TRISTAN, and we reused it. The energy deposit of a minimum-ionizing particle is estimated to be 280 MeV if the particle goes perpendicularly to an LG module. LG was removed in fall 2001 to reduce material behind SciFi and to install a new detector SciBar.

3.3.4 SciBar detector

A fully-active scintillator detector, "SciBar", was installed at the same place as LG, in summer, 2003. The detail of SciBar is described in Chapter 4.

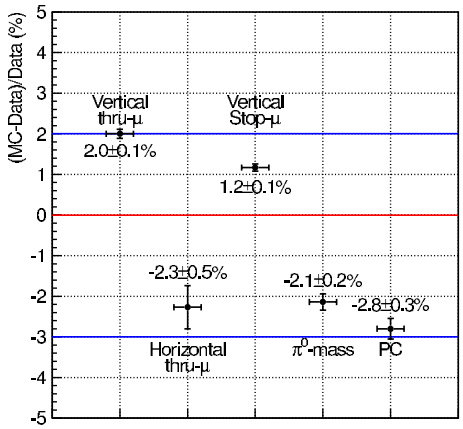

Figure 3.15: Check of the energy scale of 1KT. Using cosmic ray data, vertically through-going muons, horizontally through-going muons, and stopping muons within ID are investigated. The invariant mass of π^0 and outgoing muons (PC) from neutrino interactions are also examined. The vertical axis shows (MC–Data)/Data in %.

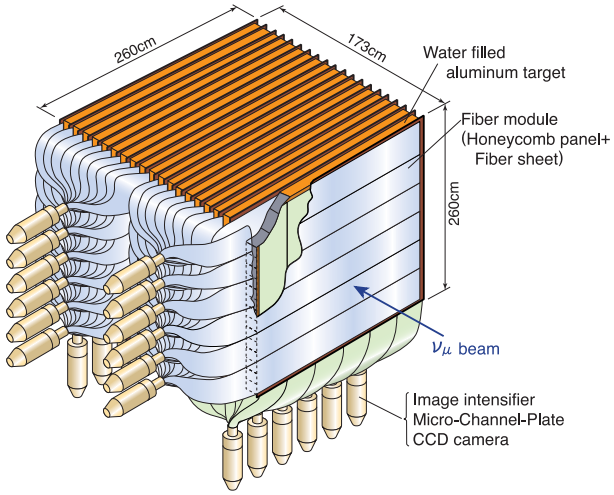

Figure 3.16: Schematic view of SciFi.

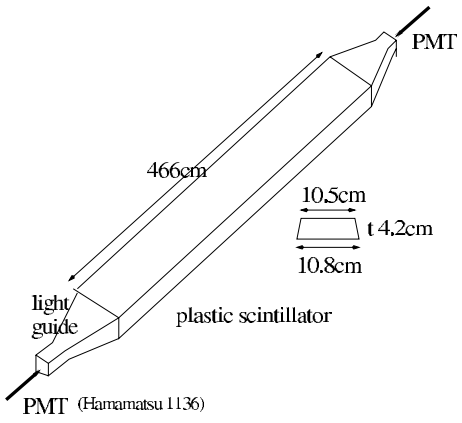

Figure 3.17: Schematic view of a scintillator of downstream TGC.

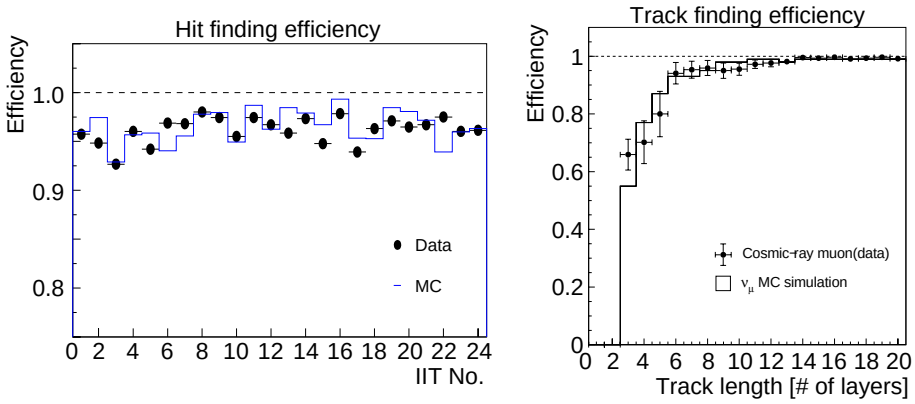

Figure 3.18: SciFi hit finding efficiency (left) and track finding efficiency (right). The horizontal axis of the left plot is a serial number of IIT-CCD, and that of the right is the number of layers which a particle penetrates.

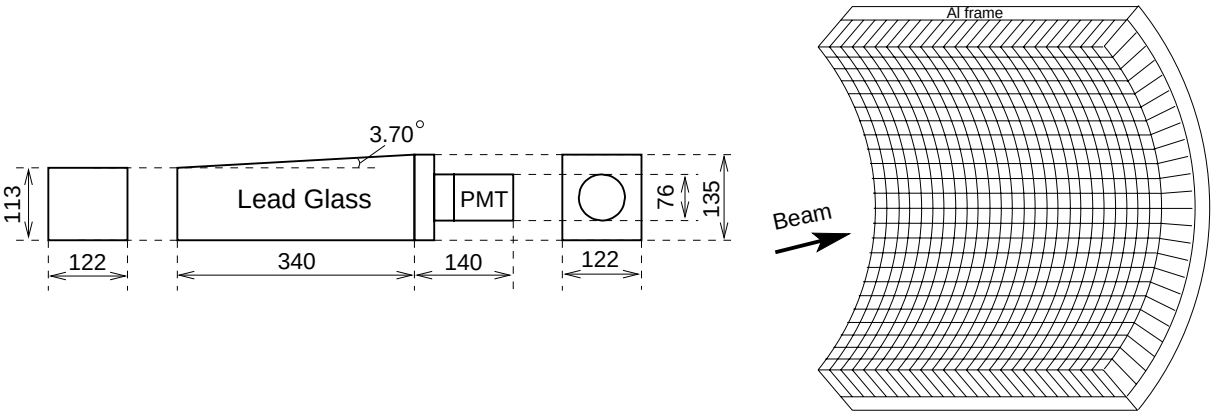

Figure 3.19: The left figure shows the drawing of an LG cell, and the right one shows a schematic view of LG.

3.3.5 Muon range detector

A muon range detector (MRD)[28, 29] is located at the most downstream of the near detector hall. One of the purposes of MRD is to measure the energy of a muon coming from SciFi or SciBar. The other functions are to monitor the neutrino beam by measuring the event rate, the beam profile, and the energy spectrum.

Figure 3.20 shows a schematic view of MRD. MRD consists of 12 iron absorbers sandwiched with 13 vertical and horizontal drift chamber layers. Each layer covers 7.6×7.6 m^2. In order to make the energy resolution of low energy muons better, upstream four iron plates are 10cm-thick, while the other plates are 20cm-thick. The total thickness of iron is 2 m, corresponding to the range of 2.8 GeV/c muons. The total weight of iron is 864 tons.

The drift chamber was manufactured for the VENUS experiment[30] at TRISTAN. A chamber module has eight drift tubes of 5×7 cm^2 cross-section and 7.6 m in length, and it is made of aluminum. In total, 829 modules are used. A tungsten wire of 70μm-diameter is located in the center of the tube. P10 gas, which is the mixture of 90% argon and 10% methane, is filled in the chamber. The timing of each hit wire is recorded by 6-bit TDC with 20 MHz clock.

The hit efficiency and the track finding efficiency are estimated by using cosmic rays. The hit efficiency is approximately 97%. Figure 3.21 shows the track finding efficiency as a function of the number of traversed chamber planes. The efficiency is approximately 65% if a muon penetrating two planes, 95% for a muon passing three planes, and 97.5% for a muon traversing more than three planes. The reason for the efficiency loss of a two-plane track is because a lower limit is imposed on the number of hits along a track candidate in order to remove fake tracks.

3.3.6 Data acquisition

The near detectors are triggered by the beam timing signal from the accelerator. 1KT data is collected by a Sun workstation with a VME bus. The data from TGC, LG, and MRD are fetched by a HP-RT VME-CPU board. Similarly, two HP-RT boards are used by SciFi. SciBar uses seven front-end PCs to take data: six are connected to VME crates, and the other combines all the SciBar data from them. Finally, a host computer (Sun workstation) collects the data from these front-end computers via Ethernet, sorts them according to the serial number of each spill, and stores them in a hard disk drive.

3.4 Far detector

The far detector, Super-Kamiokande (SK)[31], is a ring-imaging water Cherenkov detector, similar to 1KT. A schematic view of SK is shown in Figure 3.22. SK is a cylindrical tank filled with 50 ktons of pure water. SK is located at the Kamioka mine in Gifu prefecture, 250 km far from KEK, and about 1000 m under the peak of Mt. Ikenoyama to reduce cosmic rays. The depth corresponds to 2700 m of water. The flux of cosmic rays is about 10^{-5} of that on the ground. SK started taking data on April 1 1996 for physics motivations of nucleon decay search, atmospheric and solar neutrino measurement. The K2K data has been taken since 1999. There was a severe accident in fall 2001. About 60% of PMTs were broken with a chain reaction caused by a shock wave from one imploded PMT. After that, SK was rebuilt with a half of PMT density. We call the period until the accident "SK-I", and that since the rebuilding "SK-II".

The water tank of SK is a cylinder with the dimensions of 41.4 m in height and 39.3 m in diameter. The detector is optically separated into two parts: the inner detector (ID) and the outer detector (OD). ID is completely surrounded by OD. The size of ID is 36.2 m in height and 33.8 m in diameter, containing 32 ktons of water. In SK-I (SK-II), 11146 (5182) 20-inch PMTs are mounted on the support frame facing inward. The interval between PMTs is 70 cm.

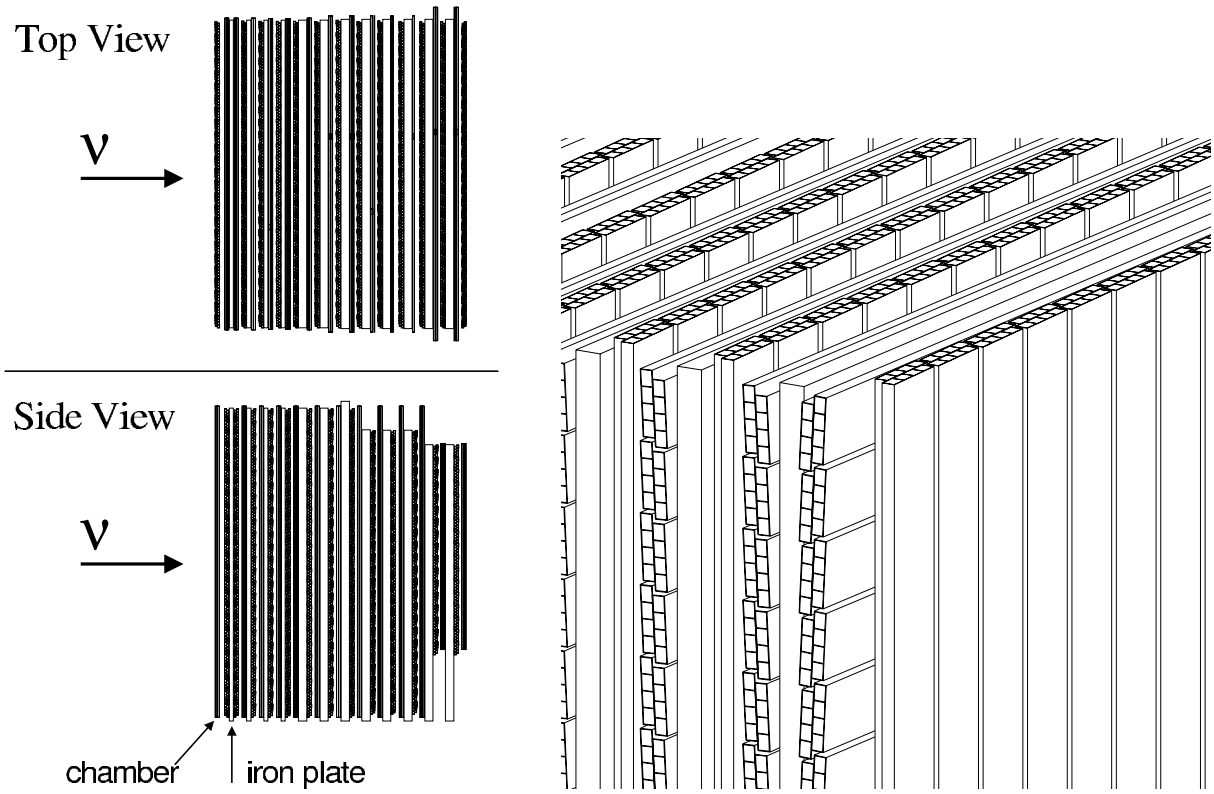

Figure 3.20: Schematic view of MRD. Left two figures show top and side views, and right figure shows a three-dimensional view.

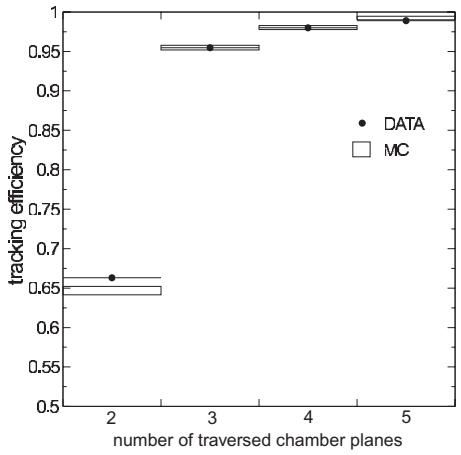

Figure 3.21: MRD track finding efficiency as a function of the number of traversed chamber planes.

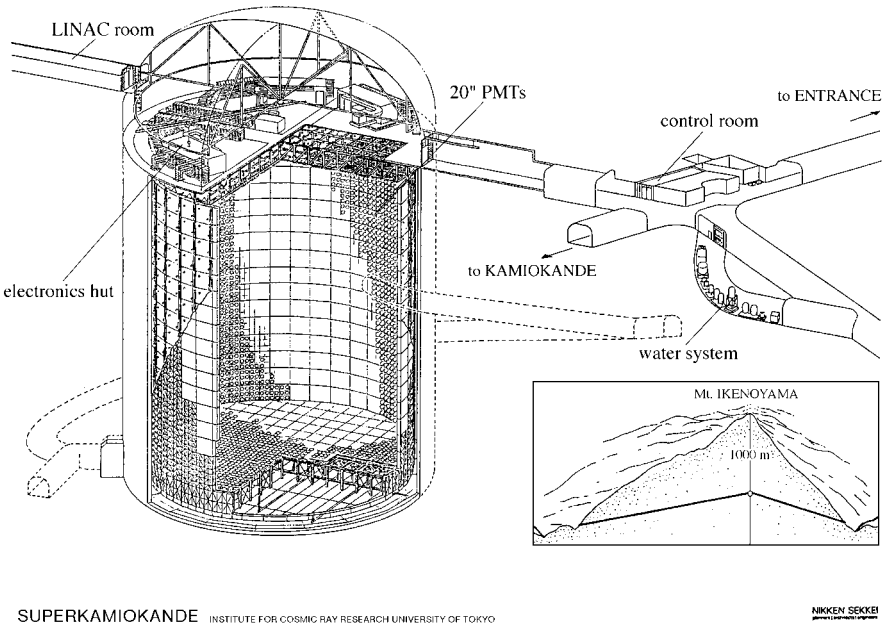

Figure 3.22: Schematic view of Super-Kamiokande.

For SK-II, PMT is attached every other PMT position. The photo-cathode coverage of SK-I (SK-II) is 40% (19%). The rest of the ID surface is covered with a black sheet to suppress light reflection and to separate optically from OD. In SK-II, the PMT is covered by acrylic around the photo-cathode and by FRP (fiber reinforced plastic) for the other part, as shown in Figure 3.23, to prevent the chain reaction of implosion. The transparency of the acrylic cover in water is 98% for the wavelength longer than 400 nm and 95% for the wave length of 350 nm.

The thickness of OD is 2.0 m for the side, and 2.2 m for the top and bottom. There are 1885 8-inch PMTs mounted outward on the support frame. The number of OD PMTs remains unchanged after rebuilding. The wall of OD is covered with reflective white sheets to maximize the detection efficiency. Purposes of OD are to veto an event by an incoming particle such as cosmic rays and to confirm whether a particle is created in ID and stops within ID.

A water purification system is working at SK. The attenuation length of the water has been kept longer than 80 m at the wavelength of 420 nm. The light scattering parameters, such as coefficients of Rayleigh scattering, Mie scattering, and absorption, are measured. These information are implemented to the detector simulator.

The readout electronics records both charge and timing of PMT signals. The signal from an ID PMT is digitized by ATM, the same module as 1KT. The signal from an OD PMT is processed by a charge-to-timing converter (QTC), which converts the charge to the width of a rectangular pulse and preserves the hit timing at the leading edge of the pulse. The QTC output is digitized by a multi-hit TDC.

The gain and timing of each ID PMT are calibrated by light sources and radio-active sources[31]. The gain is adjusted by the supplied high voltage value. The relative gain spread is 7% in the standard deviation. The remaining gain differences are corrected by a software. The calibration of the absolute energy scale is also performed, and it is described in Section 11.2.1.

There are several trigger types in SK. Among them, we use only one type called “HE trigger”, which is generated by a relatively high energy event. The condition is that the sum of all the HITSUM signal from ATMs is larger than the pulse height equivalent to 31 (16) hits for SK-I

Figure 3.23: Photograph of a 20 inch PMT covered by acrylic and FRP.

(SK-II). The trigger rate is 5–10 Hz, mainly fired by cosmic rays.

3.5 Timing synchronization between accelerator and SK

A timing synchronization system of GPS[2][32] is used to select K2K events from SK data. The GPS system of KEK records the beam spill timing, and that of SK records each event timing. The SK events synchronized with beam spills are used for the analysis. The neutrino beam is produced every 2.2 seconds with the width of 1.1 μsec, corresponding to the duty cycle of 0.5×10^{-6}. Therefore, the atmospheric neutrino backgrounds ($\sim$ 6 events/day) are reduced to be negligible by the timing synchronization.

Figure 3.24 shows a block diagram of our GPS system. It consists of GPS receivers, a VME receiver, and a 50 MHz 32 bit local time clock (LTC). The GPS receiver provides a time stamp every one second, and it is sent to the VME receiver and LTC. The accuracy of the time stamp is better than 40 nsec in average and 150 nsec at the worst. The VME receiver decodes the time stamp to universal time coordinate (UTC). LTC receives an event trigger signal for SK or a beam spill signal for KEK in addition to the time stamp. The UTC data and the LTC count are read by an online computer.

The time of an event $T_{\rm ev}$ is obtained by linear interpolation:

$$T_{\rm ev} = T_n + \frac{N_{\rm ev} - N_n}{N_n - N_{n-1}} \times 1 \ [\rm sec], \tag{3.1}$$

where T_n is the latest UTC time stamp from the GPS receiver, $N_{\rm ev}$ is the LTC count for the event, N_n is the LTC count corresponding to T_n, and N_{n-1} is the LTC count of the time stamp one more before.

The stability of the system has been checked for all the experiment periods. Since two independent GPS receivers are used at KEK, the time difference between them is examined. The results show the agreement to each other within 100 nsec (HWHM[3]). In the SK site, the stability has been continuously monitored by the LTC counts between adjacent UTC time stamps ($N_n - N_{n-1}$). Almost all data are stable within 200 nsec. If these values are larger than 200

[2]In general, GPS uses a few tens of satellites which broadcast their precise position and time by radio wave. A GPS receiver calculates its position and time by using the data from at least four satellites at the same time.

[3]half width at half maximum

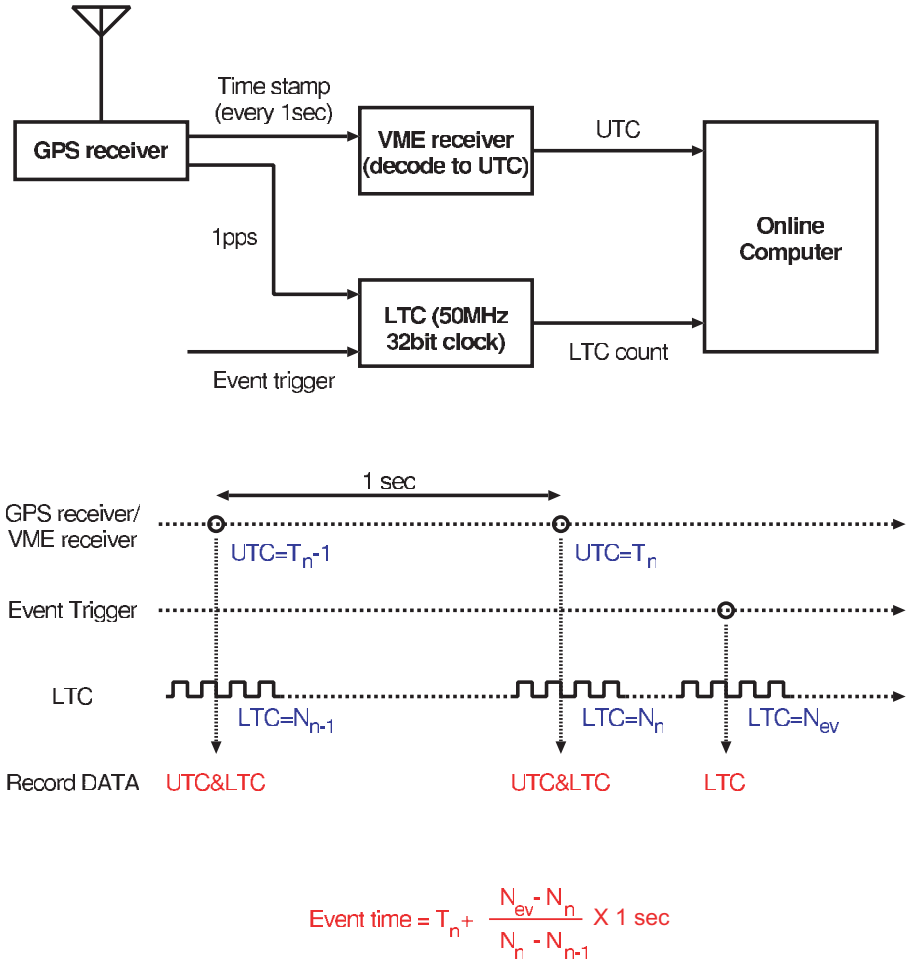

Figure 3.24: Block diagram of the GPS system.

nsec, the data at that time are not used for analysis. The system status has been also checked by the status bit of the GPS receiver, and the events with bad status are removed. The fraction of lost events due to GPS instabilities is approximately 0.1%.

Chapter 4

SciBar Detector

The SciBar detector is a fully-active tracking detector made of many scintillator bars. SciBar was newly constructed at the near detector hall in summer 2003. In this chapter, we describe the design concept, the detail of each component, and the basic performance of SciBar.

4.1 Design concept

The main purpose of the SciBar detector is to measure the neutrino energy spectrum precisely at the near site by using charged-current quasi-elastic scattering (CC-QE) events. SciBar is designed to detect CC-QE events more efficiently than the other detectors with less contamination of non-quasi-elastic scattering (nonQE) events. The signal of CC-QE is that a muon and a proton appear from a common vertex and that no other particles are produced. In addition, because of the two-body process, there is a relationship between the kinematics of the muon and the proton, such as acoplanarity. Therefore, it is important to detect both two particles from CC-QE interaction in order to identify CC-QE.

Figure 4.1 shows the momentum distributions of muons and protons produced in CC-QE interaction by using the MC simulation. The muon from a CC-QE interaction are observed easily, because the range of a muon above 0.3 GeV/c is long enough to be reconstructed as a track. On the other hand, the proton range is short: for instance, it is 20 g/cm^2 if the momentum is 0.6 GeV/c. Therefore, the detector segmentation is required to be a few cm level with small amount of dead material. Since the neutrino interaction cross-section is small, a neutrino detector should be massive. For those reasons, we designed and constructed a fully-active scintillator detector named "SciBar".

A schematic view of SciBar is shown in Figure 4.2. The main part of SciBar is an array of many plastic scintillator strips. The dimensions of a scintillator strip are $2.5 \times 1.3 \times 300$ cm^3. Approximately 15,000 scintillator strips are arranged vertically and horizontally to construct $3 \times 3 \times 1.7$ m^3 volume. The scintillation photons are absorbed by a wavelength shifting fiber inserted into a hole of each strip, and re-emitted the longer wavelength photons, as shown in Figure 4.3. These photons are transported to a photo-detector, 64-pixel multi-anode photo-multiplier tube (MA-PMT). Readout electronics record charge information for each strip and timing information on logical OR of 32 channels. A schematic view of the readout system is shown in Figure 4.4, and photographs are shown in Figure 4.5. Figure 4.6 shows an event display of a typical charged-current quasi-elastic scattering (CC-QE) candidate in SciBar.

An electro-magnetic calorimeter (EC) is installed downstream of SciBar. The purpose of EC is to measure the ν_e contamination in the beam and π^0 yield from neutrino interactions.

Characteristics of SciBar are summarized as follows:

- Almost all of the materials are active, so that all charged particles produced by neutrino

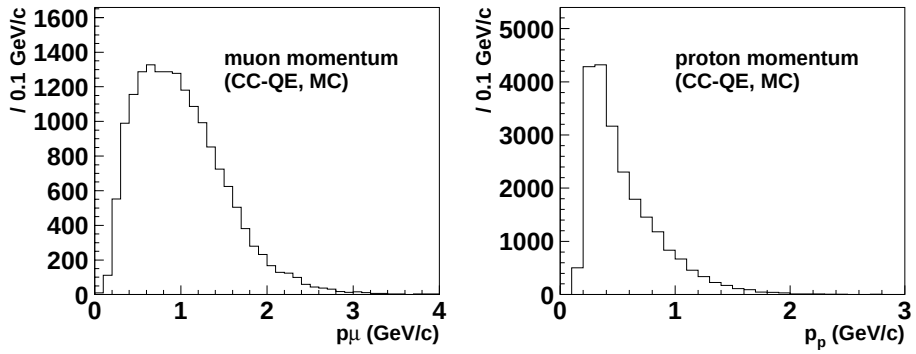

Figure 4.1: Momentum distributions of muons and protons from CC-QE interaction obtained by the MC simulation.

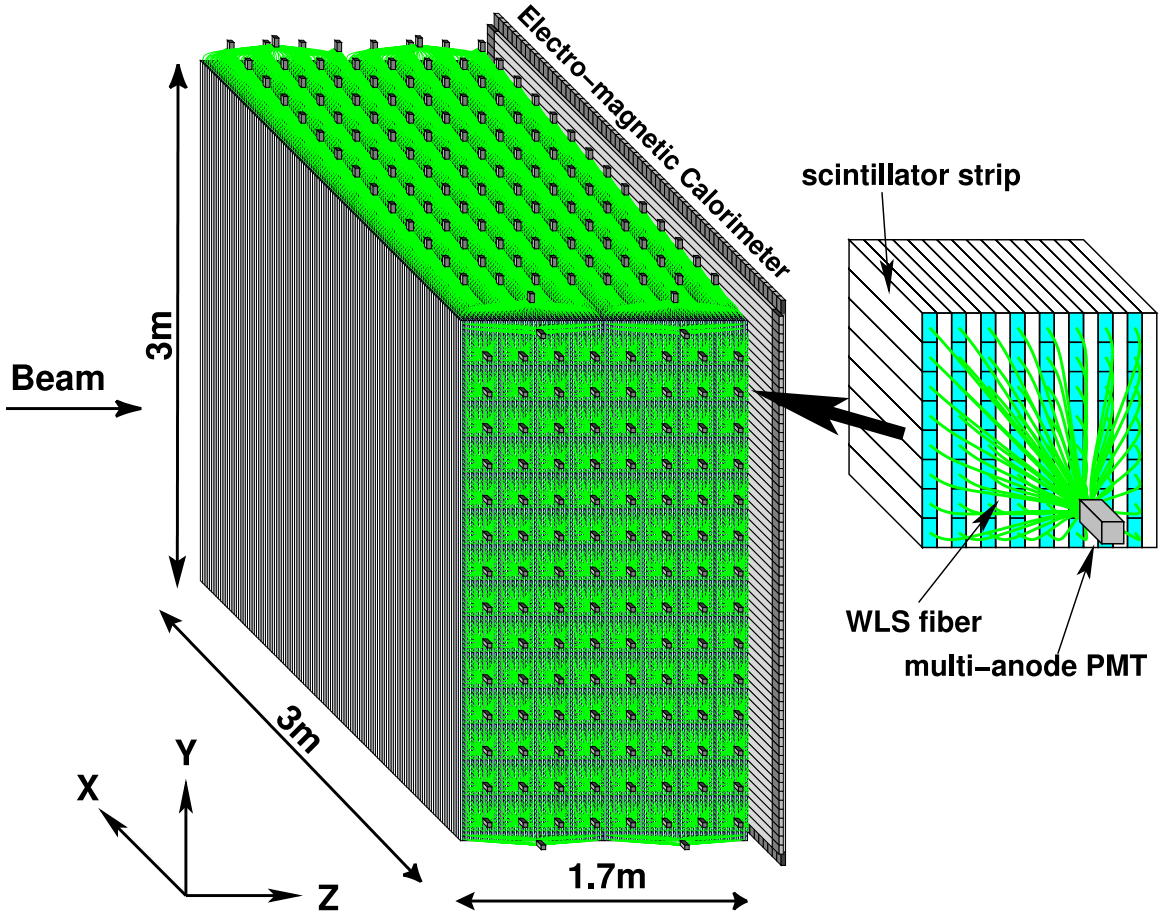

Figure 4.2: Schematic view of SciBar. Extruded scintillator strips are arranged vertically and horizontally. A WLS fiber is embedded into the hole of each strip. WLS fibers are read by 64-pixel MA-PMT. The coordinate system of SciBar is also shown.

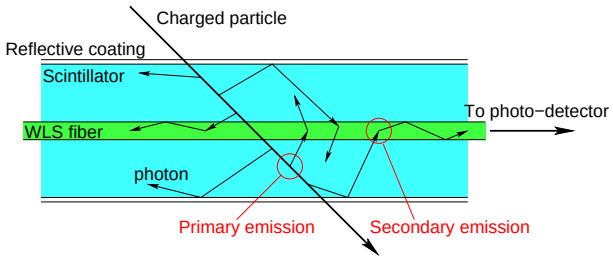

Figure 4.3: Sketch of a scintillator strip and a WLS fiber. The trajectories of scintillation photons are also shown.

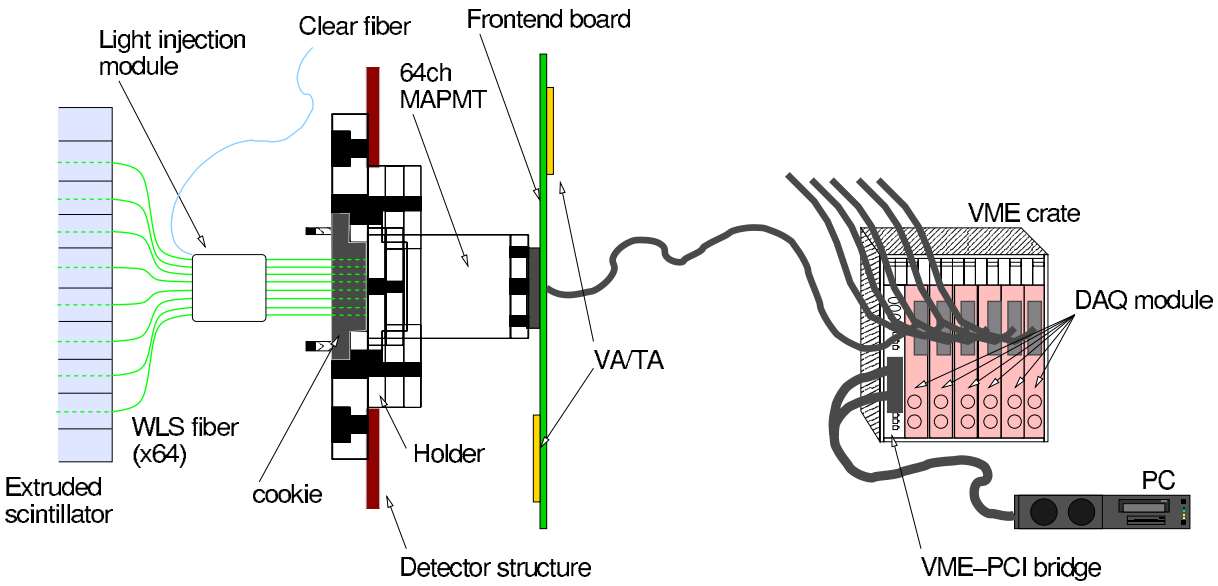

Figure 4.4: Schematic view of the readout system.

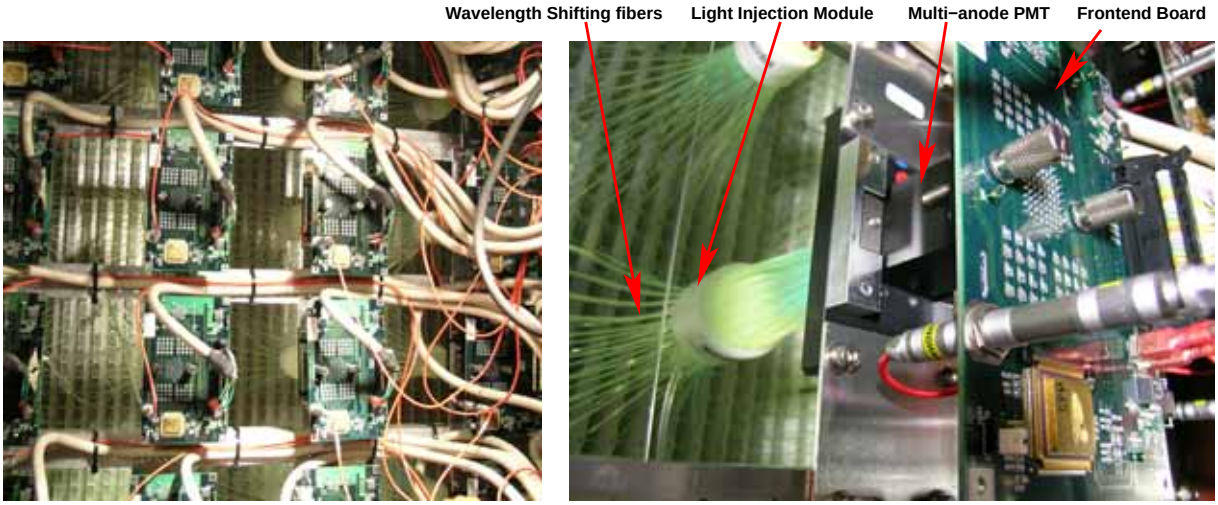

Figure 4.5: Photographs of SciBar. There are scintillator strips in the back. The WLS fibers from the strips are connected to the MA-PMT. The signal from the MA-PMT is processed by the front-end electronics and sent to the data taking system.

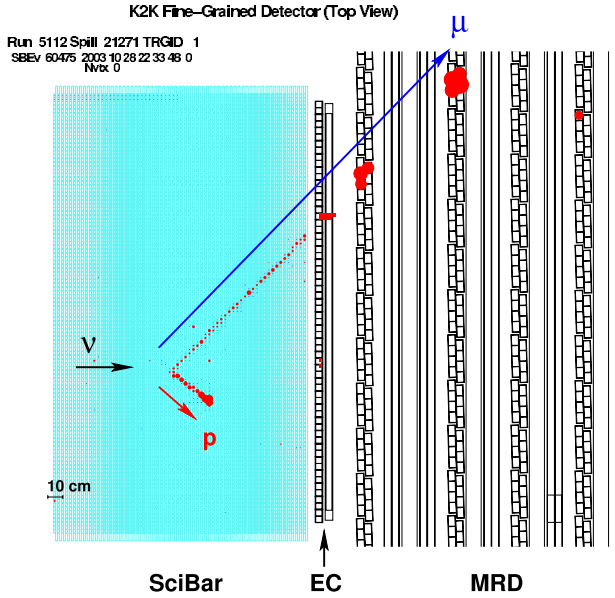

Figure 4.6: Event display of a typical CC-QE candidate in SciBar. The closed circles in SciBar show the hit cells, and their area are proportional to the ADC counts. There are two tracks with different ADC counts. The larger one is a proton candidate track and the other is a muon candidate track.

interaction are observed.

- Since each bar is thin and narrow (2.5cm $\times$ 1.3cm), SciBar detects tracks as short as 8 cm, corresponding to 0.45 GeV/c for a proton.
- The light output for each cell along a track is proportional to the energy deposit (dE/dx). Therefore, protons are distinguished from charged pions and muons[1], because protons give more energy to the scintillator around 1GeV/c. As shown in Figure 4.6, the ADC counts are clearly different between the muon track and the proton track.

These advantages enable us to identify CC-QE events effectively. When both a muon and a proton tracks are reconstructed, we select CC-QE by its kinematic condition. Even if only a muon track is reconstructed, the fraction of CC-QE is still high owing to the good tracking performance, because nonQE interactions tend to have additional tracks of pions or protons. Thus, SciBar is expected to give us a reliable neutrino energy spectrum. It is also useful for studying neutrino interaction.

In December 2002, only four layers of scintillators (6% of the total) with six PMTs were installed for engineering study. During the summer shutdown in 2003, SciBar was completely constructed. We have taken neutrino data with SciBar since October 2003.

In the following sections, we describe each component and basic performance.

4.2 Detector components

4.2.1 Extruded scintillator

The extruded scintillator strips are made of polystyrene, infused with the fluors PPO (1% by weight) and POPOP (0.03%). The composition is same as the scintillator used by the MINOS

[1]The particle identification based on dE/dx is not used in this thesis.

experiment[33]. The wavelength at the emission peak is 420 nm (blue). This compound is melted and extruded in the shape of rectangular bar with a hole at the center. The drawing of the strip is shown in Figure 4.7, and basic quantities of the scintillator are summarized in Table 4.1. The scintillator strip has the dimensions of 2.5 cm wide, 1.3 cm thick, and 300 cm long. The diameter of the hole is 1.8 mm, sufficient to contain a 1.5mm-diameter WLS fiber. A thin (0.25mm-thick) white reflective coating, composed of TiO_2 infused in polystyrene (15% by weight), surrounds the entire scintillator bar. The coating improves light collection efficiency, and it acts as an optical isolator. The scintillator, hole, and reflective coating are extruded together. The extruded scintillator is developed and produced by Fermilab[34].

The scintillator array of SciBar consists of 64 layers along beam axis. Each layer has 116 vertical bars and 116 horizontal bars to measure the two-dimensional position, and, therefore, 14,848 strips are used in total. The whole size of SciBar is $3 \times 3 \times 1.7$ m^3, and the weight is 15 tons.

In order to build a large scintillator structure, we glued a vertical and a horizontal planes together using epoxy resin, Cemedine PM-200, with aluminum frames surrounding it. It forms a thin ($300 \times 300 \times 2.6$ cm^3) module. The module was installed using a crane one by one. During the installation, 10% of strips were sampled and the dimensions and weight were measured. The mean value and root-mean-square (RMS) are summarized in Table 4.2.

Since the pixels of the 64-pixel MA-PMT are arranged in 8×8, there are 8×14 MA-PMTs to cover 64×112 strips in each projecting plane. The remaining two strips at the edge of each plane are called "outer detector (OD)". OD is read by a single-anode PMT, which is connected to 64 fibers from 2×32 strips.

4.2.2 Wave-length shifting fiber

We use wavelength shifting (WLS) fibers to collect the scintillation light. Blue photons produced in the scintillation process make many reflections by the reflective coating of the scintillator strip. The blue photons eventually hit a fiber where they are absorbed by the Y-11 fluor (wavelength shifter) and re-emitted green photons. Basic characteristics of the WLS fiber are summarized in Table 4.3. As shown in Figure 4.8, the absorption spectrum, centered at the wavelength of 430 nm (blue), has only a little overlap with the emission spectrum, centered at 476 nm (green), so that self-absorption in the fiber is small. The fibers then act as light guides to transport the green light to a photo-detector. The WLS fiber provides a very efficient light concentration into a small area.

We have chosen to use 1.5mm-diameter fibers which fit the pixel size of the photo-detector (2×2 mm^2) within the precision of alignment (0.2 mm). The diameter of OD fibers is 1.2 mm, because the OD fiber is bent much more due to a structural reason. The fibers are double-clad type to give a maximum trapping fraction for the green light, as shown in Figure 4.9: the inner core containing the WLS fluor (200 ppm) is polystyrene (refractive index $n_1 = 1.59$), a thin intermediate layer is acrylic ($n_2 = 1.49$), and the thin outer cladding is a polyfluor ($n_3 = 1.42$). The green light whose angle with respect to the fiber axis is less than 26.7 degree is trapped and transported along the fiber.

The light intensity attenuates exponentially as a function of propagation length. The attenuation length is defined as the path length at which the light intensity becomes $1/e$. Before the installation, the attenuation length of all WLS fibers were measured by using blue LED light[35]. As a result, the attenuation length distributes around 350 cm. In addition, the attenuation length was checked by cosmic rays after the installation.

In order to attach the fibers to the photo-detector (64-pixel MA-PMT), we developed an alignment fixture called "cookie"[36]. WLS fibers are glued into holes of the cookie by epoxy resin and the surface of the cookie is polished by a diamond blade. The cookie holes are precisely

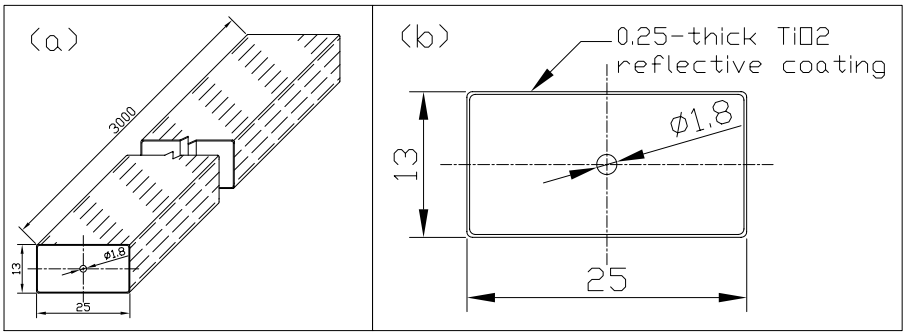

Figure 4.7: The drawing of a scintillator strip. The unit is mm. The left figure shows a 3 dimensional view and the right figure shows a detailed description of the cross-section.

Table 4.1: Basic quantities of the SciBar scintillator.

Scintillator material	polystyrene with PPO (1%) and POPOP (0.03%)
Emission wavelength	420 nm (blue)
Dimensions	$2.5 \times 1.3 \times 300$ cm^3
Hole diameter	1.8 mm
Reflector material	TiO_2 (15%) infused in polystyrene
Reflector thickness	0.25 mm
Number of strips	14,848
Whole size	$3 \times 3 \times 1.7$ m^3
Total weight	15 tons

Table 4.2: The mean value and the RMS for measured dimensions and weight of scintillator strips. 10% of strips were sampled.

	unit	mean	RMS
width	mm	25.01	0.21
thickness	mm	12.87	0.26
length	mm	3022	10
weight	g	994.6	8.4

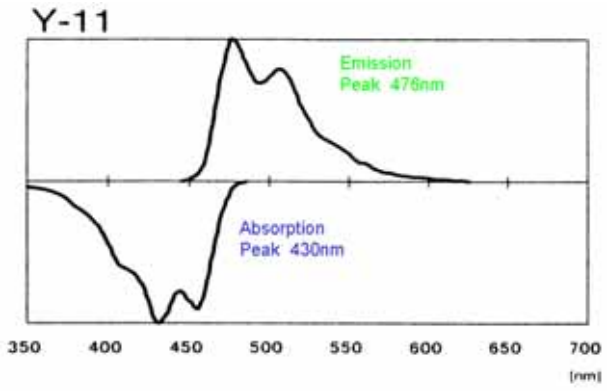

Figure 4.8: Absorption and emission spectra of Y-11 WLS fiber.

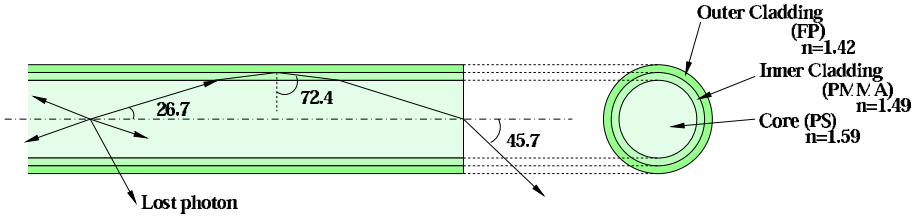

Figure 4.9: Sketch of Y-11 double-clad WLS fiber.

Table 4.3: Basic characteristics of WLS fiber.

Diameter	1.5 mm (OD 1.2 mm)
Core	polystyrene ($n = 1.59$)
Inner clad	acrylic ($n = 1.49$)
Outer clad	polyfluor ($n = 1.42$)
Wavelength shifter	Y-11 fluor (200 ppm)
Absorption wavelength	430 nm (peak)
Emission wavelength	476 nm (peak)
Attenuation length	350 cm

aligned with the 64 pixels on the MA-PMT. In the meanwhile, MA-PMT is aligned to a cookie holder with reference to guide marks on the PMT. The cookie has alignment pins, and the cookie holder has holes tightly fitting the pins. Thus, fibers are aligned to pixels on the PMT within 0.2 mm precision.

4.2.3 Multi-anode PMT

We use a 64-pixel MA-PMT manufactured by Hamamatsu Photonics for a photo-sensor of SciBar. The MA-PMT has equal performance to H7546 but only the packaging is modified in order for the PMT to be fixed to the cookie and the front-end electronics. The drawing of the MA-PMT is shown in Figure 4.10, and specifications of the MA-PMT is summarized in Table 4.4.

The MA-PMT behaves like 64 miniature single-channel PMTs. The pixel size is 2×2 mm^2. The photo-cathode is made of bialkali. The quantum efficiency for 500 nm (green) photons is 12%. Only a few additional and potentially adverse features, like cross-talk and non-uniformity of pixel response, are introduced by the dense packaging. The cross-talk with a 1.5mm-diameter fiber is measured to be 4% for adjacent pixels and 1% for othogonally opposite pixels. The pixel-to-pixel gain uniformity is measured to be 21% in RMS.

Before the installation, we determined the applied high voltage, and measured absolute gain and response linearity for all the MA-PMTs[36]. The high voltage value was adjusted so that the average gain was 6×10^5. With this gain, we checked that the response linearity is kept within 5% of the ideal case up to the input of 200 photo-electrons.

4.2.4 Gain monitoring

To guarantee the detector stability, the gain of all the PMT channels were monitored during the detector operation[37]. A schematic view of the gain monitor system is shown in Figure 4.11. A blue LED is used as a light source, and pulsed blue light is distributed to each fiber bundle through a clear fiber (1mm-diameter). In order to measure the light intensity of each pulse, the LED also illuminates a pin photo-diode and a 2 inch PMT which is calibrated by an Am-NaI stable light source. We assembled a "light injection module" to a WLS fiber bundle. Blue LED light is injected into the module, and all the fibers are uniformly illuminated. By comparing the MA-PMT outputs with the pin photo-diode or the 2 inch PMT, we measure the relative gain drift with 0.1% precision. The performance of the gain correction is discussed in Section 4.3.2.

4.2.5 Readout electronics

To deal with 15,000 readout channels, we use ASICs[2], VA and TA developed by IDEAS. The readout electronics[38] consists of front-end boards (FEB) and controller modules (DAQ board). The VA/TA chip-set is mounted on the FEB, which is directly connected to the MA-PMT in the dark room of SciBar. The model numbers of VA and TA are VA32HDR11 and TA32CG, respectively. Since the VA/TA chip-set has 32 inputs, a couple of VA/TA's are assembled on the FEB. One DAQ board controls eight FEBs, corresponding to 512 channels.

The block diagram of the readout system is shown in Figure 4.12, and Basic quantities of the system is summarized in Table 4.5. VA amplifies the PMT signals and shapes them into slowly peaking signals. The peaking time is 1.2 μsec. In the meantime, TA produces a narrow peak with 80 nsec peaking time and discriminates the signal at the threshold given by the DAQ board. The output of TA is an OR-ed signal over 32 channels. We set the threshold to 0.7 photo-electron equivalent. If the DAQ board receives the TA signal, it provides a hold signal

[2] Application Specified Integrated Circuit.

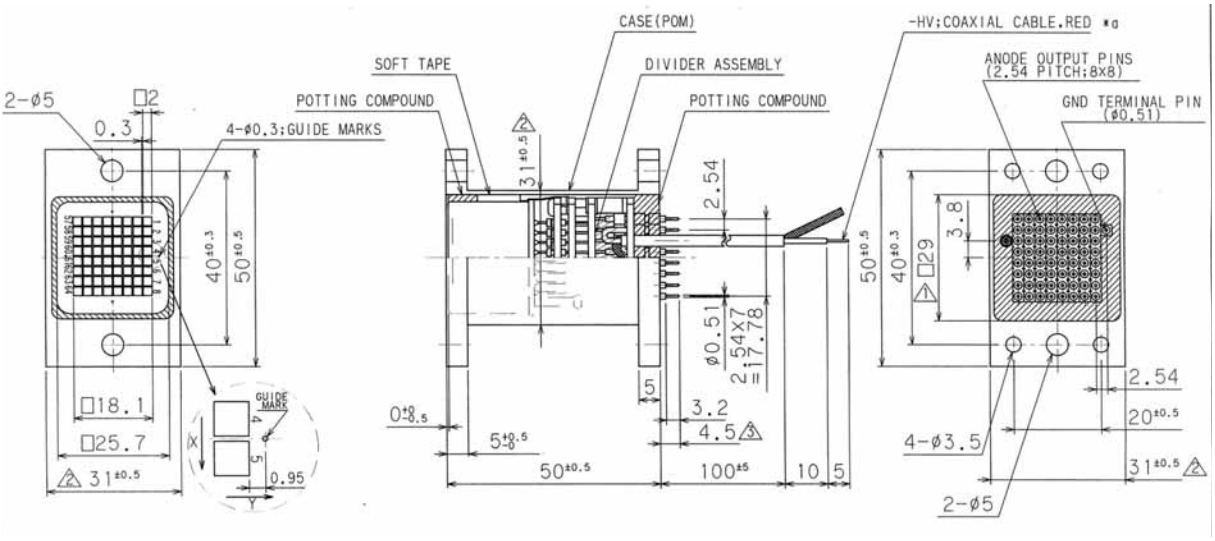

Figure 4.10: Drawing of the MA-PMT. In addition to usual H7546, fixing holes and HV cables are assembled.

Table 4.4: Specifications of the MA-PMT.

Photo-cathode	Bialkali
Quantum efficiency	12% for 500 nm photons
Number of pixels	64
Pixel size	2×2 mm^2
Typical gain	6×10^5 at $\sim$ 800 V
Response linearity	200 photo-electrons at gain 6×10^5
Cross talk	4% (adjacent pixel)
Number of MA-PMTs	224

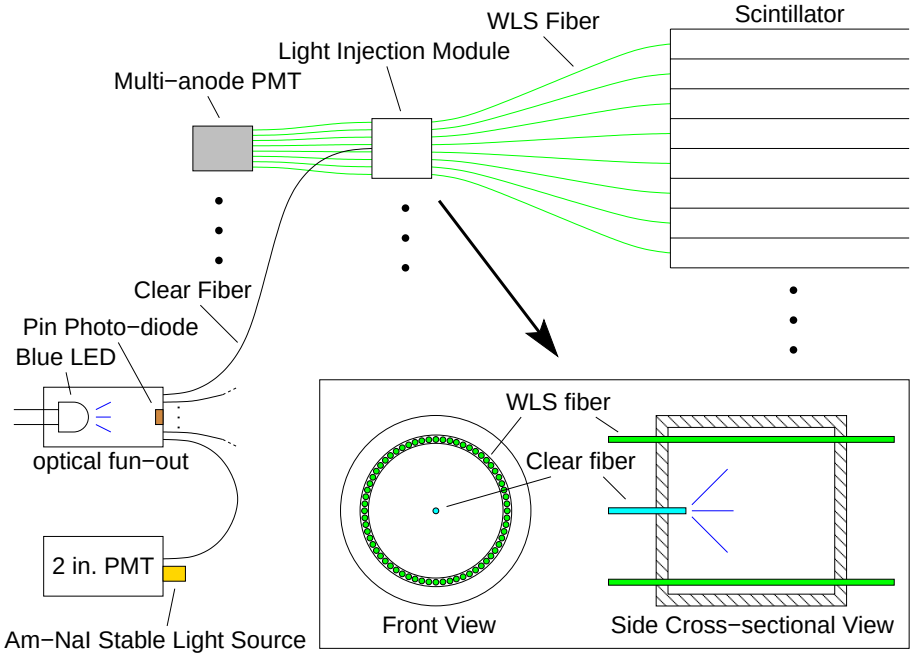

Figure 4.11: Schematic view of the gain monitor system.

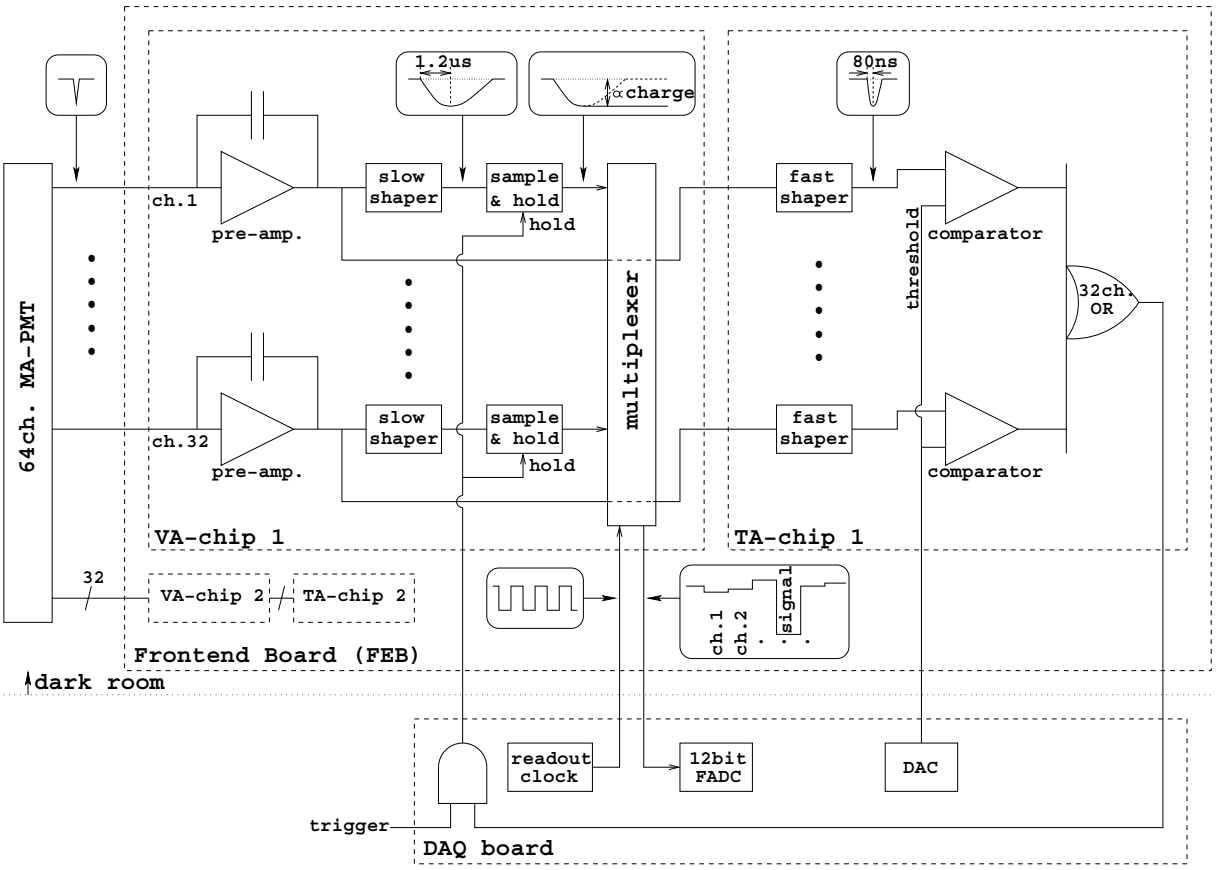

Figure 4.12: Block diagram of VA/TA readout.

to VA, by which the pulse height proportional to PMT charge is kept for reading. Just after holding, the DAQ board sends readout pulses and receives the pulse heights from VA one by one. Finally, the flush ADC on the DAQ board digitizes the VA outputs. If the PMT gain is 6×10^6, the VA output is sufficiently linear up to 300 photo-electrons and the noise level is measured to be 0.3 photo-electron level.

TA signals are also sent to time-to-digital converters (TDC) and cosmic ray trigger boards. As for the TDC, the AMT board[39] developed by ATLAS TGC group is used. AMT has multi-hit capability, 0.78 nsec resolution, and 50 μsec full range.

The cosmic ray trigger board is a general purpose logic board powered by an FPGA[3]. The trigger board are programmed to generate a signal, when a cosmic ray penetrates almost all layers[40]. A schematic diagram of the cosmic ray trigger is shown in Figure 4.13. The TA channels are arranged in 8×28 for each projecting plane. The trigger board receives the signals from every other TA layer, and it makes the OR of each TA layer. If all the eight OR signals are fired, the cosmic ray trigger is generated.

4.2.6 Electro-magnetic calorimeter

When we study $\nu_\mu \to \nu_e$ oscillation, ν_e contamination in the beam and π^0 production from neutrino interaction are dominant backgrounds. The detection of electro-magnetic shower is required to study ν_e and π^0 events. However, the scintillator part of SciBar is only four radiation lengths along the beam direction, and not enough to measure the energy of an electron and a

[3]Field Programmable Gate Array.

Table 4.5: Basic quantities of the SciBar readout system.

Shaping time	1.2 μsec (VA), 80 nsec (TA)
Noise	0.3 photo-electron at PMT gain 6×10^5
Response linearity	300 photo-electrons at PMT gain 6×10^5
TA threshold	0.7 photo-electron at PMT gain 6×10^5
TDC resolution	0.78 nsec
TDC full range	50 μsec

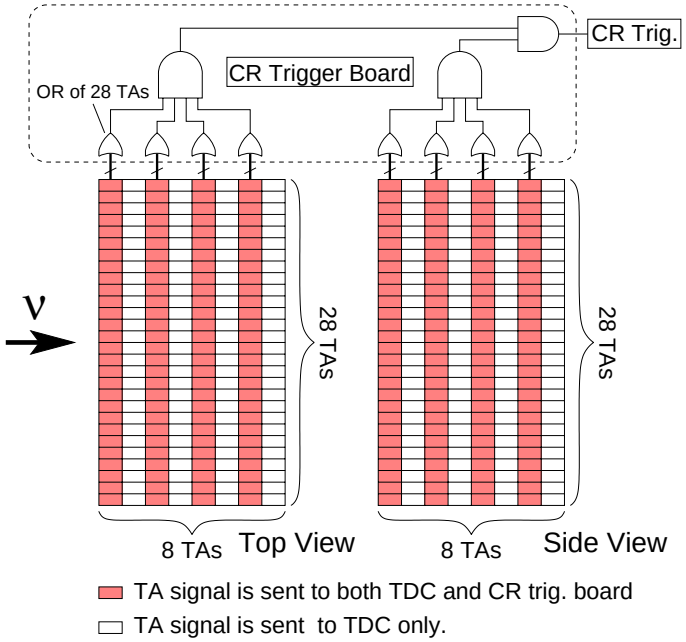

Figure 4.13: Schematic diagram of the cosmic ray trigger.

photon around 1 GeV. Therefore, we installed electro-magnetic calorimeter (EC) downstream of the scintillator part. EC is an array of "spaghetti modules"[41] which were used at the CHORUS experiment[42]. Figure 4.14 shows a schematic drawing of EC. EC is made of scintillating fibers and lead. Scintillating fibers (1mm-diameter) are embedded in the grooves on 1.9mm-thick lead sheets. The module consists of a pile of 21 layers with 740 scintillating fibers. The pile has the dimensions of $4.0 \times 8.2 \times 262$ cm^3, and it is kept together by a steel box. On both sides, fibers are arranged in two groups, defining two different readout cells with 4×4 cm^2 cross-section. Each group is coupled to a 1 inch PMT. EC is composed of a vertical plane (32 modules) and a horizontal plane (30 modules), providing additional $11X_0$ along the beam direction. The energy resolution of EC is $14\%/\sqrt{E_e[\mathrm{GeV}]}$, where E_e is the electron energy.

4.2.7 Data acquisition

The timing diagram of the SciBar data acquisition is shown in Figure 4.15. The neutrino beam is produced every 2.2 seconds as 1.1 μsec duration pulse. The beam trigger is provided by the accelerator. After the beam trigger, one pedestal and one LED triggers are generated. Until 1.5 seconds after the beam, the cosmic ray trigger is enabled to collect approximately 15 cosmic ray events per spill. The LED and cosmic ray data are used to monitor the PMT gain and the light yield.

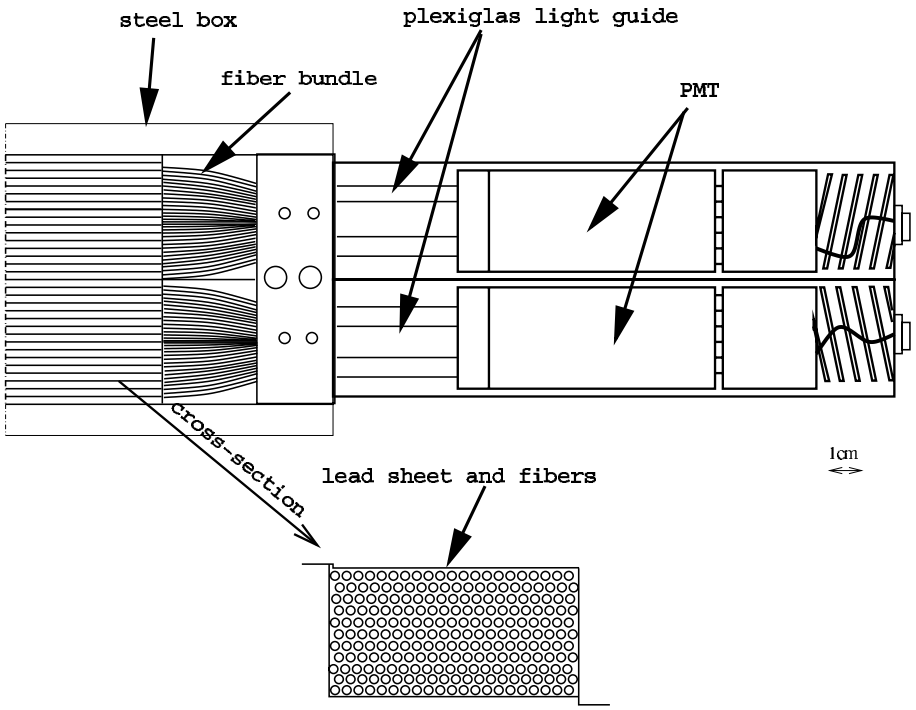

Figure 4.14: Schematic drawing of an electron-magnetic calorimeter module.

For the front-end electronics, six VME crates are used in total: four crates for DAQ boards, one crate for EC, and one crate for control, OD, and the gain monitor. The last one distributes a serial number to the other crates for the identification of each event. There are seven front end PCs (Celeron 1 GHz processor): one is an event builder and the others are connected to VME crates. The data from VME crates are sent to the event builder via Ethernet (100BASE-TX). The event builder combines all the SciBar data by means of the serial number of an event. Finally, the SciBar event builder sends the data to the global event builder of the near detector complex. The data acquisition system of SciBar collects 15 events in one second.

4.3 Basic performance

In the rest of this chapter, we describe basic performances of SciBar. The number of dead channels, light yield for each cell and its stability, and timing resolution are presented.

4.3.1 Dead channel

The number of dead channels are checked by the gain monitor system. There are only six channels which did not respond to LED light at all. The percentage of the active channels is 99.96% ($= 1 - 6/14,336$). Since four of them cluster at one MA-PMT, we investigated the reason after the K2K-IIb run. As a result, a crack was found at a corner of the photo-cathode of PMT. The reason for the other dead channels are still unknown.

4.3.2 Light yield

Light yield is measured using cosmic ray data. The analysis procedure is summarized below:

- Fit a track with linear function by a least square method.

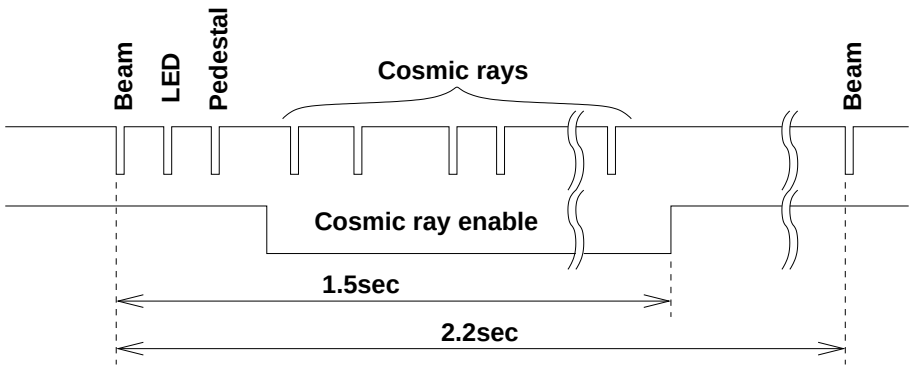

Figure 4.15: Timing diagram of the data acquisition.

- Select a track whose angle with respect to the beam direction is less than 45 degree.
- If there is one and only one hit in a plane, the ADC value is filled to the histogram shown in Figure 4.16(a). The path length in each cell and the attenuation of the fiber are corrected.

Figure 4.16(b) shows the distribution of the mean light yield for each cell. The average light yield is 18 photo-electrons for 1.0 cm muon track at 40 cm from the PMT along the fiber. It corresponds to 9 photo-electrons/MeV. The light yield is as large as expected from test bench measurements, and sufficient for track finding and particle identification.

The time variation of the light yield is also checked by cosmic ray data. Figure 4.17 shows the light yield of cosmic ray events as a function of time. Though the light yield showed several percentage variation due to a minor trouble of the air conditioner from November to December 2003, the light yield is stable within 0.7% level after the PMT gain correction with the monitor system.

4.3.3 Timing resolution

The timing resolution of SciBar is studied by the time difference between two adjacent TA channels along a cosmic ray track. After the correction for the propagation in the fiber and the correlation between timing and charge, the time difference is plotted, as shown in Figure 4.18. The standard deviation of the plot is 1.8 nsec, which is $\sqrt{2}$ times the timing resolution if the two channels have the same resolution. Therefore, the timing resolution of SciBar is 1.3 nsec. It is sufficient to select the beam timing window and to distinguish the micro-bunch structure (125 nsec spacing) of the beam spill.

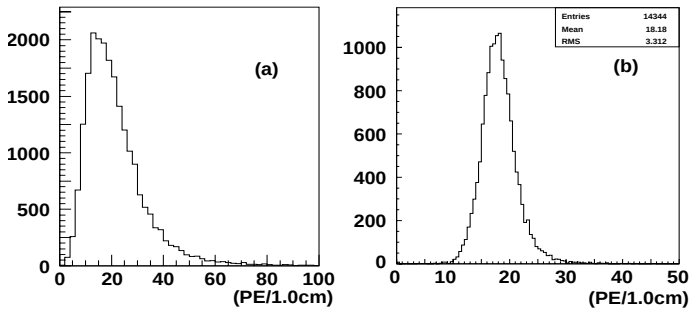

Figure 4.16: Figure (a) shows a typical light yield distribution of a strip. The unit of x-axis is photo-electrons/1.0cm. The attenuation of the fiber is corrected to be the case that the hit is 40 cm from MA-PMT along the fiber. Figure (b) shows the histogram filled with the mean light yield of each strip.

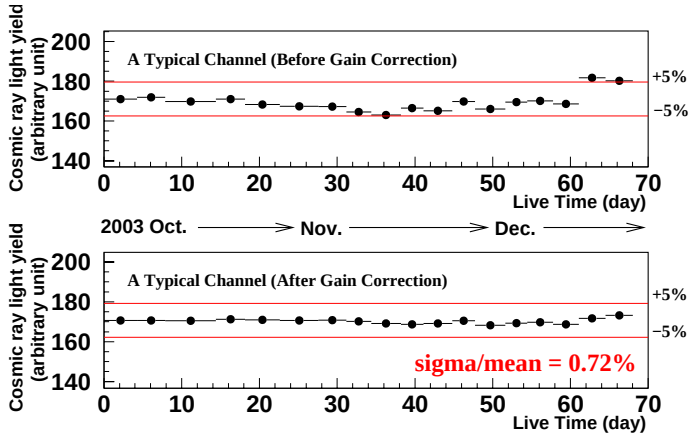

Figure 4.17: The stability of the light yield using cosmic rays. The upper figure shows the light yield of a typical channel for cosmic ray events as a function of time. From November to December in 2003, the MA-PMT gain varied by a few % due to a minor trouble of the air conditioner. Owing to the gain monitor, the deviation of the gain is corrected. The standard deviation of the light yield is 0.7% after the gain correction, as shown in the lower figure.

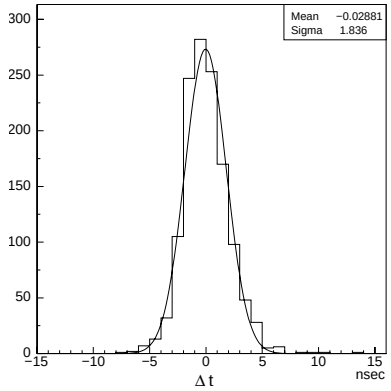

Figure 4.18: The time difference between adjacent TA channels along a cosmic ray track. The correlation between timing and charge is corrected. The standard deviation of the fitted Gaussian is 1.8 nsec.

Chapter 5

Monte Carlo Simulations

Monte Carlo (MC) simulations for the K2K experiment consist of three parts:

- A simulation for the neutrino beam. It gives the neutrino flux of each neutrino type (ν_μ, ν_e, $\bar{\nu}_\mu$, and $\bar{\nu}_e$) as a function of neutrino energy.
- A simulation for neutrino interaction. It provides final state particles from a neutrino-nucleus scattering, according to models of neutrino cross-sections and interaction.
- A simulation for detectors. It simulates the passage of particles in a material and the response from detector components.

They are described one by one in the subsequent sections.

5.1 Neutrino beam simulation

The MC simulation for the neutrino beam (Beam-MC) reproduces the proton beam hitting the target, the secondary meson production in the target, and the decay of secondary mesons into neutrinos. We describe each Beam-MC component, and we finally present the neutrino energy spectra at near and far sites.

5.1.1 Primary proton beam

Primary proton beam with 12 GeV kinetic energy is injected to the target with the measured beam profile and divergence. The proton beam profile is measured by using two SPICs between the last magnet and the target, called "V39-SPIC" and "TARGET-SPIC". The former is located just after the last magnet, and the latter is located just before the target. Figure 5.1 shows a schematic view of the target and SPICs. The outputs from these SPICs are fitted with Gaussian, and the beam profile and divergence at the target are extrapolated. The standard deviation of the horizontal beam spread is 1 mm (3.4 mm), and that of the vertical spread is 6 mm (7.2 mm) in June 1999 (since November 1999).

5.1.2 Secondary pion production

Various pion production data are available in the 12 GeV proton beam. Following three kinds of pion production models are compared in our study.

GCALOR/FLUKA Model [43, 44, 45]
The package of hadron simulation provided in a GEANT[46] simulation.

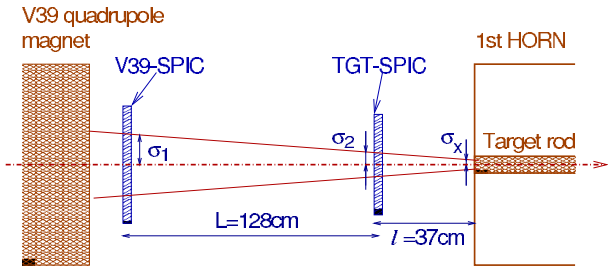

Figure 5.1: Schematic view of the target and SPICs for the beam profile measurement.

Fit to Measurements (I), Sanford-Wang [47]

The experimental parametrization using compilation of three measurements: Lundy *et al.* (13.4 GeV/c) [48], Dekkers *et al.* (11.8, 18.8, and 23.1 GeV/c)[49], and Baker *et al.* (10.9, 20.9, and 30.9 GeV/c)[50]. This compilation agrees well with a measurement by Yamamoto[51].

Fit to Measurements (II), Cho-ANL and Cho-CERN [52, 53]

Other results of the compilations to fit several measurements to the Sanford-Wang formula. The measurements done by Marmer *et al.* (12.3 GeV/c)[54], Cho *et al.* (12.4 GeV/c)[52], Asbury *et al.* (12.5 GeV/c)[55], and Allaby *et al.* (19.2 GeV/c)[56] are used in the Cho-ANL compilation[52]. There is another result of compilation called Cho-CERN[53], which uses the data set of mainly from Cho *et al.* (12.4 GeV/c). These two compilations give almost the same differential cross-sections.

These results are inconsistent with each other, which results in a large ambiguity in the MC simulation.

The Sanford-Wang formula is an empirical formula, which gives the differential yield of the secondary particles:

$$\frac{d^2n}{d\Omega dp} = C_1 p^{C_2} \left(1 - \frac{p}{p_B - 1}\right) \exp\left(-\frac{C_3 p^{C_4}}{p_B^{C_5}} - C_6\theta(p - C_7 p_B \cos^{C_8}\theta)\right), \tag{5.1}$$

where $d^2n/d\Omega dp$ is the differential particle yield per interacting proton, θ is the angle of the secondary particle with respect to the beam axis in the laboratory frame, p and p_B are the momenta of the secondary particle and the incident proton, respectively, and C_i's are the constants determined by fitting. The fit results of the positive pion production for Sanford-Wang, Cho-ANL, and Cho-CERN compilations are summarized in Table 5.1. Figure 5.2 is the comparison of the experimental measurements with the fitted curves of Cho-CERN.

In the case of the GCALOR/FLUKA model, GEANT simulates everything using the model automatically. In the other models, the hadron production is reproduced by Equation (5.1) only when a proton more than 10 GeV interacts with aluminum, and lower energy interactions are simulated by the GCALOR model. For kaon production, the parameter set described in [47] is employed.

The PIMON measurements, described in Chapter 10, favor the Cho-CERN model. Therefore, we select the Cho-CERN model as the standard pion production model. However, the other models are also consistent with the PIMON measurements within their errors. They are used for systematic error estimation.

Table 5.1: Fitted parameters of Sanford-Wang formula for the positive pions in Sanford-Wang, Cho-ANL, and Cho-CERN compilations.

	C_1	C_2	C_3	C_4	C_5	C_6	C_7	C_8
Sanford-Wang	1.09	0.65	4.05	1.63	1.66	5.03	0.17	82.7
Cho-ANL	0.96	1.08	2.15	2.31	1.98	5.73	0.13	24.1
Cho-CERN	1.05	1.01	2.26	2.45	2.12	5.66	0.14	27.3

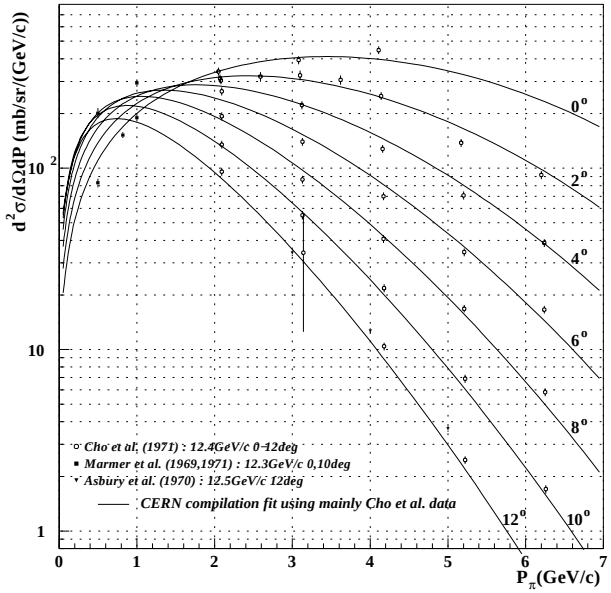

Figure 5.2: Differential cross-section of positive pion production in past experiments and fitted curves of the Cho-CERN model. Data points are shown by symbols with error bars, and the fitted curves are shown by solid lines.

5.1.3 Particle tracking through the horn magnets and the decay volume

Survived primary protons and generated secondary particles are traced though the two horn magnets and the decay volume until their decays or absorption in a material, by using GEANT with the GCALOR hadron simulator. The focusing effect of the magnetic field is also simulated. The decay channels and kinematics of pions, kaons, and muons are computed by our original codes.

5.1.4 Neutrino energy spectrum

Figure 5.3 shows the neutrino energy spectra at the near site and Super-Kamiokande for each horn current. Due to the finite volume of the decay tunnel, the energy spectra are different between near and far sites. Figure 5.4 shows the energy spectrum for each neutrino type. The fraction of ν_μ, ν_e, $\bar{\nu}_\mu$, and $\bar{\nu}_e$ are 97.9%, 0.9%, 1.2%, and 0.02%, respectively, at Super-Kamiokande.

5.2 Neutrino interaction simulation

The Monte Carlo simulation of neutrino interactions[57], called "NEUT", is described in this section. NEUT generates the final state particles from neutrino-nucleus interaction. NEUT is originally developed by the atmospheric neutrino experiment in SK[58]. The target materials are H_2O for water Cherenkov detectors and SciFi, and $(CH)_n$ for SciBar.

Neutrino interaction channels are summarized as follows:

- CC quasi-elastic scattering $\nu + N \to l^- + N'$ ($\sim 27\%$)
- NC elastic scattering $\nu + N \to \nu + N$ ($\sim 13\%$)
- CC resonance production $\nu + N \to l^- + N' + \text{meson}$ ($\sim 28\%$)
- NC resonance production $\nu + N \to \nu + N' + \text{meson}$ ($\sim 10\%$)
- CC multi-pion production $\nu + N \to l^- + N' + \text{hadrons}$ ($\sim 14\%$)
- NC multi-pion production $\nu + N \to \nu + N' + \text{hadrons}$ ($\sim 4\%$)
- CC coherent-pion production $\nu + {}^{16}\mathrm{O}\,({}^{12}\mathrm{C}) \to l^- + {}^{16}\mathrm{O}\,({}^{12}\mathrm{C}) + \pi^+$ ($\sim 2\%$)
- NC coherent-pion production $\nu + {}^{16}\mathrm{O}\,({}^{12}\mathrm{C}) \to \nu + {}^{16}\mathrm{O}\,({}^{12}\mathrm{C}) + \pi^0$ ($\sim 1\%$)

where N and N' are nucleons and l^- is a charged lepton. The fraction of each mode is also shown in the parentheses. Figure 5.5 shows the cross-section of each interaction mode with water, obtained by NEUT. The model of each interaction mode is described in the following section.

5.2.1 CC quasi-elastic scattering and NC elastic scattering

The charged-current quasi-elastic (CC-QE) and neutral-current elastic (NC-el) interactions are two-body scattering on a nucleon. Their simulations are based on Llewellyn Smith's formula[59]. The amplitude is described as a product of hadronic and leptonic weak currents:

$$T = \frac{G_F}{\sqrt{2}}\,\bar{u}(k_2)\gamma^\mu(1-\gamma^5)u(k_1)\,\langle N'(p_2)|J_\mu^{\mathrm{had}}|N(p_1)\rangle, \tag{5.2}$$

where G_F is the Fermi coupling constant, p_1 (p_2) is the initial (final) nucleon four-momentum, and k_1 (k_2) is the initial (final) lepton four-momentum. The hadronic current, $\langle N'|J^{\mathrm{had}}|N\rangle$, can

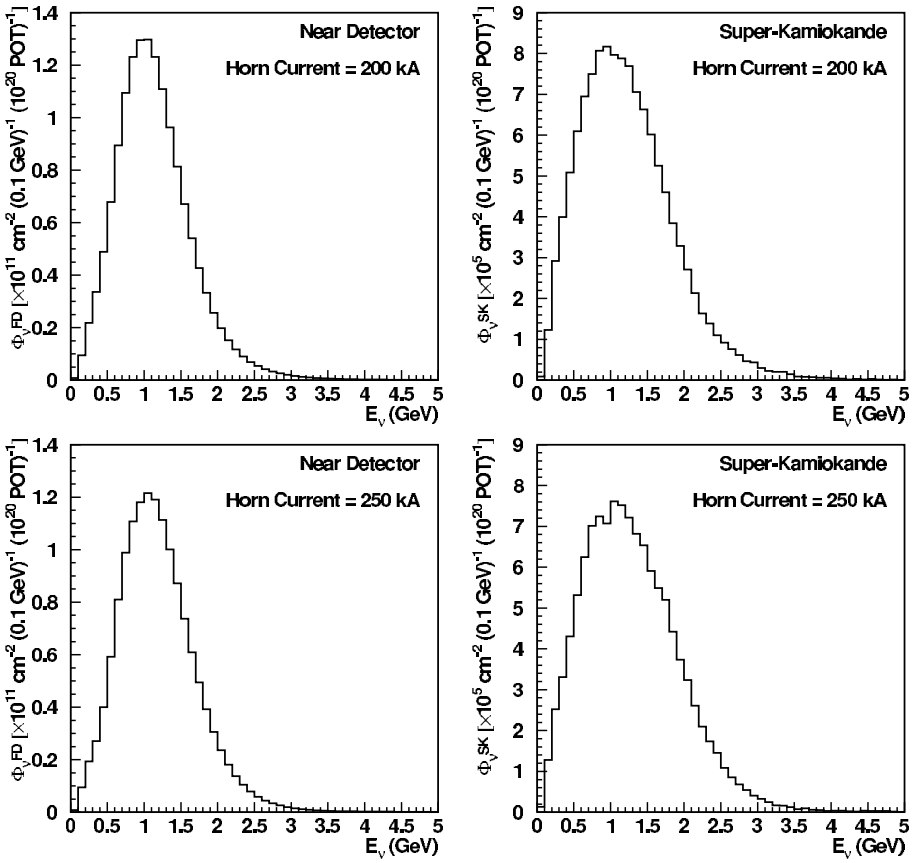

Figure 5.3: Neutrino energy spectra at near (left) and far (right) sites. The upper (lower) two figures show the spectra with horn current of 200kA (250kA).

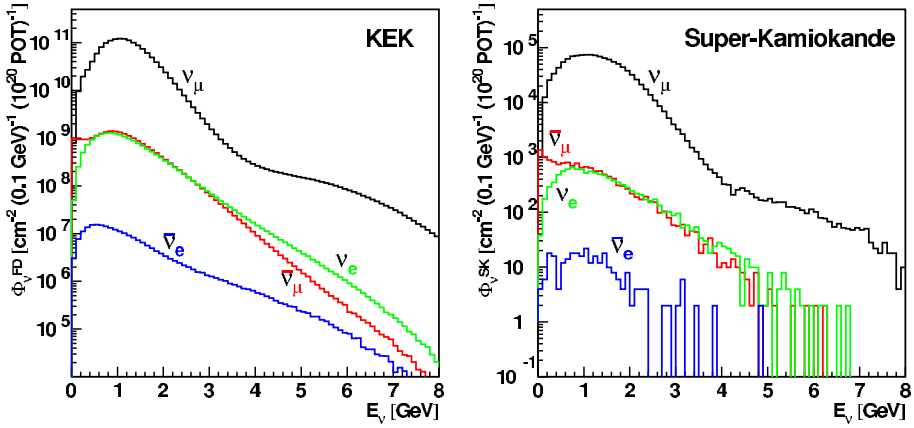

Figure 5.4: Neutrino energy spectrum for each neutrino type with 250 kA horn setting. Black, green, red, and blue lines show ν_μ, ν_e, $\bar{\nu}_\mu$, and $\bar{\nu}_e$, respectively.

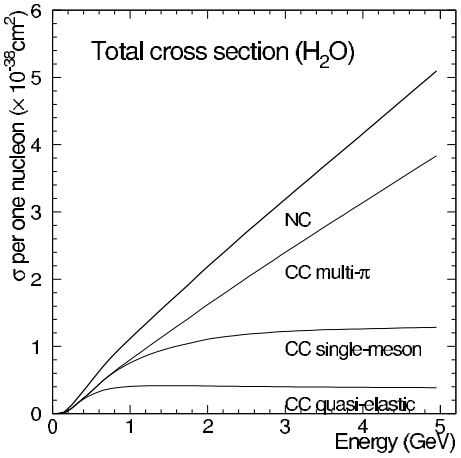

Figure 5.5: The cross-section of each neutrino interaction channel with water as a function of incident neutrino energy. This plot is calculated by NEUT. The CC resonance production and CC coherent pion production modes are assorted into "CC single-meson".

be expressed as a function of four-momentum transfer, $Q^2 \equiv -q^2 = -(p_1 - p_2)^2$:

$$\langle N'|J^{\rm had}|N\rangle = \cos\theta_c\, \bar{u}(N') \left[\gamma_\lambda F_V^1(Q^2) + \frac{i\sigma_{\lambda\nu}q^\nu \xi F_V^2(Q^2)}{2m_N} + \gamma_\lambda\gamma_5 F_A(Q^2)\right] u(N), \tag{5.3}$$

where θ_c is the Cabbibo angle, and m_N is the nucleon mass. The vector form factors, F_V^1 and F_V^2, are represented as follows:

$$F_V^1(Q^2) = \left(1 + \frac{Q^2}{4m_N^2}\right)^{-1} \left[G_E^V(Q^2) + \frac{Q^2}{4m_N^2} G_M^V(Q^2)\right], \tag{5.4}$$

$$\xi F_V^2(Q^2) = \left(1 + \frac{Q^2}{4m_N^2}\right)^{-1} \left[G_M^V(Q^2) - G_E^V(Q^2)\right], \tag{5.5}$$

$$G_E^V(Q^2) = \frac{1}{\left(1 + \frac{Q^2}{M_V^2}\right)^2}, \qquad G_M^V(Q^2) = \frac{1+\xi}{\left(1 + \frac{Q^2}{M_V^2}\right)^2}, \tag{5.6}$$

where $\xi \equiv \mu_p - \mu_n = 3.71$ is the difference of anomalous magnetic dipole moments between a proton and a neutron, and the vector mass in the dipole parametrization, M_V, is set to be 0.84 GeV/c. The axial form factor, F_A, is given by

$$F_A(Q^2) = \frac{-1.23}{\left(1 + \frac{Q^2}{M_A^2}\right)^2}, \tag{5.7}$$

where M_A is the axial vector mass. Past electron-nucleon and neutrino-nucleon scattering experiments give that M_A for (quasi-)elastic scattering is 1.0–1.1 GeV/c[60]. Since our previous analysis[9, 22] favors $M_A = 1.11$ GeV/c, we employ this value in our simulation.

Finally, the differential cross-section is expressed by

$$\frac{d\sigma}{dQ^2} = \frac{m_N^2 G_F^2 \cos^2\theta_c}{8\pi E_\nu^2} \left[A(Q^2) \mp B(Q^2)\frac{(s-u)}{m_N^2} + C(Q^2)\frac{(s-u)^2}{m_N^4}\right] \tag{5.8}$$

where E_ν is the incident neutrino energy, $(s-u) \equiv 4m_N E_\nu - Q^2 - m_l^2$, m_l is the lepton mass, and;

$$A(Q^2) = \frac{(m_l^2+Q^2)}{4m_N^2}\left[\left(4+\frac{Q^2}{m_N^2}\right)|F_A|^2 - \left(4-\frac{Q^2}{m_N^2}\right)|F_V^1|^2 + \frac{Q^2}{m_N^2}|\xi F_V^2|^2\left(1-\frac{Q^2}{4m_N^2}\right) + \frac{4Q^2 F_V^1 \xi F_V^2}{m_N^2} - \frac{m_l^2}{m_N^2}\left(|F_V^1+\xi F_V^2|^2 + |F_A|^2\right)\right], \tag{5.9}$$

$$B(Q^2) = -\frac{Q^2}{m_N^2} F_A\left(F_V^1 + \xi F_V^2\right), \tag{5.10}$$

$$C(Q^2) = \frac{1}{4}\left(|F_A|^2 + |F_V^1|^2 + \frac{Q^2}{m_N^2}\left|\frac{\xi F_V^2}{2}\right|^2\right). \tag{5.11}$$

The sign of $B(Q^2)$ in Equation (5.8) is $-$ for neutrinos and $+$ for anti-neutrinos.

Figure 5.6 shows the quasi-elastic cross section as a function of E_ν with $M_A = 0.91, 1.01, 1.11$ GeV/c^2. They are consistent with various bubble chamber measurements around 1 GeV[61, 62, 63, 64].

The cross-section of the NC elastic scattering is derived from following relations[65]:

$$\sigma(\nu p \to \nu p) = 0.153 \times \sigma(\nu n \to e^- p), \tag{5.12}$$

$$\sigma(\nu n \to \nu n) = 1.5 \times \sigma(\nu p \to \nu p). \tag{5.13}$$

The Fermi motion and the Pauli blocking effect are considered for the target nucleons bound in ^{16}O or ^{12}C. The Fermi gas model is adopted to reproduce the Pauli blocking effect. The final nucleon momentum is required to be larger than the Fermi surface momentum (225 MeV/c in ^{16}O and 217 MeV/c in ^{12}C). The Fermi surface momentum is estimated from an electron-^{12}C scattering experiment[66]. The cross-section depends on the target nucleus because of the Pauli blocking effect, and the difference of the cross-section between ^{16}O and ^{12}C is less than 1.5% in the neutrino energy region of $E_\nu > 0.5$ GeV.

5.2.2 Resonance production channel

The resonance production interaction produces one lepton and one pion intermediating a baryon resonance state N^*:

$$\begin{aligned} \nu + N &\to l^- + N^* \\ N^* &\to N' + \pi \ (\eta, K), \end{aligned} \tag{5.14}$$

which is the dominant process if the invariant mass of the hadron system is less than 2 GeV/c^2. The simulation of this mode is based on the Rein-Sehgal model[67].

The differential cross-section of the resonance production with the mass M is written by

$$\frac{d^2\sigma}{dQ^2 dE_\nu} = \frac{1}{32\pi m_N E_\nu^2} \cdot \frac{1}{2} \cdot \sum_{\text{spins}} |T(\nu N \to l N^*)|^2 \cdot \delta(W^2 - M^2), \tag{5.15}$$

where W is the invariant mass of the hadron system, and the width of the resonance decay is neglected. The amplitude of the resonance production, $T(\nu N \to l N^*)$, is calculated according to the FKR (Feynman-Kislinger-Ravndal) baryon model[68]. This model includes vector and axial-vector form factors using dipole parametrization with the same M_V and M_A values as CC-QE. The differential cross-section for the resonance with a finite decay width, Γ, is derived by replacing the δ-function in Equation (5.15) with a Breit-Wigner formula:

$$\delta(W^2 - M^2) \to \frac{1}{2\pi} \frac{\Gamma}{(W-M)^2 + \Gamma^2/4}. \tag{5.16}$$

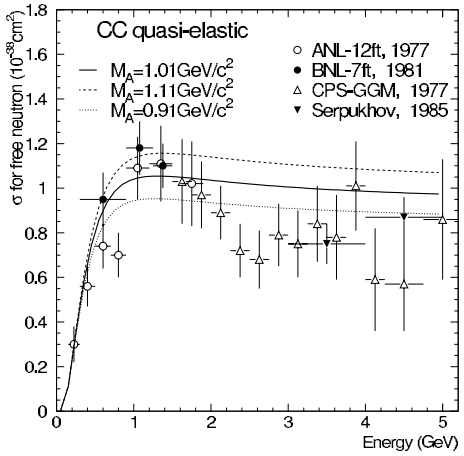

Figure 5.6: Cross-section of CC-QE interaction on a free neutron in NEUT, together with the results of measurements by bubble chamber experiments. Horizontal axis is the incident neutrino energy. Solid, dashed, and dotted lines show the calculations of the cross-section in NEUT with M_A = 1.01, 1.11, and 0.91 GeV/c, respectively. Data points are from ANL[61], BNL[62], GGM[63], and Serpukhov[64].

In NEUT, $\Delta(1232)$ and other 17 resonance states with $W < 2.0$ GeV/c^2 are considered. Figure 5.7 shows our calculation of the cross-section for each final state with $M_A = 1.01$ GeV/c^2 and experimental data[69, 70, 71]. In case of our choice, $M_A = 1.11$ GeV/c^2, and the cross-section is approximately 10% higher than that with $M_A = 1.01$ GeV/c^2. The cross-section is consistent with past experiments, no matter which M_A value we employ.

The decay kinematics of $\Delta(1232)$ is calculated by the Rein-Sehgal method. For the other resonance states, the meson direction is assumed to be isotropic in the rest frame of the resonance state.

5.2.3 Coherent pion production

The coherent pion production is the neutrino interaction with a whole nucleus instead of an individual nucleon, and it does not change the charge or the isospin of the nucleus. This reaction produces one pion with the same charge as the intermediating weak boson. The angular distribution of the recoil lepton is sharply peaked in the forward direction, and the nucleus does not break up due to the small momentum transfer.

The calculation of the cross-section and the kinematics is based on the Rein-Sehgal model[72] whose cross-section is modified to produce the model by J. Marteau *et al.*[73]. The differential cross-section of the Rein-Sehgal model is expressed by

$$\frac{d^3\sigma}{dQ^2 dy dt} = \frac{G_F^2 m_N E_\nu}{2\pi^2} f_\pi^2 A^2 (1-y) \cdot \left.\frac{d\sigma(\pi N \to \pi N)}{dq^2}\right|_{q^2=0} \cdot \left(\frac{1}{1+Q^2/M_A^2}\right)^2 e^{-bt} F_{\rm abs}, \qquad (5.17)$$

where f_π is the pion decay constant of $0.93 m_\pi$, A is the atomic number, $b = (R_0 A^{1/3})^2/3$ is of the order of the transverse dimension of the nucleus taken to be 80 GeV^{-2} for oxygen, and t is the square of the four-momentum transfer to the nucleus. $F_{\rm abs}$ is a factor coming from the pion absorption in the nucleus. Figure 5.8 shows the comparison of the cross-sections between the Rein-Sehgal model and its modification by Marteau *et al.* The cross-section of the former is slightly higher around 1 GeV.

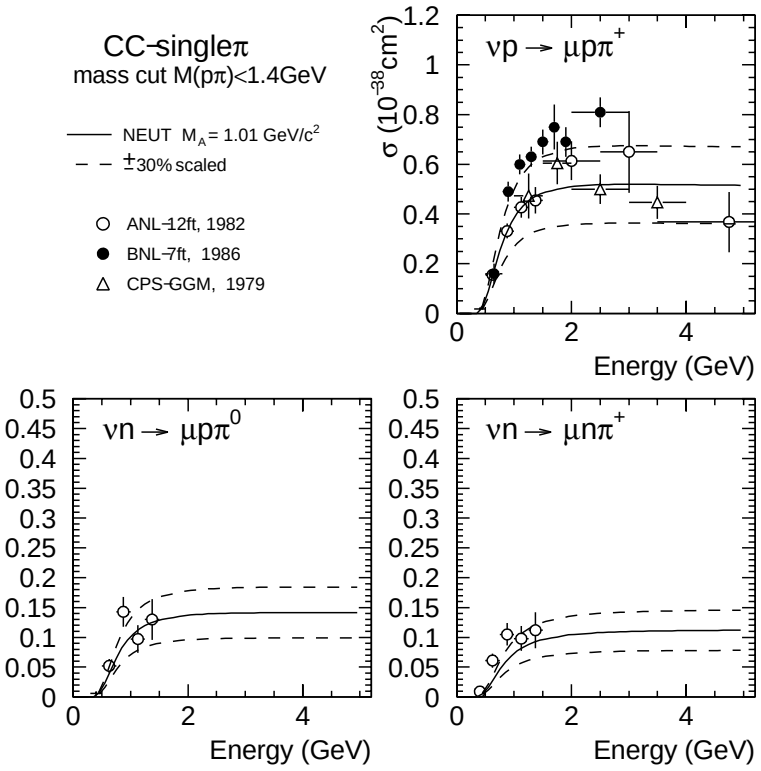

Figure 5.7: Cross-sections of CC resonance production channels in NEUT, together with experimental results. Solid lines show our calculation, and dashed lines show the the cross-section scaled by $\pm 30\%$, where $M_A = 1.01$ GeV/c^2. The experimental results are from ANL[69], BNL[70], and GGM[71].

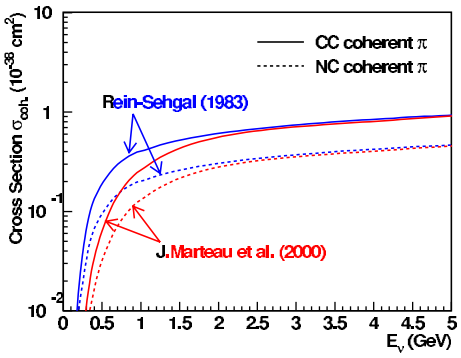

Figure 5.8: Cross-section of the coherent pion production calculated by NEUT. Solid lines show the cross-section of CC, and dashed lines show that of NC. The cross-section modeled by Rein-Sehgal[72] and Marteau *et al.*[73] are drawn with blue and red lines, respectively.

5.2.4 Deep inelastic interactions

The differential cross-section of CC deep inelastic scattering is calculated by integrating the following equation in the range of the invariant mass of the hadronic system, $W > 1.3$ GeV/c^2 [74]:

$$\frac{d^2\sigma}{dxdy} = \frac{G_F^2 m_N E_\nu}{\pi} \cdot \left[(1 - y + \frac{1}{2}y^2 + C_1)F_2(x) + y(1 - \frac{1}{2}y + C_2)[xF_3(x)] \right] \tag{5.18}$$

$$C_1 = \frac{m_l^2(y-2)}{4m_N E_\nu x} - \frac{m_N xy}{2E_\nu} - \frac{m_l^2}{4E_\nu^2}$$

$$C_2 = -\frac{m_l^2}{4m_N E_\nu x}$$

where $x = Q^2/(2m_N(E_\nu - E_l) + m_N^2)$ and $y = (E_\nu - E_l)/E_\nu$ are the Bjorken scaling parameters, and E_l is the energy of the final state lepton. The nucleon structure functions, F_2 and xF_3, are given by GRV94[75] which is modified by Bodek and Yang[76]. The Bodek-Yang modification effectively changes the cross-section by a Q^2-dependent factor:

$$\frac{d^2\sigma}{dxdy} \to \frac{Q^2}{Q^2 + 0.188} \cdot \frac{d^2\sigma}{dxdy}. \tag{5.19}$$

It reduces the cross-section in low Q^2 region, which is favored by our previous analysis[9, 22].

The kinematics of the hadronic system is simulated by two methods according to the invariant mass, W. Only pions are considered in the region of $1.3 < W < 2.0$ GeV/c^2. The mean multiplicity of pions is estimated from the result of Fermilab 15-foot hydrogen bubble chamber experiment[77]:

$$\langle n_\pi \rangle = 0.09 + 1.83 \ln W^2. \tag{5.20}$$

The number of pions for each event is determined using KNO(Koba-Nielsen-Olesen) scaling[78]. Since the range of W overlaps with that in the resonance production mode, $n_\pi \geq 2$ is required in this W region. The forward-backward asymmetry of pion multiplicity is also taken into account to be [79]:

$$\frac{\langle n_\pi^F \rangle}{\langle n_\pi^B \rangle} = \frac{0.35 + 0.41 \ln W^2}{0.50 + 0.09 \ln W^2}. \tag{5.21}$$

In the region of $W > 2.0$ GeV/c^2, the kinematics of the hadronic system is calculated by JETSET/PYTHIA package[80].

For the NC deep inelastic scattering, the ratio of NC to CC is assumed to be

$$\frac{\sigma(\mathrm{NC})}{\sigma(\mathrm{CC})} = \begin{cases} 0.26 & (E_\nu < 3 \text{ GeV}) \\ 0.26 + 0.04(E_\nu/3 - 1) & (3 < E_\nu < 6 \text{ GeV}) \\ 0.30 & (E_\nu > 6 \text{ GeV}) \end{cases}, \tag{5.22}$$

which is based on the experimental results[81].

5.2.5 Nuclear effects

Hadrons produced in an ^{16}O or ^{12}C nucleus often interact with nuclear medium inside the nucleus, called "nuclear effect". The nuclear effects of pions, nucleons, and Δ resonances are considered in NEUT. The neutrino interaction position in a nucleus is calculated using the Wood-Saxon type density distribution:

$$\rho(r) = \frac{Z}{A}\rho_0 \left\{ 1 + \exp\left(\frac{r - c}{a} \right) \right\}^{-1}, \tag{5.23}$$

where we choose $\rho = 0.48 m_\pi^3$, $a = 0.41$ fm, and $c = 2.69$ fm.

Pion

The nuclear effects for pions are classified into inelastic scattering, charge exchange, and absorption. The cross-section is calculated by the model of L. L. Salcedo *et al.*[82]. The Fermi motion and the Pauli blocking effect of nucleons are taken into account in the similar way as the CC-QE interaction. Figure 5.9 shows the calculated π^+-^{16}O interaction cross-section together with experimental data from C. H. Q. Ingram *et al.*[83], which agree well with each other. Since uncertainties in the past measurements are approximately 30%, we use this value as a systematic error on the nuclear effect for pions.

Nucleon

The nucleon-nucleon elastic scattering cross-section implemented in NEUT is based on the measurement by H. W. Bertini[84], which is used by GCALOR. The pion production interaction is also taken into account, according to the isobar production model of S. J. Lindenbaum *et al.*[85]. The effect of these models are compared with a past experiment by K. V. Alanakian *et al.*[86], which measured the yield of scattered protons in electron scattering on a ^{12}C target:

$$e + {}^{12}\mathrm{C} \rightarrow e' + p + X, \tag{5.24}$$

where the electron beam energy is 1.94 GeV, and the scattering angle of the electron is required to be 15 ± 2 degrees. The proton yield was measured at the scattering angles of 66 ± 8 degrees and 120 ± 8 degrees: the former corresponds to protons from pure QE process without nucleon-nucleon scattering, and the latter corresponds to those with scattering. This experiment is reproduced with NEUT by replacing the incident electron with an electron neutrino. Figure 5.10 shows the scattering angle of the proton using NEUT. We find that NEUT generates scattered protons 10% larger than the measurement. Therefore, we rescale the nuclear effect for nucleons by multiplying 0.9 to the cross-section, and we assign the error of 0.1 to this factor.

Δ resonance

The absorption of a Δ resonance[87] is taken into account. Approximately 20% of the Δ resonances are lost by this effect.

5.3 Detector simulation

Particles generated by NEUT are processed by a detector simulator (DetSim). We use GEANT-3.2.1 package[46] for DetSim. The materials of each detector component are implemented in the code. DetSim reproduces the passage of a particle through a matter, and simulates the detector response.

5.3.1 Fine-grained detector

The scintillation light of SciBar is generated assuming a linear relation to the energy deposit in a scintillator strip. The light yield obtained in Section 4.3.2 is employed in the simulator. The attenuation of a WLS fiber is also implemented using the attenuation length obtained by a laboratory measurement[35]. For the time response of SciBar, the light velocity in the fiber is taken into account.

In the simulation of SciFi, the light yield of the scintillating fibers and the response of IIT-CCD pixels are reproduced according to the calibration data using cosmic ray muons, a radioactive source (^{90}Sr), and LED light[25].

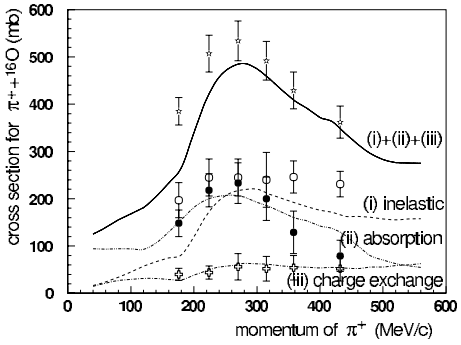

Figure 5.9: Cross-sections of π^+-^{16}O interactions. The lines show the results of our calculation based on [82], and the symbols show the experimental data[83]. Each interaction channel is illustrated in the figure.

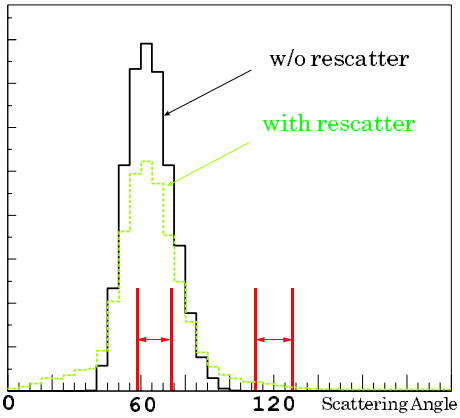

Figure 5.10: Scattering angle of the proton from a ν_e CC-QE interaction in NEUT. The incident neutrino energy is the same as the Alanakian's measurement[86]. The solid line shows the proton angle without the nuclear effect, and the dashed line shows that with the nuclear effect.

The responses of the light yield in TGC and LG are tuned to reproduce the cosmic ray muon data and the beam test results[26]. For MRD, the hit timing information is properly simulated including the drift time of ions[29]. The hit efficiency of 97.5% and the noise hits are also implemented.

5.3.2 Water cherenkov detectors

Cherenkov photons are generated along the trajectory of a charged particle. In the propagation of the Cherenkov photons in the water, Rayleigh scattering, Mie scattering, and absorption are considered[11]. The light attenuation coefficients used in the simulator are tuned to reproduce the measurements using a laser system and cosmic ray muons. The light reflection and absorption on the surface of detector materials are simulated, including the acrylic cover of a 20 inch PMT in SK-II.

The PMT response is reproduced by using the measured quantum efficiency and gain. The properties of the electronics system, such as the time width of ADC gate and the signal threshold, are also taken into account.

Chapter 6

Analysis of SciBar Detector

We describe the analysis of neutrino events in SciBar. Since we use charged-current interaction to measure the neutrino energy spectrum at the near site, we select muon events from SciBar data. There are two steps in this analysis. First, particle tracks are reconstructed by a track finding algorithm. A muon track is subsequently selected from reconstructed tracks. In addition, we estimate the track finding efficiency before and after the CC event selection.

6.1 Track finding

The track finding procedure of SciBar is summarized as follows.

1. The hit preparation routine corrects the cross-talk effect, and selects the hits larger than two photo-electrons to remove noise hits.

2. A cellular automaton tracking algorithm looks for two-dimensional (2D) tracks in each projecting plane. Each of them is fitted to a straight line by a least square method.

3. A couple of 2D tracks are combined into a three-dimensional track, if they are sufficiently overlapping along the beam direction and they have similar timing.

The hit preparation routine is described in Section 6.1.1, and the detail of the track finding algorithm is described in Appendix A. We evaluate the track finding efficiency in Section 6.1.2 and 6.1.3.

6.1.1 Hit preparation

To reduce fake hits due to the cross-talk of MA-PMT, we apply a cross-talk correction. Since the MA-PMT has 64 channels, the cross-talk is expressed by a linear transformation of a 64×64 matrix. Therefore, the cross-talk is corrected by its inverse transformation. The matrix represents 4% cross-talk to adjacent pixels and 1% to diagonally opposite pixels, based on the measurement in a laboratory[36].

After the cross-talk correction, we select the hits 3σ higher than the pedestal, where σ is the standard deviation of the pedestal distribution. This threshold corresponds to 0.5 photo-electron. In addition, a hit is required to be larger than 2.0 photo-electrons. Figure 6.1 shows the distributions of the number of photo-electrons after the 3σ cut. All hits in the neutrino beam data are used in this figure.

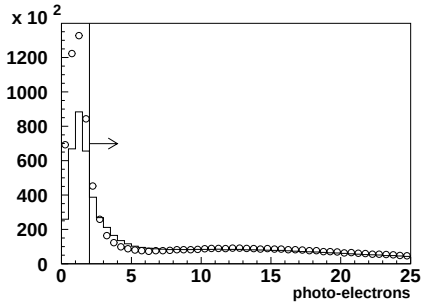

Figure 6.1: The number of photo-electrons for each SciBar hit. The open circle shows data and the solid line shows the MC simulation. The MC distribution is normalized by the entries from 2 to 25 photo-electrons. A hit is required to be larger than 2.0 photo-electrons.

6.1.2 Tracking efficiency in MC simulation

We evaluate the track finding efficiency for neutrino events using a MC simulation. Counting the common hits between a MC true track and a reconstructed 3D track, we figure out whether the particle is reconstructed or not. The fraction of common hits is defined as the number of common hits between a MC true track and a reconstructed track devided by the the number of hits in the MC true track. If more than one reconstructed tracks have common hits with a MC true track, the reconostructed track with the maximum fraction is selected. Figure 6.2 shows the fraction of common hits, for example, for the muon passing more than 10 layers in each event. We set the threshold to 0.7 to judge whether the MC track is reconstructed. Here, we define the track finding efficiency as the percentage of the tracks above the threshold. In this case, the track finding efficiency is 89.3%. Figure 6.3 shows the track finding efficiency as a function of the number of layers for muons, protons and charged pions. Since most of the charged particles are generated from a common vertex, the track finding efficiency of a short track is small because of overlapping of tracks.

6.1.3 Tracking efficiency in real data

To check the tracking efficiency in real data, we use the neutrino event in SciFi. A schematic event display is shown in Figure 6.4. The event selection criteria are given by:

- Select the track that starts from the upstream half of SciFi, to avoid the misfitting of the SciFi track finder.
- The track goes out from the last layer of SciFi.
- The extrapolation of the track is matched to the hit of the trigger counter.
- The extrapolation of the track is matched to the hits on both the first layer and the fifth layer of SciBar.

Here, the matching condition of SciFi track to both trigger counter and SciBar hits is that the position difference is less than 50 cm for each projection. From these criteria, we select a simple isolated track in SciBar. We define the number of these events as $N_{\mathrm{SF}\to\mathrm{SB}}$. From this event sample, we look for the SciBar track which is matched to the SciFi track. The number of events with matched SciBar tracks is defined as N_{SB}. The matching condition is that the position residual between the extrapolation of SciFi track and the start point of the SciBar

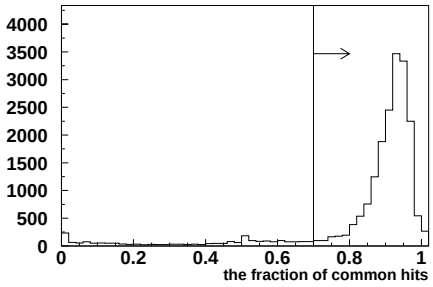

Figure 6.2: The fraction of common hits for the muon passing more than 10 layers. The threshold to judge whether the MC track is reconstructed is set to 0.7. The percentage of the events above the threshold is 89.3% in this plot.

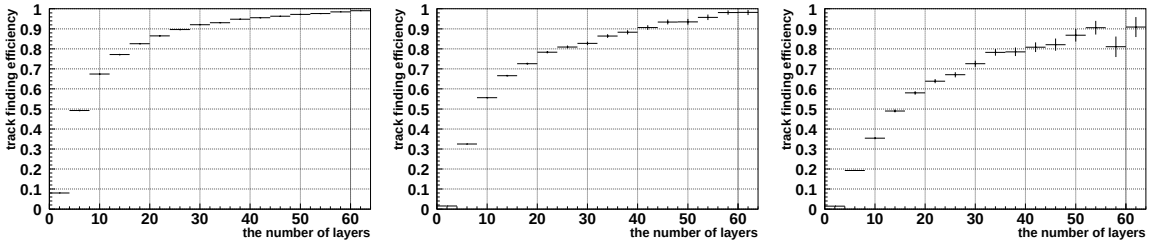

Figure 6.3: The track finding efficiency as a function of the number of layers for muons (left), protons (center) and charged pions (right). The error bars show statistical error.

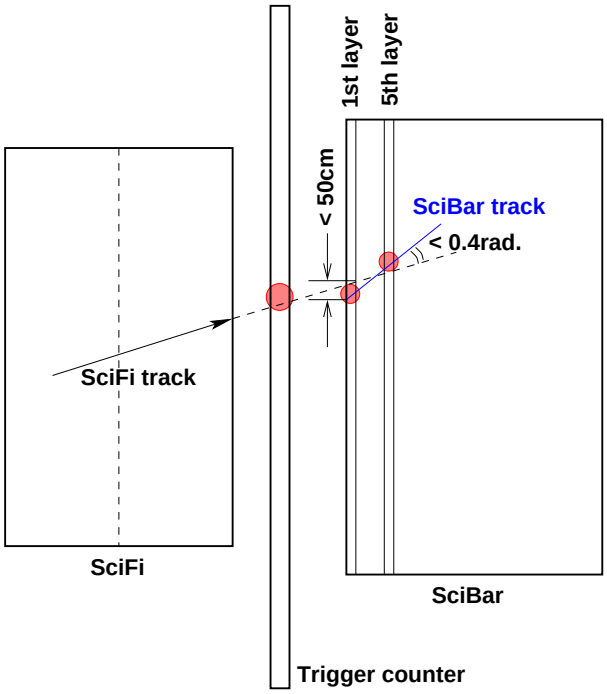

Figure 6.4: The schematic event displays of SciFi events matching to SciBar. The matching condition between SciFi and SciBar tracks are also shown.

track is less than 50 cm, and that the angle between them is less than 0.4 radian. Here, we define the tracking efficiency as $N_{\rm SB}/N_{\rm SF\to SB}$. $N_{\rm SF\to SB}$, $N_{\rm SB}$ and the track finding efficiency are summarized in Table 6.1. The track finding efficiency of the particle passing more than four layers is estimated to be 99.2%. Thus, the track finding efficiency of simple tracks is very high.

However, this sample is too simple to evaluate the actual track finding efficiency of neutrino events in SciBar, because more than one charged particles are often produced in neutrino interaction. Therefore, we estimate the efficiency of charged current events at the end of this chapter.

6.2 Charged-current event selection

The goal of the analysis of SciBar is to determine the neutrino energy spectrum at the near site by using CC-QE, in which there is a strong correlation between the neutrino energy and the muon momentum and direction. It is also important to measure the fraction of non-quasi-elastic (nonQE) component, because they are backgrounds for the analysis of the energy spectrum measurement. Therefore, we select a CC event which contains a muon in the final state.

There are an electro-magnetic calorimeter (EC) and a muon range detector (MRD) downstream of SciBar. They are mainly made of lead and iron, respectively, which are good muon filters. Consequently, we select the particle track which is created within SciBar and matched to a MRD track or MRD hits. There are two kinds of MRD matching events: MRD 3D matching (MRD-3D) and MRD first layer matching (MRD-1L). The event displays are shown in Figure 6.5. The definition of MRD-3D is that a particle track is reconstructed by both SciBar and MRD and that the SciBar track and the MRD track are connected three-dimensionally. MRD-1L means that no MRD track is reconstructed but the hits on the first plane of MRD drift-tubes are matched with a SciBar track. The event selection procedure is described in the following sections.

6.2.1 Requirements for the SciBar track

Before connecting between SciBar and MRD, we apply some common cuts to SciBar tracks as summarized below.

Timing cut

Figure 6.6 shows a timing distribution of SciBar tracks. We select the events within beam spill window, $-100 < t < 1300$ nsec. Here, the origin of the time t is defined as roughly 100 nsec before the first bunch. There are flat components before and after the beam. The early events are cosmic rays, and most of the late events are called sky-shine backgrounds[88] which are thought to be induced by neutrons from the production target and decay volume etc. The sky-shine makes short tracks (less than 50 cm) in SciBar and does not generates a muon.

First layer veto

A particle, due to neutrino interaction elsewhere or a cosmic ray, often comes from upstream of SciBar. In order to select neutrino events happened inside SciBar, the event with a particle coming upstream of SciBar is rejected by requiring no hits on the most upstream layer of SciBar. If there are any hits above five photo-electrons on either X-plane or Y-plane of the first layer, we do not use any tracks within 50 nsec from the hits. In the case that the timing of a track is more than 50 nsec apart from those of any first layer hits above five photo-electrons, we keep the track. This requirement is shown in Figure 6.7 and 6.8. The large peak below five photo-electrons is mainly caused by cross-talk and a grazing particle at the corner of a scintillator strip. The

Table 6.1: The tracking efficiency in real data. $N_{\mathrm{SF}\to\mathrm{SB}}$ is the number of events in which a SciFi track is penetrating through the fifth layer of SciBar. N_{SB} is the number of events in which a SciBar track is matched to the SciFi track. The tracking efficiency of the particle passing more than 4 layers is defined as $N_{\mathrm{SB}}/N_{\mathrm{SF}\to\mathrm{SB}}$.

$N_{\mathrm{SF}\to\mathrm{SB}}$	N_{SB}	Track finding efficiency
1083	1074	99.2%

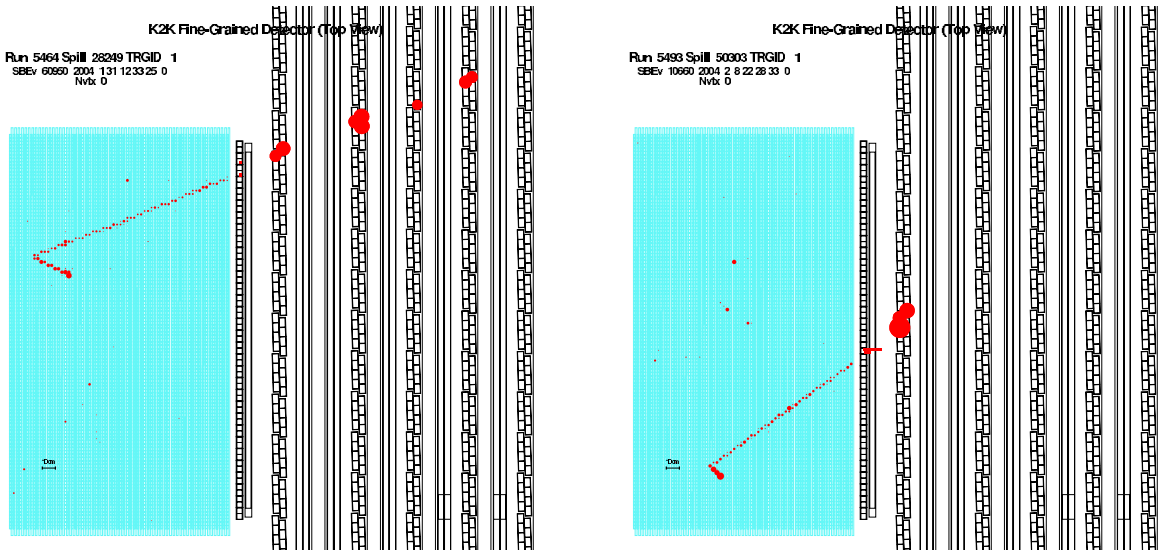

Figure 6.5: The event displays of SciBar events matched to MRD. The left figure shows 3D matching event and the right figure shows MRD first layer matching event.

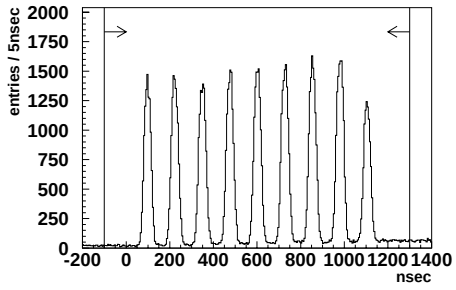

Figure 6.6: The timing distribution of SciBar tracks. The micro-bunch structure of the beam is clearly seen. We select $-100 < t < 1300$ nsec as a beam timing window.

threshold of five photo-electrons rejects 99.6% of incoming particles from the upstream plane. According to the MC simulation, 2.7% of neutrino events are lost by the first layer veto owing to backward scattering particles.

Exiting track selection

Obviously, the track matched to MRD exits from SciBar. The downstream edge of a track is required to satisfy either of following two conditions:

1. On the most downstream layer of SciBar.
2. $|X_{\rm down}| > 130$ cm or $|Y_{\rm down}| > 130$ cm.

Here, $X_{\rm down}$ and $Y_{\rm down}$ are the coordinates of the downstream edge of a track. The origin is the center of SciBar. Since the tracking area of the XY plane is $|X_{\rm down}| < 140$ cm and $|Y_{\rm down}| < 140$ cm, the second condition is that the downstream edge of a track is within the 10 cm margin of the XY tracking area. Most of the contained events in SciBar are rejected by this requirement.

6.2.2 Matching a SciBar track to MRD

3D track matching

First, an MRD track to be matched is required to start from the first chamber plane of MRD. To connect SciBar and MRD tracks, we require that the extrapolation of the SciBar track is within 20 cm from the start point of the MRD track for both X and Y, and that the angle between them is less than 0.5 radian. Figure 6.9 and 6.10 show the residual distributions of position and angle, respectively.

Matching to MRD first layer hits

If no MRD-3D track is found, we look for the MRD first layer hits matched with the SciBar track (MRD-1L). For both X and Y, the difference between the extrapolation of a SciBar track and MRD first layer hits is required to be less than 20 cm, as shown in Figure 6.11.

Since the MRD tracking efficiency is too low for short tracks (only 65% for tracks passing two chamber layers, as shown in Figure 3.21), the MRD-1L track may also have hits in the second layer or more. If we miss the hits at the second layer, the muon range is reconstructed to be shorter. To obtain correct muon range, therefore, we look for the downstream hits associated to a MRD-1L track. To search for the matching hit in the second layer, we draw a line from the first layer hit to one of the second layer hits. The matching condition is that the angle between the line and the MRD-1L track is less than 0.5 radian. The distribution of this angle is shown in Figure 6.12. Similarly, the condition for the third layer hits is that the angle between the lines from first layer to second and from second to third is less than 0.5 radian for each projection. The same is true for more downstream layers.

6.2.3 Final requirement

Containment

Since the muon energy is determined by the range, the matched track is required to stop inside MRD. If the track has a hit at the most downstream drift-tube, the event is not used. For the track stopping near a side wall, the extrapolation to the next layer is required to be 5 cm away from the wall of MRD.

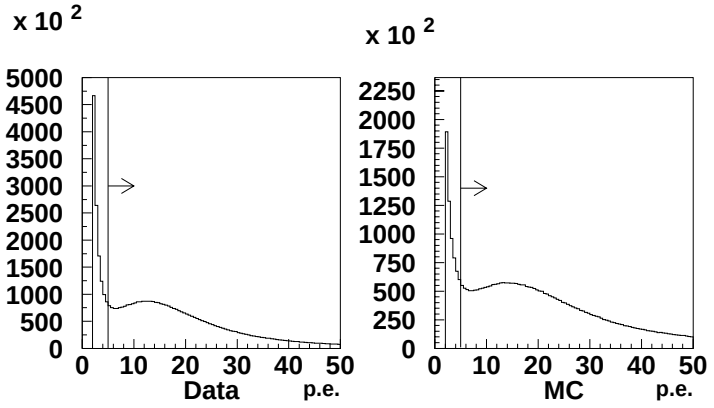

Figure 6.7: The number of photo-electrons for the hits on the first layer of SciBar. All events are used. The left figure shows data and the right figure shows MC simulation. The threshold for the first layer veto is five photo-electrons.

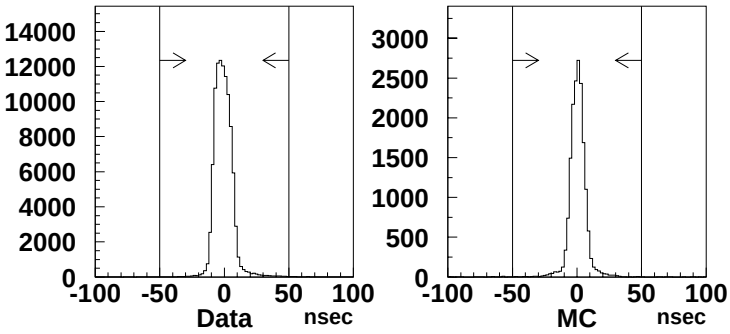

Figure 6.8: The time difference between a track and a hit on the first layer for data (left) and MC simulation (right). The veto condition is that the difference is less than 50 nsec.

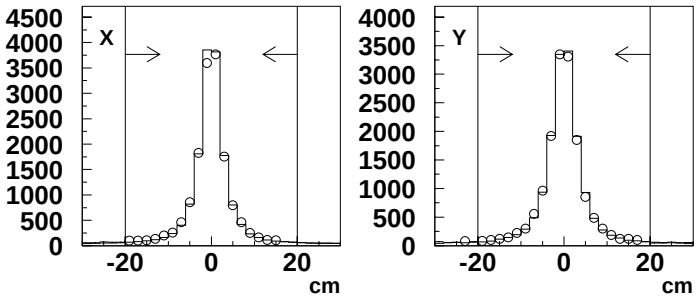

Figure 6.9: Residual distributions of the position between a SciBar track and a MRD track. The circles show data and the histograms show the MC simulation. The matching condition (< 20cm) is also illustrated.

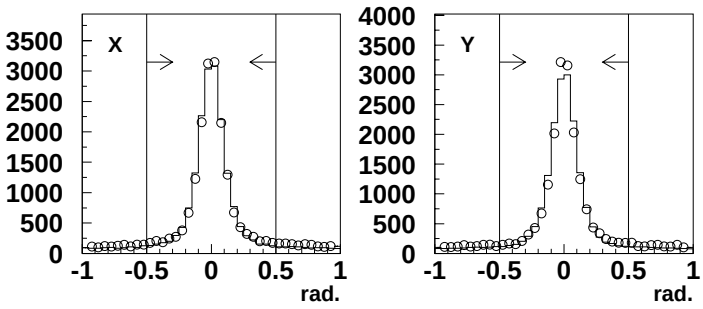

Figure 6.10: Residual distributions of the direction between a SciBar track and a MRD track. The matching condition is that the residual is less than 0.5 radian.

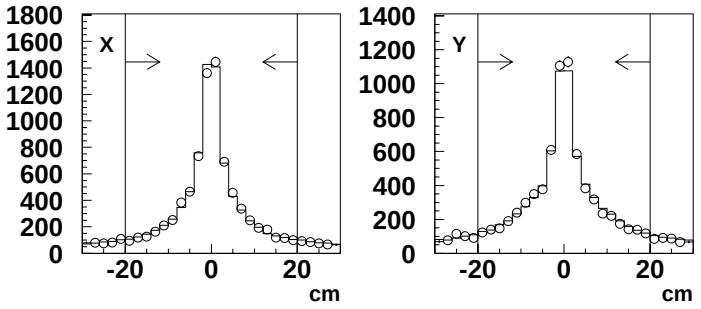

Figure 6.11: The residual distributions of the position between a SciBar track and a MRD first layer hit.

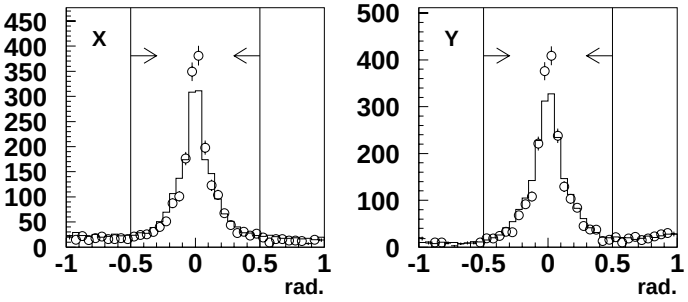

Figure 6.12: The residual distributions for the angle between a SciBar track and the straight line from a MRD first layer hit to a second layer hit.

Vertex

The neutrino interaction vertex is defined to be the starting point of a matched track. The vertex is required to be inside the fiducial volume which is defined as $260 \times 260 \times 135.2\text{cm}^2$, corresponding to the target mass of 9.38 tons. The vertex distribution and the fiducial volume definition is shown in Figure 6.13. Because of incoming particles induced by neutrino interaction in surrounding materials, the entries of the real data is much more than that of the MC simulation outside of the fiducial volume.

Figure 6.14 shows the distance between a true vertex and a reconstructed vertex by using MC simulation. The vertex resolution is 0.8 cm for each direction. For X and Y, the resolution is close to the expectation from the cell size, $2.5/\sqrt{12} \sim 0.7$cm. However, the Z resolution is the twice of the expectation, $1.3/\sqrt{12} \sim 0.4$cm, and about 40% of events are biased for upstream. It is explained by cross-talk: the hit at the vertex produce a cross-talk hit at the upstream cell, and the track finder reconstructs the vertex at the cross-talk hit.

Timing

Figure 6.15 shows the timing distribution of survived events. There are no background events at all before or after the beam. Thus, we do not apply timing cut any more.

6.2.4 Reduction summary and efficiency

The number of events at each reduction step is summarized in Table 6.2. In total, 9651 CC candidate events are selected, where the number of MRD-3D samples is 7406 and that of MRD-1L samples is 2245.

Using the MC simulation, we estimate the neutrino detection efficiency in this sample. The detection efficiency is defined as the number of reconstructed events divided by the number of events generated in the fiducial volume. The overall efficiency is estimated to be 43.8%. Figure 6.16 shows the MC true neutrino energy distribution and the efficiency as a function of neutrino energy. In the low energy region, the efficiency is small because the muon momentum is too small to reach MRD. On the other hand, since a number of muons induced by neutrinos more than 3.5 GeV are not contained by MRD, the efficiency also becomes smaller in the high energy region.

6.2.5 Muon energy reconstruction

Muon energy E_μ is reconstructed from the range information of each detector by the following formulas,

$$\begin{aligned} E_\mu &= E_\mu^{\text{SciBar}} + E_\mu^{\text{EC}} + E_\mu^{\text{MRD}}, \\ E_\mu^{\text{SciBar}} &= \left(\frac{dE}{dx}\right)^{\text{SciBar}} \cdot L^{\text{SciBar}}, \\ E_\mu^{\text{EC}} &= \left(\frac{dE}{dx}\right)^{\text{EC}} \cdot L^{\text{EC}}, \end{aligned} \tag{6.1}$$

where E_μ^{SciBar}, E_μ^{EC}, and E_μ^{MRD} are the energy deposit in SciBar, EC, and MRD, respectively. The muon mass is included in E_μ^{MRD}. L^{SciBar} is the track length in SciBar, and L^{EC} is the path length in EC calculated by extrapolating the SciBar track. $(dE/dx)^{\text{SciBar}}$ and $(dE/dx)^{\text{EC}}$ are the average stopping power of SciBar and EC, respectively. The input values are $(dE/dx)^{\text{SciBar}} = 2.10$ MeV/cm and $(dE/dx)^{\text{EC}} = 11.25$ MeV/cm. E_μ^{MRD} is determined by a range-to-energy conversion table obtained from the GEANT MC code.

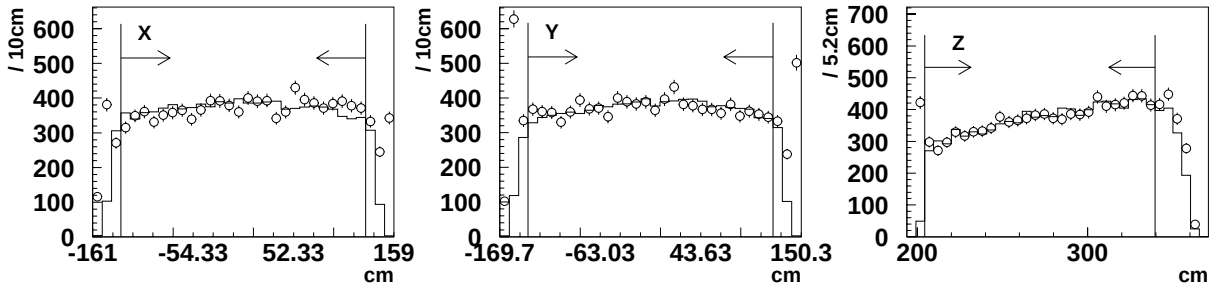

Figure 6.13: The vertex distribution of SciBar-to-MRD matched events. The fiducial volume cut is also shown.

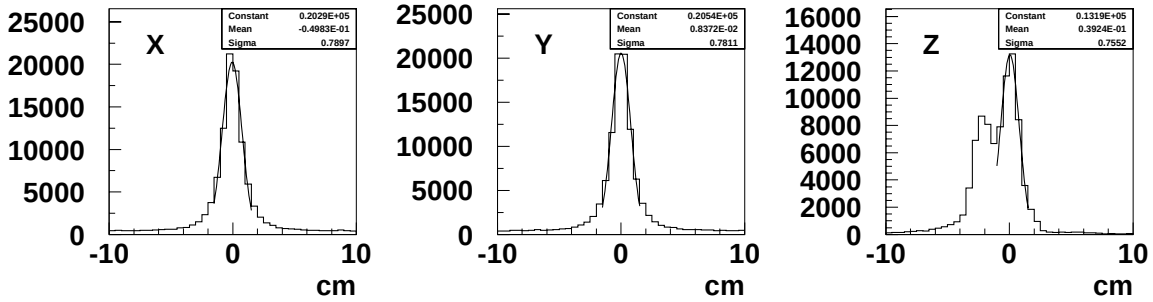

Figure 6.14: The distance between a true vertex and a reconstructed vertex for each direction. Each peak is fitted with gaussian.

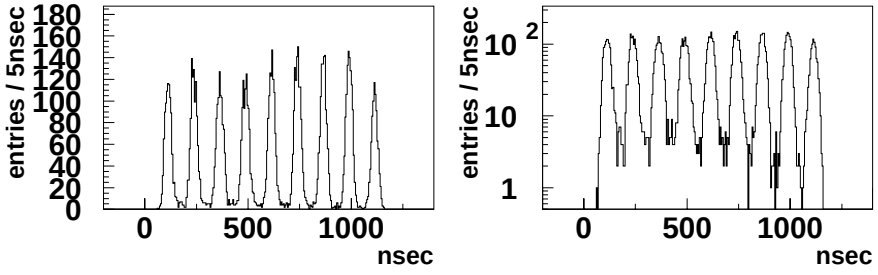

Figure 6.15: The timing distribution of survived events. These two figures show the same data, but the scale of the vertical axis is linear for the left figure and logarithm for the right one.

Table 6.2: The reduction summary of SciBar charged-current selection. The number of events at each reduction step is arranged in the table.

Selection	Data			MC		
	3D	1L	Total	3D	1L	Total
Good beam and SciBar alive			3222301			—
Generated events in SciBar			—			345332
SciBar track exists			87309			266915
Timing cut			80466			266915
First layer VETO			43289			251554
SciBar track exiting			32005			199187
MRD track from the first layer	16471			112048		
3D position and angle matching	13030			94214		
No 3D matching track		18975			104973	
MRD 1L position matching		5033			33318	
Containment	12011	4368	16379	92252	30391	122643
Vertex cut	7406	2245	9651	70225	20448	90673

The difference between reconstructed muon energy and MC true energy is shown in Figure 6.17. The muon energy resolution is 0.08 GeV, dominated by the MRD resolution. The uncertainty in the MRD energy deposit is estimated to be 2.7%. It is the sum of the error on density measurement (1.0%) and the difference between the GEANT MC code and the PDG calculation[1] (1.7%). The density of SciBar is measured with 1.0% accuracy during the installation. Therefore, the error on the SciBar energy scale is thought to be the same level as MRD. The systematic error on the stopping power of EC is estimated to be 10%. If the error on the energy scale is quadratically added according to the mean energy deposit for each component ($\langle E^{\rm SciBar}\rangle$, $\langle E^{\rm EC}\rangle$, and $\langle E^{\rm MRD}\rangle$), the total energy scale error $\Delta E^{\rm total}$ is

$$\Delta E^{\rm total} = \frac{\sqrt{(\langle E^{\rm SciBar}\rangle \cdot \Delta E^{\rm SciBar})^2 + (\langle E^{\rm EC}\rangle \cdot \Delta E^{\rm EC})^2 + (\langle E^{\rm MRD}\rangle \cdot \Delta E^{\rm MRD})^2}}{\langle E^{\rm SciBar}\rangle + \langle E^{\rm EC}\rangle + \langle E^{\rm MRD}\rangle} = 2.2\%, \quad (6.2)$$

where

$$\Delta E^{\rm SciBar} = 2.7\%, \qquad \Delta E^{\rm EC} = 10\%, \qquad \Delta E^{\rm MRD} = 2.7\%,$$
$$\langle E^{\rm SciBar}\rangle = 0.20 \text{ GeV}, \qquad \langle E^{\rm EC}\rangle = 0.08 \text{ GeV}, \qquad \langle E^{\rm MRD}\rangle = 0.98 \text{ GeV}.$$

To be conservative, we quote 2.7% for the total systematic error on the energy scale, because the muon energy is mainly absorbed by SciBar and MRD.

6.2.6 Basic distributions

Muon momentum and direction

Figure 6.18 shows the distributions of the muon momentum (p_μ) and the angle with respect to the beam (θ_μ). The data agree well with the MC distributions except for $\theta_\mu < 10$ degrees. The deficit of the forward going muons is discussed in Section 8.8.

The angle between the reconstructed muon direction and the true direction is shown in Figure 6.19. The three-dimensional angular resolution of the muon is 1.6 degrees, where the resolution is defined as the value at which 68% (one standard deviation) of events are contained. We also define the two-dimensional angular resolution of the muon as the standard deviation of Figure 6.19 (B) and (C), which is 1.0 degree.

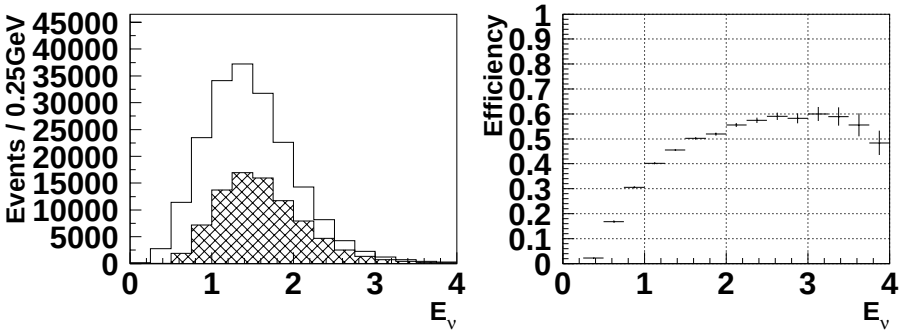

Figure 6.16: The solid line in the left figure shows the all generated events in the fiducial volume by the MC simulation as a function of the neutrino energy. The hatched region shows the reconstructed events. The right figure shows the efficiency curve. The efficiency is defined as the ratio of the hatched region to the solid line in the left figure.

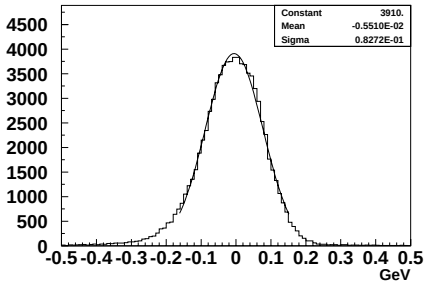

Figure 6.17: The difference between reconstructed muon energy and true energy obtained by the MC simulation. The distribution is fitted with gaussian.

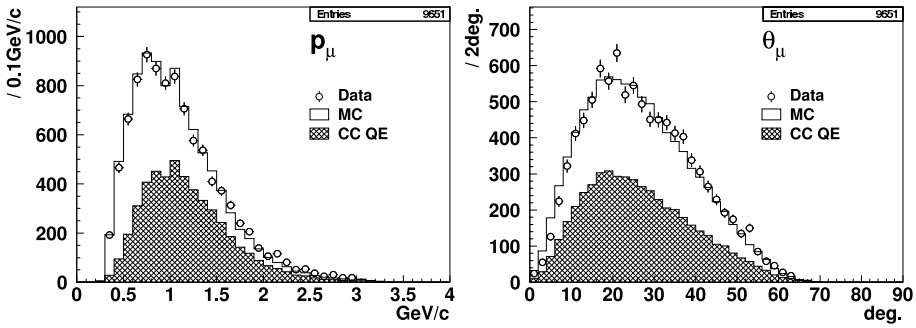

Figure 6.18: The left figure shows the muon momentum distribution and the right figure shows the muon angle with respect to the beam. Open circles, solid lines and hatched regions are data, the MC simulation, and the CC-QE component in the MC simulation, respectively. The MC distributions are normalized by entries.

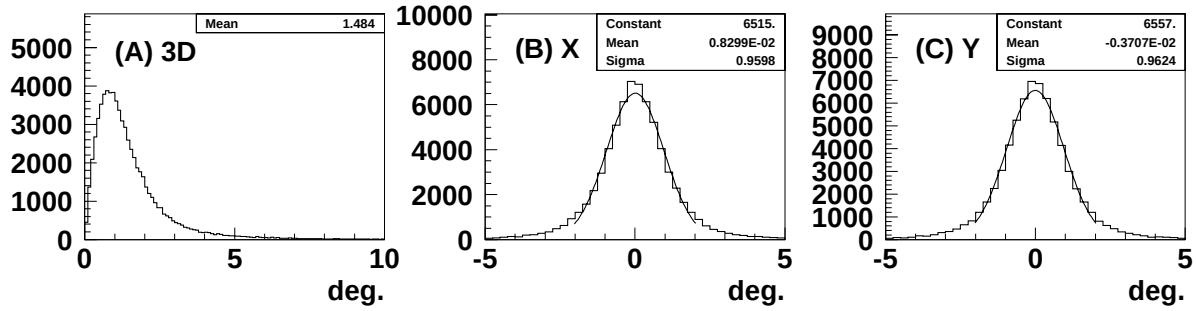

Figure 6.19: The angle between the reconstructed muon angle and the MC true angle obtained by the MC simulation. Figure (A) shows the angle calculated three-dimensionally. Figure (B) and (C) show the angle in the projection to X view and Y view, respectively. (B) and (C) are fitted with gaussian.

The systematic error on the angle measurement is estimated by comparing the direction of a SciBar track with that of a MRD track. The average of the angle difference between the SciBar track and the MRD track is 0.19 degree for X projection and 0.06 degree for Y projection, from the distributions in Figure 6.10. We assign the quadratic sum of them, 0.20 degree, to the systematic error. The deficit of the forward going muon cannot be explained by this error.

Event rate stability

The weekly variation of the event rate is shown in figure 6.20. The event rate is stable within the statistical error.

6.3 Track finding efficiency for CC sample

We estimate the track finding efficiency again, because the discussion in Section 6.1.3 is the single track case. Not only muon but other particles such as a proton and a pion are produced at a CC interaction vertex, and they make the hit pattern around the vertex complicated. Therefore, we study the track finding efficiency of neutrino interactions happened in SciBar by using the real data. In this section, we evaluate the efficiency of both a primary muon track and a second track.

6.3.1 Primary muon track finding efficiency

Event selection

In the analysis of a muon track finding efficiency, we apply new CC selection criteria. CC events in SciBar are selected without any tracking information of SciBar. We subsequently examine whether a SciBar track is reconstructed properly or not. The event selection procedure is summarized below:

1. We choose an MRD track starting from the first chamber layer and stopping within MRD. The track is required to penetrate at least three chamber layers to avoid the mis-reconstruction of the MRD track finder.

2. SciBar hits near the extrapolation of the MRD track are collected. We create the distribution of the distance between an MRD track and SciBar hits for each layer in advance. The matching condition between an MRD track and SciBar hits is that the distance is less than three standard deviations of the distribution.

3. The neutrino interaction vertex is defined as the most upstream hit associated to the MRD track, and it is required to be inside the fiducial volume of SciBar.

4. The most downstream hit matching to the MRD track is regarded as the end point. We count the number of planes which have associated hits between the vertex and the end point. We require that more than 80% of the planes have associated hits.

5. If there is a hit on the first layer of SciBar, the event is rejected to avoid muons coming from upstream.

Basic distributions

Figure 6.21 shows the distance from a true vertex position to a reconstructed vertex position by using an MC simulation. The X and Y positions are reconstructed properly. However, the Z distribution is slightly biased, and it has a long tail due to backward scattering particles. It is thought to be a limitation of the vertex finding method. We allow it in this analysis. Figure 6.22 shows reconstructed vertex distributions. The data agree with the MC simulation well. Figure 6.23 shows the timing distribution of data. The nine-bunch structure of the beam is seen clearly. There are no backgrounds before and after the beam.

Track finding efficiency

The SciBar-to-MRD 3D matching condition (Section 6.2.2) is applied to the selected CC sample. The track finding efficiency for muons is defined as the fraction of the matching events in the selected CC events. The number of events and the efficiency are summarized in Table 6.3. The events are classified by their exiting points. If a particle goes out from the most downstream layer, the Z positions at the end points of the both 2D tracks are the most downstream. Therefore, the combination between the 2D tracks are found more easily than the case that a particle exits from the side. In fact, the track finding efficiency is slightly higher, if the exiting point is downstream. The overall efficiency is approximately 94% for data and 92% for the MC simulation. The efficiency for the real data is slightly higher than that for the MC simulation.

To investigate the reason for the lost events and for the difference between data and the MC simulation, we visually scanned the lost events. The results are summarized in Table 6.4. The meaning of each row is:

- **3D track OK**
  A muon is properly reconstructed as a 3D track.
  - **MRD matching requirement**
    The event does not satisfy the SciBar-to-MRD matching condition written in Section 6.2.2.
- **2D tracks OK**
  The 2D muon tracks are properly reconstructed in both X and Y views, but the 3D track is wrong or lost.
  - **Wrong combination**
    There is another particle than the muon, and two 3D tracks are reconstructed along

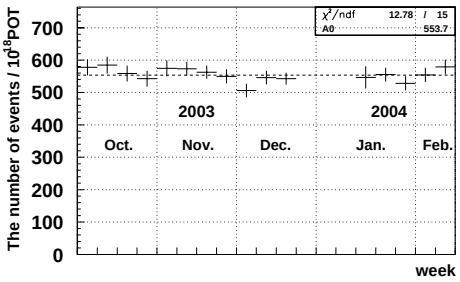

Figure 6.20: The event rate stability for the SciBar charged-current sample. The horizontal axis is the time binned by week and the vertical axis is the number of events per 10^{18} protons on target. The error bars show statistical error only. The dashed line shows the constant function fitted to the plot. The event rate is stable within the statistics.

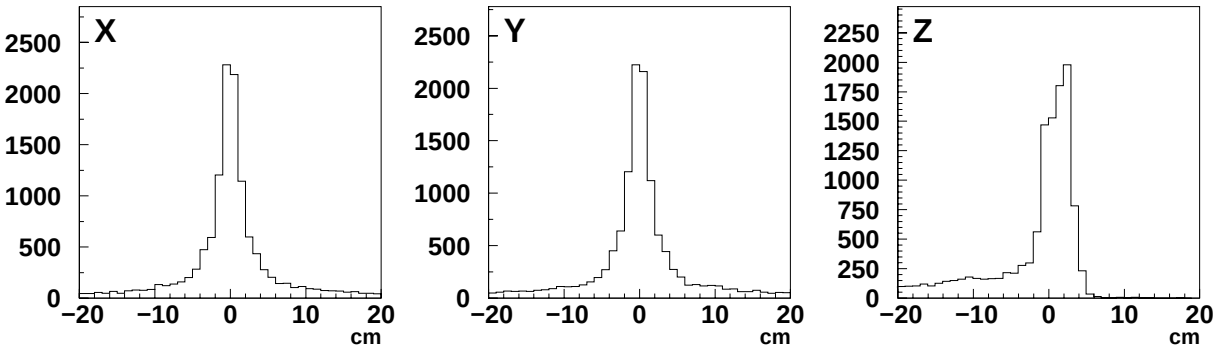

Figure 6.21: The position difference between the true vertex and the reconstructed vertex. The horizontal axes represent (reconstructed position – true position).

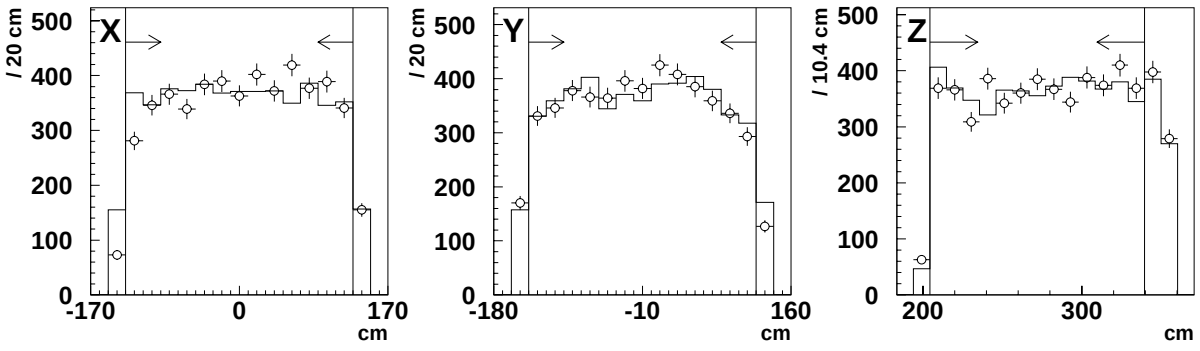

Figure 6.22: Reconstructed vertex distributions of selected events. All requirements except for the fiducial volume cut are imposed. Open circles are data, and solid lines are the MC simulation. The boundaries of the fiducial volume are also illustrated.

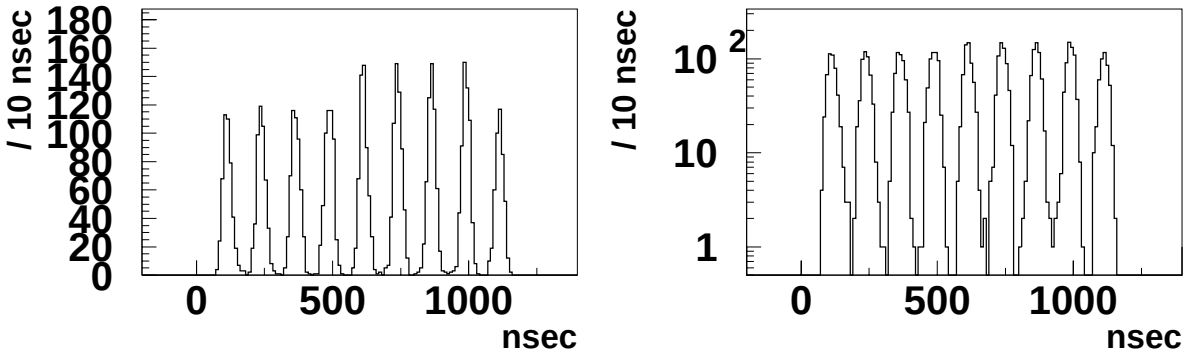

Figure 6.23: The timing distribution of selected events. These figures are identical but the vertical axis of the left histogram is linear scale while that of the other is log scale. Only the real data is shown. The nine-bunch structure is clearly seen. There are no backgrounds before and after the beam spill.

the two particles. However, the combination of 2D tracks is swapped with each other. For example, one of the 3D tracks is composed of X-track of the muon and Y-track of the other particle, and the other 3D track is vice versa.

- **Not combined in one view**
  There is another particle than the muon, and all the 2D tracks along the two particles are properly fitted. However, only one 3D track is reconstructed. It is composed of either X-track or Y-track along the muon and the 2D track along the other particle in the other view.
- **Not combined in both views**
  Both X-track and Y-track of the muon are correctly fitted, but no 3D track is reconstructed along the muon.

- **2D track lost**
  At least one of the 2D tracks along the muon is lost.
  - **Cellular automaton**
    The 2D track finding process fails in connecting hits along the muon.
  - **Hit inefficiency**
    No hits are seen in some layers due to the inefficiency of the reflector of the scintillator strip.
  - **Bad neutrino event**
    The vertex is out of the fiducial volume, or there is no muon-like track in SciBar.

Most of 2D tracks are properly reconstructed, but many events are lost at combining 2D tracks. The hit inefficiency of the MC simulation is larger than that of data. It is considered to come from the geometry setting of the simulation. Since the track finding efficiency is sufficient for the CC analysis, it is not the subject in this thesis to improve these problems.

6.3.2 Second track finding efficiency

We use the CC sample obtained in Section 6.2 for the second track finding efficiency. We visually scanned many events, and counted the number of hits along a second track from a vertex. We

Table 6.3: The track finding efficiency of a muon track in the CC sample. Both data and MC are listed. In addition, results are classified according to exiting points (the downstream plane or the side wall).

	Exiting point	Selected event (A)	SciBar–MRD match (B)	Efficiency (B/A) [%]
Data	Downstream	4102	3871	94.4 ± 0.4
	Side	662	620	93.7 ± 0.9
	Total	4764	4491	94.3 ± 0.3
MC	Downstream	5284	4898	92.7 ± 0.4
	Side	930	838	90.1 ± 1.0
	Total	6214	5736	92.3 ± 0.3

Table 6.4: Results from scanning of lost events. Both data and MC are listed.

		Data	MC
3D track OK	MRD matching requirement	2	2
2D tracks OK	Wrong combination	60	44
	Not combined in one view	43	30
	Not combined in both views	55	76
2D track lost	Cellular automaton	12	6
	Hit inefficiency	27	41
	Bad neutrino event	1	1
Total		200	200

examined whether the second track are properly reconstructed as a 3D track. Figure 6.24 shows the track finding efficiency as a function of the number of hits. One hit corresponds to about 1.5 cm track length. The efficiency exceeds 80% at 20 hits, corresponding to approximately 0.7 GeV/c for a proton. It is sufficient for the analysis of 2-track CC-QE events. The agreement between data and the MC simulation is good.

6.3.3 Summary

The track finding efficiency for both a primary muon track and a second track are studied. The performance is sufficient for the selection of CC events and for the separation between CC-QE and nonQE. Both data and the MC simulation have been used in this analysis, and the MC simulation reproduces data well. Consequently, the CC sample is ready for the determination of the neutrino energy spectrum.

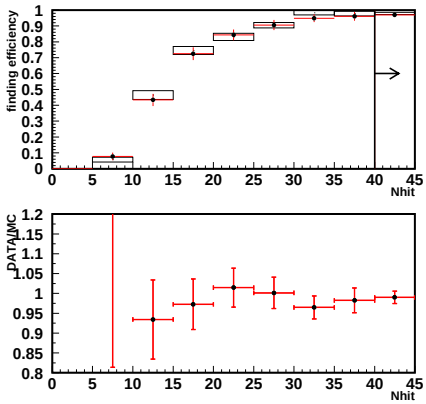

Figure 6.24: The upper figure shows the track finding efficiency of a second track in SciBar as a function of the number of hits. Crosses are data and boxes are the MC simulation. The lower figure shows the ratio of data to the MC simulation.

Chapter 7

Analysis Overview

We introduce the outline of the neutrino oscillation analysis. In addition, we describe the selection criteria of good beam spills and the stability of the neutrino beam.

7.1 Outline of the neutrino oscillation analysis

Figure 7.1 shows the block diagram of the analysis flow. The analysis procedure is already described in Section 2.2. The goal of the neutrino oscillation analysis is to compare both the neutrino energy spectra and the number of events between ND and SK. The neutrino energy spectrum at SK, $\Phi_{\rm SK}(E_\nu)$, is extrapolated by Equation (2.3) from the neutrino energy spectrum at ND, $\Phi_{\rm ND}(E_\nu)$, by using the Far/Near flux ratio, $R_{F/N}(E_\nu)$. The expected number of events in SK, $N_{\rm SK}^{\rm exp}$, is estimated by Equation (2.4) from the number of events in ND, $N_{\rm ND}^{\rm obs}$. The reconstructed neutrino energy of CC-QE candidate events in SK are compared with $\Phi_{\rm SK}(E_\nu)$, and the number of observed events in SK, $N_{\rm SK}^{\rm obs}$, are compared with $N_{\rm SK}^{\rm exp}$. When neutrino oscillation is taken into account, $\Phi_{\rm SK}(E_\nu)$ for CC interaction is multiplied by the neutrino oscillation probability, $P(E_\nu; \Delta m^2, \sin^2 2\theta)$:

$$\Phi_{\rm SK}(E_\nu; \Delta m^2, \sin^2 2\theta) = P(E_\nu; \Delta m^2, \sin^2 2\theta) \cdot R_{F/N}(E_\nu) \cdot \Phi_{\rm ND}(E_\nu), \tag{7.1}$$

where

$$P(E_\nu; \Delta m^2, \sin^2 2\theta) = 1 - \sin^2 2\theta \cdot \sin^2 \left(1.27 \cdot \Delta m^2\,[\mathrm{eV}^2] \cdot \frac{250\,[\mathrm{km}]}{E_\nu\,[\mathrm{GeV}]} \right). \tag{7.2}$$

$N_{\rm SK}^{\rm exp}$ depends on $\Phi_{\rm SK}(E_\nu; \Delta m^2, \sin^2 2\theta)$ as a function of $(\Delta m^2, \sin^2 2\theta)$.

To obtain $\Phi_{\rm SK}(E_\nu)$ and $N_{\rm SK}^{\rm exp}$, we measure following quantities:

- The neutrino energy spectrum at the near site, $\Phi_{\rm ND}(E_\nu)$.
- The number of events in the near detector, $N_{\rm ND}^{\rm obs}$.
- The Far/Near neutrino flux ratio as a function of E_ν, $R_{F/N}(E_\nu)$.

In Chapter 8 – 10, we describe these measurements in this order. Especially for the SciBar detector, the event selection is already described in Chapter 6. Neutrino events in SK are selected in Chapter 11 to obtain the CC-QE candidate events and the total number of SK events, $N_{\rm SK}^{\rm obs}$. Finally, we compare the observation in SK with the expectation, and examine neutrino oscillation in Chapter 12.

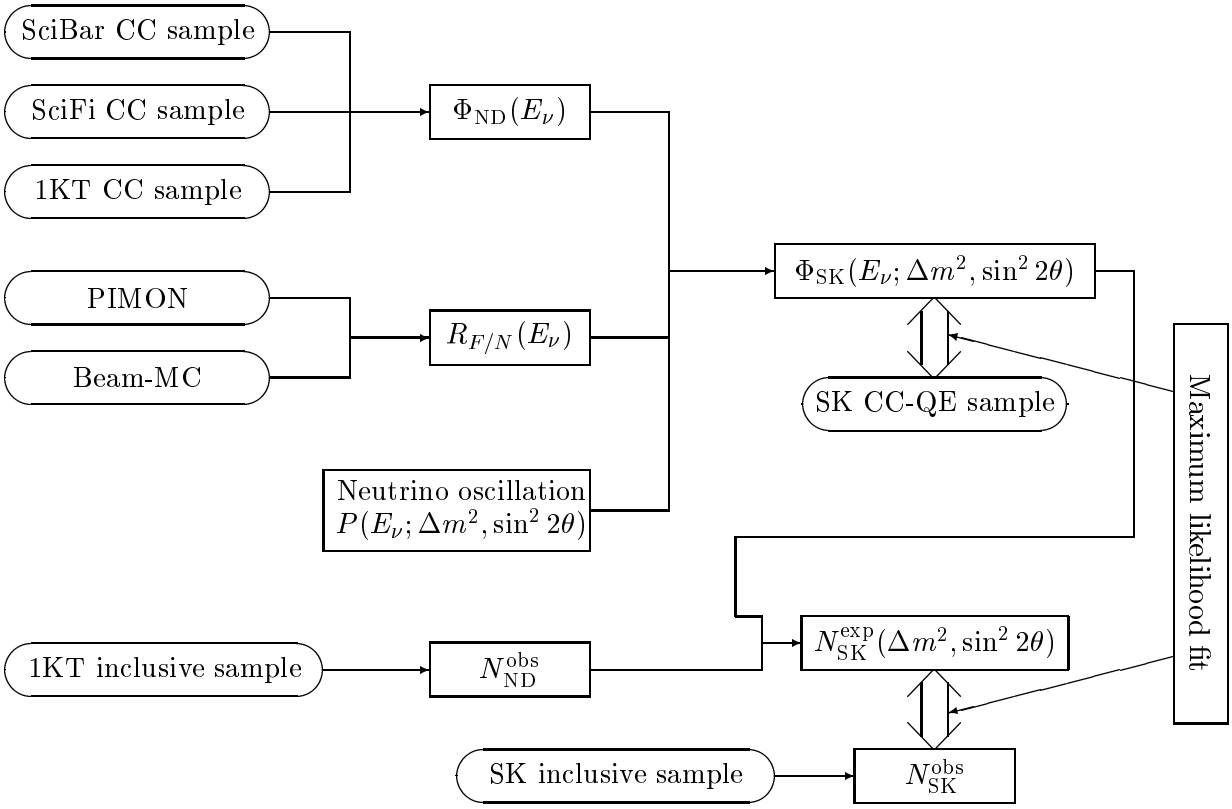

Figure 7.1: Block diagram of the neutrino oscillation analysis.

7.1.1 Neutrino energy spectrum at near site

We measure $\Phi_{\rm ND}(E_\nu)$ by using the CC samples of SciBar, SciFi, and 1KT, since CC-QE interaction in the CC samples has a relationship between E_ν and muon kinematics as Equation (2.2). We fit the (p_μ, θ_μ) two-dimensional histograms of the CC samples with the MC prediction. The free parameters of the fit are the height of each E_ν bin, which is equivalent to $\Phi_{\rm ND}(E_\nu)$.

7.1.2 Neutrino event rate at near site

The neutrino event rate at the near site, $N_{\rm ND}^{\rm obs}$, is measured by 1KT, because the detector response is the most similar to SK among the near detectors. This choice maximizes the cancellation effect of the systematic error on the expected number of SK events, $N_{\rm SK}^{\rm exp}$. In this analysis, we use all the neutrino event types to maximize the statistical sensitivity to neutrino oscillation.

7.1.3 Far/Near neutrino flux ratio

We evaluate the Far/Near neutrino flux ratio, $R_{F/N}(E_\nu)$, by using the PIMON detector and the MC simulation for the neutrino beam (Beam-MC). Since the decay of a pion is simple two-body reaction, $R_{F/N}(E_\nu)$ is obtained from the property of secondary pions. The PIMON detector measures the two-dimensional distribution of the momentum versus the angle of the pion beam just after the magnetic horns. In the meanwhile, Beam-MC predicts the secondary pion beam. The Beam-MC simulation is verified by the measurement of PIMON, and used for the evaluation of $R_{F/N}(E_\nu)$.

7.1.4 Super-Kamiokande analysis

SK events are selected by using the beam timing information and the Cherenkov ring image. We count the total number of events, $N_{\rm SK}^{\rm obs}$, for the comparison with $N_{\rm SK}^{\rm exp}$. We extract CC-QE candidate events to reconstruct the E_ν spectrum. The CC-QE candidate event of SK is defined as the event which has only one ring identified as a muon, where the proton in CC-QE interaction does not radiate Cherenkov photons.

7.1.5 Neutrino oscillation analysis

We fit the reconstructed E_ν with $\Phi_{\rm SK}(E_\nu; \Delta m^2, \sin^2 2\theta)$ and $N_{\rm SK}^{\rm obs}$ with $N_{\rm SK}^{\rm exp}(E_\nu; \Delta m^2, \sin^2 2\theta)$, by using a maximum likelihood method. The free parameters of the fit are Δm^2 and $\sin^2 2\theta$. Thus, we examine neutrino oscillation, and determine the oscillation parameters.

7.2 Good beam spill selection

For the analysis of each detector, we use only the beam spills which satisfy the good beam spill condition. Good beam spills are selected by the following criteria:

- Reject the period for the machine study, the beam tuning, and the PIMON measurements.
- All the beamline components and the data acquisition system are fine.
- Proton intensity is greater than 1.0×10^{12} protons/pulse to guarantee the accuracy of beamline monitors.
- The horn current is greater than 240 kA for K2K-Ib and K2K-II, or greater than 190 kA for K2K-Ia.
- The GPS status of both KEK and SK are good.
- Super-Kamiokande is alive.

The requirement of the GPS status is described in Section 3.5. For the analysis of SK, all the selected spills are used. The accumulated POT for the SK analysis is summarized in Table 7.1. The total analyzed POT is 8.9×10^{19}. For the analysis of the near detectors, the condition of each detector is imposed.

7.3 Neutrino beam stability

Since the neutrino oscillation analysis is performed on the assumption that the neutrino beam is stable, we confirm the stability of the neutrino beam. The detail of the measurement is described in Appendix B. In this section, we briefly present the results.

The neutrino yield and the beam direction is monitored by MUMON. The deviation of the neutrino yield is 2.5% in RMS, which is sufficiently small compared to the statistical uncertainty in the number of SK events ($\sim 10\%$). The beam direction is stable within 1 mrad, corresponding to the flux change of less than 1%.

MRD monitors the neutrino event rate and the beam profile. The event rate is stable within 2.6%, and the fluctuation of beam center is 1 mrad level. MRD also measures the muon energy (E_μ) and the muon angle (θ_μ) from a neutrino interaction. The stability of E_μ and θ_μ guarantee the stability of the neutrino energy spectrum. Both E_μ and θ_μ spectra are confirmed to be stable within the statistical sensitivity.

Table 7.1: Summary of the accumulated POT for the SK analysis.

Run	K2K-Ia	K2K-Ib		K2K-IIa	K2K-IIb	Total
From	Jun.'99	Nov.'99	Jan.'01	Jan.'03	Oct.'03	
To	Jun.'99	Jun.'00	Jul.'01	Jun.'03	Feb.'04	
$\mathrm{POT_{SK}}$ ($\times 10^{18}$)	3.1	19.8	25.0	22.6	18.6	89.1

Chapter 8

Neutrino Energy Spectrum at Near Site

To study the neutrino energy spectrum distortion, we determine the neutrino energy spectrum at the near site, $\Phi_{\mathrm{ND}}(E_\nu)$. Since charged-current quasi-elastic (CC-QE) interaction has a correlation between neutrino energy and muon kinematics as Equation (2.2), we select event samples containing CC-QE interaction from SciBar, SciFi, and 1KT data. The neutrino energy spectrum is determined by fitting muon momentum versus angle two-dimensional distributions with the MC expectation. Since we have found that the forward going muons are fewer than the MC expectation in the analysis of SciBar data, we also discuss the treatment of this issue.

8.1 Outline

At first, we introduce the outline of the event selection and the energy spectrum measurement.

8.1.1 Event selection

We summarize the event selection procedure for each detector in this section. The detail of SciBar, SciFi, and 1KT data are described in Section 8.2, 8.3, and 8.4, respectively. The comparison among the three detectors are discussed in Section 8.5.

SciBar

We use the CC events selected in Chapter 6. By using the number of tracks from an interaction vertex and kinematic condition of the tracks, the CC events are classified into three subsamples:

- 1-track sample (1-track).
- 2-track CC-QE-enriched sample (2-track-QE).
- 2-track CC-nonQE-enriched sample (2-track-nonQE).

Here, CC-nonQE is defined as other CC interaction except for CC-QE. Since CC-QE interaction produces two particles (muon and proton), we do not use the event with more than two tracks from the interaction vertex. The 1-track sample is the case that the proton track is too short to be reconstructed. Since the proton direction is predicted from the muon momentum and the muon direction assuming CC-QE interaction, we classify a two-track event into the CC-QE-enriched sample and the CC-nonQE-enriched sample by comparing the direction of the second track with the expected proton direction.

The expected proton angle with respect to the beam (θ_p) is given as

$$\tan\theta_p = \frac{p_\mu \sin\theta_\mu}{E_\nu^{\rm rec} - p_\mu \cos\theta_\mu}, \tag{8.1}$$

by momentum conservation, where p_μ, θ_μ, and $E_\nu^{\rm rec}$ are the muon momentum, the muon angle with respect to the beam, and the reconstructed neutrino energy assuming CC-QE interaction. The azimuthal angle of the proton (ϕ_p) is opposite to that of the muon (ϕ_μ):

$$\phi_p = \phi_\mu + \pi, \tag{8.2}$$

because of the two-body kinematics. Therefore, the cosine of the angle between the observed second track and the expected proton direction ($\Delta\theta_p$) is obtained as

$$\cos\Delta\theta_p = \sin\theta_p \sin\theta_2 \cos(\phi_\mu + \pi - \phi_2) + \cos\theta_p \cos\theta_2, \tag{8.3}$$

where θ_2 and ϕ_2 are zenith and azimuthal angles of the observed second track, respectively. Events with small $\Delta\theta_p$ are classified as the 2-track-QE sample, and the other events are categorized as the 2-track-nonQE sample.

SciFi

A CC event for SciFi is defined as the event with a track matching to an MRD track, MRD hits, or an LG cluster. Selected CC events are classified into the three subsamples (1-track, 2-track-QE, and 2-track-nonQE) in the same way as SciBar.

1KT

We select an event with only one muon-like ring, since the momentum of the proton in CC-QE interaction is usually below the Cherenkov threshold. In addition, the muon is required to stop inside the inner detector of 1KT in order to measure the muon momentum.

8.1.2 Determination of neutrino energy spectrum

The neutrino energy spectrum is determined by fitting (p_μ, θ_μ) two-dimensional distributions with the MC expectation. Since the stability of the neutrino energy spectrum is confirmed by MRD data (Section 7.3), we measure a common spectrum for K2K-Ib and K2K-II runs.

We use a chi-square fitting method for this analysis. Free parameters of the fit are bin contents of the neutrino energy spectrum. Since the selected CC-QE samples have contamination of CC-nonQE interaction, we also obtain the cross-section ratio of CC-nonQE to CC-QE. During the fit, (p_μ, θ_μ) distributions of the MC simulation is varied according to the E_ν bin contents and the nonQE/QE ratio. We take the chi-square between data and the MC simulation for each subsample, and we minimize the sum of the chi-squares for all subsamples. Uncertainty of the muon energy scale for each detector is taken into account.

For SciBar and SciFi, the migration among the three subsamples due to the detector systematics etc. is taken into account. Systematic errors relevant to the migration effect are estimated before the fit. The systematic error for SciBar is evaluated in Section 8.2.3, and that for SciFi is described in Section 8.7.3.

The strategy for the energy spectrum measurement is discussed again in Section 8.6 according to the characteristics of selected events for each detector.

8.2 SciBar data

8.2.1 Event classification

Figure 8.1 shows the number of track ($N_{\rm track}$) distribution from the muon vertex. The definition of $N_{\rm track}$ is the number of tracks originated from the muon vertex within 9.0 cm for X and Y and 4.5 cm for Z (beam direction), as shown in Figure 8.2. We use events with $N_{\rm track} \leq 2$, where CC-QE interaction is concentrated. Figure 8.3 shows $\Delta\theta_p$ distribution for 2-track events. We define the 2-track-QE sample as $\Delta\theta_p < 25$ degrees. The others are classified as the 2-track-nonQE sample.

The fraction and efficiency of CC-QE interaction for each event category are estimated using the MC simulation and listed in Table 8.1. The efficiency is defined as the ratio of the number of reconstructed events to the number of generated events for CC-QE in the fiducial volume. SciBar has 70% efficiency for CC-QE in total.

8.2.2 Basic distributions

The p_μ, θ_μ, and q^2 distributions for each event category are shown in Figure 8.4. Here, q^2 is the square of the four-momentum transfer assuming CC-QE, which is given by

$$q^2 = 2E_\nu(E_\mu + p_\mu \cos\theta_\mu) - m_\mu^2. \tag{8.4}$$

Since formulas of neutrino interactions are often described in terms of q^2, it is a probe to study neutrino interactions. The p_μ distributions agree well between data and the MC simulation. However, the θ_μ and q^2 distributions show discrepancies in $\theta_\mu < 10$ degrees and $q^2 < 0.1$ (GeV/c)^2 for 1-track and 2-track-nonQE samples. Neglecting the muon mass, we approximate q^2 by

$$q^2 \simeq 4E_\nu p_\mu \sin^2\frac{\theta_\mu}{2}. \tag{8.5}$$

In Equation (8.5), small θ_μ corresponds to low q^2.

Figure 8.5 shows the difference between the reconstructed q^2 and MC true q^2 for CC-QE events. The q^2 resolution for $q^2 < 0.1$ (GeV/c)^2 is 0.01 (GeV/c)^2. Therefore, SciBar has sufficient resolution to see the deficit at low q^2. The q^2 may be affected by the uncertainties in muon energy scale and angle. If the energy scale is intentionally changed by its systematic error ($\pm$2.7%), the q^2 distributions is deformed a little, as shown in Figure 8.6 (a)–(c). If the angle is shifted by 1 degree (5 times its error) or if the angle resolution is smeared twice as large as itself, the q^2 looks like Figure 8.6 (d)–(f). The disagreement in the small q^2 region is not explained by these systematic error sources. The detector systematics are too small to explain the observed forward muon deficit. The treatment of low-q^2 deficit will be discussed later in Section 8.8.

8.2.3 Systematic errors

Since we have introduced two new cuts in this chapter, $N_{\rm track}$ and $\Delta\theta_p$, we evaluate the systematic errors on these cuts. Systematic errors on these cuts cause the migration of events among 1-track, 2-track-QE, and 2-track-nonQE samples. To estimate the migration effects, we evaluate the errors on the **ratio** of the number of **2-track** events to the number of **1-track** events ($R^{\rm SciBar}_{\rm 2trk/1trk}$) and the **ratio** of the number of 2-track-**QE** sample to the number of 2-track-**nonQE** sample ($R^{\rm SciBar}_{\rm nonQE/QE}$). The systematic errors on $R^{\rm SciBar}_{\rm 2trk/1trk}$ and $R^{\rm SciBar}_{\rm nonQE/QE}$ are summarized in Table 8.2.

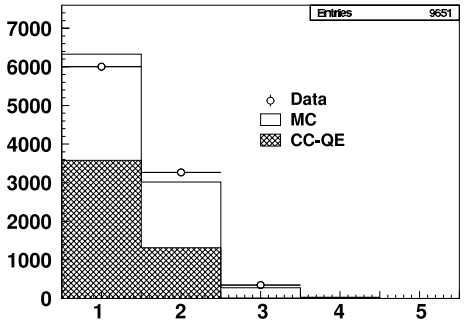

Figure 8.1: The number of tracks from a muon vertex. The open circles show data. The solid line shows MC simulation and the hatched region is CC-QE interaction. The MC simulation is normalized by entries.

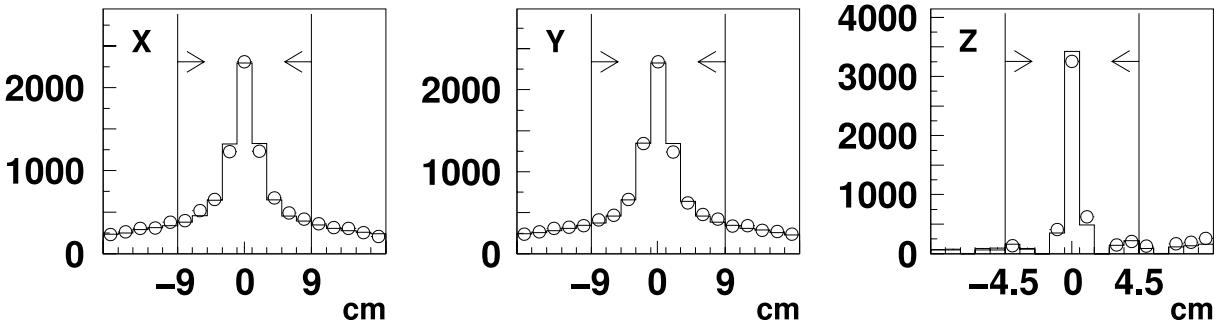

Figure 8.2: The start position difference between a muon track and a second track for each axis. Open circles and solid lines show data and the MC simulation, respectively. The criteria for counting the number of tracks is also shown.

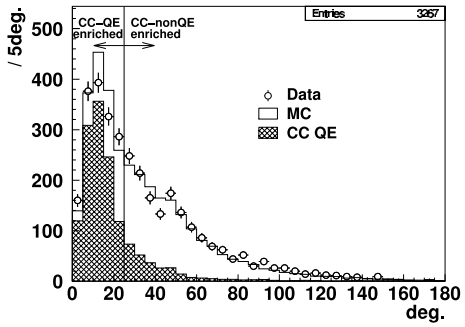

Figure 8.3: The angle between an observed second track and expected proton direction.

Table 8.1: The fraction and efficiency of CC-QE events for each event category. The unit is %.

Event category	1-track	2-track		Total
		QE	nonQE	
Fraction of CC-QE	57	72	17	—
Efficiency for CC-QE	51	15	4	70

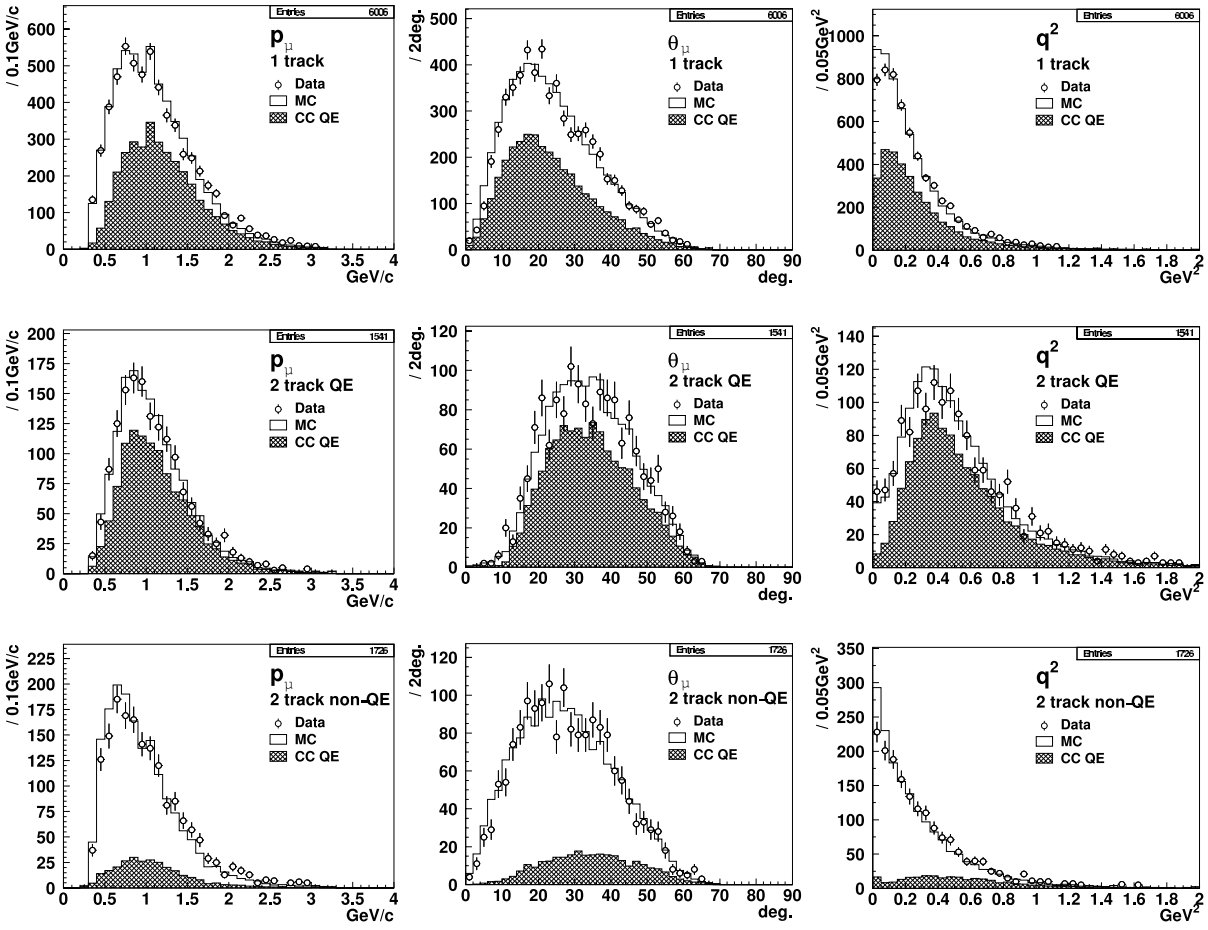

Figure 8.4: The p_μ, θ_μ and q^2 distributions of SciBar for each event category. Open circles are data, solid lines are MC simulation, and hatched regions are CC-QE component in MC. The MC distribution is normalized by entries in each figure.

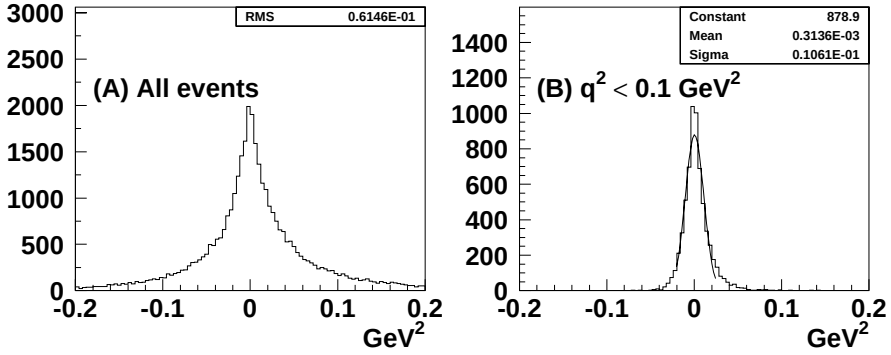

Figure 8.5: The difference between the reconstructed q^2 and the MC true q^2 for CC-QE events. The events in all q^2 region are used in Figure (A), and events with only $q^2 < 0.1$ (GeV/c)^2 are used in Figure (B). Figure (B) is fitted with Gaussian. Since the q^2 resolution depends on q^2 itself, it is difficult to define the q^2 resolution for entire events. The q^2 resolution for $q^2 < 0.1$ (GeV/c)^2 is 0.01 (GeV/c)^2.

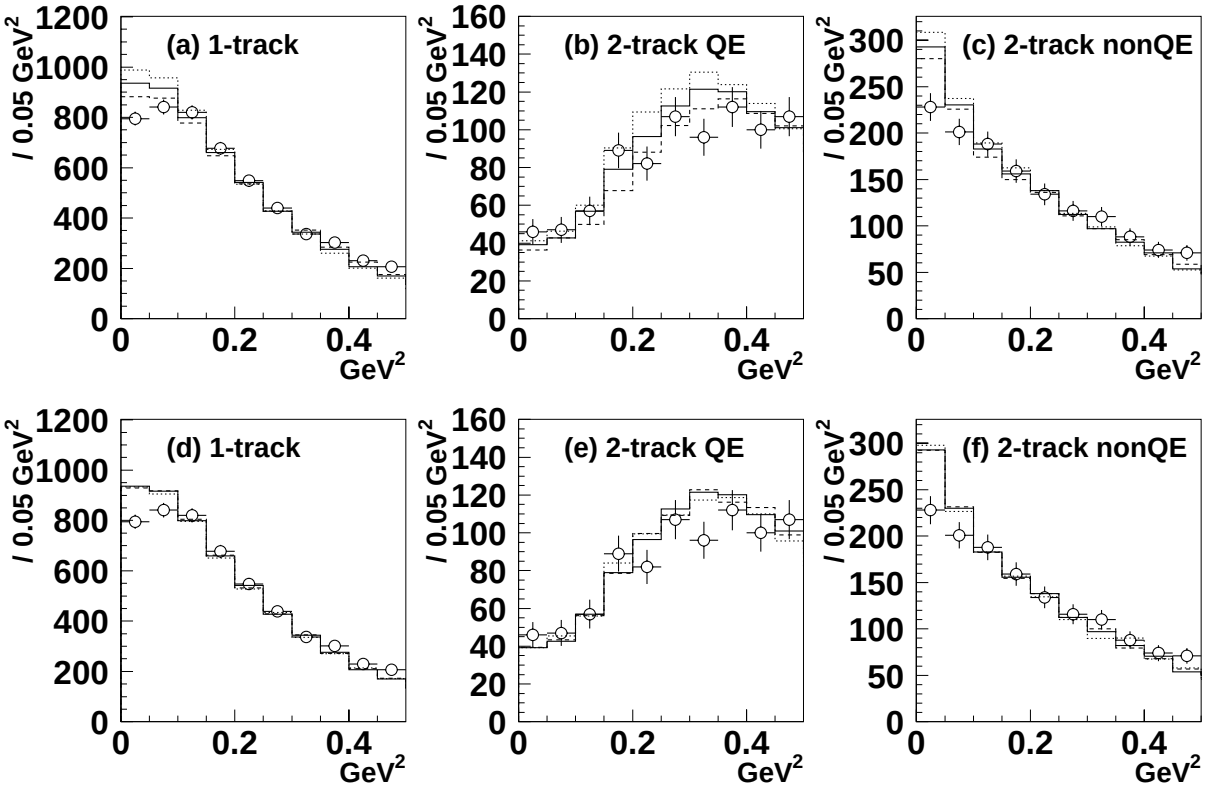

Figure 8.6: Systematic effects on the q^2 distribution for each event category. Open circles are data and solid lines are the normal MC simulation. Figures (a)–(c) show the effects from the energy scale uncertainty. If the energy scale is intentionally increased (decreased) by 2.7%, the q^2 distributions become dashed (dotted) lines. Figures (d)–(f) show the effects from angle shift and smearing. Dashed lines show the q^2 if the angle is shifted by 1 degree. If the angle is smeared by twice of the resolution, the q^2 distribution becomes dotted lines.

Table 8.2: The systematic errors on $R^{\mathrm{SciBar}}_{\mathrm{2trk/1trk}}$ and $R^{\mathrm{SciBar}}_{\mathrm{nonQE/QE}}$.

Source	$R^{\mathrm{SciBar}}_{\mathrm{2trk/1trk}}$ [%]		$R^{\mathrm{SciBar}}_{\mathrm{nonQE/QE}}$ [%]	
Threshold for p.e.	+0.7	−0.0	—	—
Cross-talk	+1.1	−1.1	+2.2	−2.9
Track finding efficiency	+0.9	−4.3	—	—
Vertex matching efficiency	+2.7	−1.0	—	—
Angular resolution	—	—	+1.0	−0.0
Energy scale	—	—	+1.5	−4.3
Proton re-scattering	+2.9	−2.6	+2.9	−2.8
Pion absorption	+1.7	−1.7	+0.0	−5.4
Pion inelastic scattering	+4.1	−4.2	+0.3	−7.7
Total	+5.1	−6.2	+4.0	−9.3

Cross-talk of MA-PMT

The cross-talk of the MA-PMT is emulated in the MC simulation. The cross-talk has the uncertainty of ±50% from a laboratory measurement[36]. If the cross-talk emulation parameters are increased or decreased by 50%, $R^{\rm SciBar}_{\rm 2trk/1trk}$ changes ±1.1% and $R^{\rm SciBar}_{\rm nonQE/QE}$ varies +2.2% −2.9%. Therefore, we use these numbers as the systematic error from the cross-talk.

Threshold for photo-electron

For track finding, we select the hits with the threshold of 2.0 photo-electrons (Section 6.1.1). The light yield for each cell distributes with the standard deviation of approximately 15% (Figure 4.16). In order to study the systematic effect, we varied the threshold by ±15%. When the threshold is set to 2.3 photo-electrons, $R^{\rm SciBar}_{\rm 2trk/1trk}$ increases by 0.7%. If the threshold is 1.7 photo-electrons, $R^{\rm SciBar}_{\rm 2trk/1trk}$ also increases by 0.4%. Thus, the uncertainty of the threshold gives +0.7% −0.0% error on $R^{\rm SciBar}_{\rm 2trk/1trk}$.

Track finding efficiency

The track finding efficiency of the second track may be different between data and the MC simulation. Therefore, we checked the efficiency as a function of the number of hits for the second track by eye scanning. As a result, $R^{\rm SciBar}_{\rm 2trk/1trk}$ between data and MC is different by +0.9% −4.3%. We assign it to the systematic error.

Vertex matching efficiency

To obtain the number of tracks, we have required the second track to start within a certain volume from the vertex, as shown in Figure 8.2. If we change the requirement by ±50% and $R^{\rm SciBar}_{\rm 2trk/1trk}$ deviate by +2.7% −1.0%. We use this number as the systematic error.

Angular resolution of a track

The track angular resolution of SciBar (1.6 degrees) is checked by comparing the angle of tracks between SciBar and MRD, as shown in Figure 6.10. Assuming the disagreement of the width of the figure between data and the MC simulation is originated from the SciBar track resolution, the angular resolution of SciBar is 2.7 degrees. Therefore, the angular resolution of both primary and second tracks are intensionally smeared so that the angular resolution may be 2.7 degrees. The error on $R^{\rm SciBar}_{\rm nonQE/QE}$ is then obtained to be +1.0% −0.0%.

Energy scale

Since $\Delta\theta_p$ is calculated from the muon energy as Equation (8.1), the uncertainty of the energy scale (2.7%) is the source of the error on $R^{\rm SciBar}_{\rm nonQE/QE}$. As a result, $R^{\rm SciBar}_{\rm nonQE/QE}$ changes by +1.5% −4.3%, if the energy scale is shifted by ±2.7%. We quote this number as the systematic error.

Nuclear effects

Nuclear final state interactions affects the second track. The possible sources are proton rescattering (±10%), pion absorption (±30%), and pion inelastic scattering (±30%). The uncertainties of them are assigned based on the errors on the past measurements. These effects change both $R^{\rm SciBar}_{\rm 2trk/1trk}$ and $R^{\rm SciBar}_{\rm nonQE/QE}$. The systematic errors on the nuclear effects are summarized in Table 8.2.

Summary

In total, $R^{\rm SciBar}_{\rm 2trk/1trk}$ has the error of +5.1% −6.2% and $R^{\rm SciBar}_{\rm nonQE/QE}$ has the error of +4.0% −9.3%. A small discrepancy in the $N_{\rm track}$ and $\Delta\theta_p$ distributions between data and the MC simulation is explained by the systematic errors. In Table 8.2, the correlation between different sources is taken into account.

8.3 SciFi data

8.3.1 Data set

We use two data sets of SciFi to determine the neutrino energy spectrum. One is K2K-Ib (with LG), and the other is K2K-IIa (without LG). In K2K-IIa, there was a four-layer prototype of SciBar (Mini-SciBar) instead of LG. Although K2K-IIb (with SciBar) is not used in the present analysis, it is a task for the near future.

8.3.2 Event selection

We select CC events of SciFi with the similar way as SciBar. To reconstruct a primary muon track, we look for the particle starting from SciFi and stopping within MRD or LG [25, 89]. A typical CC event is shown in Figure 8.7. The event selection procedure is described below:

1. **Trigger counter match**
   The SciFi track is required to have an associate hit on the downstream trigger counter in order to obtain the track timing[1].

2. **No veto counter hit**
   The track coming from upstream is rejected by using upstream veto counters.

3. **LG cluster match** (K2K-Ib only)
   If the track matches to an LG cluster larger than the electron equivalent energy of 0.1 GeV, the cluster is regarded as associated to the track. If a track matches to an LG cluster without any associate MRD hits as shown in Figure 8.8(C), the track is identified as an 'LG-stopping' track.

4. **MRD match**
   We select two types of tracks: 'MRD-3D' and 'MRD-1L'. The schematic view of each event type is shown in Figure 8.8 (A) and (B). An MRD-3D track is that a SciFi track matches to an MRD track three-dimensionally. MRD-1L is defined as the SciFi track matching to the hits on the first drift-tube layer of MRD. For K2K-Ib, we use both MRD-3D and MRD-1L events. For K2K-IIa, we do not employ MRD-1L tracks but only MRD-3D tracks (Figure 8.9), because they have significant contamination of hadrons due to a small amount of material between SciFi and MRD.

5. **Second track search and vertex determination**
   We look for the second track generated near the start point of the primary track. If second track is found, the vertex is determined at the intersection point between primary and second tracks. If not, the vertex is reconstructed at the middle of the water tank in which the primary track is produced.

[1] The IIT for the SciFi readout does not have timing information.

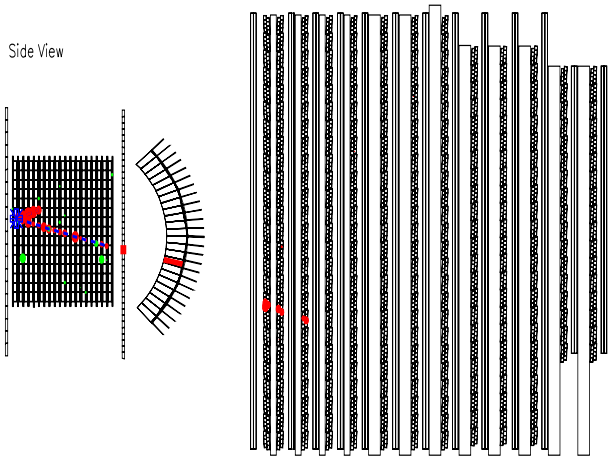

Figure 8.7: The event display of a typical CC event in SciFi.

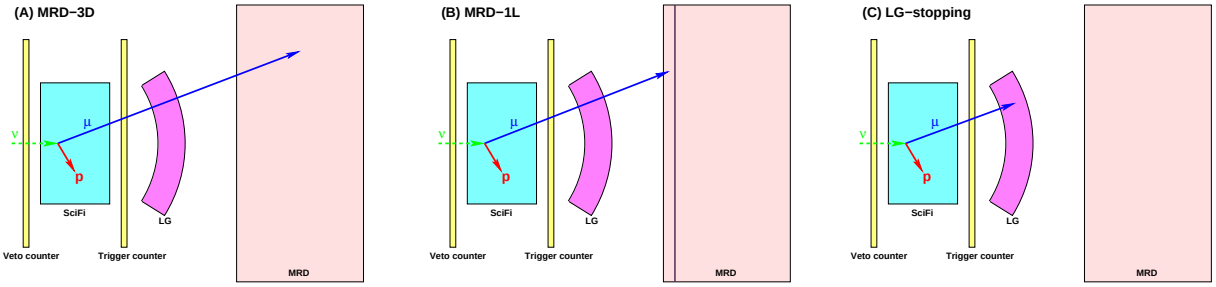

Figure 8.8: Schematic view for each event type of SciFi in K2K-Ib. Figures (A), (B), and (C) show MRD 3D matching, MRD first layer matching, and LG stopping events, respectively.

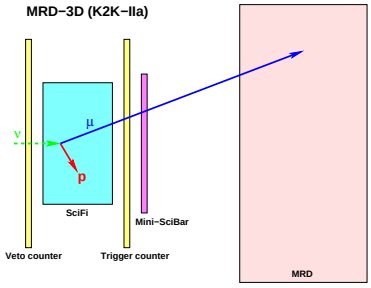

Figure 8.9: The schematic view of the SciFi MRD-3D event in K2K-IIa.

6. **Fiducial volume**
   The vertex is required to be within the fiducial volume of SciFi. The fiducial volume is defined as the 2.2×2.2 m^2 region for X and Y from first to seventeenth water tank, corresponding to 5.9 tons. Exceptionally, the vertex of the 1-track event in the LG-Stopping sample is allowed to be only from first to **fourteenth** tank, since the neutrino events occurred in LG with backward going particles entering to SciFi.

8.3.3 Muon energy reconstruction

The muon energy is obtained from the sum of the energy deposit in all penetrated parts:

$$\textbf{K2K-Ib MRD-3D,1L:} \quad E_\mu = E_\mu^{\rm SciFi} + E_\mu^{\rm TG} + E_\mu^{\rm LG} + E_\mu^{\rm MRD}, \tag{8.6}$$

$$\textbf{K2K-Ib LG-Stopping:} \quad E_\mu = E_\mu^{\rm SciFi} + E_\mu^{\rm TG} + E_\mu^{\rm LGcluster}, \tag{8.7}$$

$$\textbf{K2K-IIa MRD-3D:} \quad E_\mu = E_\mu^{\rm SciFi} + E_\mu^{\rm TG} + E_\mu^{\text{Mini-SciBar}} + E_\mu^{\rm MRD}, \tag{8.8}$$

where $E_\mu^{\rm SciFi}$, $E_\mu^{\rm TG}$, $E_\mu^{\rm LG}$, $E_\mu^{\rm MRD}$, and $E_\mu^{\text{Mini-SciBar}}$ are the energy deposit in SciFi, the trigger counter, LG, MRD, and Mini-SciBar, respectively, calculated by the range. Although $E_\mu^{\rm LGcluster}$ is also the energy deposit in LG, the pulse height information of the cluster is used.

Dominant uncertainties in E_μ come from $E_\mu^{\rm LG}$, $E_\mu^{\rm LGcluster}$, and $E_\mu^{\rm MRD}$. As stated in Section 6.2.5, the systematic error on $E_\mu^{\rm MRD}$ is 2.7%. The energy deposit in LG was measured by a test beam experiment (KEK-PS T501) [89]. As a result, $E_\mu^{\rm LG}$ is 5% smaller than the GEANT MC expectation with the error of $\pm 5\%$. Therefore, we multiply 0.95 to $E_\mu^{\rm LG}$ by default, and we assign the systematic error of $\pm 5\%$ to $E_\mu^{\rm LG}$. Since the conversion factor of the LG pulse height to the energy deposit is different by 30 MeV between data and the MC simulation in the T501 experiment, the systematic error on $E_\mu^{\rm LGcluster}$ is quoted as ± 30 MeV.

8.3.4 Event classification

The SciFi event is classified into 1-track, 2-track-QE, and 2-track-nonQE samples in the same way as SciBar. The number of tracks ($N_{\rm track}$) and the $\cos\Delta\theta_p$ distributions are shown in Figure 8.10 and 8.11. If $\Delta\theta_p$ of a 2-track event is less than 25 degrees, it is classified as the QE enriched sample. If $\Delta\theta_p$ is more than 30 degrees. the event is categorized as the nonQE enriched sample. The fraction and efficiency of CC-QE in each category is summarized in Table 8.3. The CC-QE efficiency for K2K-Ib and K2K-IIa are 46% and 42%, respectively, in total.

8.3.5 Basic distributions

Figure 8.12 shows p_μ, θ_μ, and q^2 distributions for each of experiment period, matching condition, and event category. The p_μ distributions of data agree well with those of the MC simulation. Deficits are observed in $\theta_\mu < 10$ degrees and $q^2 < 0.1$ GeV/c regions similar as SciBar.

8.4 1KT data

8.4.1 Event selection

We select 'fully-contained (FC) single-ring muon-like (1Rμ)' events for the measurement of the neutrino energy spectrum. Since the proton momentum in CC-QE is usually below the Cherenkov threshold, we use a 1Rμ event, which is defined as the event with only one muon-like ring. In addition, to measure the muon momentum, we require that the muon-like particle is fully-contained within the inner detector of 1KT. Figure 8.13 shows an event display of a

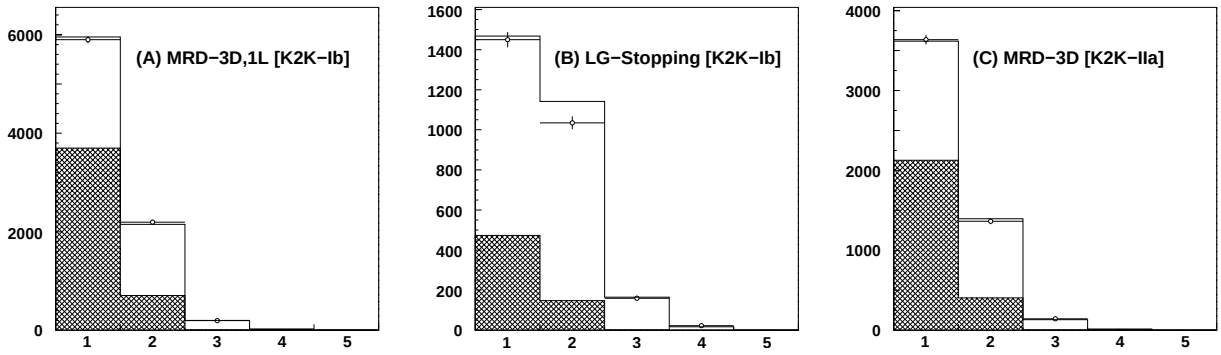

Figure 8.10: The $N_{\rm track}$ distribution of each event category for SciFi. Open circles are data, solid lines are MC simulation, and hatched regions are CC-QE components.

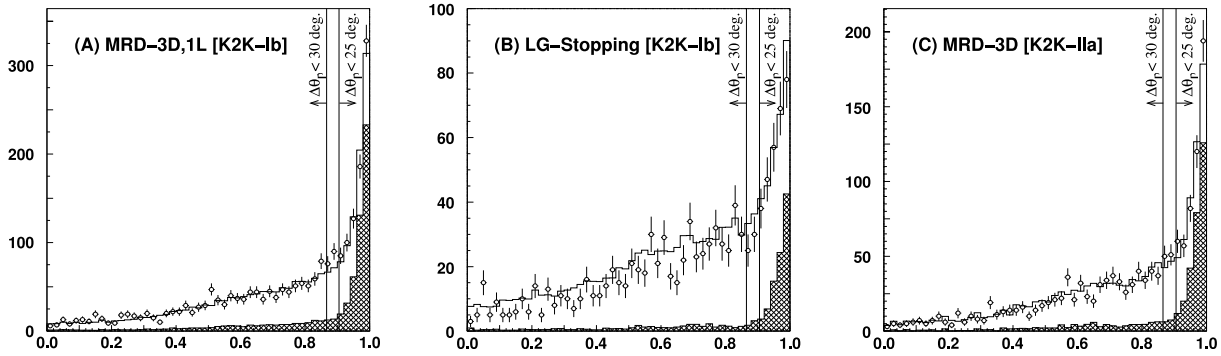

Figure 8.11: The $\cos\Delta\theta_p$ distribution of each event category for SciFi 2-track events. Symbols are the same as Figure 8.10. The event with $\Delta\theta_p < 25$ degrees is classified as the QE enriched sample. The event with $\Delta\theta_p < 30$ degrees is categorized as the nonQE enriched sample.

Table 8.3: The fraction and efficiency of CC-QE events for each event category of SciFi. The unit is %.

Event category		1-track	2-track QE	2-track nonQE	Total
Fraction	K2K-Ib	50	53	11	—
	K2K-IIa	57	58	12	—
Efficiency	K2K-Ib	39	5	2	46
	K2K-IIa	36	5	2	42

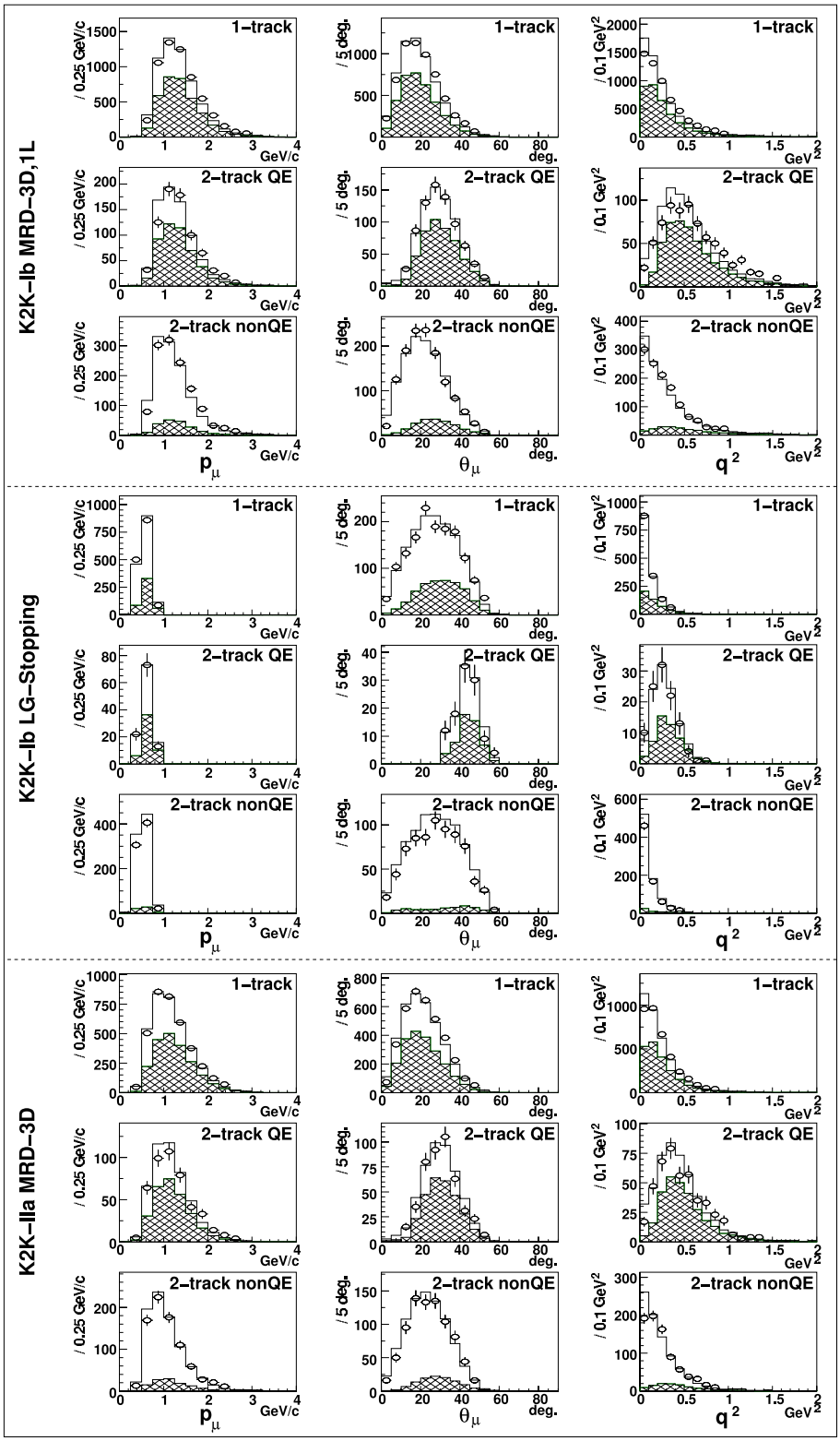

Figure 8.12: The p_μ, θ_μ, and q^2 distributions of SciFi. Histograms are divided into three groups according to the experiment period and the event types. Left, center and right columns show p_μ, θ_μ, and q^2 distributions, respectively. Each row represents the event category. Open circles are data, solid lines are the MC simulation, and hatched regions are the CC-QE component.

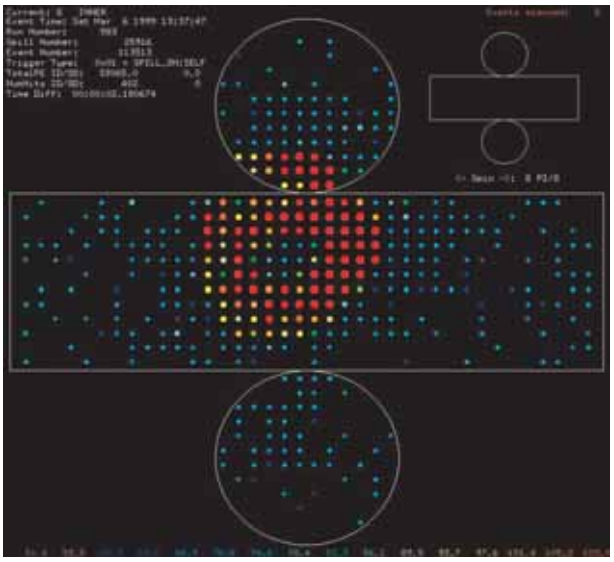

Figure 8.13: A typical event display of a single muon event in 1KT.

typical FC 1Rμ event. In this section, we describe the event selection step by step. More detail description is found in [22].

Pre-activity cut

We do not use the spill which has activity within 1.2μsec before the beam.

Low-energy event rejection

We reject the event less than 200 photo-electrons in total, which corresponds to the electron energy of 30 MeV.

Event reconstruction

Cherenkov rings are reconstructed, and the neutrino interaction vertex is determined. Each process is summarized below.

1. **Auto-fit**
   By looking for the direction and edge of the most energetic ring, the vertex of the ring is determined with the timing information of each PMT. This process is called Auto-fit.

2. **Ring counting**
   The other rings are searched for, and the number of rings (N_{ring}) is counted.

3. **Particle identification**
   A ring is identified as either μ-like and e-like by using the ring image and opening angle. Both a muon and a charged pion make a sharp ring edge called μ-like, since it travels almost straight in a matter. On the other hand, both an electron and a gamma ray make a fuzzy ring called e-like, because a cascade shower is created.

4. **MS-fit for a single-ring event**
   For a single-ring event, another vertex finding algorithm, called MS-fit, is applied to improve the precision of the vertex position, assuming the particle type identified at the previous step.

5. **Momentum reconstruction**
   The momentum of each ring is reconstructed by the number of photo-electrons inside the Cherenkov ring. The systematic error on the momentum scale is estimated to be +2.0% −3.0%, as described in Section 3.3.1.

Total photo-electrons threshold

To reject low energy background events such as a muon decay of a cosmic ray, the threshold of FADC pulse height is set to 1000 photo-electrons, equivalent to the electron energy of 100 MeV.

Single event selection

The number of FADC peaks in a spill is required to be one to reject multiple events happened in one spill. Approximately 10% of spills are rejected by this requirement.

Fiducial volume cut

The vertex of a reconstructed event is required to be within a fiducial volume, as shown in Figure 8.14. The fiducial volume is defined as a cylindrical volume with a radius of 2 m and a length of 2 m. It is oriented along the beam and shifted by 1 m upstream from the center of the tank. The fiducial mass is 25 tons.

Fully-contained single-ring μ-like event

The requirements for a 1Rμ event are that $N_{\rm ring}$ is one and that the particle type is μ-like. To identify an FC event, we define POMAX20deg as the number of photo-electrons in a PMT located within 20 degrees around the particle direction. Figure 8.15 shows the POMAX20deg distribution. The condition for an FC event is that POMAX20deg is less than 200 photo-electrons, because the number of Cherenkov photons is the largest in the PMT at the exiting point of an outgoing muon. If POMAX20deg is greater than 200 photo-electrons, the muon is recognized as an outgoing particle, called 'partially-contained (PC)'.

The selection efficiency for the CC-QE interaction is estimated to be 53%. The fraction of CC-QE in the FC 1Rμ sample is 58%.

8.4.2 Basic distributions

Ring counting

To separate a single-ring event ($N_{\rm ring} = 1$) from a multi-ring event ($N_{\rm ring} > 1$), a ring counting estimator, $\mathcal{F}$, is constructed. The ring counting estimator returns a positive value if there is another ring than the primary ring found by Auto-fit. Figure 8.16 shows the distributions of $\mathcal{F}$ and $N_{\rm ring}$ for the FC sample. The requirement for a single-ring event is $\mathcal{F} < 0$.

Particle ID

Figure 8.17 shows the particle identification likelihood ($\mathcal{P}$) for FC single-ring events. Events with $\mathcal{P} > 0$ are identified as μ-like, and the others are e-like.

Vertex resolution

The vertex resolution is estimated by the distance between a reconstructed vertex and a true vertex using the MC simulation. The vertex resolution is then defined as the length at which

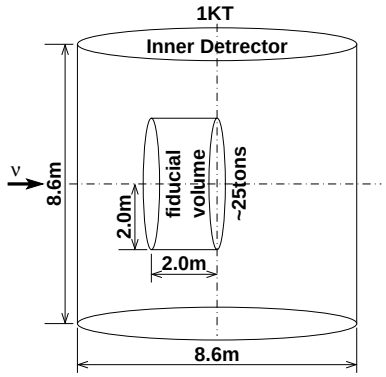

Figure 8.14: The definition of the fiducial volume of 1KT. It is a cylindrical region which has a radius of 2 m and a length of 2 m.

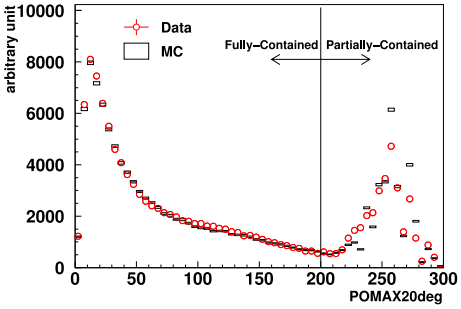

Figure 8.15: The POMAX20deg distribution of 1KT.

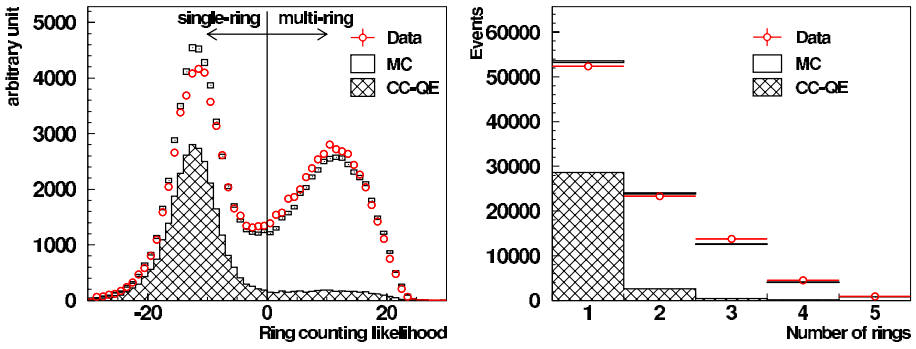

Figure 8.16: The ring counting likelihood, $\mathcal{F}$, (left) and $N_{\rm ring}$ (right) distributions of the 1KT FC sample. Open circles are the data, and boxes are the MC simulation. The CC-QE component in the simulation is shown by a hatched area.

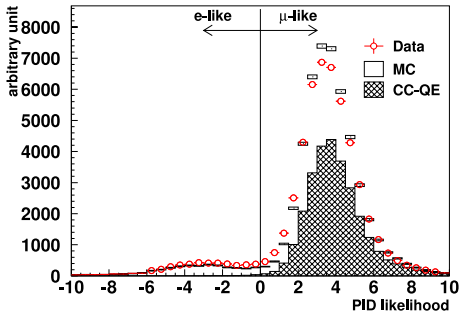

Figure 8.17: The PID likelihood ($\mathcal{P}$) distribution of the 1KT FC single-ring sample.

the 68%[2] of events are contained. The angular resolution is similarly obtained from the angle between a reconstructed direction and a MC true direction. The vertex and angular resolutions for each event type is listed in Table 8.4. Single-ring events have better vertex resolution than multi-ring events owing to MS-fit.

The vertex and angular resolutions are also estimated by using cosmic rays[90]. The vertex is found to be shifted by 10 cm toward the particle direction only for data. In addition, the angular resolution of the MC simulation is 1.6 degrees better than data. (The angular resolution of the MC simulation is 2.5 degrees, and that of data is 4.1 degrees).

Muon momentum, angle, and q^2

Figure 8.18 shows the p_μ, θ_μ, and q^2 distributions of the FC 1Rμ sample. The momentum threshold is approximately 0.3 GeV/c, and muons above 1 GeV/c are rejected by the FC requirement. Another feature of 1KT data is that the angular acceptance is larger than SciBar and SciFi. Disagreements are observed in $\theta_\mu < 20$ degrees and $q^2 < 0.1$ (GeV/c)^2. Since the muon sample of 1KT has lower momentum than that of SciBar and SciFi, θ_μ of 1KT is larger for the same q^2, according to Equation (8.5).

8.5 Comparison of three detectors

In the following two sections, we compare the results of the CC event selection from each detector. We discuss the coverage of p_μ and θ_μ and the deficit in the low-q^2 region.

8.5.1 Acceptance of muon

Figure 8.19 shows p_μ and θ_μ acceptance of each detector, estimated by MC simulations. The acceptance is defined as the ratio of selected evens to generated events. SciBar and SciFi select relatively large momentum and forward going muons, while 1KT covers low momentum and wide angular region. Although SciFi seems to have some efficiency in $p_\mu < 0.4$ GeV/c and $\theta_\mu > 60$ degrees in Figure 8.19, it comes from the hadron track misidentified as a muon track. In general, muons from high energy neutrinos have small θ_μ and high p_μ, whereas those from low energy neutrinos have large θ_μ and low p_μ, Therefore, SciBar and SciFi are efficient at relatively high energy neutrinos, and 1KT is sensitive to low energy neutrinos. Due to the FC requirement, 1KT does not have sensitivity to high energy neutrinos. Thus, these three detectors are complementary to each other. Consequently, we deal with all data simultaneously to obtain the neutrino energy spectrum.

[2]The coverage within one standard deviation of Gaussian distribution.

Table 8.4: The vertex and angular resolution for each event type of 1KT.

		FC	PC
vertex [cm]	single-ring	17.3	17.3
	multi-ring	33.1	35.3
angle [degree]	single-ring	1.80	1.47

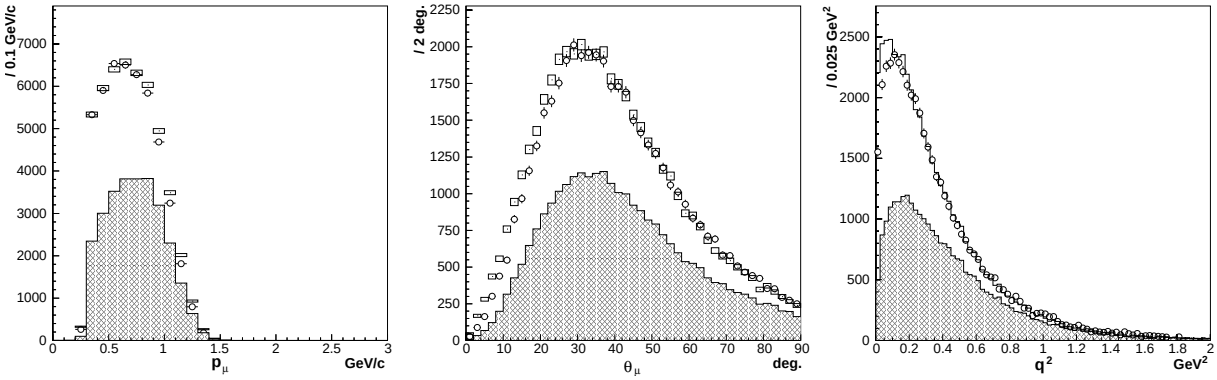

Figure 8.18: The p_μ (left), θ_μ (center), and q^2 (right) distributions of the FC 1Rμ sample of 1KT before fitting. Open circles are data, boxes are MC simulation, and hatched regions are CC-QE components. The error bars show statistical error only. The MC distributions are normalized by entries.

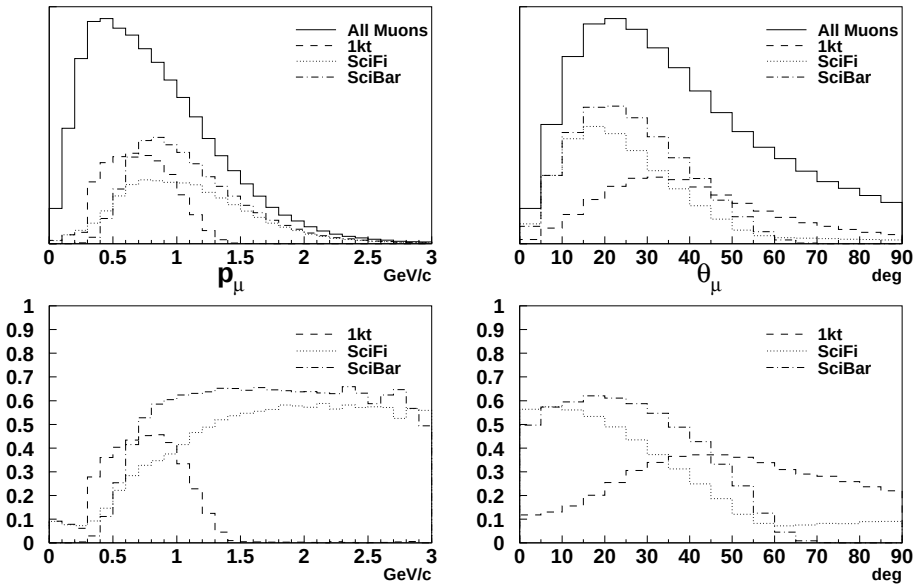

Figure 8.19: The p_μ and θ_μ acceptance of each detector. Solid lines show all muons generated by MC simulation. Dashed, dotted and dash-dotted lines show selected events in 1KT, SciFi, and SciBar, respectively. X-axes of left two figures and right two figures are p_μ and θ_μ, respectively. Y-axes of upper two figures are the number of events in each bin, and those of lower two figures are the acceptance, which is defined as the ratio of selected events to generated events.

8.5.2 Deficit in the low-q^2 region

All three detectors observe a lack of low-q^2 events in 1-track and 2-track-nonQE samples compared to the MC expectations. Figure 8.20 and 8.21 show q^2 and θ_μ distributions, respectively, of these samples together with the ratio of bin-by-bin difference [(data − MC)/MC]. The interaction channels of the MC simulation are indicated by the color of hatched regions. The discrepancy of the q^2 distribution is seen in $q^2 < 0.1$ (GeV/c)^2 of Figure 8.20. On the other hand, the disagreement on the θ_μ distribution of 1KT is observed in the different region from those of SciBar and SciFi. The deficit of 1KT is seen in $\theta_\mu < 20$ degrees, while SciBar and SciFi show the inconsistency in $\theta_\mu < 10$ degrees. Since the p_μ of 1KT is lower and the q^2 behavior is the same, the difference in the θ_μ deficit is explained by the p_μ acceptance. Thus, the property of the low-q^2 deficit is consistent each other, and q^2 appears to be the quantity to express this phenomenon.

We discuss what interaction channel is the source of the deficit. The behavior of the low-q^2 part is very similar between 1-track and 2-track-nonQE samples. Since the CC-QE component is only a little in the low-q^2 part of the 2-track-nonQE sample, the source is possibly the nonQE mode. With our neutrino beam energy, the CC resonance production channel is dominant in the nonQE-enriched sample. Therefore, it is the most probable source. The CC coherent pion production mode is also likely to be the source, because this mode occurs only in the small q^2 region. Thus, these two channels are suspicious. We discuss the low-q^2 properties later in Section 8.8.

8.6 Strategy for spectrum measurement

We discuss the strategy for the determination of the neutrino energy spectrum at the near site. As described in Section 8.1.2, we fit the (p_μ, θ_μ) two-dimensional distribution with the MC expectation, and we obtain the neutrino energy spectrum and the nonQE/QE ratio. Before the fit, we have encountered the deficit of low-q^2 events in all the detectors, and it could give a bias to the measurement. In this section, we introduce the strategy of the analysis to avoid the effect of the low-q^2 deficit.

For neutrino oscillation analysis, we should use both the correct energy spectrum and the reliable interaction model. We study them separately: first, the E_ν spectrum is determined by the fit, and, second, the low-q^2 region is tuned with the obtained spectrum.

Since the energy spectrum at the near site is the input to the neutrino oscillation analysis, it should be determined unambiguously. Since we do not understand the source of the low-q^2 deficit clearly, the spectrum is determined without using forward scattering muons. When we perform the fit without low-q^2 events, a requirement on q^2 suffers from the uncertainty in the p_μ scale. Therefore, we use events with $\theta_\mu > 10$ degrees for SciBar and SciFi and events with $\theta_\mu > 20$ degrees for 1KT, based on the discussion in Section 8.5.2. We do not use any fitting parameters relevant to neutrino interactions or low-q^2 deficit except for the nonQE/QE ratio. The detail of the fitting procedure is described in Section 8.7.1. We confirm the validity of the θ_μ cut by using toy Monte Carlo technique in Appendix C.

Since low-q^2 events are not used in the fit, the validity of the result is not guaranteed to the low-q^2 region. It means that low-q^2 events in SK may be abandoned. However, the lack of SK statistics results in the significant loss of the sensitivity to the neutrino oscillation. Therefore, we investigate the phenomenological suppression factor of low-q^2 events in the MC simulation. This study is based on the q^2 distributions of SciBar. We look for the suitable modification of both the resonance production channel and the coherent pion production channel, which are the suspicious sources of the disagreement as specified by Section 8.5.2. In the analysis of low-q^2 tuning, the free parameters in the spectrum fit are fixed at the best fit values obtained without

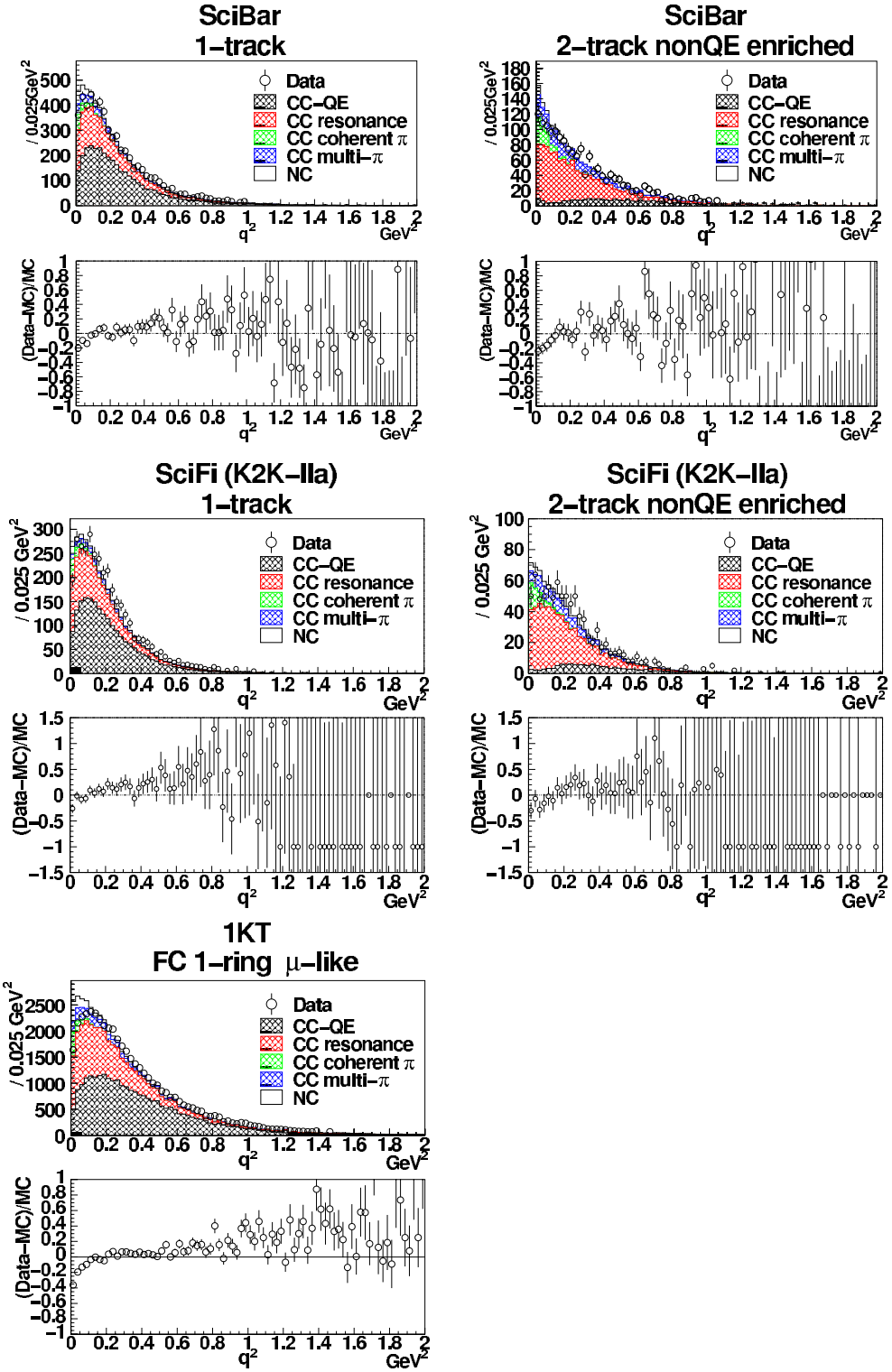

Figure 8.20: The q^2 distributions of SciBar 1-track, 2-track-nonQE, SciFi (K2K-IIa) 1-track, 2-track-nonQE, and 1KT FC 1Rμ samples. Open circles are data, solid lines are the MC simulation. The color of a hatched region represents the interaction mode. Black, red, green, blue and white are CC-QE, CC resonance production, CC coherent pion production, CC multi-pion production, and NC interaction, respectively. The bin-by-bin ratio of the difference between the data and the MC expectation [(data − MC)/MC] for each distribution is also shown.

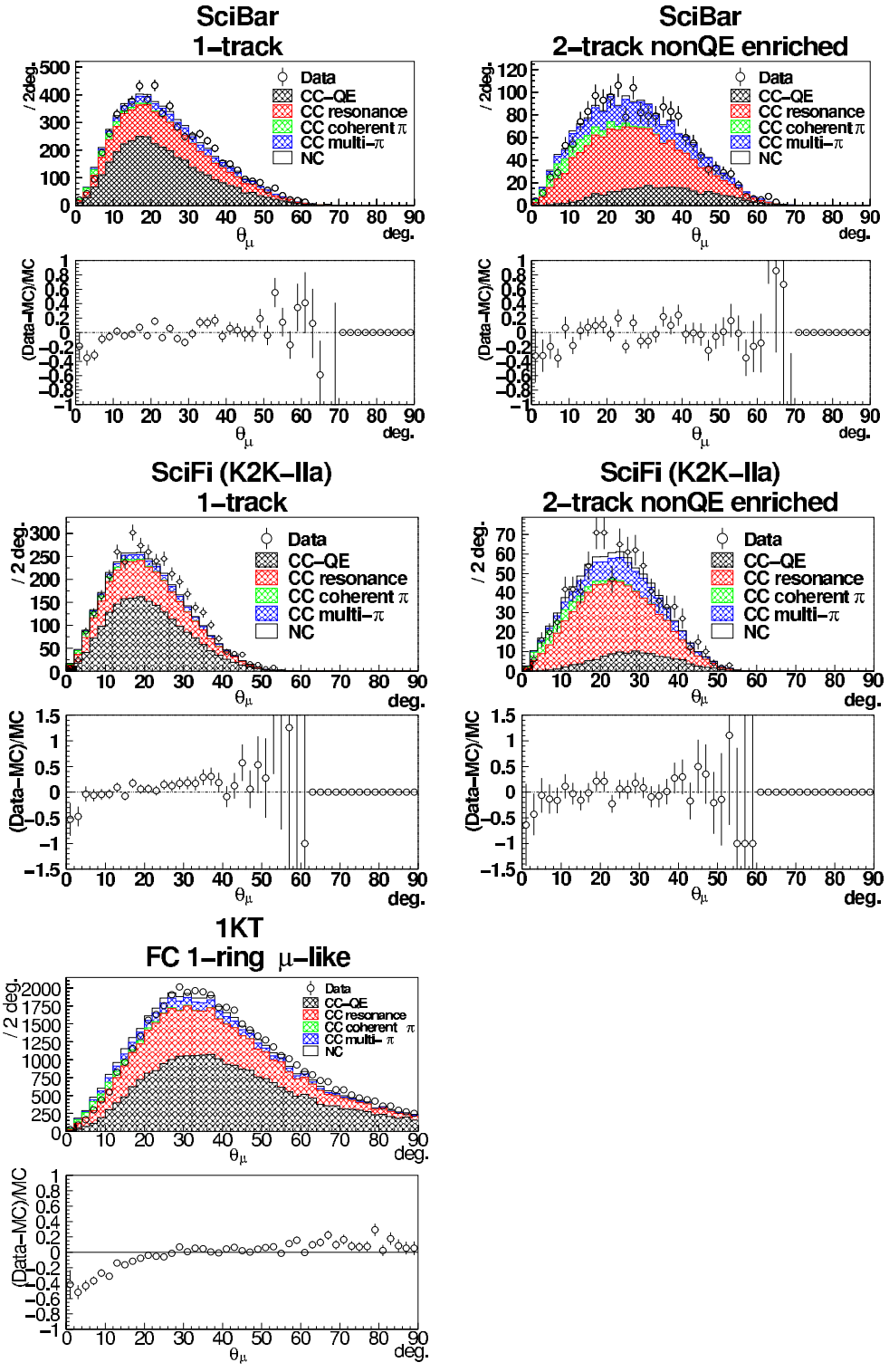

Figure 8.21: The θ_μ distributions of SciBar 1-track, 2-track-nonQE, SciFi (K2K-IIa) 1-track, 2-track-nonQE, and 1KT FC 1Rμ samples. Open circles are data, solid lines are the MC simulation. The color of a hatched region represents the interaction mode. Black, red, green, blue and white are CC-QE, CC resonance production, CC coherent pion production, CC multi-pion production, and NC interaction, respectively. The bin-by-bin ratio of the difference between the data and the MC expectation [(data − MC)/MC] for each distribution is also shown.

using forward going muons.

Finally, we apply the low-q^2 correction, and do the fit again with the entire q^2 region. During this fit, the neutrino energy spectrum remains unchangeable, but the nonQE/QE ratio is variable. At last, the spectrum is validated for all events.

8.7 Determination of neutrino energy spectrum

We determine the neutrino energy spectrum at the near site without forward scattering muons. The fitting procedure is summarized in Section 8.7.1, and the detailed description for each detector is subsequently described. In Section 8.7.6, we show the results of the fit.

8.7.1 Fitting procedure

The neutrino energy spectrum is determined by fitting the two-dimensional distribution of p_μ versus θ_μ with the free parameter of each E_ν bin content (f_i^ϕ for i-th bin). The cross-section ratio of CC-nonQE to CC-QE interaction ($R_{\rm nQE}$) is also obtained simultaneously. We define f_i^ϕ and $R_{\rm nQE}$ as the weighting factors to the baseline MC simulation with the central value of one. The MC data is divided into eight E_ν bins, and each of them is split into QE and nonQE. The E_ν interval of each f_i^ϕ are listed in Table 8.5. The content in i-th p_μ and j-th θ_μ bin of the fitted MC histogram is expressed by

$$N^{\rm MC}(i,j) = \sum_{k=1}^{8} f_k^\phi \cdot \left[N^{\rm MC}_{k,{\rm QE}}(i,j) + R_{\rm nQE} \cdot N^{\rm MC}_{k,{\rm nonQE}}(i,j) \right], \tag{8.9}$$

where $N^{\rm MC}_{k,{\rm QE}}(i,j)$ and $N^{\rm MC}_{k,{\rm nonQE}}(i,j)$ are the bin contents of QE and nonQE distributions, respectively, for k-th E_ν bin. We take the chi-square (χ^2) between the observed distribution, $N^{\rm data}(i,j)$, and $N^{\rm MC}(i,j)$. The event categories to be fitted are summarized as follows:

SciBar We use three event categories of 1-track, 2-track-QE, and 2-track-nonQE samples. The experiment period is K2K-IIb only.

SciFi The event classification is the same as SciBar. In addition, there are three kinds of CC event selection: K2K-Ib MRD-matching, K2K-Ib LG-stopping, and K2K-IIa MRD-matching. In total, nine distributions are used.

1KT We use the FC 1Rμ sample taken in K2K-Ib, K2K-IIa, and K2K-IIb runs.

In total, thirteen distributions are fitted at the same time. The PIMON result is also employed as the constraint term on f_i^ϕ above 1 GeV. The χ^2 to be minimized is defined as

$$\chi^2 = \chi^2_{\rm SciBar} + \chi^2_{\rm SciFi} + \chi^2_{\rm 1KT} + \chi^2_{\rm PIMON}, \tag{8.10}$$

where $\chi^2_{\rm SciBar}$, $\chi^2_{\rm SciFi}$, $\chi^2_{\rm 1KT}$, and $\chi^2_{\rm PIMON}$ are chi-square from SciBar, SciFi, 1KT, and PIMON data, respectively. They are defined in the following sections.

Some other fitting parameters are introduced to deal with the detector systematics such as p_μ scale and track finding efficiency. They are restricted within the systematic errors by additional χ^2 terms. The normalization factor for each detector is freely variable during the fit, because the aim of the fit is to obtain only the shape of the spectrum. The overall normalization is given by setting f_4^ϕ to unity (constant).

8.7.2 SciBar part

We describe (p_μ, θ_μ) distributions and the chi-square of SciBar.

Table 8.5: The E_ν interval of each f_i^ϕ bin.

i	1	2	3	4	5	6	7	8
E_ν [GeV]	0.0–0.5	0.5–0.75	0.75–1.0	1.0–1.5	1.5–2.0	2.0–2.5	2.5–3.0	3.0–

(p_μ, θ_μ) distribution

The bin width of the (p_μ, θ_μ) two-dimensional distribution is 0.1 GeV/c for p_μ and 10 degrees for θ_μ. Figure 8.22 shows the (p_μ, θ_μ) two-dimensional distributions of the SciBar 1-track sample for instance. The (p_μ, θ_μ) distributions for the MC simulation are divided into eight E_ν bins and two interactions.

The MC histograms for neutrino energy of $E_\nu \gtrsim 1.5$ GeV have additional event clusters at $p_\mu \sim 0.5$ GeV/c. They are hadrons mis-reconstructed as muons. The amount of hadron contamination is affected by the uncertainties in the hadron production off a nucleus. If we intensionally change pion absorption by ±30%, pion inelastic scattering by ±30%, and proton re-scattering by ±10%, the hadron contamination varies ±10%. Therefore, we assign the systematic error of 10% to the hadron component.

The bin contents of the MC distribution for each event category is given by

$$N^{\text{MC 1trk}}(i,j) = P^{\text{SciBar}}_{\text{Norm}} \cdot \sum_{k=1}^{8} f_k^\phi \cdot \left[N^{\text{MC 1trk}}_{k,\text{QE}}(i,j) + R_{\text{nQE}} \cdot N^{\text{MC 1trk}}_{k,\text{nonQE}}(i,j) \right], \tag{8.11}$$

$$N^{\text{MC 2trk-QE}}(i,j) = P^{\text{SciBar}}_{\text{Norm}} \cdot P^{\text{SciBar}}_{\text{2trk/1trk}} \times \sum_{k=1}^{8} f_k^\phi \cdot \left[N^{\text{MC 2trk-QE}}_{k,\text{QE}}(i,j) + R_{\text{nQE}} \cdot N^{\text{MC 2trk-QE}}_{k,\text{nonQE}}(i,j) \right], \tag{8.12}$$

$$N^{\text{MC 2trk-nonQE}}(i,j) = P^{\text{SciBar}}_{\text{Norm}} \cdot P^{\text{SciBar}}_{\text{2trk/1trk}} \cdot P^{\text{SciBar}}_{\text{nonQE/QE}} \times \sum_{k=1}^{8} f_k^\phi \cdot \left[N^{\text{MC 2trk-nonQE}}_{k,\text{QE}}(i,j) + R_{\text{nQE}} \cdot N^{\text{MC 2trk-nonQE}}_{k,\text{nonQE}}(i,j) \right], \tag{8.13}$$

where $P^{\text{SciBar}}_{\text{Norm}}$, $P^{\text{SciBar}}_{\text{2trk/1trk}}$ and $P^{\text{SciBar}}_{\text{nonQE/QE}}$ are fitting parameters. $P^{\text{SciBar}}_{\text{Norm}}$ is the normalization factor, which is freely variable. $P^{\text{SciBar}}_{\text{2trk/1trk}}$ and $P^{\text{SciBar}}_{\text{nonQE/QE}}$ are the parameters to vary $R^{\text{SciBar}}_{\text{2trk/1trk}}$ and $R^{\text{SciBar}}_{\text{nonQE/QE}}$[3] within their systematic errors. In addition, the MC distributions are scaled along the p_μ axis by

$$p'_\mu = \frac{p_\mu}{P^{\text{SciBar}}_{p\text{-scale}}}, \tag{8.14}$$

where $P^{\text{SciBar}}_{p\text{-scale}}$ is a fitting parameter to vary the p_μ scale within its systematic error.

Definition of χ^2

The chi-square of SciBar (χ^2_{SciBar}) is computed from the ratio of Poisson likelihood[91]. In general, the likelihood of binned data $\boldsymbol{n} = (n_1, n_2, \ldots, n_N)$ with expectation values $\boldsymbol{\mu}(\boldsymbol{\theta})$ at a certain parameter set $\boldsymbol{\theta} = (\theta_1, \theta_2, \ldots, \theta_M)$ is given by

$$f(\boldsymbol{n}; \boldsymbol{\mu}(\boldsymbol{\theta})) \equiv \prod_{i=1}^{N} \frac{\mu_i(\boldsymbol{\theta})^{n_i} \exp[-\mu_i(\boldsymbol{\theta})]}{n_i!}, \tag{8.15}$$

[3] $R^{\text{SciBar}}_{\text{2trk/1trk}}$ and $R^{\text{SciBar}}_{\text{nonQE/QE}}$ are defined in Section 8.2.3.

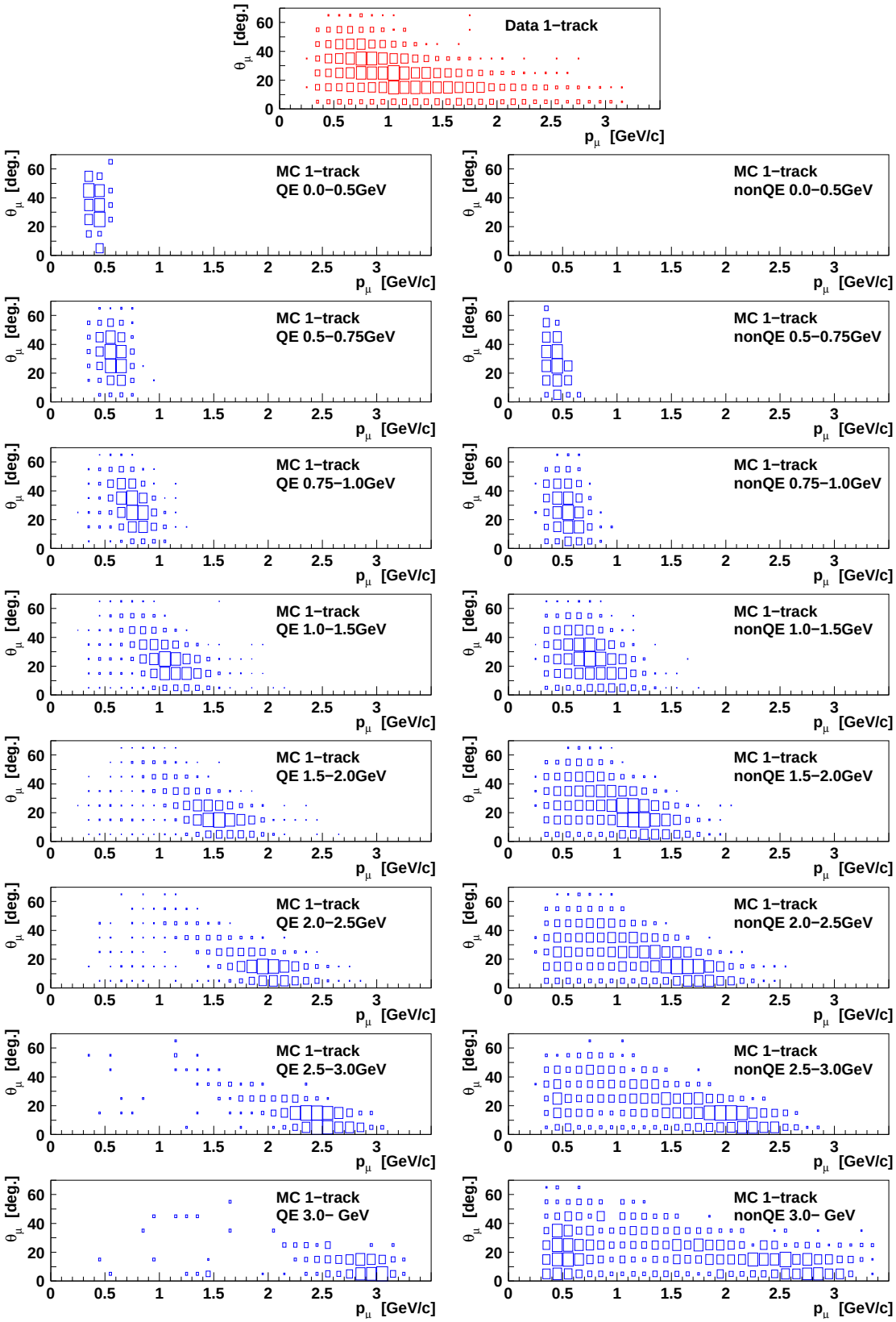

Figure 8.22: The (p_μ, θ_μ) two-distributions of the SciBar 1-track sample. The area of each box is proportional to the bin content. The topmost figure shows the observed data, and the others are the MC simulation divided into each E_ν and each interaction.

where N is the number of bins and M is the number of free parameters. Maximizing this likelihood is equivalent to minimizing the quantity:

$$-2\ln\frac{f(\boldsymbol{n};\boldsymbol{\mu}(\boldsymbol{\theta}))}{f(\boldsymbol{n};\boldsymbol{n})} = 2\sum_{i=1}^{N}\left[\mu_i(\boldsymbol{\theta}) - n_i + n_i\ln\frac{n_i}{\mu_i(\boldsymbol{\theta})}\right]. \tag{8.16}$$

It is known to follow the χ^2 distribution with $(N-M)$ degrees of freedom in the large sample limit. This method is more reliable than usual Peason's χ^2:

$$\chi^2 = \sum_{i=1}^{N}\frac{(n_i-\mu_i(\boldsymbol{\theta}))^2}{\mu_i(\boldsymbol{\theta})}, \tag{8.17}$$

especially if $\mu_i(\boldsymbol{\theta})$ is small. For the calculation of $\chi^2_{\rm SciBar}$, we use (p_μ,θ_μ) bins with at least five entries. Systematic errors on hadron contamination assigned bin-by-bin are implemented by the convolution of Equation (8.15) with Gaussian. If the MC prediction $\boldsymbol{\mu}(\boldsymbol{\theta})$ varies within the error of $\boldsymbol{\sigma} = (\sigma_1,\sigma_2,\ldots,\sigma_N)$, the likelihood is expressed by:

$$f'(\boldsymbol{n};\boldsymbol{\mu}(\boldsymbol{\theta});\boldsymbol{\sigma}) \equiv \prod_{i=1}^{N}\int_0^\infty \frac{1}{\sqrt{2\pi}\sigma_i}\exp\left[-\frac{(x-\mu_i(\boldsymbol{\theta}))^2}{2\sigma_i^2}\right]\cdot\frac{x^{n_i}e^{-x}}{n_i!}\,dx. \tag{8.18}$$

Finally, the χ^2 of SciBar is defined as

$$\chi^2_{\rm SciBar} = -2\sum_{\mathcal{C}}\ln\frac{f'(N^{{\rm data},\mathcal{C}};N^{{\rm MC},\mathcal{C}};\boldsymbol{\sigma})}{f'(N^{{\rm data},\mathcal{C}};N^{{\rm data},\mathcal{C}};\boldsymbol{\sigma})} + (\boldsymbol{P}-\langle\boldsymbol{P}\rangle)^T V^{-1}(\boldsymbol{P}-\langle\boldsymbol{P}\rangle), \tag{8.19}$$

where $\mathcal{C}$ runs 1trk, 2trk-QE, and 2trk-nonQE, and the second term constrains the systematic parameters within their errors. $\boldsymbol{P}$ and $\langle\boldsymbol{P}\rangle$ are the vectors of systematic parameters and their central values, respectively, defined as

$$\boldsymbol{P} \equiv \begin{pmatrix} P^{\rm SciBar}_{p\text{-scale}} \\ P^{\rm SciBar}_{\rm 2trk/1trk} \\ P^{\rm SciBar}_{\rm nonQE/QE}\end{pmatrix} \qquad \langle\boldsymbol{P}\rangle \equiv \begin{pmatrix} 1 \\ 1.030 \\ 0.967\end{pmatrix}. \tag{8.20}$$

The central values of $P^{\rm SciBar}_{\rm 2trk/1trk}$ and $P^{\rm SciBar}_{\rm nonQE/QE}$ are not unity, because the proton re-scattering cross-section is 13% smaller than the normal MC simulation (Section 5.2.5). V is the covariance matrix of P, expressed by

$$V \equiv \begin{pmatrix} (0.027)^2 & 0 & 0 \\ 0 & 0.0026 & -0.0027 \\ 0 & -0.0027 & 0.0075\end{pmatrix}. \tag{8.21}$$

The (1,1) element is the systematic error on the momentum scale (Section 6.2.5). The other elements are the systematic errors on $R^{\rm SciBar}_{\rm 2trk/1trk}$ and $R^{\rm SciBar}_{\rm nonQE/QE}$ obtained from the errors estimated in Section 8.2.3. The asymmetric error is averaged, and the correlation is taken into account.

8.7.3 SciFi part

The (p_μ,θ_μ) distribution of SciFi is binned into the same momentum intervals as E_ν (Table 8.5) for p_μ and every 10 degrees for θ_μ. The systematic errors on $E^{\rm MRD}_\mu$, $E^{\rm LG}_\mu$, and $E^{\rm LGcluster}_\mu$ are separately taken into account by three fitting parameters, $P^{\rm SciFi}_{E\text{-scale}}$, $P^{\rm SciFi}_{\rm LG\text{-}density}$, and $P^{\rm SciFi}_{\rm LG\text{-}cluster}$, respectively. During the fit, Equation (8.6)–(8.8) for the observed data are modified into

$$\textbf{K2K-Ib MRD-3D,1L:}\quad E'_\mu = E^{\rm SciFi}_\mu + E^{\rm TG}_\mu + E^{\rm LG}_\mu\cdot P^{\rm SciFi}_{\rm LG\text{-}density} + E^{\rm MRD}_\mu\cdot P^{\rm SciFi}_{E\text{-scale}}, \tag{8.22}$$

K2K-Ib LG-Stopping: $E'_\mu = E_\mu^{\rm SciFi} + E_\mu^{\rm TG} + E_\mu^{\rm LGcluster} + P_{\rm LG\text{-}cluster}^{\rm SciFi}$, (8.23)

K2K-IIa MRD-3D: $E'_\mu = E_\mu^{\rm SciFi} + E_\mu^{\rm TG} + E_\mu^{\rm Mini\text{-}SciBar} + E_\mu^{\rm MRD} \cdot P_{E\text{-}{\rm scale}}^{\rm SciFi}$. (8.24)

The definitions of MC (p_μ, θ_μ) distributions are given by

$$N^{\rm MC,1trk}(i,j) = P_{\rm Norm}^{\rm SciFi} \cdot \sum_{k=1}^{8} f_k^\phi \cdot \left[N_{k,{\rm QE}}^{\rm MC,1trk}(i,j) + R_{\rm nQE} \cdot N_{k,{\rm nonQE}}^{\rm MC,1trk}(i,j) \right], \tag{8.25}$$

$$\begin{aligned} N^{\rm MC,2trk\text{-}QE}(i,j) = P_{\rm Norm}^{\rm SciFi} \cdot \sum_{k=1}^{8} f_k^\phi \cdot \Big[& N_{k,{\rm QE}}^{\rm MC,2trk\text{-}QE}(i,j) \\ & + \frac{R_{\rm rescat}^{\rm SciFi}}{1 - R_{\rm rescat}^{\rm SciFi}} (1 - P_{\rm rescat}^{\rm SciFi}) \cdot N_{k,{\rm QE}}^{\rm MC,2trk\text{-}QE}(i,j) \\ & + R_{\rm nQE} \cdot N_{k,{\rm nonQE}}^{\rm MC,2trk\text{-}QE}(i,j) \Big], \end{aligned} \tag{8.26}$$

$$\begin{aligned} N^{\rm MC,2trk\text{-}nonQE}(i,j) = P_{\rm Norm}^{\rm SciFi} \cdot \sum_{k=1}^{8} f_k^\phi \cdot \Big[& N_{k,{\rm QE}}^{\rm MC,2trk\text{-}nonQE}(i,j) \\ & - \frac{R_{\rm rescat}^{\rm SciFi}}{1 - R_{\rm rescat}^{\rm SciFi}} (1 - P_{\rm rescat}^{\rm SciFi}) \cdot N_{k,{\rm QE}}^{\rm MC,2trk\text{-}QE}(i,j) \\ & + R_{\rm nQE} \cdot N_{k,{\rm nonQE}}^{\rm MC,2trk\text{-}nonQE}(i,j) \Big], \end{aligned} \tag{8.27}$$

where $P_{\rm Norm}^{\rm SciFi}$ and $P_{\rm rescat}^{\rm SciFi}$ are fitting parameters. The overall normalization is adjusted by $P_{\rm Norm}^{\rm SciFi}$, and the proton re-scattering cross-section is tuned by $P_{\rm rescat}^{\rm SciFi}$. The second terms in the summations of Equation (8.26) and (8.27) represent the migration between 2-track-QE and 2-track-nonQE samples due to the proton re-scattering. Here, $R_{\rm rescat}^{\rm SciFi}$ is the proton re-scattering probability in the CC-QE interaction, estimated to be 0.33 from the NEUT MC simulation. In Section 5.2.5, the proton re-scattering cross-section is found to be $(87 \pm 10)\%$ of our simulation according to an electron scattering experiment. Therefore, the central value of $P_{\rm rescat}^{\rm SciFi}$ is set to 0.87 with the systematic error of 0.10.

The systematic error on the second track finding efficiency is taken into account. The migration between the three categories is implemented by

$$N'^{\rm MC,1trk}(i,j) = (1 - P_{\rm 2nd\text{-}eff}^{\rm SciFi}) \cdot [N^{\rm MC,2trk\text{-}QE}(i,j) + N^{\rm MC,2trk\text{-}nonQE}(i,j)], \tag{8.28}$$

$$N'^{\rm MC,2trk\text{-}QE}(i,j) = P_{\rm 2nd\text{-}eff}^{\rm SciFi} \cdot N^{\rm MC,2trk\text{-}QE}(i,j), \tag{8.29}$$

$$N'^{\rm MC,2trk\text{-}nonQE}(i,j) = P_{\rm 2nd\text{-}eff}^{\rm SciFi} \cdot N^{\rm MC,2trk\text{-}nonQE}(i,j), \tag{8.30}$$

where $P_{\rm 2nd\text{-}eff}^{\rm SciFi}$ is the fitting parameter to vary the second track finding efficiency. The central value of $P_{\rm 2nd\text{-}eff}^{\rm SciFi}$ is unity, and the systematic error on $P_{\rm 2nd\text{-}eff}^{\rm SciFi}$ is 5%.

Finally, the chi-square for the SciFi data is defined as

$$\begin{aligned} \chi^2_{\rm SciFi} = & 2 \sum_{\mathcal{T}} \sum_{\mathcal{C}} \sum_{i,j} \left[N'^{{\rm MC},\mathcal{T},\mathcal{C}}(i,j) - N'^{{\rm data},\mathcal{T},\mathcal{C}}(i,j) + N'^{{\rm data},\mathcal{T},\mathcal{C}}(i,j) \ln \frac{N'^{{\rm data},\mathcal{T},\mathcal{C}}(i,j)}{N'^{{\rm MC},\mathcal{T},\mathcal{C}}(i,j)} \right] \\ & + \sum_{\mathcal{S}} \frac{(P_{\mathcal{S}}^{\rm SciFi} - \langle P_{\mathcal{S}}^{\rm SciFi} \rangle)^2}{(\sigma_{\mathcal{S}}^{\rm SciFi})^2}, \end{aligned} \tag{8.31}$$

$$\mathcal{T} = \{\text{K2K-Ib-MRD, K2K-Ib-LG, K2K-IIa-MRD}\}, \tag{8.32}$$

$$\mathcal{C} = \{\text{1trk, 2trk-QE, 2trk-nonQE}\}, \tag{8.33}$$

$$\mathcal{S} = \{E\text{-scale, LG-density, LG-cluster, rescat, 2nd-eff}\}. \tag{8.34}$$

The first term represents the chi-square between data and the MC simulation based on Equation (8.16). The second term constrains the systematic parameters. The central value ($\langle P_S^{\rm SciFi} \rangle$) and the systematic error ($\sigma_S^{\rm SciFi}$) of each systematic parameter are summarized in Table 8.6.

8.7.4 1KT part

Definition of χ^2

The bin width of the (p_μ, θ_μ) distribution of 1KT is same as that of SciBar, except that the events above 90 degrees are integrated into one angular bin. To implement the systematic error on the muon momentum scale, the muon momentum of the MC simulation is modified into

$$p'_\mu = \frac{p_\mu}{P^{\rm 1KT}_{p\text{-scale}}}, \tag{8.35}$$

where $P^{\rm 1KT}_{p\text{-scale}}$ is a fitting parameter. The central value of $P^{\rm 1KT}_{p\text{-scale}}$ is unity, and the error, $\sigma^{\rm 1KT}_{p\text{-scale}}$, is $^{+2}_{-3}$%. The two-dimensional distribution of the MC simulation is given by

$$N^{\rm MC}(i,j) \equiv P^{\rm 1KT}_{\rm Norm} \cdot \sum_{k=1}^{8} f_k^\phi \cdot \left[N^{\rm MC}_{k,{\rm QE}} + R_{\rm nQE} \cdot N^{\rm MC}_{k,{\rm nonQE}} \right], \tag{8.36}$$

where $P^{\rm 1KT}_{\rm Norm}$ is a free parameter for normalization. The chi-square of 1KT is defined as

$$\chi^2_{\rm 1KT} \equiv \sum_{i,j} \frac{\left[N^{\rm data}(i,j) - N^{\rm MC}(i,j) \right]^2}{[\sigma^{\rm data}_{\rm stat}(i,j)]^2 + [\sigma^{\rm MC}_{\rm stat}(i,j)]^2 + [\sigma_{\rm syst}(i,j)]^2} + \frac{(P^{\rm 1KT}_{p\text{-scale}} - 1)^2}{(\sigma^{\rm 1KT}_{p\text{-scale}})^2}, \tag{8.37}$$

where $\sigma^{\rm data}_{\rm stat}(i,j)$ and $\sigma^{\rm MC}_{\rm stat}(i,j)$ are the statistical errors of data and the MC simulation, respectively. The bin-by-bin systematic error, $\sigma_{\rm syst}(i,j)$, is also put into $\chi^2_{\rm 1KT}$. The sources of $\sigma_{\rm syst}(i,j)$ are summarized below:

Vertex reconstruction :
In cosmic ray data, a discrepancy of the reconstructed vertex position between data and the MC simulation is found[90], and the difference is 10 cm. Therefore, the size and position of the fiducial volume are changed by 10 cm, and the systematic error is estimated to be the deviation of each bin content.

Angular resolution :
The angular resolution of data is worse by 1.6 degrees than the MC simulation (Section 8.4.2). We conservatively assign 2.0 degrees to the systematic error on the angular resolution. We smeared the θ_μ of the MC simulation by 2.0 degrees, and evaluated the systematic error as the difference between before and after the smearing.

Ring counting :
To select single-ring events, we cut the ring counting likelihood, $\mathcal{F}$, at zero. Since the $\mathcal{F}$ distribution (Figure 8.16) shows a discrepancy between data and the MC simulation, we change the cut position within the uncertainty of $\mathcal{F}$, and quote the systematic error as the fluctuation of each bin.

Particle identification :
The particle identification is applied to select a μ-like ring. We remove this requirement and quoted the systematic error as the difference.

The sum of the above errors is assigned to $\sigma_{\rm syst}(i,j)$.

Table 8.6: The central values and errors of the constraint terms in $\chi^2_{\rm SciFi}$.

Parameter	Central value	Error
$P^{\rm SciFi}_{E\text{-scale}}$	1.00	0.027
$P^{\rm SciFi}_{\rm LG\text{-}density}$	1.00	0.10
$P^{\rm SciFi}_{\rm LG\text{-}cluster}$ [GeV]	0.00	0.03
$P^{\rm SciFi}_{\rm rescat}$	0.87	0.10
$P^{\rm SciFi}_{\rm 2nd\text{-}eff}$	1.00	0.05

8.7.5 PIMON part

The information from PIMON is employed to constrain the E_ν spectrum shape (f_i^ϕ). From the measurement of secondary pions above 2 GeV/c, we have obtained the spectrum shape of $E_\nu > 1$ GeV. Here, we express the PIMON spectrum as $f_i^{\rm PIMON}$ $(i = 4, 5, 6, 7)$. The subscript i indicates the same E_ν bin as f_i^ϕ. The eighth bin ($f_8^{\rm PIMON}$) does not exist, because the neutrino flux above 2.5 GeV is integrated in the PIMON measurement. We set $f_4^{\rm PIMON}$ at unity so that $f_i^{\rm PIMON}$ is normalized with f_i^ϕ. Therefore, $f_i^{\rm PIMON}$ is written as

$$f_i^{\rm PIMON} = \frac{\Phi_i^{\rm PIMON}/\Phi_i^{\rm MC}}{\Phi_4^{\rm PIMON}/\Phi_4^{\rm MC}} \qquad (i = 5, 6, 7), \tag{8.38}$$

where $\Phi_i^{\rm PIMON}$ and $\Phi_i^{\rm MC}$ are the neutrino fluxes of the PIMON measurement and the MC simulation, respectively. The chi-square of the PIMON part is given by

$$\chi^2_{\rm PIMON} = \sum_{i=5}^{7} \frac{(f_i^\phi - f_i^{\rm PIMON})^2}{(\sigma_i^{\rm PIMON})^2}, \tag{8.39}$$

where $\sigma_i^{\rm PIMON}$ is the error on $f_i^{\rm PIMON}$. In this equation, f_8^ϕ is combined into f_7^ϕ. The input values into Equation (8.38) and (8.39) are summarized in Table 8.7. The detail of the PIMON measurement is described in Chapter 10.

8.7.6 Fit results

The minimum of the χ^2 is searched for by using MINUIT[92], and the best parameter set is determined. In this fit, the regions of $\theta_\mu < 10$ (20) degrees for SciBar and SciFi (1KT) are not used because of the low-q^2 deficit. Table 8.8 is the summary of the best fit parameters and χ^2. The result from each detector only is also listed. Here, we call the spectrum fit with all detectors "Merged fit" in contrast to the fit with each detector only. The goodness-of-fit is estimated from the coverage of χ^2 distribution above the best fit χ^2. Although the goodness-of-fit from the merged fit is not sufficient, we use this E_ν spectrum for the study of the low-q^2 deficit. The validity of the spectrum is discussed after the low-q^2 correction.

8.8 Low-q^2 tuning

We study the correction method of the low-q^2 deficit. In this study, the neutrino energy spectrum is fixed to the fit result in the previous section. From the discussion in Section 8.5.2, the possible sources are CC resonance production and CC coherent pion production modes. We look for the tuning method of each mode.

Table 8.7: The input values to compute the chi-square of PIMON. The units of $\Phi_i^{\rm PIMON}$ and $\Phi_i^{\rm MC}$ are arbitrary.

E_ν [GeV] (index i)	1.0–1.5 ($i=4$)	1.5–2.0 ($i=5$)	2.0–2.5 ($i=6$)	2.5– ($i=7$)
$\Phi_i^{\rm PIMON}$	6.30	3.21	1.01	0.427
$\Phi_i^{\rm MC}$	6.19	3.35	1.05	0.396
$f_i^{\rm PIMON}$	$\equiv 1$	0.941	0.945	1.059
$\sigma_i^{\rm PIMON}$	—	$^{+10.7}_{-9.9}$%	$^{+12.1}_{-17.7}$%	$^{+47.7}_{-34.0}$%

Table 8.8: Results from the E_ν spectrum fit without small angle. The best fit value and the error of each parameter are listed. Chi-square, degrees of freedom (d.o.f.), and goodness-of-fit are also shown. $N_{\rm bins}$ is the number of bins in (p_μ, θ_μ) distributions used by the fit.

Parameter	**Merged**	SciBar only	SciFi only	1KT only
f_1^ϕ	$\mathbf{0.784 \pm 0.364}$	$\equiv 1$	$\equiv 1$	1.413 ± 0.418
f_2^ϕ	$\mathbf{1.012 \pm 0.086}$	1.181 ± 0.270	0.652 ± 0.284	1.136 ± 0.102
f_3^ϕ	$\mathbf{1.119 \pm 0.065}$	1.158 ± 0.144	1.369 ± 0.215	1.098 ± 0.079
f_4^ϕ	$\mathbf{\equiv 1}$	$\equiv 1$	$\equiv 1$	$\equiv 1$
f_5^ϕ	$\mathbf{0.901 \pm 0.044}$	0.994 ± 0.085	1.020 ± 0.132	0.856 ± 0.078
f_6^ϕ	$\mathbf{1.069 \pm 0.064}$	1.171 ± 0.124	1.013 ± 0.117	0.936 ± 0.174
f_7^ϕ	$\mathbf{1.334 \pm 0.171}$	1.793 ± 0.306	1.279 ± 0.287	0.776 ± 0.670
f_8^ϕ	$\mathbf{1.041 \pm 0.179}$	$\equiv 1$	1.102 ± 0.207	$\equiv 1$
$R_{\rm nQE}$	$\mathbf{0.955 \pm 0.045}$	1.073 ± 0.104	0.983 ± 0.061	0.705 ± 0.112
$P_{\rm Norm}^{\rm SciBar}$	$\mathbf{1.012 \pm 0.011}$	1.016 ± 0.011	—	—
$P_{p\text{-scale}}^{\rm SciBar}$	$\mathbf{0.980 \pm 0.003}$	0.983 ± 0.005	—	—
$P_{\rm 2trk/1trk}^{\rm SciBar}$	$\mathbf{1.043 \pm 0.027}$	1.056 ± 0.029	—	—
$P_{\rm nonQE/QE}^{\rm SciBar}$	$\mathbf{1.121 \pm 0.044}$	1.048 ± 0.059	—	—
$P_{\rm Norm}^{\rm SciFi}$	$\mathbf{1.018 \pm 0.032}$	—	0.963 ± 0.066	—
$P_{E\text{-scale}}^{\rm SciFi}$	$\mathbf{0.952 \pm 0.005}$	—	0.948 ± 0.006	—
$P_{\rm LG\text{-}density}^{\rm SciFi}$	$\mathbf{0.956 \pm 0.014}$	—	0.952 ± 0.014	—
$P_{\rm LG\text{-}cluster}^{\rm SciFi}$	$\mathbf{5.106 \pm 2.577}$	—	5.571 ± 2.673	—
$P_{\rm 2nd\text{-}eff}^{\rm SciFi}$	$\mathbf{0.966 \pm 0.016}$	—	0.965 ± 0.019	—
$P_{\rm rescat}^{\rm SciFi}$	$\mathbf{0.951 \pm 0.057}$	—	0.942 ± 0.060	—
$P_{\rm Norm}^{\rm 1KT}$	$\mathbf{0.993 \pm 0.025}$	—	—	1.095 ± 0.050
$P_{p\text{-scale}}^{\rm 1KT}$	$\mathbf{0.985 \pm 0.003}$	—	—	0.986 ± 0.006
$\chi^2_{\rm total}$/d.o.f.	**538.5 / 479**	209.5 / 194	253.9 / 219	51.8 / 54
Goodness [%]	**3.1**	21.2	5.3	56.1
$\chi^2_{\rm SciBar}/N_{\rm bins}$	**219.4 / 204**	209.5 / 204	—	—
$\chi^2_{\rm SciFi}/N_{\rm bins}$	**258.4 / 232**	—	253.9 / 232	—
$\chi^2_{\rm 1KT}/N_{\rm bins}$	**59.4 / 60**	—	—	50.8 / 60
$\chi^2_{\rm PIMON}/N_{\rm bins}$	**1.3 / 3**	—	—	1.0 / 3

8.8.1 Tuning of CC resonance production

The CC resonance production channel is mainly intermediated by $\Delta(1232\text{MeV})$. To see the q^2 dependence of the deficit, therefore, we introduce $q^2_{\Delta(1232)}$, which is the squared four-momentum transfer assuming $\Delta(1232)$ production. The definition of $q^2_{\Delta(1232)}$ is same as Equation (8.4), but the reconstructed neutrino energy is calculated by using 1232 MeV/c^2 for the mass of the scattered hadron. Figure 8.23 shows the $q^2_{\Delta(1232)}$ distribution of the SciBar 2-track-nonQE sample. The (Data–MC)/MC distribution shows a linear dependence from 0.0 to 0.1 $(\text{GeV}/c)^2$, and the resonance production component is nearly zero at $q^2_\Delta(1232) = 0.0$ $(\text{GeV}/c)^2$. Therefore, we introduce a suppression factor, $F(q^2_{\text{true}})$, given by

$$F(q^2_{\text{true}}) \equiv \begin{cases} \dfrac{q^2_{\text{true}}}{\Lambda} & 0 \leq q^2_{\text{true}} < \Lambda \\ 1 & q^2_{\text{true}} \geq \Lambda, \end{cases} \tag{8.40}$$

where q^2_{true} is the MC true squared four-momentum transfer, and Λ is a cut off parameter. We multiply it to the cross-section of the CC resonance production mode. Figure 8.24 shows a graph of $F(q^2_{\text{true}})$.

To find the best value of Λ, we compute chi-square of θ_μ distributions between data and the MC simulation, and look for the minimum by scanning Λ. The fitted E_ν spectrum and R_{nQE} are applied to the MC θ_μ distributions. We do not use q^2 distributions because q^2 is influenced by the energy scale uncertainty. In this study, we use only the 1-track and 2-track-nonQE samples of SciBar. The bin width of θ_μ distributions is 5 degrees. Figure 8.25 shows the θ_μ distributions before the suppression ($\Lambda = 0$).

We minimize the chi-square of the 1-track sample (χ^2_{1trk}), that of 2-track-nonQE sample ($\chi^2_{\text{2trk-nonQE}}$), and the sum of them ($\chi^2_{\text{1trk}} + \chi^2_{\text{2trk-nonQE}}$). The graphs of χ^2 versus Λ are shown in Figure 8.26, and the best values are summarized in Table 8.9 together with the default case. Both two samples are consistent with each other, and the goodness of the combined result is appropriate. Figure 8.27 shows θ_μ distributions in case of $\Lambda = 0.101$ $(\text{GeV}/c)^2$. Data shows good agreement with the MC simulation. On the contrary, the default case is strongly disfavored. Thus, we use $\Lambda = 0.1$ $(\text{GeV}/c)^2$ for the oscillation analysis.

8.8.2 Tuning of CC coherent pion production

The coherent pion scattering events are concentrated in a low-q^2 region. The shape of the cross-section is very similar to the low-q^2 deficit, as shown in Figure 8.28. Therefore, we multiply a overall re-weighting factor, G, to the coherent pion production cross-section. In the same way as the previous section, we look for the best G by using the θ_μ distributions of SciBar 1-track and 2-track-nonQE samples. Figure 8.29 shows the θ_μ distributions in the default case ($G = 1$).

We scan G between -1 and 1, and find the minimum. Figure 8.30 shows the graph of χ^2 for each sample. The best G value and its χ^2 is summarized in Table 8.10 together with the default case. Although the physical region is $G \geq 0$, the best value of 1-track sample is significantly smaller than zero. In addition, there is a conflict between 1-track and 2-track-nonQE samples. However, the combined result is compatible with zero, and the χ^2 is much better than the default case ($G = 1$). Consequently, we employ $G = 0$ for the oscillation analysis.

8.9 Fit with low-q^2 correction

We confirm that each low-q^2 correction method is satisfactory to the entire (p_μ, θ_μ) region. We use the E_ν spectrum fitting method again, but the spectrum (f_i^ϕ) and energy scale parameters are fixed to the best fit values without small angle regions (θ_μ-cut result, Table 8.8).

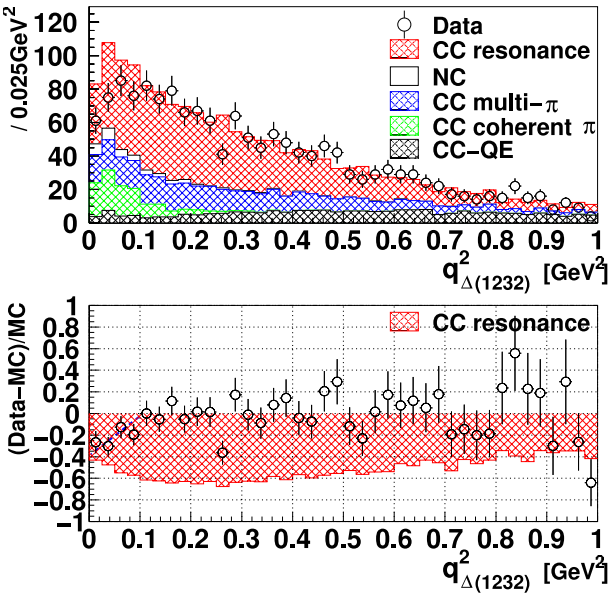

Figure 8.23: The upper figure shows the q^2 distribution of the SciBar 2-track-nonQE sample assuming the $\Delta(1232\text{MeV})$ production. The lower figure shows the fractional difference between data and the MC simulation, (Data–MC)/MC, together with the CC resonance production component.

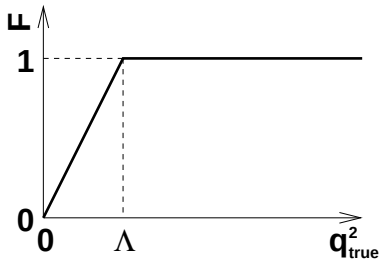

Figure 8.24: A graph of the suppression factor (F) for the CC resonance production mode.

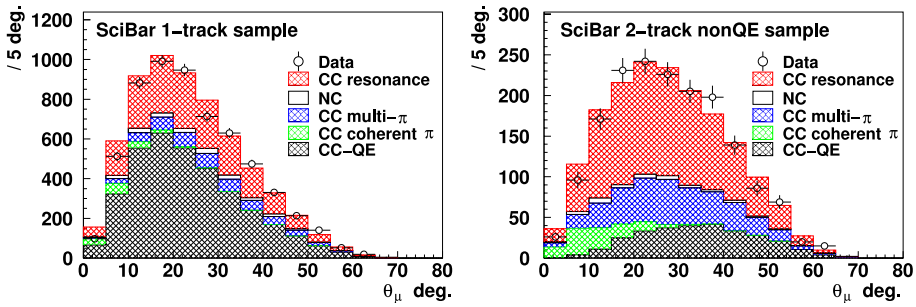

Figure 8.25: The θ_μ distributions of SciBar 1-track (left) and 2-track-nonQE (right) samples before the suppression of CC resonance production mode. Open circles are data and solid lines are the MC simulation. Interaction channels are distinguished by the color of hatched areas.

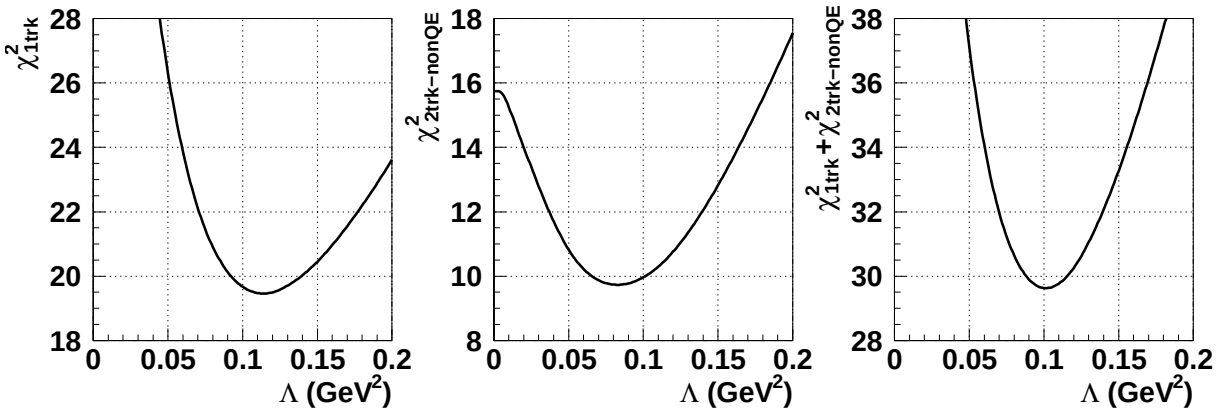

Figure 8.26: The χ^2 curve as a function of Λ. The left figure shows the chi-square of 1-track sample ($\chi^2_{\rm 1trk}$), and the center figure shows that of 2-track-nonQE sample ($\chi^2_{\rm 2trk\text{-}nonQE}$). The right figure shows the sum of them ($\chi^2_{\rm 1trk} + \chi^2_{\rm 2trk\text{-}nonQE}$).

Table 8.9: The best cut off parameters Λ of CC resonance pion production channel. The default case is also listed for reference.

Sample	**Combined**	1-track	2-track-nonQE
Best Λ [(GeV/c)^2]	$\mathbf{0.101^{+0.024}_{-0.021}}$	$0.114^{+0.037}_{-0.029}$	$0.083^{+0.037}_{-0.032}$
χ^2/d.o.f.	**29.6 /27**	19.5 / 13	9.7 / 13
Goodness [%]	**33.1**	11.0	71.6
Default Λ [(GeV/c)^2]	0	0	0
χ^2/d.o.f.	68.3 / 27	52.6 / 13	15.7 / 13
Goodness [%]	0.0019	0.00011	26.3

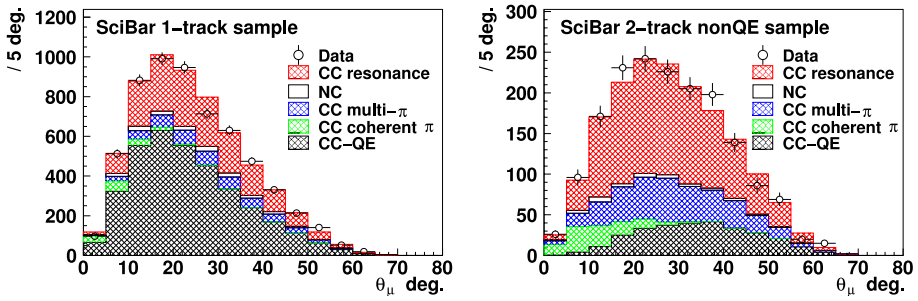

Figure 8.27: The θ_μ distributions of SciBar 1-track (left) and 2-track-nonQE (right) samples by applying the best cut off parameter (Λ = 0.101 (GeV/c)^2) of CC resonance production mode. Open circles are data and solid lines are the MC simulation. Interaction channels are distinguished by the color of hatched areas.

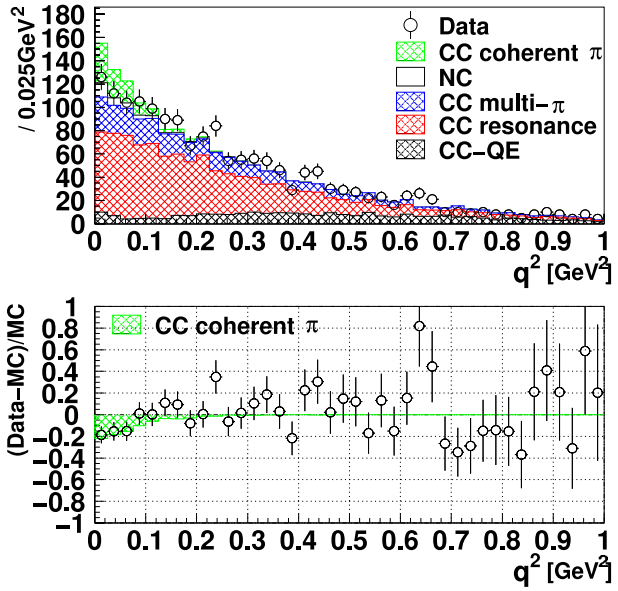

Figure 8.28: The upper figure shows the q^2 distribution of the SciBar 2-track-nonQE sample. Open circles are data and solid lines are the MC simulation. The color of each hatched area indicates the interaction channel. The fitted E_ν spectrum is applied to the MC simulation. The lower figure shows (data − MC)/MC. The hatched region shows the contribution of the CC coherent pion production.

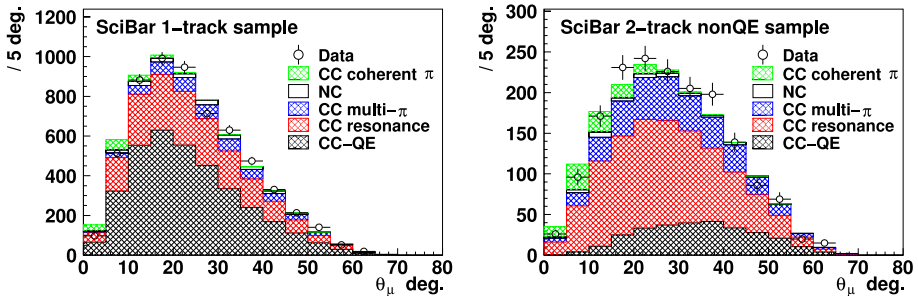

Figure 8.29: The θ_μ distributions of SciBar 1-track (left) and 2-track-nonQE (right) samples before the suppression of CC coherent pion production mode. Open circles are data and solid lines are the MC simulation. Interaction channels are distinguished by the color of hatched areas.

Table 8.10: The best re-weighting factors (G) of CC coherent pion production channel. The default case is also listed for reference.

Sample	**Combined**	1-track	2-track-nonQE
Best G	$\mathbf{-0.04 \pm 0.19}$	-0.73 ± 0.27	$+0.50 \pm 0.25$
χ^2/d.o.f.	**38.7 / 27**	15.5 / 13	12.0 / 13
Goodness [%]	**6.7**	27.8	53.0
Default G	1	1	1
χ^2/d.o.f.	68.3 / 27	52.6 / 13	15.7 / 13
Goodness [%]	0.0019	0.00011	26.3

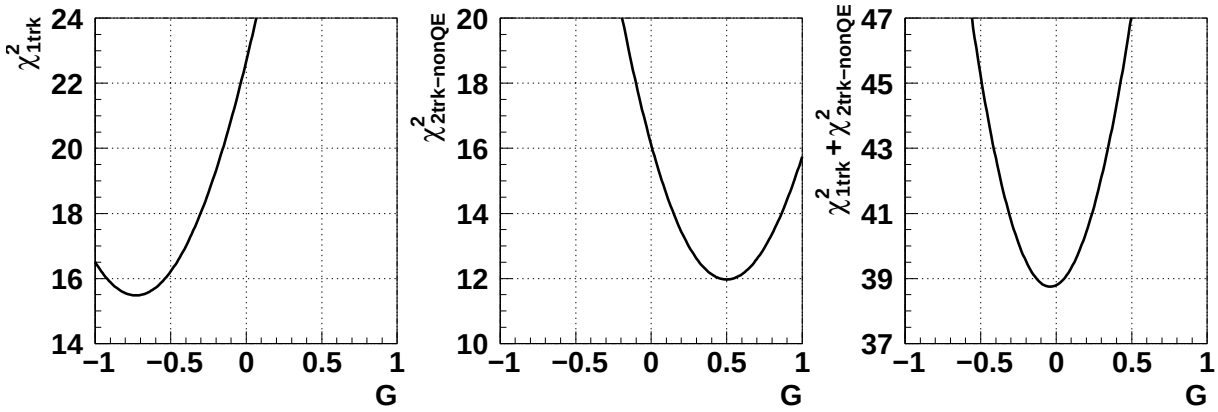

Figure 8.30: The χ^2 curve as a function of G. The left figure shows the chi-square of 1-track sample ($\chi^2_{\rm 1trk}$), and the center figure shows that of 2-track-nonQE sample ($\chi^2_{\rm 2trk\text{-}nonQE}$). The right figure shows the sum of them ($\chi^2_{\rm 1trk}+\chi^2_{\rm 2trk\text{-}nonQE}$).

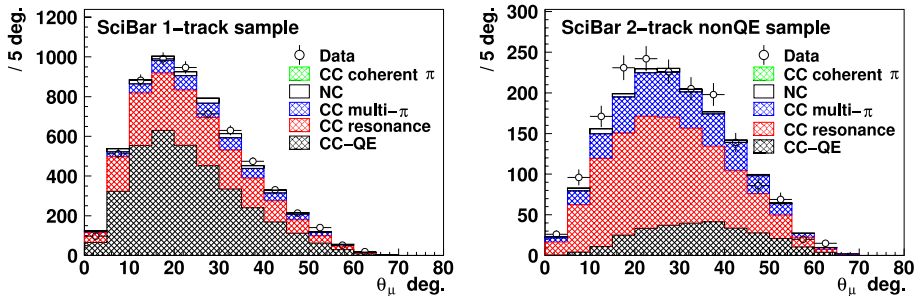

Figure 8.31: The θ_μ distributions of SciBar 1-track (left) and 2-track-nonQE (right) samples by applying the best re-weighting factor ($G=0$) of CC coherent pion production mode. Open circles are data and solid lines are the MC simulation. Interaction channels are distinguished by the color of hatched areas.

The results for the suppression of the CC resonance production mode ($\Lambda = 0.1$ (GeV/c)^2) is summarized in Table 8.11. The goodness-of-fit is reasonable, and most of the parameters are consistent with Table 8.8. For the elimination of CC coherent pion production channel ($G=0$), the fit results are summarized in Table 8.12. This result is also acceptable. For comparison, we perform the fit without low-q^2 suppression, and the results are summarized in Table 8.13. In this case, the goodness-of-fit is worse by several orders of magnitude. Obviously, we cannot use the MC simulation without low-q^2 correction for the oscillation analysis. We employ the suppression of the CC resonance production channel by default, because it reproduce data better than the removal of the CC coherent pion production channel. The suppression of the CC coherent pion scattering channel is used for the systematic error estimation and for the comparison of the results.

Figure 8.32, 8.33, and 8.34 show basic distributions of SciBar, SciFi, and 1KT, respectively, at the best fit point with the suppression of CC resonance production channel. For SciFi, only the K2K-IIa data is shown. All figures show good agreement between data and the best fit MC simulation. Despite the fact that the suppression factor of the low-q^2 region is obtained from only SciBar data, the low-q^2 distributions in SciFi and 1KT data are well reproduced by the MC simulation. Consequently, the fit result reproduces data well, and the obtained E_ν spectrum is appropriate for the neutrino oscillation analysis.

Table 8.11: Results from the re-fitting with suppression of CC resonance production mode.

Parameter	**Merged**	SciBar only	SciFi only	1KT only
R_{nQE}	$\mathbf{1.020 \pm 0.032}$	1.135 ± 0.079	1.060 ± 0.048	0.881 ± 0.054
$P^{\mathrm{SciBar}}_{\mathrm{Norm}}$	$\mathbf{0.994 \pm 0.011}$	0.995 ± 0.011	—	—
$P^{\mathrm{SciBar}}_{\mathrm{2trk/1trk}}$	$\mathbf{1.047 \pm 0.026}$	1.059 ± 0.028	—	—
$P^{\mathrm{SciBar}}_{\mathrm{nonQE/QE}}$	$\mathbf{1.096 \pm 0.039}$	1.044 ± 0.048	—	—
$P^{\mathrm{SciFi}}_{\mathrm{Norm}}$	$\mathbf{0.983 \pm 0.017}$	—	0.965 ± 0.024	—
$P^{\mathrm{SciFi}}_{\mathrm{2nd\text{-}eff}}$	$\mathbf{0.954 \pm 0.013}$	—	0.948 ± 0.014	—
$P^{\mathrm{SciFi}}_{\mathrm{rescat}}$	$\mathbf{0.923 \pm 0.055}$	—	0.906 ± 0.058	—
$P^{\mathrm{1KT}}_{\mathrm{Norm}}$	$\mathbf{0.973 \pm 0.016}$	—	—	1.030 ± 0.025
χ^2_{total}/d.o.f.	**638.1 / 609**	253.5 / 244	305.3 / 279	70.2 / 84
Goodness [%]	**20.0**	32.4	13.4	85.9
$\chi^2_{\mathrm{SciBar}}/N_{\mathrm{bins}}$	**255.9 / 248**	253.5 / 248	—	—
$\chi^2_{\mathrm{SciFi}}/N_{\mathrm{bins}}$	**306.0 / 283**	—	305.3 / 283	—
$\chi^2_{\mathrm{1KT}}/N_{\mathrm{bins}}$	**74.9 / 83**	—	—	68.9 / 83
$\chi^2_{\mathrm{PIMON}}/N_{\mathrm{bins}}$	**1.3 / 3**	—	—	1.3 / 3

There is an adverse point that the R_{nQE} value is significantly different between the three fitting conditions (θ_μ-cut, the suppression of resonance production channel, and the removal of coherent pion production mode), as listed below.

	θ_μ-cut	Suppression of resonance mode	Removal of coherent mode
R_{nQE}	0.955 ± 0.045	1.020 ± 0.032	1.059 ± 0.033

The maximum difference is 10%, whareas the fitting error is at most 5%. Therefore, we add the systematic error of 0.1 to R_{nQE}.

In the oscillation analysis, both the best fit values of f_i^ϕ and R_{nQE} and the error matrix are employed, so that correlations between parameters are taken into account. Since f_i^ϕ is fixed during the fit with the low-q^2 correction, we use the error matrix obtained by the fit without small θ_μ. The systematic error on R_{nQE} (± 0.1) is added to the matrix including the correlation. For the central value of R_{nQE}, we use the best fit value with the low-q^2 correction. Table 8.14 shows best fit values, errors, and components of the error matrix in case of the suppression of the CC-resonance production mode. Figure 8.35 shows the obtained E_ν spectrum at the near site. In this figure, each bin content is generated randomly many times according to the best fit values and the error matrix, and its mean and standard deviation are illustrated.

Table 8.12: Results from the re-fitting with suppression of coherent pion production mode.

Parameter	**Merged**	SciBar only	SciFi only	1KT only
R_{nQE}	$\mathbf{1.059 \pm 0.033}$	1.135 ± 0.076	1.037 ± 0.048	1.039 ± 0.063
$P^{\mathrm{SciBar}}_{\mathrm{Norm}}$	$\mathbf{0.994 \pm 0.011}$	0.994 ± 0.011	—	—
$P^{\mathrm{SciBar}}_{\mathrm{2trk/1trk}}$	$\mathbf{1.054 \pm 0.026}$	1.062 ± 0.028	—	—
$P^{\mathrm{SciBar}}_{\mathrm{nonQE/QE}}$	$\mathbf{1.109 \pm 0.039}$	1.075 ± 0.048	—	—
$P^{\mathrm{SciFi}}_{\mathrm{Norm}}$	$\mathbf{0.965 \pm 0.017}$	—	0.975 ± 0.023	—
$P^{\mathrm{SciFi}}_{\mathrm{2nd\text{-}eff}}$	$\mathbf{0.959 \pm 0.013}$	—	0.962 ± 0.014	—
$P^{\mathrm{SciFi}}_{\mathrm{rescat}}$	$\mathbf{0.907 \pm 0.056}$	—	0.917 ± 0.057	—
$P^{\mathrm{1KT}}_{\mathrm{Norm}}$	$\mathbf{0.968 \pm 0.015}$	—	—	0.974 ± 0.023
χ^2_{total}/d.o.f.	**667.1 / 606**	265.1 / 244	315.8 / 279	84.7 / 81
Goodness [%]	**4.3**	16.8	6.4	36.7
$\chi^2_{\mathrm{SciBar}}/N_{\mathrm{bins}}$	**266.2 / 248**	265.1 / 248	—	—
$\chi^2_{\mathrm{SciFi}}/N_{\mathrm{bins}}$	**316.0 / 283**	—	315.8 / 283	—
$\chi^2_{\mathrm{1KT}}/N_{\mathrm{bins}}$	**83.5 / 80**	—	—	83.4 / 80
$\chi^2_{\mathrm{PIMON}}/N_{\mathrm{bins}}$	**1.3 / 3**	—	—	1.3 / 3

Table 8.13: Results from the re-fitting without any low-q^2 suppression.

Parameter	**Merged**	SciBar only	SciFi only	1KT only
R_{nQE}	$\mathbf{0.883 \pm 0.027}$	0.981 ± 0.065	0.922 ± 0.040	0.757 ± 0.045
$P^{\mathrm{SciBar}}_{\mathrm{Norm}}$	$\mathbf{0.994 \pm 0.011}$	0.994 ± 0.011	—	—
$P^{\mathrm{SciBar}}_{\mathrm{2trk/1trk}}$	$\mathbf{1.049 \pm 0.026}$	1.062 ± 0.028	—	—
$P^{\mathrm{SciBar}}_{\mathrm{nonQE/QE}}$	$\mathbf{1.148 \pm 0.040}$	1.094 ± 0.049	—	—
$P^{\mathrm{SciFi}}_{\mathrm{Norm}}$	$\mathbf{1.057 \pm 0.018}$	—	1.035 ± 0.024	—
$P^{\mathrm{SciFi}}_{\mathrm{2nd\text{-}eff}}$	$\mathbf{0.977 \pm 0.013}$	—	0.970 ± 0.014	—
$P^{\mathrm{SciFi}}_{\mathrm{rescat}}$	$\mathbf{0.986 \pm 0.053}$	—	0.967 ± 0.055	—
$P^{\mathrm{1KT}}_{\mathrm{Norm}}$	$\mathbf{1.031 \pm 0.015}$	—	—	1.089 ± 0.024
χ^2_{total}/d.o.f.	**758.3 / 606**	297.3 / 244	353.8 / 279	96.5 / 81
Goodness [%]	**0.0023**	1.1	0.16	11.5
$\chi^2_{\mathrm{SciBar}}/N_{\mathrm{bins}}$	**299.9 / 248**	297.3 / 248	—	—
$\chi^2_{\mathrm{SciFi}}/N_{\mathrm{bins}}$	**354.8 / 283**	—	353.8 / 283	—
$\chi^2_{\mathrm{1KT}}/N_{\mathrm{bins}}$	**102.3 / 80**	—	—	95.2 / 80
$\chi^2_{\mathrm{PIMON}}/N_{\mathrm{bins}}$	**1.3 / 3**	—	—	1.3 / 3

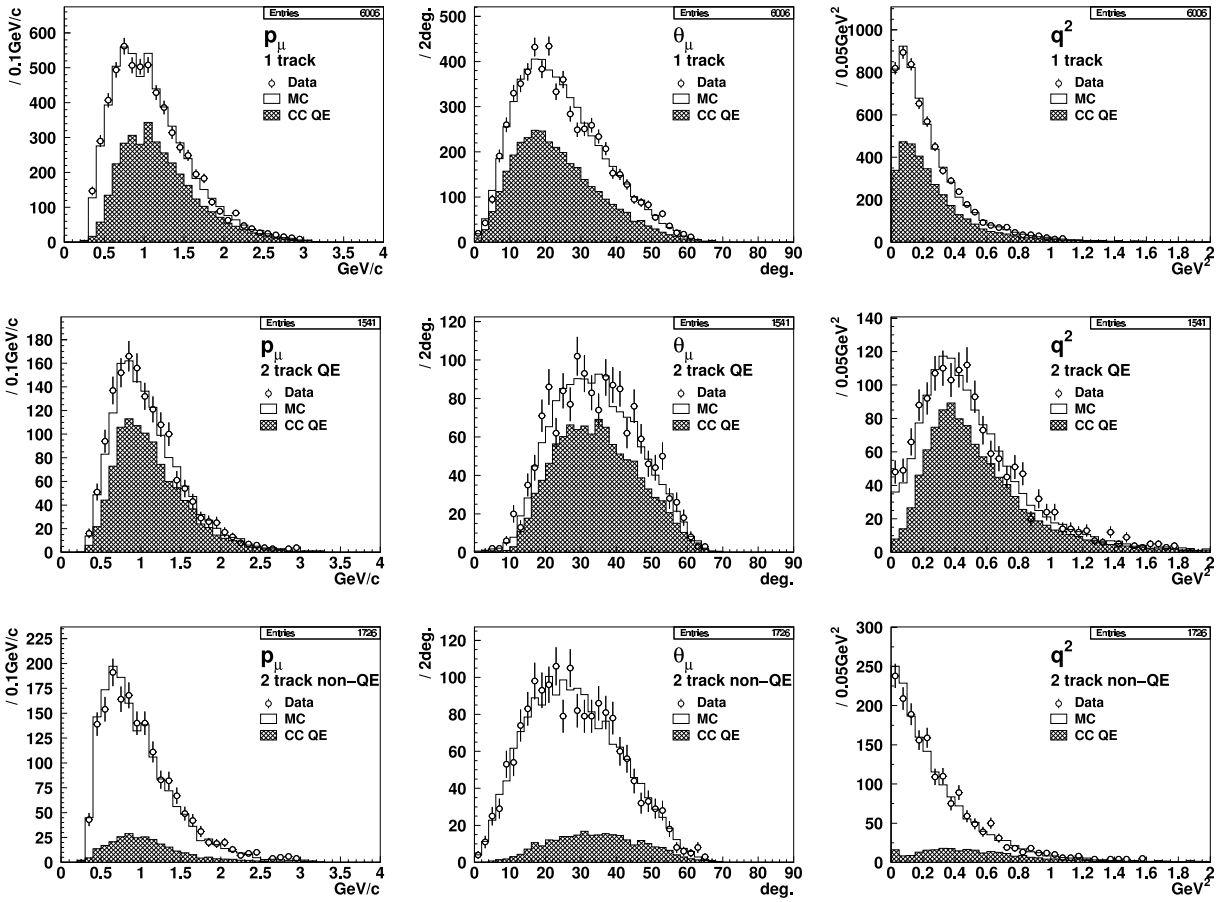

Figure 8.32: SciBar p_μ, θ_μ, and q^2 distributions for each event category at the best fit point with the suppression of CC resonance production mode. Open circles are data with their statistical error, and solid lines are the best fit histograms. CC-QE components are shown by hatched areas.

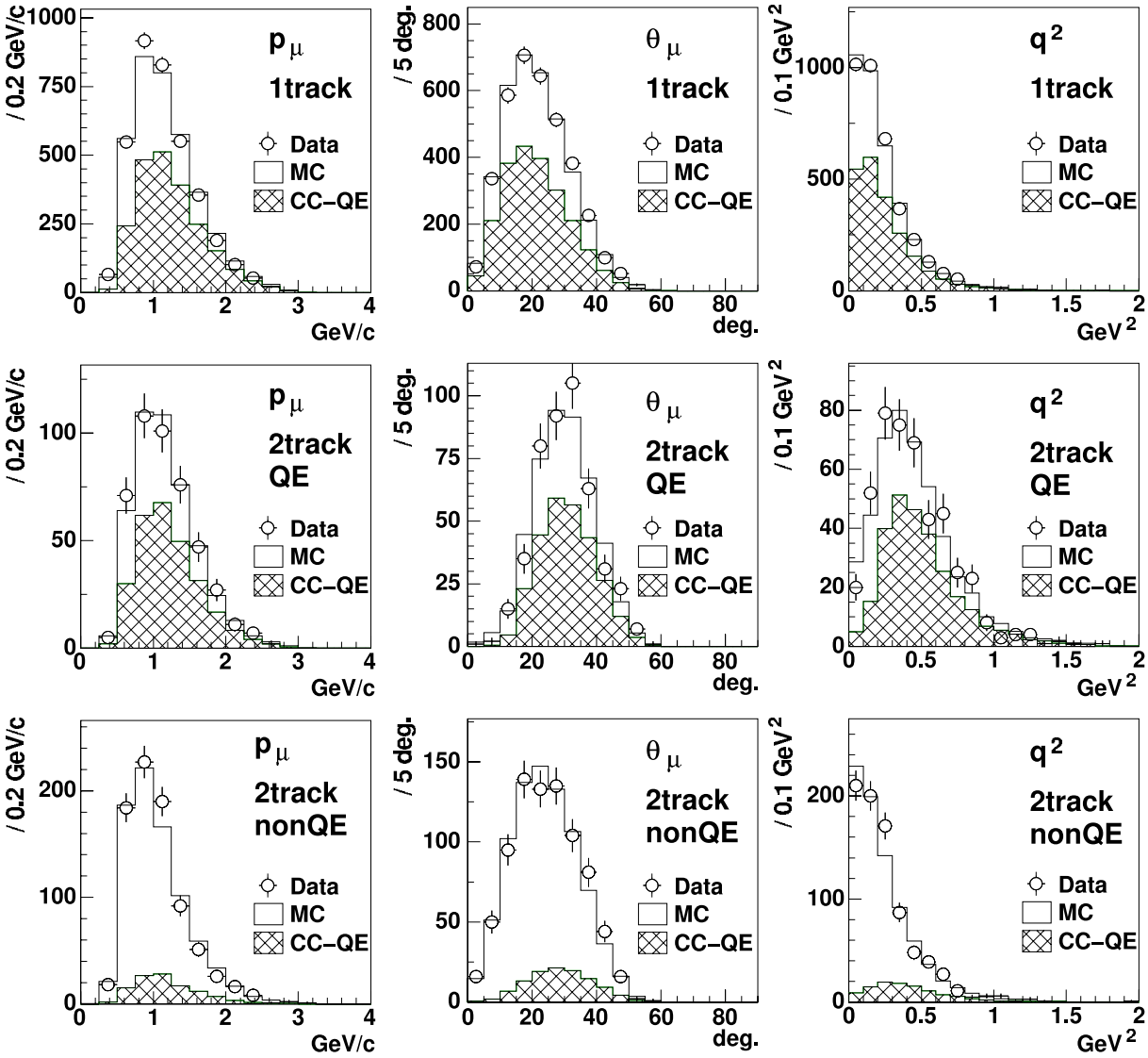

Figure 8.33: SciFi p_μ, θ_μ, and q^2 distributions for each event category at the best fit point with the suppression of CC resonance production mode. Only K2K-IIa data is shown.

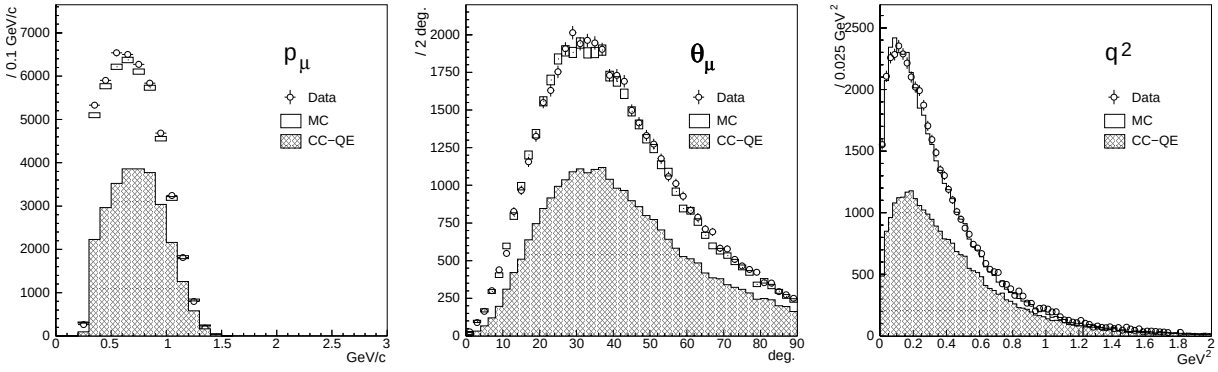

Figure 8.34: 1KT p_μ, θ_μ, and q^2 distributions of the 1Rμ sample at the best fit point with the suppression of CC resonance production mode.

Table 8.14: Best fit values, errors and error matrix from the fit with the suppression of the CC resonance mode.

	f_1^ϕ 0.0–0.5 GeV	f_2^ϕ 0.5–0.75 GeV	f_3^ϕ 0.75–1.0 GeV	f_4^ϕ 1.0–1.5 GeV	f_5^ϕ 1.5–2.0 GeV	f_6^ϕ 2.0–2.5 GeV	f_7^ϕ 2.5–3.0 GeV	f_8^ϕ 3.0 GeV –	R_{nQE}
Best fit	0.784	1.012	1.119	$\equiv 1$	0.901	1.069	1.334	1.041	1.020
Error	0.366	0.098	0.067	—	0.044	0.065	0.171	0.179	0.109
f_1^ϕ	1.34×10^{-1}	3.14×10^{-3}	4.62×10^{-3}	—	-1.34×10^{-3}	-7.37×10^{-4}	-2.33×10^{-3}	5.76×10^{-4}	-1.02×10^{-2}
f_2^ϕ	3.14×10^{-3}	9.60×10^{-3}	4.89×10^{-4}	—	-1.02×10^{-4}	-5.66×10^{-4}	-2.62×10^{-5}	2.78×10^{-4}	-6.11×10^{-3}
f_3^ϕ	4.62×10^{-3}	4.89×10^{-4}	4.49×10^{-3}	—	1.21×10^{-3}	9.91×10^{-6}	1.44×10^{-3}	3.41×10^{-4}	-2.00×10^{-3}
f_4^ϕ	—	—	—	—	—	—	—	—	—
f_5^ϕ	-1.34×10^{-3}	-1.02×10^{-4}	1.21×10^{-3}	—	1.98×10^{-3}	-5.55×10^{-4}	2.88×10^{-3}	6.01×10^{-4}	1.17×10^{-4}
f_6^ϕ	-7.37×10^{-4}	-5.66×10^{-4}	9.91×10^{-6}	—	-5.55×10^{-4}	4.21×10^{-3}	-5.29×10^{-3}	3.01×10^{-3}	1.18×10^{-3}
f_7^ϕ	-2.33×10^{-3}	-2.62×10^{-5}	1.44×10^{-3}	—	2.88×10^{-3}	-5.29×10^{-3}	2.92×10^{-2}	-1.33×10^{-2}	-6.22×10^{-4}
f_8^ϕ	5.76×10^{-4}	2.78×10^{-4}	3.41×10^{-4}	—	6.01×10^{-4}	3.01×10^{-3}	-1.33×10^{-2}	3.21×10^{-2}	-7.37×10^{-4}
R_{nQE}	-1.02×10^{-2}	-6.11×10^{-3}	-2.00×10^{-3}	—	-1.17×10^{-4}	1.18×10^{-3}	-6.22×10^{-4}	-7.37×10^{-4}	1.20×10^{-2}

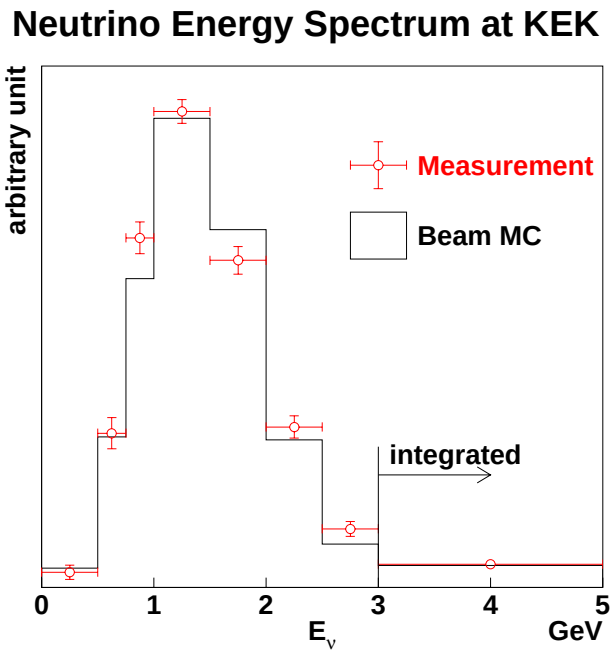

Figure 8.35: The fitted E_ν spectrum at the near site. Crosses are the best fit results and the solid line is the baseline MC simulation.

Chapter 9

Number of Events in Near Detector

We measure the number of events at the near site, $N_{\rm ND}^{\rm obs}$, to estimate the expected number of events in SK. We use the 1KT detector to obtain $N_{\rm ND}^{\rm obs}$. Therefore, we denote $N_{\rm ND}^{\rm obs}$ by $N_{\rm 1KT}^{\rm obs}$ hereafter. We first describe the outline of the event selection. We present the basic distributions, and evaluate several quantities to obtain $N_{\rm 1KT}^{\rm obs}$. Finally, we estimate systematic errors of $N_{\rm 1KT}^{\rm obs}$.

9.1 Outline

9.1.1 Suitable detector for event rate measurement

We discuss what detector is the most suitable for the measurement of the neutrino event rate. Since the detection technique of 1KT is same as SK, the response to each interaction channel is very similar. Therefore, most of the systematic errors on neutrino interactions for SK and 1KT are canceled out each other, when we compute the expected number of SK events. On the other hand, NC interactions are hardly observed by SciFi, while SK and 1KT have finite efficiency in NC. The SciFi prediction accordingly has the error on the NC cross-section. For SciBar, the neutrino interaction target is $(CH)_n$, whereas that of SK is H_2O. Therefore, the neutrino-nucleus cross-section is slightly different. In addition, if SciBar attempts to select NC interactions, the contamination of sky-shine neutrons etc. are the source of the systematic error. Although sky-shine neutrons also strike 1KT, these backgrounds is negligible because the fiducial volume is sufficiently shielded by water. For those reasons, we employ only 1KT data to measure the number of events in the near detector.

9.1.2 Event rate measurement

The event selection criteria of 1KT is already described in Section 8.4.1. In contrast to the measurement of the neutrino energy spectrum, we use all the events reconstructed in the fiducial volume to obtain an inclusive event rate. In other words, we do not impose the cut on the number of rings nor the particle identification.

We derive the formula to evaluate the number of events in the fiducial volume of 1KT ($N_{\rm 1KT}^{\rm obs}$). In the early stage of the event selection, the number of FADC peaks is required to be one, because of the following two reasons:

- 1KT often observes two or more detector activities within a beam spill, called "multiple events". The fraction of spills with multiple events is approximately 10%.
- 1KT cannot separate two events within a beam spill.

Therefore, we count the number of total FADC peaks ($N_{\rm peak}^{\rm total}$) and the number of single-peak events ($N_{\rm peak}^{1}$), and we obtain $N_{\rm 1KT}^{\rm obs}$ by multiplying the ratio between $N_{\rm peak}^{\rm total}$ and $N_{\rm peak}^{1}$ to the

number of selected events ($N^{\rm sel}_{\rm 1KT}$):

$$N^{\rm obs}_{\rm 1KT} = N^{\rm sel}_{\rm 1KT} \cdot \frac{N^{\rm total}_{\rm peak}}{N^{1}_{\rm peak}} \cdot C_{\rm multi} \cdot \frac{1}{1+R_{\rm BG}} \ (\cdot C_{7\to 9}), \tag{9.1}$$

where the definitions of $C_{\rm multi}$, $R_{\rm BG}$, and $C_{7\to 9}$ are:

- $C_{\rm multi}$: The correction factor to the ratio $N^{\rm total}_{\rm peak}/N^{1}_{\rm peak}$, since multiple events are sometimes misidentified as the smaller number of events due to the overlapping of FADC peaks.
- $R_{\rm BG}$: The fraction of backgrounds.
- $C_{7\to 9}$: The scaling factor for missing bunches in May and June 2000. In this period, eighth and ninth bunches were not recorded by the FADC, due to the disorder of the timing generator for the FADC.

Each factor in Equation (9.1) is evaluated in Section 9.3.

9.2 Basic distributions

Figure 9.1 shows the vertex distributions of 1KT events. We select the events within the fiducial volume defined as $R < 2$ m and $-2 < Z < 0$ m, where R is the distance from the beam axis and Z is the position along the beam direction originating at the tank center. The definition of the fiducial volume is illustrated in Figure 8.14.

Figure 9.2 shows the neutrino detection efficiency as a function of E_ν since January 2000. The efficiency is defined as the ratio of the number of reconstructed events to the number of generated events in the fiducial volume by using the MC simulation. The lower edge of the efficiency curve is owing to the FADC threshold. The overall efficiency is obtained to be 71% for 1999 data[1] and 75% for the others.

Figure 9.3 shows the stability of the event rate. The event rate is defined as the number of events normalized by the muon yield measured by MUMON-SSD. If Figure 9.3 is projected onto the vertical axis, the distribution has the standard deviation of 1.6%. The stability of the neutrino flux is also confirmed by MRD with the standard deviation of 1.4%.

9.3 Correction factors

9.3.1 Multi-event correction

The multi-event correction factor, $C_{\rm multi}$, is evaluated by the MC simulation. Multiple events in a spill are generated by the simulation, and the behavior of the FADC is reproduced. By comparing the number of peaks with the number of generated events, $C_{\rm multi}$ is estimated to be 1.008.

9.3.2 Background estimation

Possible background sources are cosmic rays and neutrino induced muons coming from outside. For only 1999 data, there were some reflection of PMT signals at the electronics. Therefore, we also estimate fake events due to them.

[1] In November 1999, one fourth of the cables to the FADC were not connected by mistake. For this reason, the efficiency is lost by a few %.

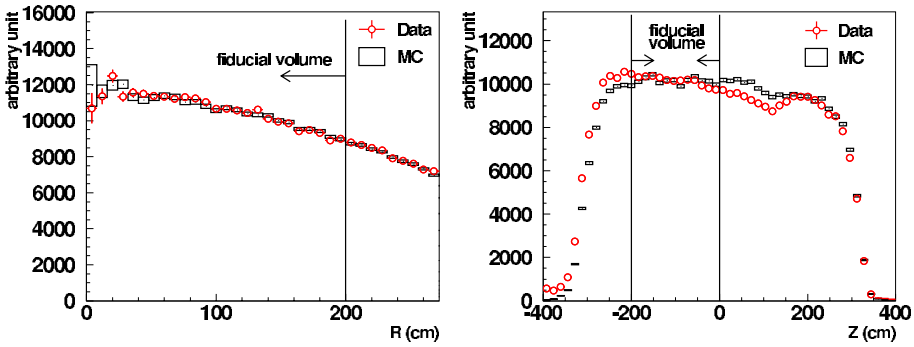

Figure 9.1: The vertex distributions of 1KT. The horizontal axis of the left figure is R, and that of the right one is Z. The target mass for each bin is corrected. The slope in the R distribution comes from the beam profile.

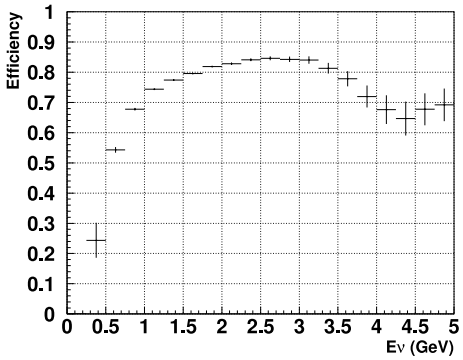

Figure 9.2: The neutrino detection efficiency of 1KT as a function of E_ν.

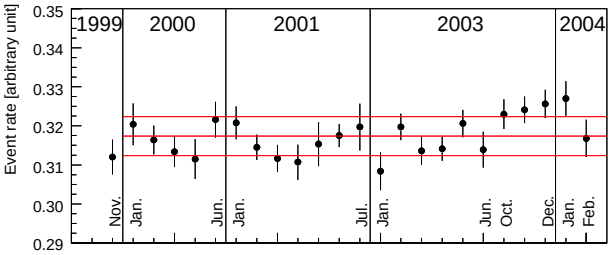

Figure 9.3: The event rate stability of 1KT. The horizontal axis shows month. The event rate is normalized by MUMON-SSD signal (muon yield). The interval between red lines corresponds to 1.6%, which is the standard deviation of the event rate.

Cosmic rays

The contamination of cosmic rays is estimated by the randomly triggered data. The neutrino event selection criteria is applied to this data, and the fraction of the contamination is obtained to be 1.0% in the fiducial volume.

Neutrino induced muons

Neutrino induced muons are produced in the materials around 1KT. Some of them enter 1KT and satisfy the event selection criteria. Since most of the incoming muons penetrates the outer detector (OD), OD hits are visually inspected by physicists. As a result, the contamination of neutrino induced muons is estimated to be 0.5%.

Reflection of PMT signal

In 1999 data, there exist fake events due to the reflection of PMT pulse at the electronics. The fraction of these events are estimated to be 2.6%. Since buffer amplifiers were installed to the electronics after the 1999 run, fake events have disappeared since then.

9.3.3 Scaling factor from 7 to 9 bunches

In May and June 2000, eighth and ninth bunches were sometimes lost because of the unstableness of the timing generator for the FADC. Therefore, we use the first to seventh bunches for the analysis in this period. The number of events are scaled by the correction factor $C_{7\to 9}$, which is estimated from the spills recorded properly.

9.3.4 Summary

The results of the $N_{1\mathrm{KT}}^{\mathrm{obs}}$ measurement and the input values to the $N_{1\mathrm{KT}}^{\mathrm{obs}}$ calculation are listed in Table 9.1. Since the diameter of the target and the horn current in June 1999 is different, the event rate is smaller than the other periods.

9.4 Systematic errors

The systematic errors on the 1KT event rate are summarized in Table 9.2. The total systematic error is approximately 5%. It is dominated by the uncertainty of the fiducial volume. Each systematic error source is described below.

Fiducial volume

The performance of the vertex fitter has been studied using cosmic ray muons[90]. The reconstructed vertex is found to be biased by 10 cm. This bias changes $N_{1\mathrm{KT}}^{\mathrm{obs}}$ by 3.2%.

If the center position of the fiducial volume is varied by ± 50 cm, the number of events changes by 2%. If the radius of the fiducial volume is increased by 20 cm or 40 cm, the number of events per unit mass varies by 1%.

These errors are quadratically summed, and the systematic error on the fiducial volume is obtained to be 4.0%.

Energy scale

The uncertainty in the energy scale of 1KT is $+3\%$ -2%. It affects the threshold of the FADC peak (1000 photo-electrons). The systematic error from this effect is estimated to be $\pm 0.3\%$.

Table 9.1: The summary of the number of events in 1KT. A right arrow means that the value is same as the left column.

Period	Jun.'99	Nov.'99	Jan.–Mar.'00	May.–Jun.'00
Run	K2K-Ia	K2K-Ib	→	→
Target diameter	2 cm	3 cm	→	→
Horn current	200kA	250kA	→	→
$\mathrm{POT}_{\mathrm{1KT}}$ [$\times 10^{18}$]	2.60	2.62	8.90	5.59
# total peaks ($N^{\mathrm{total}}_{\mathrm{peak}}$)	109119	118321	417841	203133
# single peaks (N^{1}_{peak})	89782	96304	331021	170115
Backgrounds (R_{BG})	0.031	→	0.015	→
Multi-event corr. (C_{multi})	1.008	→	→	→
7-to-9-bunch corr. ($C_{7\to 9}$)	—	—	—	1.283
# selected events ($N^{\mathrm{sel}}_{\mathrm{1KT}}$)	4282	4923	17136	8672
# observed events ($N^{\mathrm{obs}}_{\mathrm{1KT}}$)	5088	5914	21481	13194
Event rate [/10^{15} POT]	1.96	2.26	2.41	2.36

Period	Jan.–Jul.'01	Jan.–Jul.'03	Oct.'03–Feb.'04
Run	K2K-Ib	K2K-IIa	K2K-IIb
Target diameter	3 cm	→	→
Horn current	250kA	→	→
$\mathrm{POT}_{\mathrm{1KT}}$ [$\times 10^{18}$]	23.22	21.62	17.15
# total peaks ($N^{\mathrm{total}}_{\mathrm{peak}}$)	1095658	1031754	795046
# single peaks (N^{1}_{peak})	876113	814085	634066
Backgrounds (R_{BG})	0.015	→	→
Multi-event corr. (C_{multi})	1.008	→	→
7-to-9-bunch corr. ($C_{7\to 9}$)	—	—	—
# selected events ($N^{\mathrm{sel}}_{\mathrm{1KT}}$)	45579	43462	34271
# observed events ($N^{\mathrm{obs}}_{\mathrm{1KT}}$)	56608	54703	42676
Event rate [/10^{15} POT]	2.44	2.53	2.49

FADC fluctuation

The long term fluctuation of the FADC pulse height is measured to be approximately 10%. This fluctuation changes $N^{\mathrm{obs}}_{\mathrm{1KT}}$ by 0.8%. It is assigned as the systematic error.

FADC threshold dependence

The FADC peak counting efficiency with various FADC threshold setting from 200 to 1800 photo-electrons are evaluated. Since the efficiency deviates by 1.5%, it is quoted as the systematic error.

Background

The statistical errors on the measurement of the background rate are 1.0% for 1999 runs and 0.5% for the others. Therefore, these numbers are quoted as the systematic error.

Multi-event correction

We assign the statistical error on C_{multi} as the systematic error on $N^{\mathrm{obs}}_{\mathrm{1KT}}$.

Table 9.2: The summary of the systematic errors on the number of interactions in 1KT. The right arrow means that the value is same as the left column.

Period	Jun.'99	Nov.'99	Jan.–Mar.'00	May.–Jun.'00
Run	K2K-Ia	K2K-Ib	→	→
Fiducial volume	4.0%	→	→	→
Energy scale	0.3%	→	→	→
FADC fluctuation	1.0%	1.4%	0.8%	→
FADC threshold	1.5%	→	→	→
Background rate	1.0%	→	0.5%	→
Multi-event corr.	0.7%	→	→	→
Stability	1.6%	→	→	→
Beam profile	0.3%	→	→	→
7-to-9-bunch corr.	—	—	—	1.2%
Total	4.8%	4.9%	4.7%	4.9%

Period	Jan.–Jul.'01	Jan.–Jul.'03	Oct.'03–Feb.'04
Run	K2K-Ib	K2K-IIa	K2K-IIb
Fiducial volume	4.0%	→	→
Energy scale	0.3%	→	→
FADC fluctuation	0.8%	→	→
FADC threshold	1.5%	→	→
Background rate	0.5%	→	→
Multi-event corr.	0.7%	→	→
Stability	1.6%	→	→
Beam profile	0.3%	→	→
7-to-9-bunch corr.	—	—	—
Total	4.7%	4.7%	4.7%

Stability

Since the stability of $N_{\mathrm{1KT}}^{\mathrm{obs}}$ is 1.6%, we quote it as the systematic error.

Beam profile

Figure 9.4 shows the beam profile measured by 1KT[2]. The Y profile has a discrepancy between the data and the MC simulation, while the X profile shows a good agreement. The difference of the Y profile center is approximately 20 cm. If we shift the fiducial volume by 20 cm, the number of events changes by 0.3%. Therefore, we use this number as the systematic error.

Correction from seven to nine bunches

The correction factor, $C_{7\to 9}$, for the data taken in May and June 2000 has the statistical uncertainty of 1.0%. If this correction is applied to another period, the event rate differs by 0.4%. In addition, the requirement of $N_{\mathrm{peak}} = 1$ is affected, if eighth and ninth bunches are missing. Therefore, we masked eighth and ninth bunches of the FADC data for another period, and the

[2]For the profile measurement, we use another fiducial volume, which is the 6m-high and 6m-diameter cylindrical volume orienting the same way as the 1KT tank, and the effective target mass for each bin is corrected.

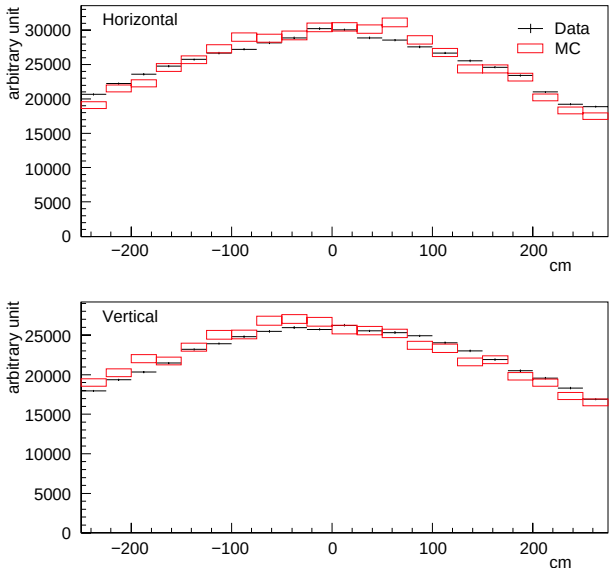

Figure 9.4: Beam profile measured by 1KT. The upper figure shows horizontal profile, the lower one shows vertical profile. Crosses are the data and boxes are the MC simulation.

effect is estimated to be 0.6%. We assign the systematic error on $C_{7\to 9}$ as the quadratic sum of these uncertainties (1.2%).

Chapter 10

Extrapolation of Neutrino Flux from ND to SK

Since the neutrino flux does not follow L^{-2} law at the near site due to the long decay volume, we evaluate the ratio of the neutrino flux between Super-Kamiokande (SK) and the near site (ND), $R_{F/N}(E_\nu)$. It is utilized to the following two purposes:

- Extrapolate the energy spectrum from ND to SK.
- Estimate the expected number of SK events from the number of observed events in 1KT.

In the following sections, we give an overview of the $R_{F/N}(E_\nu)$ analysis, describe the PIMON measurement, and evaluate the systematic error of $R_{F/N}(E_\nu)$.

10.1 Overview

The Far/Near flux ratio, $R_{F/N}(E_\nu)$, is calculated with a (p_π, θ_π) two-dimensional distribution for parent pions, because of their simple two-body decay kinematics. Here, p_π is the pion momentum, and θ_π is the pion angle with respect to the beam. The pion monitor (PIMON)[21] (Section 3.2.5) measured the distribution of pions above 2 GeV/c, which corresponds to the neutrino energy (E_ν) above 1 GeV. Using the PIMON data, we confirm that the beam MC simulation is valid. We use the verified MC simulation for the central values of $R_{F/N}(E_\nu)$, and we employ the error of the PIMON measurement for the systematic error of $R_{F/N}(E_\nu)$ above 1 GeV. The systematic errors below 1 GeV are estimated from the uncertainty in the pion production model etc.

10.2 PIMON measurement

The PIMON measurements have ever been performed twice, in June 1999 and November 1999, because the horn configuration was different between them. The former was done with the single-bunch operation of 7×10^{10} protons per pulse (ppp), while the latter was done with the nine-bunch operation of 7×10^{11} ppp. In the both cases, the proton intensity is lower than the normal run ($\sim 6\times10^{12}$ ppp), because the Cherenkov light is too intense to keep the response linearity of the PMTs. In June 1999, the PMT saturation existed, but it was not in November 1999 by adjusting the PMT gain. The configuration of PIMON is summarized in Table 10.1.

We took data with nine sets of refractive indices (n). To obtain a finer Cherenkov image, we shifted the PMT array by a half PMT interval in each index and took data. Additional data with the mirror directed off from the PMT array (mirror-off data) were taken in order to

Table 10.1: Summary of the configuration of the PIMON measurements.

	Jun. 1999	Nov. 1999
Target diameter	2cm	3cm
Horn current	200kA	250kA
Beam intensity	7×10^{10}	7×10^{11}
Number of bunches	1	9
Refractive index	9 points	9 points
PMT gain	300	20 or 50
PMT saturation	exist	none

subtract background. The background coming from a electro-magnetic shower is estimated from the MC simulation which is tuned by the data of the lowest refractive index. Figure 10.1 shows the Cherenkov light distribution for each refractive index after the background subtraction in November 1999 data.

We obtain the (p_π, θ_π) two-dimensional (2D) distribution by applying a χ^2 fitting method to Cherenkov light distributions (Figure 10.1). The 2D distribution is binned into 5×10: five bins in p_π above 2 GeV/c with 1 GeV/c step ($p_\pi > 6$ GeV/c is integrated), and ten bins in θ_π from -50 mrad to 50 mrad with 10 mrad step. The free parameters of the fit are contents of each bin in the 2D distribution. The fit result for the November-1999 run is shown in Figure 10.2.

From the obtained (p_π, θ_π) distribution, the E_ν spectra for both ND and Super-Kamiokande (SK) are evaluated by using the MC simulation. $R_{F/N}(E_\nu)$ is then calculated by taking the ratio between the spectra of ND and SK. The results are shown in Figure 10.3. The systematic errors on the PIMON measurement are included in the error bars of the figure. The MC simulation, based on the Cho-CERN pion production model, is consistent with the PIMON measurement. Therefore, we use this model to estimate the central value of $R_{F/N}(E_\nu)$. For the errors of $R_{F/N}(E_\nu)$ above 1 GeV, we employ the PIMON result.

The major sources of the uncertainties in the Far/Near ratio are estimated as follows:

Low intensity during the PIMON measurement :
The effect from the beam profile difference due to the lower beam intensity than the normal run.

Wavelength dependence of the refractive index :
The difference of the MC simulation between with and without the wavelength dependence of the refractive index.

Beam stability :
The effect from the fluctuation of the proton beam center during the PIMON run.

Radial asymmetry of the horn magnetic field :
The uncertainty in the non-uniformity of the horn current.

Fitting method :
The difference between the pion production models for the MC simulations used in the fit.

In the oscillation analysis, these errors are taken into account including the correlation between E_ν bins. The detail descriptions of the systematic errors are found in [21, 22].

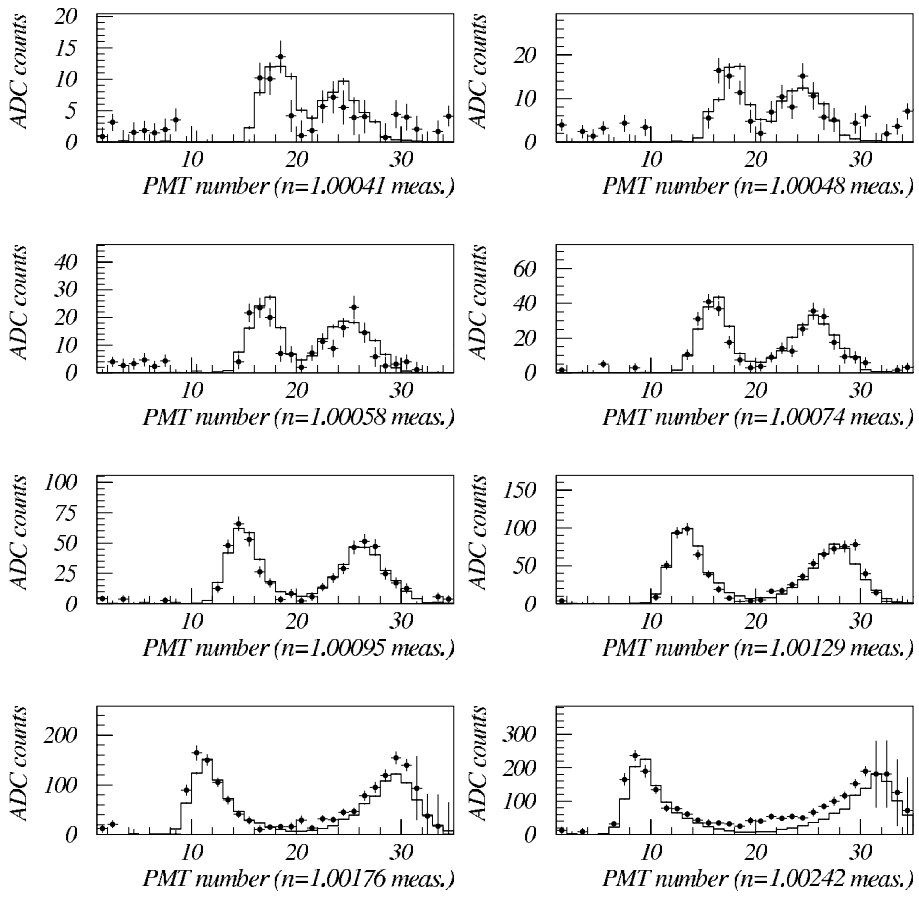

Figure 10.1: Cherenkov light distribution of PIMON for each refractive index. Dots are data and histograms are the MC simulation.

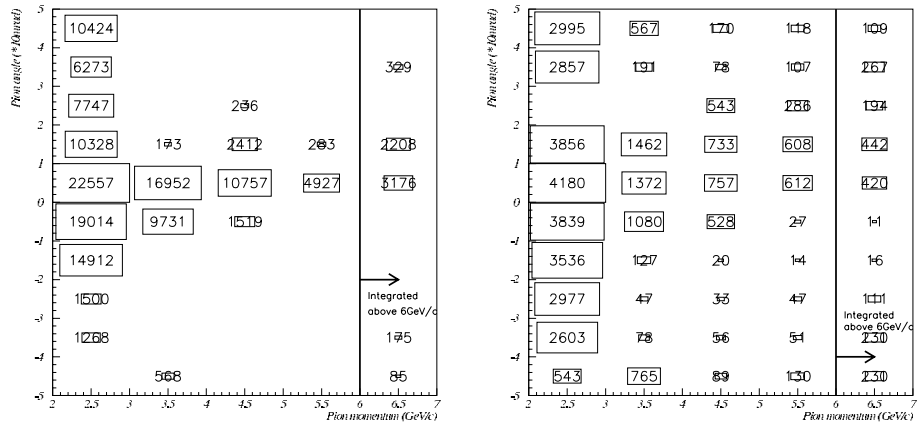

Figure 10.2: The fit result of (p_π, θ_π) distribution for November 1999 run. The left figure shows the bin content of each bin, and right figure shows the fitting error.

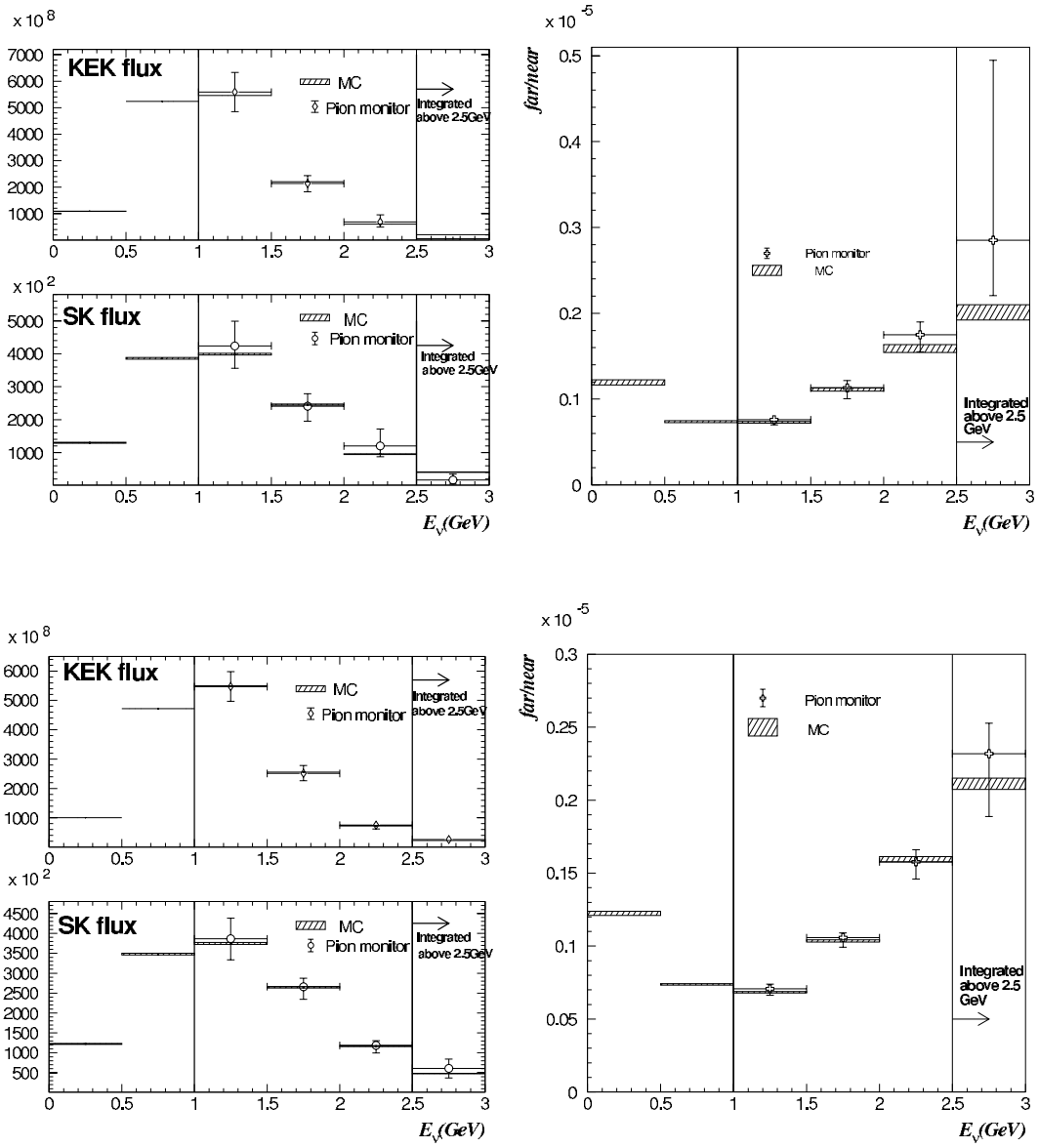

Figure 10.3: Energy spectra and Far/Near flux ratio measured by PIMON. The upper half figures are the results for the June-1999 run, and the lower are those for the November-1999 run. The E_ν spectra at near and far sites are shown in the left figures, and the Far/Near ratios are shown in the right. Crosses are the PIMON results, and hatched boxes are the MC simulation.

Table 10.2: Error matrix of the Far/Near ratio since November 1999. Each value in the row, "Error", is the square root of the diagonal element.

E_ν [GeV]	0.0–0.5	0.5–1.0	1.0–1.5	1.5–2.0	2.0–2.5	2.5–
Error	0.026	0.043	0.065	0.104	0.111	0.122
0.0–0.5	6.6×10^{-4}	-2.7×10^{-4}	0	0	0	0
0.5–1.0	-2.7×10^{-4}	1.8×10^{-3}	0	0	0	0
1.0–2.5	0	0	4.3×10^{-3}	5.7×10^{-4}	-3.2×10^{-4}	-1.6×10^{-3}
1.5–2.0	0	0	5.7×10^{-4}	1.1×10^{-2}	9.1×10^{-3}	2.5×10^{-3}
2.0–2.5	0	0	-3.2×10^{-4}	9.1×10^{-3}	1.2×10^{-2}	5.2×10^{-3}
2.5–	0	0	-1.6×10^{-3}	2.5×10^{-3}	5.2×10^{-3}	1.5×10^{-2}

10.3 Error matrix of the Far/Near ratio

The error matrix of the Far/Near ratio for $E_\nu > 1$ GeV is obtained from the PIMON measurement. Since PIMON is insensitive to the neutrino energy below 1 GeV, the error matrix in this region is separately estimated with another method.

10.3.1 Error matrix below 1 GeV

Errors on $R_{F/N}(E_\nu)$ below 1 GeV are estimated from four sources: the uncertainty in Sanford-Wang fitting, the difference of the target of past measurements, kaon contributions, and the uncertainty in the primary proton beam profile. The error matrix for $E_\nu < 1$ GeV is the sum of the contributions from these error sources. The detail of the calculation is described in [22].

10.3.2 Full error matrix

The error matrices from the PIMON result ($E_\nu > 1$ GeV) and the above method ($E_\nu < 1$ GeV) are combined without any correlation between them. The full error matrix is shown in Table 10.2. This is used for the oscillation analysis.

Chapter 11

Far Detector Analysis

We describe the event selection of Super-Kamiokande (SK). It is based on two techniques. One is the timing synchronization with the accelerator, and the other is the atmospheric neutrino event selection[11]. We select the events that are fully-contained (FC) in the inner detector (ID) of SK. In addition, their vertices are required to be inside a certain fiducial volume. Figure 11.1 shows a typical event display of SK. We measure the number of observed events ($N_{\rm SK}^{\rm obs}$) and the reconstructed neutrino energy ($E_\nu^{\rm rec}$) of single-ring μ-like (1Rμ) events, where $E_\nu^{\rm rec}$ is defined by Equation (2.2).

In Section 11.1, we describe each selection step and the basic performance of SK. Since the number of ID PMTs for SK-II is about a half of that for SK-I, we confirm whether the performance of SK-II is comparable to SK-I. We evaluate the systematic errors on $N_{\rm SK}^{\rm obs}$ and the 1Rμ event selection in Section 11.2.

11.1 Event selection

11.1.1 Outline

To synchronize an SK event with a neutrino beam spill, we use the UTC[1] time stamps of both the beginning of beam spills ($T_{\rm KEK}$) and SK events ($T_{\rm SK}$) recorded by GPS systems. We define the time difference between $T_{\rm KEK}$ and $T_{\rm SK}$ as

$$\Delta T \equiv T_{\rm SK} - T_{\rm KEK} - TOF, \tag{11.1}$$

where TOF is the time-of-flight of neutrinos from KEK to SK ($\simeq 833$ μsec). K2K events satisfy $0.0 \lesssim \Delta T \lesssim 1.1$ μsec, which is the duration of the beam spill. Since the duty cycle of the beam is $1.1[\mu{\rm sec}]/2.2[{\rm sec}] = 0.5\times10^{-6}$, the timing information reduces background events by six orders of magnitude.

In the meanwhile, we select fully-contained events reconstructed in the fiducial volume (FCFV) corresponding to 22.5 ktons, by using an analysis algorithm similar to the atmospheric neutrino study[11]. The outline of the analysis is summarized as background rejection, event reconstruction, and FCFV selection.

Possible background sources are listed below:

- Cosmic ray muons coming from outside.
- Decay-electrons from stopping cosmic rays in ID.
- Low energy gamma rays ($\lesssim 10$ MeV) from radon in the water or surrounding rock.

[1] Universal Time Coordinated.

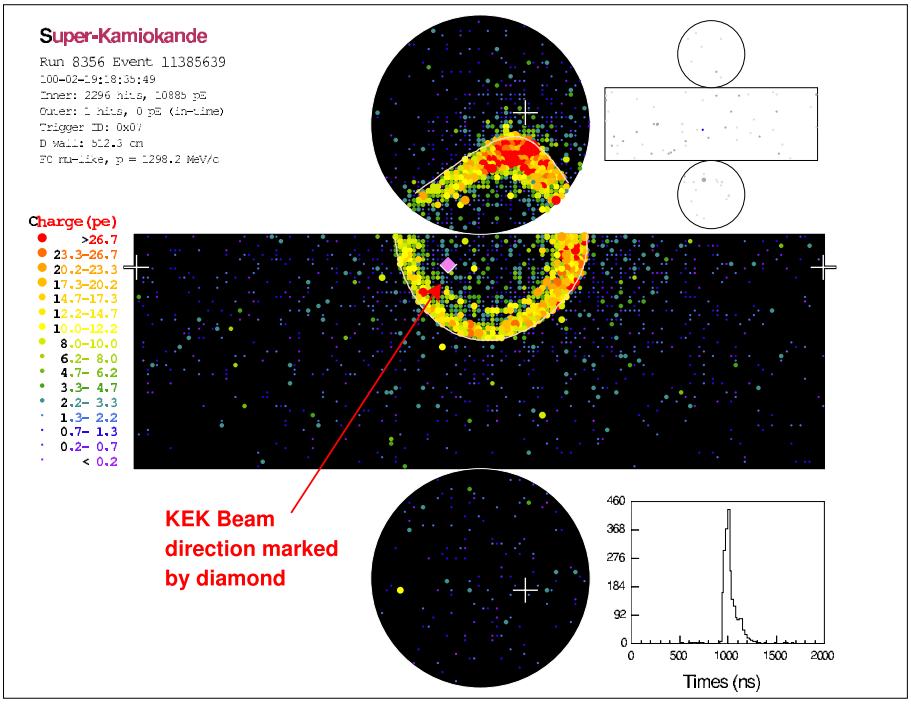

Figure 11.1: A typical event display of SK.

- Flashing PMT events due to electric discharges of dynodes.
- Atmospheric neutrino events.

Almost all of them except for atmospheric neutrinos are excluded by the FCFV event selection.

The event reconstruction method is almost same as 1KT. The reconstruction algorithm consists of vertex fitting, ring counting, and particle identification. The performance of the reconstruction is described in Section 11.1.3.

11.1.2 Each reduction step

The detail of each event selection step is described. Since the number of ID PMTs for SK-II is about a half of that for SK-I, some of the selection criteria are different between SK-I and SK-II.

Good beam spill

The condition of the beamline data and the GPS system are inspected, as described in Section 7.2.

Rough timing cut

We select the events with $|\Delta T| < 500$ μsec. This time window is thousand times larger than the duration of the beam spill.

High energy trigger

Event taken by the high energy (HE) trigger are used. The trigger threshold is 31 (16) hit PMTs within 200 nsec time window corresponding to 50–100 (20–50) photo-electrons for SK-I (SK-II).

Decay-electron cut

Cosmic ray muons stopping inside the tank usually produce electrons through their decays (life time ~ 2 μsec). Since these electrons are often identified as neutrino events, we remove events if there are any detector activities within 30 μsec before them. Not more than 1/1000 of the events are lost at this step.

Total photo-electron cut

To reject low energy backgrounds such as gamma rays from radon or surrounding rock, more than 200 (94) photo-electrons for SK-I (SK-II) are required to be observed within 300 nsec time window (Figure 11.2). This threshold corresponds to about 20 MeV/c for electrons and about 190 MeV/c for muons.

Flashing PMT cut

There are some flashing PMTs due to sparks inside the PMTs. Since a flashing-PMT event often looks like a neutrino event, we require the following criteria to remove it.

1. **Maximum photo-electron cut** :
   Since the signal from a sparking PMT is very large, $PE_{\rm max}/PE_{300} \leq 0.2$ (0.4) are required for SK-I (SK-II). Here, $PE_{\rm max}$ is the maximum number of photo-electrons among the PMTs, and PE_{300} is the number of total photo-electrons within 300 nsec time window.

2. **Timing distribution cut** :
   Most of the flushing events make relatively broad hit timing distributions. We search for the minimum number of hits within 100 nsec sliding time window ($N^{\rm min}_{\rm 100ns}$) from the range between 300 nsec and 800 nsec after the trigger. We select the events with $N^{\rm min}_{\rm 100ns} < 15$ (20) for SK-I (SK-II). If the number of ID hits is less than 800, events with $N^{\rm min}_{\rm 100ns} > 10$ are rejected.

3. **Goodness of fit** :
   If the number of ID hits is less than 500 (250) for SK-I (SK-II), we use the goodness of fit from a vertex fitter. The goodness is required to be more than or equal to 0.4.

Outer detector cut

Cosmic rays coming from outside are removed by outer detector (OD) information. The number of hits in the largest OD cluster is required to be less than 10 hits, as shown in Figure 11.3. In addition, if the number of hits within 800 nsec time window is greater than 50, the event is rejected. These requirements effectively select FC events. Since the PMT density of OD is unchanged, the cut threshold for SK-II is same as that for SK-I.

Visible energy cut

Since the total photo-electron cut is ambiguous about energy, we remove the events with $E_{\rm vis} < 30$ MeV, as shown in Figure 11.4. Here, $E_{\rm vis}$ means visible energy which is the sum of electron-equivalent energy for each ring. The conversion factors from PMT charge to $E_{\rm vis}$ are separately prepared for SK-I and SK-II. The threshold of $E_{\rm vis}$ (30 MeV) corresponds to the muon momentum of 197 MeV/c.

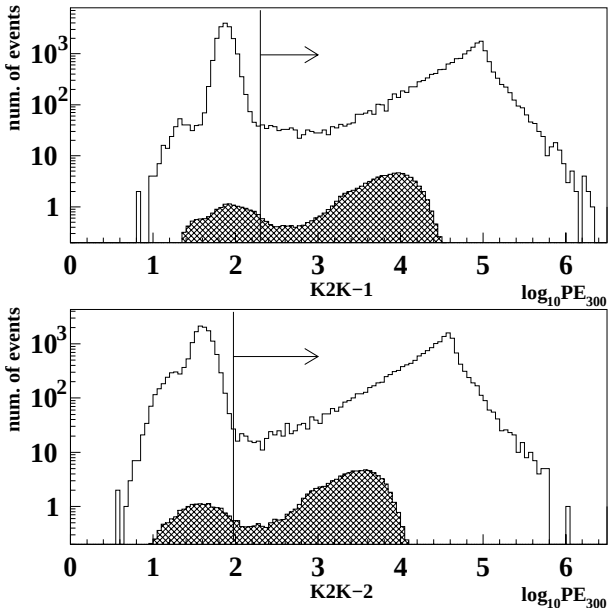

Figure 11.2: The total number of photo-electrons within 300 nsec time window for SK-I (top) and SK-II (bottom). The horizontal axis is the logarithm of the number of photo-electrons. Solid lines show data, and hatched areas show the neutrino MC simulation. The lower limit of this value is also illustrated.

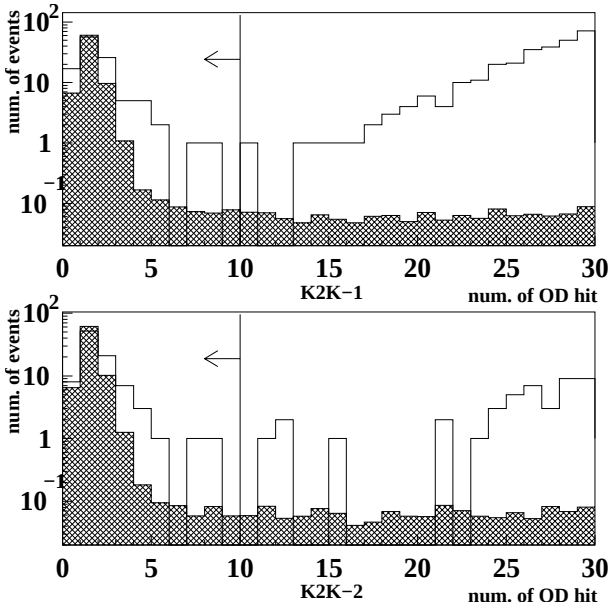

Figure 11.3: The number of hits in the largest cluster of OD for SK-I (top) and SK-II (bottom). Solid lines show data, and hatched areas show the MC simulation. This value is required to be less than 10. The rejected part of data is mainly composed of cosmic rays. The long tail of the MC simulation is due to outgoing muons from ID.

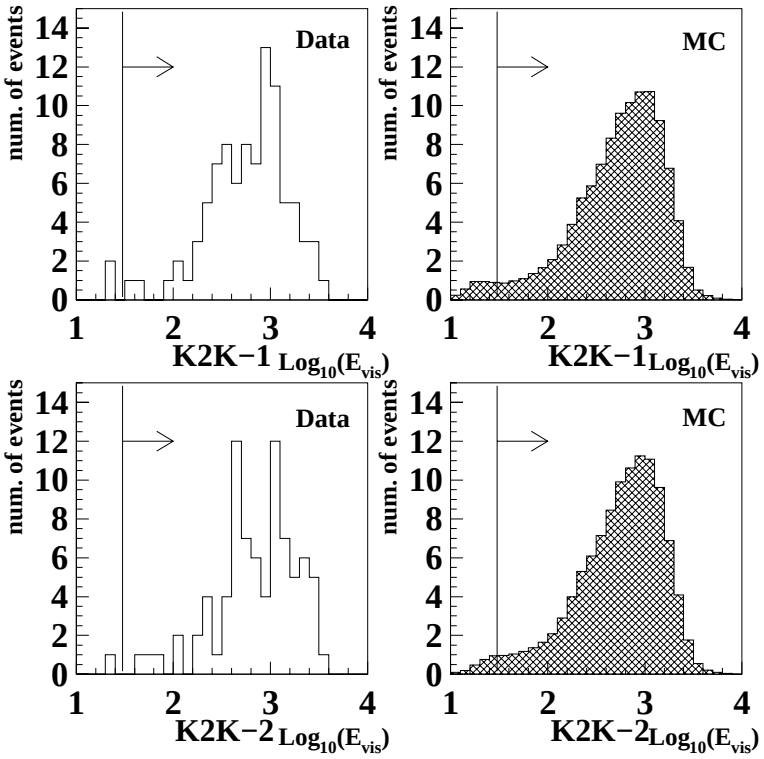

Figure 11.4: $E_{\rm vis}$ distributions for SK-I (top) and SK-II (bottom). The horizontal axes show $\log_{10} E_{\rm vis}$[MeV]. The selected areas ($E_{\rm vis} > 30$ MeV) are also illustrated.

Scanning

The selected events are visually scanned to make sure whether the selected events are really neutrino events. Although a few flashing-PMT events remain here, they are removed by scanning.

Fine timing cut

To select the events synchronized properly with the accelerator, we impose the timing cut: $-0.2 < \Delta T < 1.3$ μsec. Since the uncertainty of the UTC time stamp is less than 0.2 μsec, the time window has 0.2 μsec margins before and after the beam.

Fiducial volume cut

The reconstructed vertex is required to be within the fiducial volume defined as $D_{\rm wall} \geq 2.0$ m, where $D_{\rm wall}$ is the distance from the vertex to the nearest surface of ID. It corresponds to water mass of 22.5 ktons. Figure 11.5 shows a schematic drawing of the fiducial volume, and Figure 11.6 shows $D_{\rm wall}$ distributions.

11.1.3 Event reconstruction

The event reconstruction procedure is almost same as 1KT. We introduce the outline of the procedure, and confirm that the performance of both SK-I and SK-II are appropriate for the oscillation analysis. Each reconstruction process is itemized below:

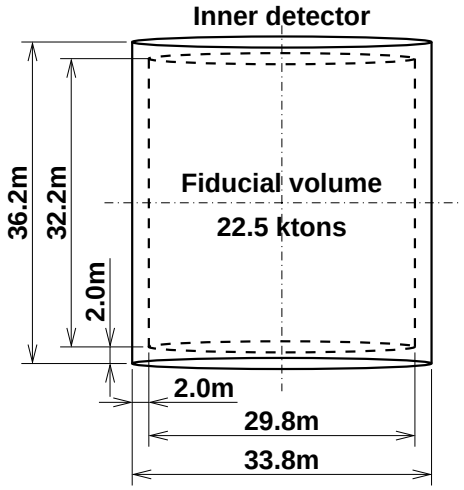

Figure 11.5: A schematic drawing of the fiducial volume of SK.

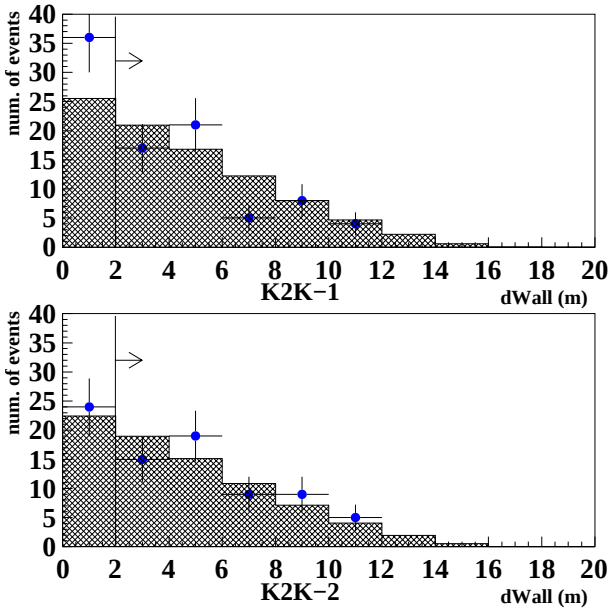

Figure 11.6: D_{wall} distributions of SK-I (top) and SK-II (bottom). Dots with error bars show data, and hatched areas are the MC simulation. The requirement for D_{wall} (> 2.0 m) is also shown.

Auto-Fit

Using the charge information from each PMT, the direction and the outer edge of the most energetic ring are obtained, and the vertex is determined by the timing information. If the Auto-fit of SK-I with a simple extension of PMT density is applied to SK-II, the performance is not sufficient. Therefore, the edge finding method for SK-II is improved. Figure 11.7(left) shows the vertex resolution of Auto-fit for each particle type. The same performance is obtained for electrons, and the performance of SK-II for muons is better than that of SK-I in spite of the less PMT density. The vertex resolution is less than 1 m for both SK-I and SK-II.

Ring counting

This process searches for the other rings by using the charge pattern, and counts the number of rings ($N_{\rm ring}$). Single-ring events are separated from multi-ring events by a ring counting estimator ($\mathcal{F}$). If there is another ring, $\mathcal{F}$ takes a positive value. This algorithm is simply extended to SK-II. The condition of a single-ring event is $\mathcal{F} < 0$. Figure 11.8 shows the comparison of $\mathcal{F}$ distributions between SK-I and SK-II using the MC simulation. Single-ring events are sufficiently separated from multi-ring events. Although the peaks of SK-II are slightly closer to zero, the separation power remains almost unchanged.

Particle identification (PID)

The reconstructed rings are divided into two particle types, μ-like and e-like, by using the ring image and the opening angle. The same process is applied to SK-II. Figure 11.9 shows the mis-ID probability of each particle type estimated by the MC simulation. The mis-ID probability is a few % level, which is sufficient for the charged-current event selection. The performance of SK-II is comparable to that of SK-I.

MS-fit for single-ring event

MS-fit is a more precise fitter than Auto-fit, which is applied to only single-ring events. It uses the PID information in addition to the charge and the timing. The same algorithm is utilized for SK-II. Figure 11.7(right) shows the vertex resolution of MS-fit for each particle type, and Figure 11.10 shows the resolution of momentum and angle. Only a small deterioration is seen in the vertex and angular resolution of SK-II. However, SK-II suffers a decline of the momentum resolution from the reduction of the PMT density, because the momentum is almost linear to the total charge. Nevertheless, the momentum resolution of SK-II is several % level. Consequently, the momentum and angular resolution of both SK-I and SK-II are satisfactory to observe the E_ν spectrum distortion.

11.1.4 Basic distributions

The number of selected events for each category is summarized in Table 11.1. The MC expectation, which is evaluated in the next chapter, is also listed. The number of total observed events are 107, while the expectation in the null oscillation case is 150.9. The number of 1Rμ events is 57. The interpretation of the results is discussed in the next chapter.

The event selection efficiency as a function of E_ν is shown in Figure 11.11. Here, the efficiency is defined as the ratio of FCFV events to generated events within the fiducial volume using the MC simulation. The efficiency curves are almost same between K2K-I and K2K-II. The overall efficiency for K2K-I and K2K-II are 77.1% and 78.2%, respectively. Regardless of the reduction of PMTs, the efficiency for K2K-II is higher than that for K2K-I. This is because the improvement

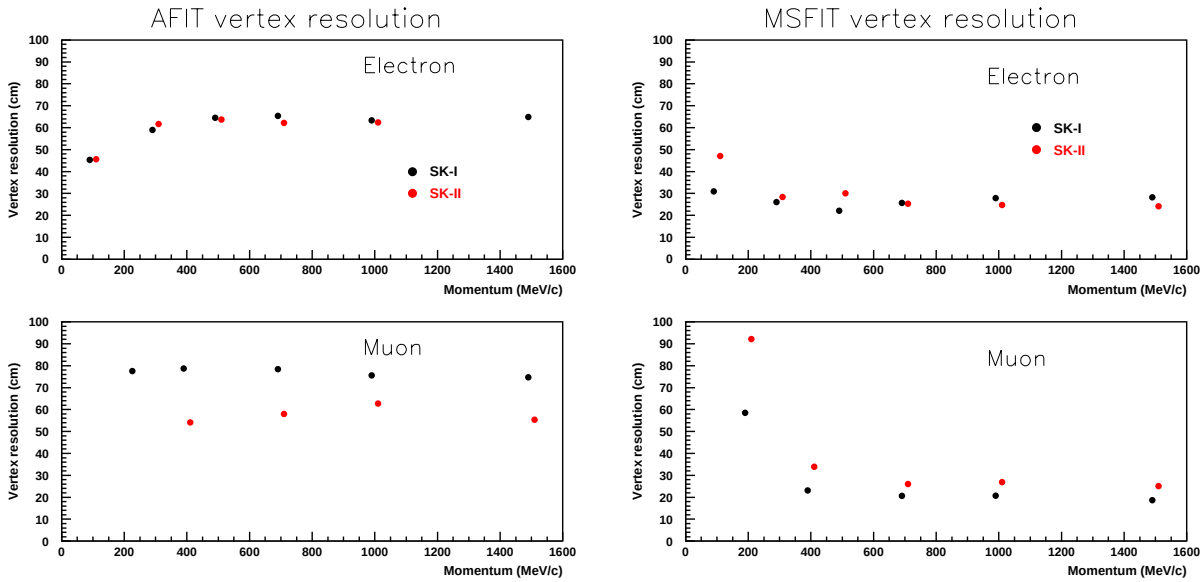

Figure 11.7: Vertex resolution of SK for Auto-fit (left) and MS-fit (right) as a function of momentum. Upper figures show the resolution for electrons, and lower figures show that for muons. SK-I (SK-II) is specified as black (red) points. A particle is generated by the MC simulation many times, and the 68% coverage of the distance between the true vertex and the reconstructed vertex is plotted.

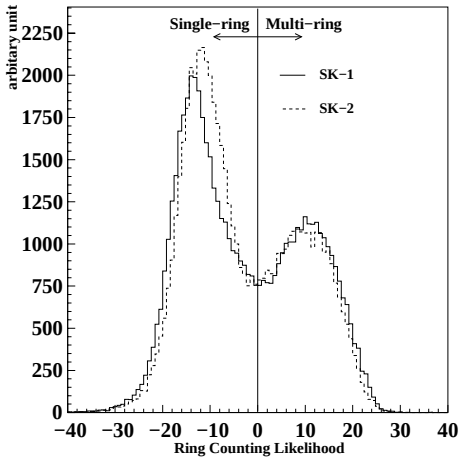

Figure 11.8: Comparison of the ring counting likelihood ($\mathcal{F}$) between SK-I and SK-II using the MC simulation. The solid line shows SK-I, and the dashed line shows SK-II. The definition of a single-ring event is $\mathcal{F} < 0$.

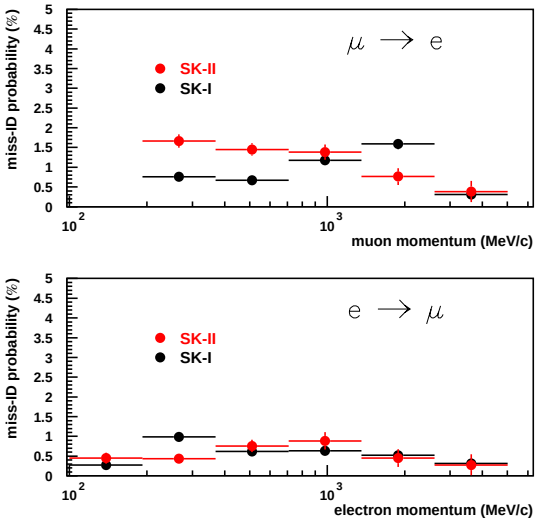

Figure 11.9: The mis-ID probability of particle type as a function of momentum. The horizontal axis is momentum in log scale. The upper figure shows the fraction of the events classified as muon-like while electrons are generated, and the lower one shows vice versa. Black points represent SK-I, and red ones represent SK-II.

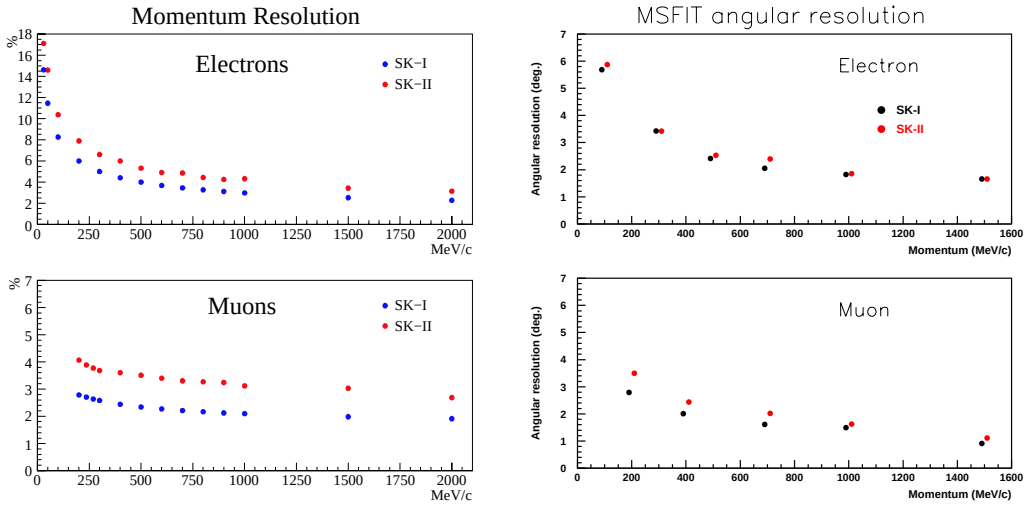

Figure 11.10: Momentum and angular resolution of MS-fit as a function of momentum. The left figures show the momentum resolution, and the right ones show the angular resolution. Blue or black circles show SK-I, and red ones show SK-II. A single particle is generated by the MC simulation many times, and the standard deviation of the reconstructed value from the true value is plotted.

Table 11.1: The number of events observed in SK.

	K2K-I		K2K-II		Total	
	Data	MC	Data	MC	Data	MC
Total	55	79.1	52	71.8	107	150.9
→ Single-ring	33	48.9	34	45.1	67	94.0
→ μ-like	30	44.9	27	40.5	57	85.4
→ e-like	3	4.0	7	4.5	10	8.6
→ Multi-ring	22	30.2	18	26.7	40	56.9

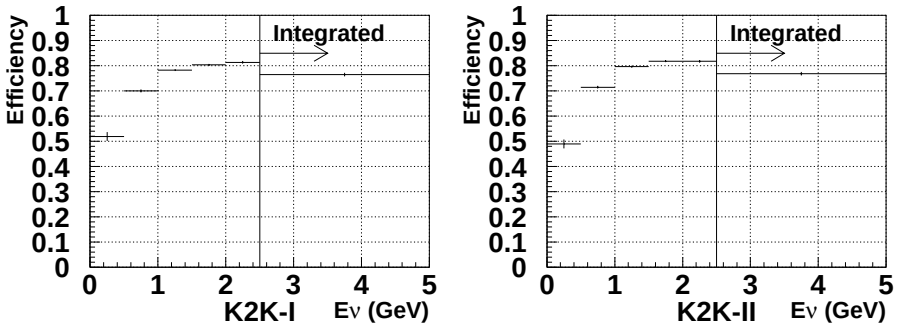

Figure 11.11: Event selection efficiency as a function of E_ν for K2K-I (left) and K2K-II (right).

of Auto-fit, and because the vertex shift effect toward the ID wall is slightly different due to the decrease of the PMT density.

Figure 11.12 shows ΔT distributions. K2K events cluster within the beam timing window. Figure 11.13 shows ΔT distribution with fine binning. The nine-bunch structure of the beam is seen. It indicates the sufficient precision of the GPS system. Figure 11.14 shows the vertex distributions. There are no clusters nor voids. Figure 11.15 shows the number of SK events as a function of the accumulated protons on target (POT). The Kolmogorov-Smirnov (KS) test[93] is performed between data and a proportional relation, and it shows the agreement with 78.6% probability.

Figure 11.16, 11.17, and 11.18 show p_μ, $\cos\theta_\mu$, and $E_\nu^{\rm rec}$ distributions, respectively, of 1Rμ sample, where p_μ is the muon momentum and θ_μ is the muon angle with respect to the beam. Although we do not discuss the difference between data and the MC simulation until the next chapter, $\cos\theta_\mu$ clusters around one as we expect. The KS test is applied to the observed $E_\nu^{\rm rec}$ distributions between K2K-I and K2K-II, and they are found to be consistent each other with the probability of 77%.

11.2 Systematic uncertainties

We evaluate the systematic errors on the energy scale, $N_{\rm SK}^{\rm obs}$, and the 1Rμ event selection.

11.2.1 Energy scale

Calibration sources

The energy range of the K2K neutrino events is widely spread from a few 10 MeV to a few GeV. To check the absolute energy scale in this range, four kinds of calibration sources are examined.

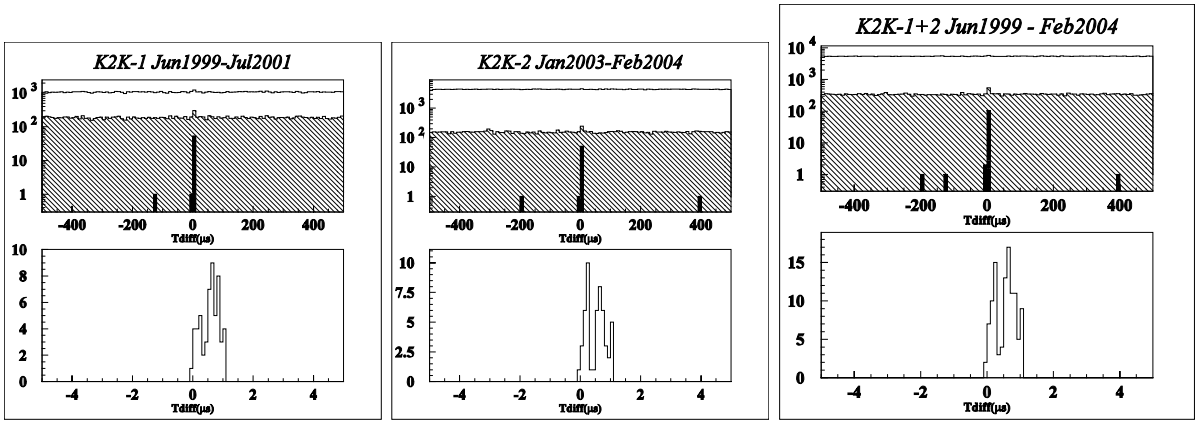

Figure 11.12: ΔT distributions for K2K-I (left), K2K-II (center), and K2K-I+II (right). Upper figures show the events in ± 500 μsec time window after the decay-electron cut (solid lines), after the flashing PMT cut (hatched regions), and after the fiducial volume cut (filled regions). Lower figures show the final samples with ± 5 μsec time window.

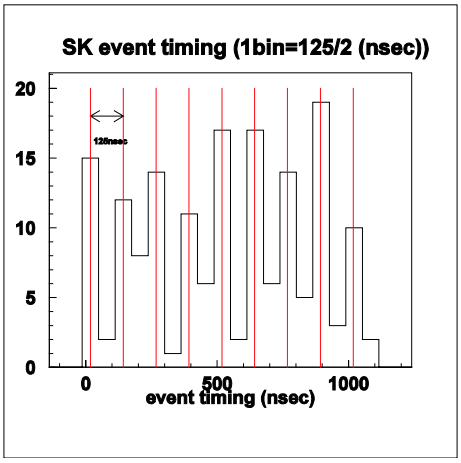

Figure 11.13: The ΔT distribution with fine binning. The nine-bunch structure of K2K beam is observed.

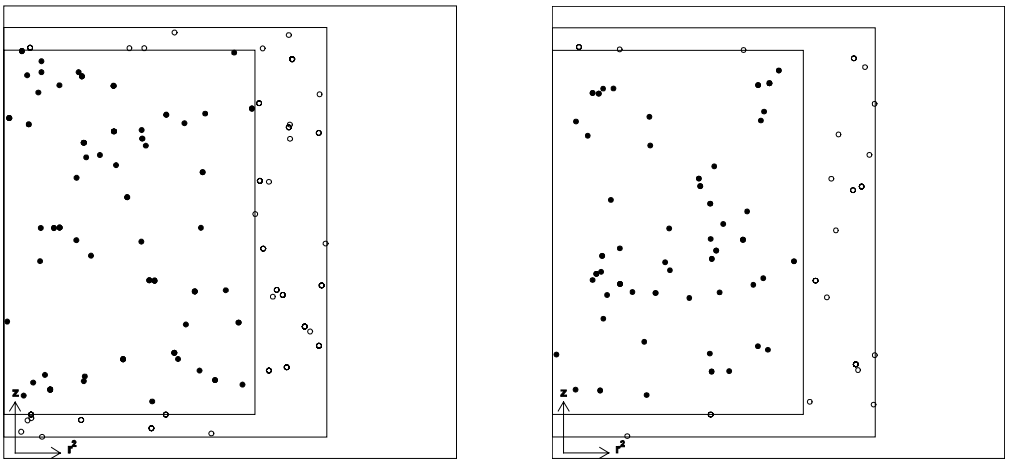

Figure 11.14: Vertex distributions of SK for K2K-I (left) and K2K-II (right). Closed circles are FCFV events and open circles are FC events out of the fiducial volume. The fiducial volume is shown by the smallest box. The horizontal axis shows r^2, and the vertical axis shows z. Here, r and z are positions in the cylindrical coordinates.

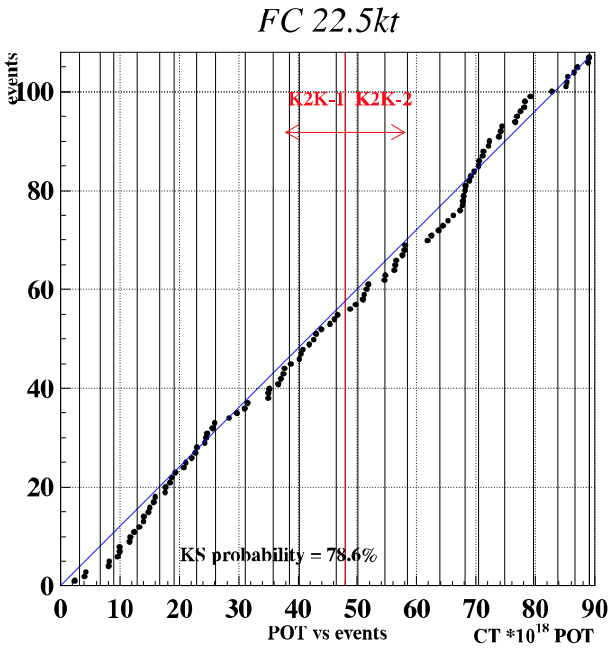

Figure 11.15: The number of SK events as a function of POT. Dots are data and the solid line is proportional to the average event rate. The KS probability that data obey the solid line is 78.6%.

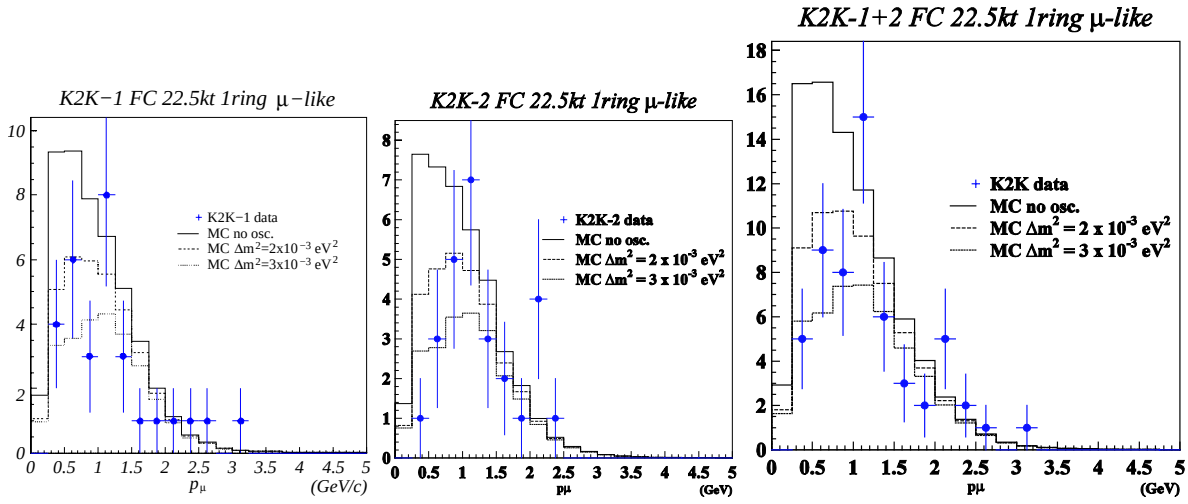

Figure 11.16: Muon momentum distributions of SK 1Rμ sample for K2K-I (left), K2K-II (center), and K2K-I+II (right). Closed circles with error bars are data, and solid lines show the MC expectation without the neutrino oscillation. Dashed (dotted) lines show the oscillated spectrum with $\Delta m^2 = 3\times10^{-3}$ (2×10^{-3}) eV^2 and $\sin^2 2\theta = 1$.

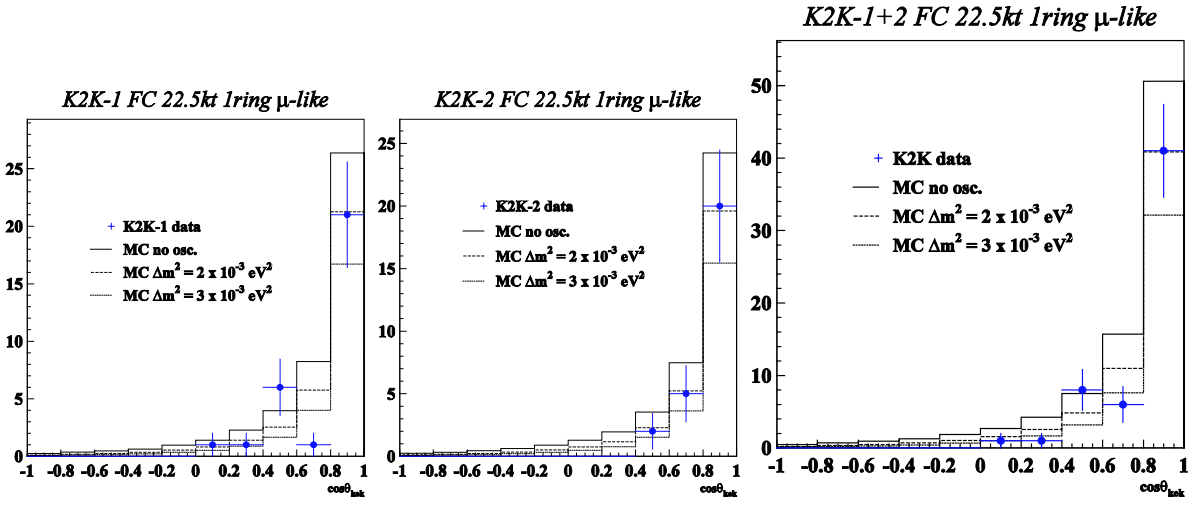

Figure 11.17: $\cos\theta_\mu$ distributions of SK 1Rμ sample. The legend is same as Figure 11.16.

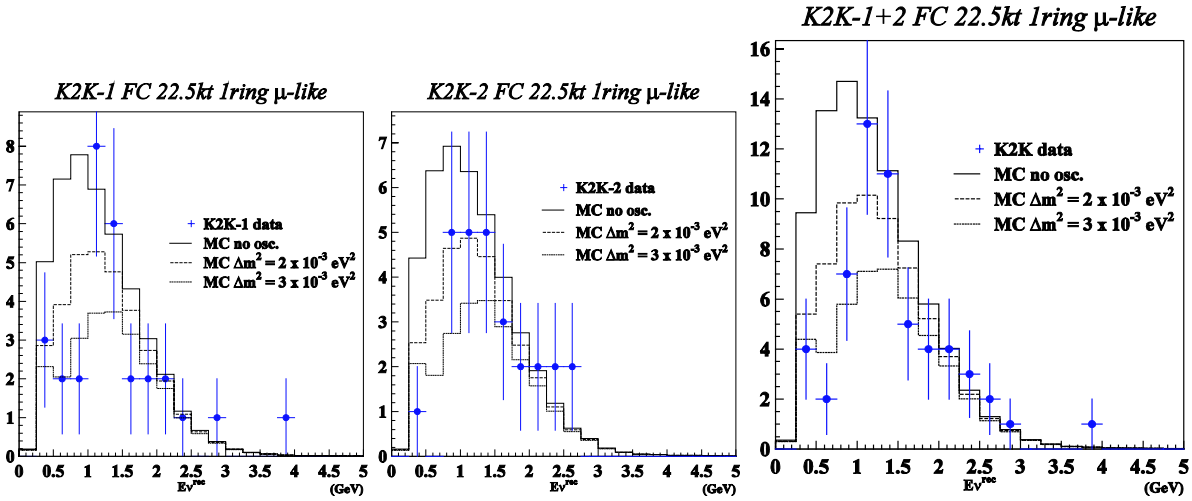

Figure 11.18: $E_\nu^{\rm rec}$ distributions of SK 1Rμ sample. The legend is same as Figure 11.16.

1. **Decay electron**
   For the energy region of a few tens of MeV, decay electrons from stopping cosmic rays are employed. The mean value of the energy spectrum of Michel electrons is compared with the MC simulation.

2. **π^0 mass**
   Invariant mass distribution of π^0 events produced by atmospheric neutrino interactions are used to check the energy scale around 135 MeV (π^0 mass). We check whether the invariant mass distribution of π^0 agrees with the MC simulation.

3. **Cherenkov angle of stopping muon**
   For cosmic ray muons less than 350 MeV/c, we estimate the muon momentum from the Cherenkov angle, and compare it with the momentum measured by the event reconstruction algorithm. The ratio of the reconstructed momenta between the two methods is compared between data and the MC expectation.

4. **Track length of stopping muon**
   For a stopping cosmic ray track longer than 7 m ($p_\mu > 1.7$ GeV/c), we calculate the ratio of the reconstructed momentum to the track length, and compare it with the MC simulation.

Figure 11.19 shows the summary of absolute energy scale for each of SK-I and SK-II. The difference between data and the MC simulation is within 1.8% (1.9%) for SK-I (SK-II).

Time variation

In addition to the above calibration sources, the time variation of the energy response is monitored. The RMS of the deviation is 0.9% for both SK-I and SK-II.

Summary

Finally, we take the quadratic sum of the difference from the MC simulation and the RMS of the time variation. The systematic errors on the absolute energy scale is quoted as 2.0% (2.1%) for SK-I (SK-II). These errors are summarized in Table 11.2.

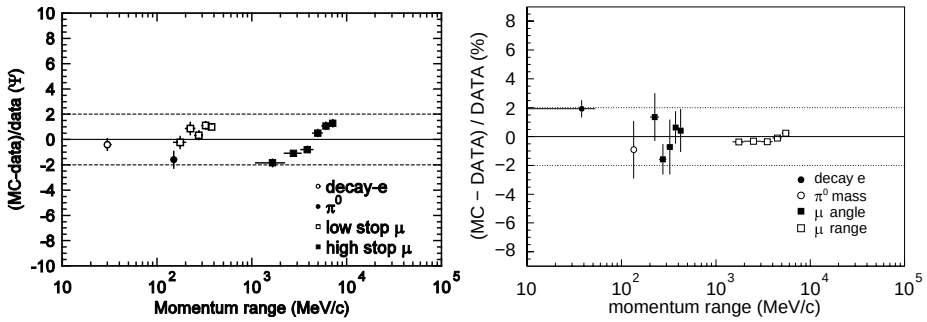

Figure 11.19: Measurements of the absolute energy scale of SK-I (left) and SK-II (right). The horizontal axis shows muon momentum in log scale, and the vertical axis represents fractional difference between data and the MC simulation in percent.

Table 11.2: The summary of the systematic errors on the absolute energy scale.

Source	Difference from MC	Time variation	Total
SK-I	1.8%	0.9%	2.0%
SK-II	1.9%	0.9%	2.1%

11.2.2 Uncertainties of the total number of events

We evaluate the uncertainties of the total number of events ($N_{\rm SK}$). Each error source is described below.

Fiducial volume cut

Since there are two vertex fitters, Auto-fit and MS-fit, the number of events in the fiducial volume is compared between the two. When they are applied to the 1Rμ sample of atmospheric neutrino data, the difference in data-to-MC ratio is 2%. Therefore, it is assigned as the systematic error.

OD cut

The number of hits in an OD cluster is compared with the MC simulation by using the partially-contained sample[2] of atmospheric neutrino data. The discrepancy between data and the MC simulation is 15% (30%) for SK-I (SK-II). If OD cut threshold is changed by 15% (30%), the number of events in the K2K MC simulation varies 0.2% (0.4%) for K2K-I (K2K-II). We quote it as the systematic error.

Energy scale

Since a lower limit is imposed on $E_{\rm vis}$, the threshold is shifted by the systematic error on the energy scale to evaluate the systematic error. As a result, the number of events in the MC simulation changes 0.1% for both K2K-I and K2K-II.

Ring counting

Since $E_{\rm vis}$ is the sum of the electron-equivalent energy in all reconstructed rings, the $E_{\rm vis}$ cut is affected by the ring counting process. Using atmospheric neutrino data around $E_{\rm vis} \simeq 30$ MeV,

[2]Events with outgoing muons from ID.

we estimate the difference of ring counting estimator ($\mathcal{F}$) between data and the MC simulation. If $\mathcal{F}$ of the K2K MC simulation is shifted by the difference of $\mathcal{F}$, $N_{\rm SK}$ changes 0.1% at most.

Decay-electron from an invisible muon

If a muon below the Cherenkov threshold is produced by the neutrino beam, its decay-electron may be detected as the neutrino interaction. The uncertainty in this kind of events is estimated to be 0.1% by using the MC simulation.

MC statistics

The statistical error of the MC simulation is 0.6% for both K2K-I and K2K-II. Therefore, we quote it as the systematic error.

Summary

The quadratic sum of the above errors is 2.4% for both runs. To be conservative, we assign 3% as the systematic uncertainty in $N_{\rm SK}$.

11.2.3 E_ν-dependent errors on the single-ring μ-like sample

To study a spectral distortion, reconstructed neutrino energy ($E_\nu^{\rm rec}$) of the 1Rμ sample is used. Therefore, we evaluate the systematic errors related to the E_ν shape. The neutrino energy is divided into six bins, and the systematic error of each bin is estimated, as listed in Table 11.3. The total error is quadratic sum of the error on each source described below.

Fiducial volume cut

As stated in the previous section, the systematic error on the fiducial volume cut is 2.0% (2.1%) for K2K-I (K2K-II). We put this error into each E_ν bin.

Ring counting

The ring counting estimator ($\mathcal{F}$) of atmospheric neutrino data is compared with the MC simulation in the energy range up to several GeV. The difference of the peak position between data and the MC simulation is regarded as the systematic error on $\mathcal{F}$, and the estimator $\mathcal{F}$ of the K2K MC simulation is shifted by this error. The deviation in each E_ν bin is calculated and quoted as the systematic error.

Particle identification

The systematic error on the separation into μ-like and e-like is estimated in a similar way to that on the ring counting. The difference of the particle identification likelihood between data and the MC simulation are obtained from an atmospheric neutrino sample. The effect of the difference is estimated from the K2K MC simulation, and regarded as a systematic error.

Pion contamination

A 1Rμ event induced by a charged pion is a systematic error source, since the particle identification likelihood of a charged pion is slightly different between data and the MC simulation. By using the atmospheric neutrino data, we select the lower energy ring of the event with two μ-like rings, because this ring is mainly created by a charged pion from the CC resonance production channel. We found that the particle identification likelihood of data is shifted by 8%

Table 11.3: The summary of the systematic errors on 1Rμ events of SK.

E_ν [GeV]		0.0–0.5	0.5–1.0	1.0–1.5	1.5–2.0	2.0–2.5	2.5–
K2K-I	Fiducial volume [%]	2.0	2.0	2.0	2.0	2.0	2.0
	Ring counting [%]	2.9	2.3	2.8	4.3	4.3	4.3
	Particle ID [%]	0.7	0.3	0.5	0.4	0.4	0.4
	$\pi^\pm$ contamination [%]	0.5	0.0	0.0	0.0	0.0	0.0
	Total [%]	3.7	3.0	3.4	4.9	4.9	4.9
K2K-II	Fiducial volume [%]	2.1	2.1	2.1	2.1	2.1	2.1
	Ring counting [%]	2.6	2.2	7.9	7.5	7.1	7.1
	Particle ID [%]	2.5	0.9	0.6	0.5	0.5	0.5
	$\pi^\pm$ contamination [%]	1.2	0.0	0.0	0.0	0.0	0.0
	Total [%]	4.5	3.2	8.2	7.8	7.4	7.4

from the MC simulation. When the particle identification estimator of the K2K MC simulation is shifted by 8%, the number of 1Rμ events of K2K-I (K2K-II) varies 0.5% (1.2%). Since most of the pion-induced rings are reconstructed as $E_\nu^{\rm rec} < 0.5$ GeV, we assign 0.5% (1.2%) to the systematic error on the $0.0 < E_\nu < 0.5$ GeV bin for K2K-I (K2K-II).

Chapter 12

Neutrino Oscillation Analysis

We compare SK data with the expectation from ND measurements and study muon neutrino oscillation by using a maximum likelihood method. Using the reconstructed energy ($E_\nu^{\rm rec}$) of the single-ring μ-like sample (1Rμ), we investigate the E_ν-dependence in the disappearance of muon neutrinos (ν_μ). In the meantime, by comparing the number of SK events ($N_{\rm SK}^{\rm obs}$) with the expectation from the 1KT measurement, the deficit of the total ν_μ flux is tested.

In this chapter, we define the likelihood for the neutrino oscillation analysis. We then maximize it, and obtain the best fit oscillation parameters. We evaluate the probability for the null oscillation hypothesis and the allowed region for the oscillation parameters by using the likelihood ratio method.

12.1 Definition of likelihood

We give an outline of the likelihood function in Section 12.1.1, and we describe the detail of each term in Section 12.1.2 – 12.1.4.

12.1.1 Outline

The likelihood function to be maximized is defined as

$$\mathcal{L}(\Delta m^2, \sin^2 2\theta, \boldsymbol{f}) \equiv \mathcal{L}_{\rm shape}(\Delta m^2, \sin^2 2\theta, \boldsymbol{f}) \times \mathcal{L}_{\rm norm}(\Delta m^2, \sin^2 2\theta, \boldsymbol{f}) \times \mathcal{L}_{\rm syst}(\boldsymbol{f}), \qquad (12.1)$$

where $\mathcal{L}_{\rm shape}$, $\mathcal{L}_{\rm norm}$, and $\mathcal{L}_{\rm syst}$ are likelihood functions for the spectrum shape, the number of events ($N_{\rm SK}$), and the constraint on the systematic parameters ($\boldsymbol{f}$), respectively. The parameter set $\boldsymbol{f}$ is introduced to represent the variations of physical quantities within their uncertainties. The oscillation parameters, Δm^2 and $\sin^2 2\theta$, are free parameters.

The summary of each term is itemized below.

$E_\nu^{\rm rec}$ shape term

The $E_\nu^{\rm rec}$ spectrum shape term, $\mathcal{L}_{\rm shape}$, is expressed as the product of the probability density at the $E_\nu^{\rm rec}$ for each 1Rμ event:

$$\mathcal{L}_{\rm shape} \equiv \prod_{i=1}^{N_{\rm K2K\text{-}Ib}^{\rm 1R\mu}} PDF_{\rm I}(E_i^{\rm rec}; \Delta m^2, \sin^2 2\theta, \boldsymbol{f}) \times \prod_{i=1}^{N_{\rm K2K\text{-}II}^{\rm 1R\mu}} PDF_{\rm II}(E_i^{\rm rec}; \Delta m^2, \sin^2 2\theta, \boldsymbol{f}), \qquad (12.2)$$

where $N_{\rm K2K\text{-}Ib}^{\rm 1R\mu}$ and $N_{\rm K2K\text{-}II}^{\rm 1R\mu}$ are the number of 1Rμ events in K2K-Ib[1] and K2K-II, respectively, and $E_i^{\rm rec}$ is the $E_\nu^{\rm rec}$ of i-th 1Rμ event. The probability density functions, $PDF_{\rm I}$ and $PDF_{\rm II}$,

[1] We do not use K2K-Ia data for the shape analysis, because the E_ν spectrum for K2K-Ia is not understood well.

represent the $E_\nu^{\rm rec}$ distribution of 1Rμ events for a certain oscillation parameter set. Since the number of PMTs is different between SK-I and SK-II, the probability density functions are different. In Section 12.1.2, we describe the definition of the probability density function.

Normalization term

The normalization term, $\mathcal{L}_{\rm norm}$, for the number of events is given by the Poisson probability to observe $N^{\rm obs}$ events if the expected number of events is $N^{\rm exp}$:

$$\mathcal{L}_{\rm norm} \equiv \frac{[N^{\rm exp}(\Delta m^2, \sin^2 2\theta; \boldsymbol{f})]^{N^{\rm obs}}}{N^{\rm obs}!} \cdot \exp[-N^{\rm exp}(\Delta m^2, \sin^2 2\theta; \boldsymbol{f})], \tag{12.3}$$

where $N^{\rm obs}$ and $N^{\rm exp}$ are summed up for all experiment periods. The expected number of SK events is estimated from the number of 1KT events by Equation (2.4). In Section 12.1.3, we define $N^{\rm exp}$ and discuss the systematic error.

Constraint term for systematic parameters

The constraint term, $\mathcal{L}_{\rm syst}$, restricts the systematic parameters, $\boldsymbol{f}$, within their systematic errors assuming the Gaussian probability. The contents of $\boldsymbol{f}$ are

$$\boldsymbol{f} \equiv (\boldsymbol{f}^{\phi}, f^{\rm nonQE}, f^{\rm NC}, \boldsymbol{f}^{F/N}, \boldsymbol{f}^{\epsilon_{\rm SK\text{-}I}}, f^{E\text{-scale}}_{\rm SK\text{-}I}, \boldsymbol{f}^{\epsilon_{\rm SK\text{-}II}}, f^{E\text{-scale}}_{\rm SK\text{-}II}, f^{\rm norm}_{\rm K2K\text{-}Ia}, f^{\rm norm}_{\rm K2K\text{-}Ib}, f^{\rm norm}_{\rm K2K\text{-}II}), \tag{12.4}$$

where each component is summarized below:

- $\boldsymbol{f}^{\phi}$: The E_ν spectrum measured by ND.
- $f^{\rm nonQE}, f^{\rm NC}$: CC-nonQE/CC-QE and NC/CC-QE cross-section ratios.
- $\boldsymbol{f}^{F/N}$: The Far/Near flux ratio.
- $\boldsymbol{f}^{\epsilon_{\rm SK\text{-}X}}$: The detection efficiency of single-ring μ-like events in SK for each E_ν bin. X takes I and II, representing SK runs.
- $f^{E\text{-scale}}_{\rm SK\text{-}X}$: The energy scale of SK.
- $f^{\rm norm}_{\rm K2K\text{-}X}$: The number of events predicted by 1KT and the MC simulation. X takes Ia, Ib and II, representing experimental periods.

Each systematic parameter is defined as the ratio of the target quantity to the prediction from the baseline MC simulation. Therefore, each systematic parameter is varied around unity within its error.

12.1.2 $E_\nu^{\rm rec}$ shape term

Probability Density Function

The probability density function for $\mathcal{L}_{\rm shape}$ is written as

$$\begin{aligned} &PDF_X(E_\nu^{\rm rec}; \sin^2 2\theta, \Delta m^2, \boldsymbol{f}) \\ &\quad \equiv \int dE_\nu^{\rm true} \cdot \Phi_{\rm SK}(E_\nu^{\rm true}; \Delta m^2, \sin^2 2\theta, \boldsymbol{f}) \sum_{\mathcal{I}} \cdot \sigma^{\mathcal{I}}(E_\nu^{\rm true}, \boldsymbol{f}) \cdot r^{\mathcal{I}}(E_\nu^{\rm rec};\ E_\nu^{\rm true}, \boldsymbol{f}), \end{aligned} \tag{12.5}$$

where each term is defined as:

- $E_\nu^{\rm true}$: The true neutrino energy.

$\Phi_{\rm SK}$: The ν_μ energy spectrum at SK including the oscillation effect.

$\mathcal{I}$: Index of each neutrino interaction channel.

$\sigma^{\mathcal{I}}$: The neutrino-nucleus cross-section.

$r^{\mathcal{I}}$: The detector response function representing the probability density to observe the 1Rμ event as $E_\nu^{\rm rec}$ if the true neutrino energy is $E_\nu^{\rm true}$.

We describe the detail of each term in Equation (12.2). The neutrino flux $\Phi_{\rm SK}$ is defined as

$$\Phi_{\rm SK}(E_\nu^{\rm true};\Delta m^2,\sin^2 2\theta,\boldsymbol{f}) \equiv f_i^\phi \cdot f_j^{F/N} \cdot P(E_\nu^{\rm true};\Delta m^2,\sin^2 2\theta)\cdot \Phi_{\rm SK}^{\rm 250kA}(E_\nu^{\rm true}), \tag{12.6}$$

where i and j are corresponding energy bin indexes of the ND energy spectrum (Table 8.14) and the Far/Near flux ratio (Table 10.2), respectively. P is the neutrino oscillation probability written as

$$P(E_\nu^{\rm true};\Delta m^2,\sin^2 2\theta,\boldsymbol{f}) = \begin{cases} 1-\sin^2 2\theta\cdot\sin^2\dfrac{1.27\cdot\Delta m^2\cdot L}{E_\nu^{\rm true}} & \text{CC} \\ 1 & \text{NC}, \end{cases} \tag{12.7}$$

where $L = 250$km is the neutrino flight distance. $\Phi_{\rm SK}^{\rm 250kA}$ is the neutrino flux predicted by the MC simulation.

The neutrino cross-section term $\sigma^{\mathcal{I}}$ is defined as

$$\sigma^{\mathcal{I}}(E_\nu^{\rm true},\boldsymbol{f}) = f^{\mathcal{I}}\cdot\sigma^{\rm MC}(E_\nu^{\rm true}), \tag{12.8}$$

where $f^{\mathcal{I}}$ is a fit parameter to vary the cross-section for each interaction channel, and $\sigma^{\rm MC}$ is the neutrino cross-section evaluated by the MC simulation. The definition of $f^{\mathcal{I}}$ is

$$f^{\mathcal{I}} \equiv \begin{cases} 1 & \mathcal{I} = \text{CC-QE} \\ f^{\rm nonQE} & \mathcal{I} = \text{CC-nonQE} \\ f^{\rm NC} & \mathcal{I} = \text{NC} \end{cases}. \tag{12.9}$$

Since $f^{\rm nonQE}$ is determined by the ND spectrum analysis[2], it varies around the best fit value in terms of the error matrix together with f_i^ϕ. The error on $f^{\rm nonQE}$ is approximately 11%. The central value of the NC cross-section parameter $f^{\rm NC}$ is unity, and the error is 15%. The error of $f^{\rm NC}$ is the compilation of the error on the NC single-π^0 measurement by 1KT (11%)[94] and the error on the other NC channels (30%).

The detector response function $r^{\mathcal{I}}$ is estimated by the MC simulation. To implement the energy scale error of SK, the reconstructed neutrino energy for $r^{\mathcal{I}}$ is scaled by $f_{\text{SK-}X}^{E\text{-scale}}$.

Probability density function from Toy-MC

Figure 12.1 shows PDF_X in the case of no oscillation. The systematic parameter $\boldsymbol{f}$ is randomly generated within its error many times, and the mean and the standard deviation of each bin of PDF_X are plotted in this figure. Figure 12.2 shows the contribution of each systematic error source to PDF_X. The error is dominated by the SK energy scale.

[2] In Chapter 8, $f^{\rm nonQE}$ is denoted by $R_{\rm nQE}$.

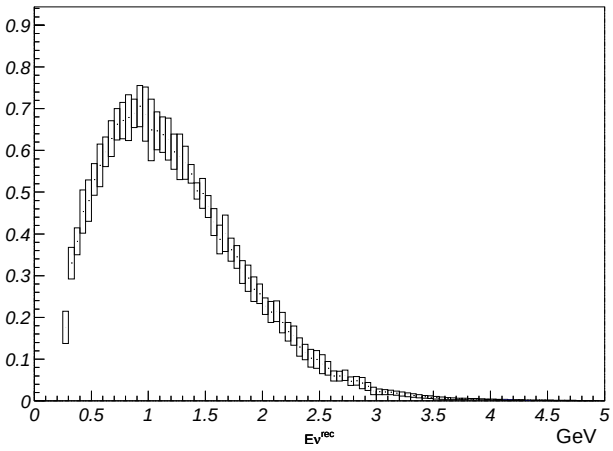

Figure 12.1: The probability density function for the $E_\nu^{\rm rec}$ shape likelihood without an oscillation. Each error bar shows the standard deviation of each bin, if the systematic parameter set $\boldsymbol{f}$ is varied within its error.

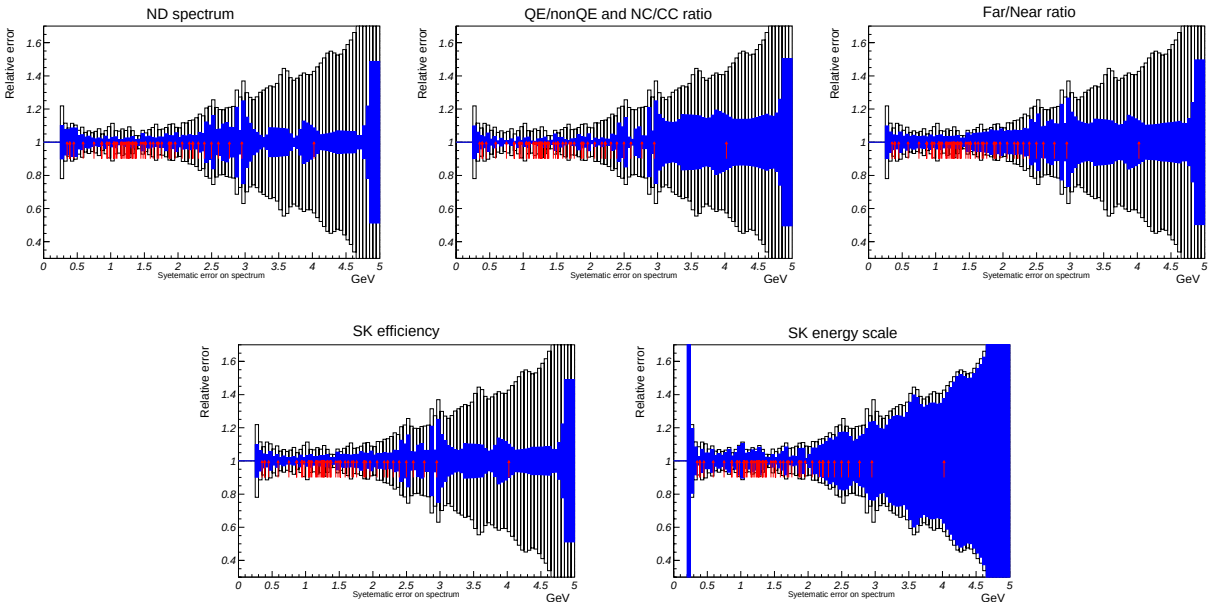

Figure 12.2: Contributions of each systematic error to the $E_\nu^{\rm rec}$ shape. Filled boxes are systematic errors from a specified error source, and open boxes are total errors. The vertical axis shows the relative error to *PDF*. The $E_\nu^{\rm rec}$ of each observed 1Rμ event is shown by the arrow.

12.1.3 Normalization term

The Number of Events for Likelihood Function

The likelihood function for normalization is already given by Equation (12.3). We define $N^{\rm obs}$ and $N^{\rm exp}$ as follows:

$$N^{\rm obs} \equiv N^{\rm obs}_{\rm K2K\text{-}Ia} + N^{\rm obs}_{\rm K2K\text{-}Ib} + N^{\rm obs}_{\rm K2K\text{-}II} = 107, \tag{12.10}$$

$$\begin{aligned} N^{\rm exp}(\Delta m^2, \sin^2 2\theta; \boldsymbol{f}) \equiv & N^{\rm exp}_{\rm K2K\text{-}Ia}(\Delta m^2, \sin^2 2\theta; \boldsymbol{f}) \\ & + N^{\rm exp}_{\rm K2K\text{-}Ib}(\Delta m^2, \sin^2 2\theta; \boldsymbol{f}) \\ & + N^{\rm exp}_{\rm K2K\text{-}II}(\Delta m^2, \sin^2 2\theta; \boldsymbol{f}), \end{aligned} \tag{12.11}$$

where each experimental period is indicated by the subscript. We treat K2K-Ia, K2K-Ib, and K2K-II separately.

The expected number of events with neutrino oscillation is written as

$$\begin{aligned} N^{\rm exp}_{\rm K2K\text{-}X}(\Delta m^2, \sin^2 2\theta; \boldsymbol{f}) \equiv & f^{\rm norm}_{\rm K2K\text{-}X} \cdot (N^{\rm obs}_{\rm 1KT})_{\rm K2K\text{-}X} \\ & \times \frac{\displaystyle\int dE^{\rm true}_\nu \cdot \Phi^{\rm K2K\text{-}X}_{\rm SK}(E^{\rm true}_\nu; \Delta m^2, \sin^2 2\theta, \boldsymbol{f}) \cdot \sum_{\mathcal{I}} \sigma^{\mathcal{I}}(E^{\rm true}_\nu, \boldsymbol{f}) \cdot \epsilon^{\mathcal{I}}_{\rm SK\text{-}X}(E^{\rm true}_\nu)}{\displaystyle\int dE^{\rm true}_\nu \cdot \Phi^{\rm K2K\text{-}X}_{\rm 1KT}(E^{\rm true}_\nu; \boldsymbol{f}) \cdot \sum_{\mathcal{I}} \sigma^{\mathcal{I}}(E^{\rm true}_\nu, \boldsymbol{f}) \cdot \epsilon^{\mathcal{I}}_{\rm 1KT}(E^{\rm true}_\nu)} \\ & \times \frac{M_{\rm SK}}{M_{\rm 1KT}} \cdot \frac{{\rm POT}^{\rm K2K\text{-}X}_{\rm SK}}{{\rm POT}^{\rm K2K\text{-}X}_{\rm 1KT}} \cdot C_{\nu_e}, \end{aligned} \tag{12.12}$$

where the definition of each term is

- $f^{\rm norm}_{\rm K2K\text{-}X}$: Defined by Equation (12.4)
- $(N^{\rm obs}_{\rm 1KT})_{\rm K2K\text{-}X}$: The number of events in 1KT.
- $\Phi^{\rm K2K\text{-}X}_{\rm SK\,(1KT)}$: The neutrino flux at SK (1KT) defined by Equation (12.13) and (12.14) below.
- $\sigma^{\mathcal{I}}$: Defined by Equation (12.8).
- $\epsilon^{\mathcal{I}}_{\rm SK\text{-}X\,(1KT)}$: The detection efficiency for SK (1KT) estimated by the MC simulation.
- $M_{\rm SK\,(1KT)}$: The fiducial mass of SK (1KT), which is 22.5 ktons (25 tons).
- ${\rm POT}^{\rm K2K\text{-}X}_{\rm SK\,(1KT)}$: The number of protons on target for SK (1KT).
- C_{ν_e} : The correction for the electron neutrino component in the neutrino beam.

Here, $\Phi^{\rm K2K\text{-}X}_{\rm SK}$ and $\Phi^{\rm K2K\text{-}X}_{\rm 1KT}$ are defined as

$$\Phi^{\rm K2K\text{-}X}_{\rm SK}(E^{\rm true}_\nu; \Delta m^2, \sin^2 2\theta, \boldsymbol{f}) \equiv \begin{cases} P(E^{\rm true}_\nu; \Delta m^2, \sin^2 2\theta) \cdot \Phi^{\rm 200kA}_{\rm SK}(E^{\rm true}_\nu) & X = {\rm Ia} \\ \text{Equation (12.6)} & X = {\rm Ib, II}\,, \end{cases} \tag{12.13}$$

$$\Phi^{\rm K2K\text{-}X}_{\rm 1KT}(E^{\rm true}_\nu; \boldsymbol{f}) \equiv \begin{cases} \Phi^{\rm 200kA}_{\rm 1KT}(E^{\rm true}_\nu) & X = {\rm Ia} \\ f^{\phi}_i \cdot \Phi^{\rm 250kA}_{\rm 1KT}(E^{\rm true}_\nu) & X = {\rm Ib, II}\,, \end{cases} \tag{12.14}$$

where $\Phi^{\rm 250kA}_{\rm 1KT}$ ($\Phi^{\rm 200kA}_{\rm 1KT}$) is the neutrino flux obtained from the MC simulation for the horn current of 250kA (200kA). Finally, we evaluate the value of C_{ν_e}. If the ν_e component is taken into

account in the MC simulation, the number of events in SK increases 0.6% and that in 1KT increases 1.3%. Therefore, we obtain

$$C_{\nu_e} = 1.006/1.013 = 0.996\ . \tag{12.15}$$

Effect of systematic parameters

We discuss the contribution of each systematic parameter to $N^{\rm exp}$. Some systematic errors on $N^{\rm exp}$ are expected to be canceled out, since f^ϕ and $f^{\mathcal{I}}$ are common to both the numerator and the denominator of Equation (12.12). To see this effect, we vary systematic parameters by small amount:

$$f_i^\phi \to f_i^\phi + \Delta f_i^\phi, \tag{12.16}$$

$$f_j^{F/N} \to f_j^{F/N} + \Delta f_j^{F/N}, \tag{12.17}$$

$$f^{\mathcal{I}} \to f^{\mathcal{I}} + \Delta f^{\mathcal{I}}. \tag{12.18}$$

The second line of Equation (12.12) becomes

$$\frac{\int dE_\nu^{\rm true}\cdot\Phi_{\rm SK}\cdot(1+\frac{\Delta f^\phi}{f^\phi})\cdot(1+\frac{\Delta f^{F/N}}{f^{F/N}})\cdot\sum_{\mathcal{I}}(1+\frac{\Delta f^{\mathcal{I}}}{f^{\mathcal{I}}})\cdot\sigma^{\mathcal{I}}\cdot\epsilon^{\mathcal{I}}_{\rm SK}}{\int dE_\nu^{\rm true}\cdot\Phi_{\rm 1KT}\cdot(1+\frac{\Delta f^\phi}{f^\phi})\cdot\sum_{\mathcal{I}}(1+\frac{\Delta f^{\mathcal{I}}}{f^{\mathcal{I}}})\cdot\sigma^{\mathcal{I}}\cdot\epsilon^{\mathcal{I}}_{\rm 1KT}} \tag{12.19}$$

$$\simeq \frac{\int dE_\nu^{\rm true}\cdot\Phi_{\rm SK}\cdot\sum_{\mathcal{I}}\cdot(1+\frac{\Delta f^\phi}{f^\phi}+\frac{\Delta f^{F/N}}{f^{F/N}}+\frac{\Delta f^{\mathcal{I}}}{f^{\mathcal{I}}})\cdot\sigma^{\mathcal{I}}\cdot\epsilon^{\mathcal{I}}_{\rm SK}}{\int dE_\nu^{\rm true}\cdot\Phi_{\rm 1KT}\cdot\sum_{\mathcal{I}}(1+\frac{\Delta f^\phi}{f^\phi}+\frac{\Delta f^{\mathcal{I}}}{f^{\mathcal{I}}})\cdot\sigma^{\mathcal{I}}\cdot\epsilon^{\mathcal{I}}_{\rm 1KT}}. \tag{12.20}$$

Here, the product of two small numbers is neglected. We then make substitutions as follows:

$$N^{\rm MC}_{\rm SK} \equiv \int dE_\nu^{\rm true}\cdot\Phi_{\rm SK}\cdot\sum_{\mathcal{I}}\sigma^{\mathcal{I}}\cdot\epsilon^{\mathcal{I}}_{\rm SK}, \tag{12.21}$$

$$N^{\rm MC}_{\rm 1KT} \equiv \int dE_\nu^{\rm true}\cdot\Phi_{\rm 1KT}\cdot\sum_{\mathcal{I}}\sigma^{\mathcal{I}}\cdot\epsilon^{\mathcal{I}}_{\rm 1KT}, \tag{12.22}$$

and Equation (12.20) is approximated by

$$\frac{N^{\rm MC}_{\rm SK}}{N^{\rm MC}_{\rm 1KT}}\cdot\left[1+\frac{1}{N^{\rm MC}_{\rm SK}}\cdot\int dE_\nu^{\rm true}\cdot\Phi_{\rm SK}\cdot\sum_{\mathcal{I}}\left(\frac{\Delta f^\phi}{f^\phi}+\frac{\Delta f^{F/N}}{f^{F/N}}+\frac{\Delta f^{\mathcal{I}}}{f^{\mathcal{I}}}\right)\cdot\sigma^{\mathcal{I}}\cdot\epsilon^{\mathcal{I}}_{\rm SK}\right.$$
$$\left.-\frac{1}{N^{\rm MC}_{\rm 1KT}}\cdot\int dE_\nu^{\rm true}\cdot\Phi_{\rm 1KT}\cdot\sum_{\mathcal{I}}\left(\frac{\Delta f^\phi}{f^\phi}+\frac{\Delta f^{\mathcal{I}}}{f^{\mathcal{I}}}\right)\cdot\sigma^{\mathcal{I}}\cdot\epsilon^{\mathcal{I}}_{\rm 1KT}\right] \tag{12.23}$$

$$=\frac{N^{\rm MC}_{\rm SK}}{N^{\rm MC}_{\rm 1KT}}\cdot\left[1+\Delta^{F/N}+\Delta^\phi+\Delta^{\mathcal{I}}\right], \tag{12.24}$$

$$\Delta^{F/N} \equiv \int dE_\nu^{\rm true}\cdot\frac{\Delta f^{F/N}}{f^{F/N}}\sum_{\mathcal{I}}\frac{\Phi_{\rm SK}\cdot\sigma^{\mathcal{I}}\cdot\epsilon^{\mathcal{I}}_{\rm SK}}{N^{\rm MC}_{\rm SK}}, \tag{12.25}$$

$$\Delta^\phi \equiv \int dE_\nu^{\rm true}\cdot\frac{\Delta f^\phi}{f^\phi}\sum_{\mathcal{I}}\left(\frac{\Phi_{\rm SK}\cdot\sigma^{\mathcal{I}}\cdot\epsilon^{\mathcal{I}}_{\rm SK}}{N^{\rm MC}_{\rm SK}}-\frac{\Phi_{\rm 1KT}\cdot\sigma^{\mathcal{I}}\cdot\epsilon^{\mathcal{I}}_{\rm 1KT}}{N^{\rm MC}_{\rm 1KT}}\right), \tag{12.26}$$

$$\Delta^{\mathcal{I}} \equiv \int dE_{\nu}^{\rm true} \cdot \sum_{\mathcal{I}} \frac{\Delta f^{\mathcal{I}}}{f^{\mathcal{I}}} \left(\frac{\Phi_{\rm SK} \cdot \sigma^{\mathcal{I}} \cdot \epsilon^{\mathcal{I}}_{\rm SK}}{N^{\rm MC}_{\rm SK}} - \frac{\Phi_{\rm 1KT} \cdot \sigma^{\mathcal{I}} \cdot \epsilon^{\mathcal{I}}_{\rm 1KT}}{N^{\rm MC}_{\rm 1KT}} \right). \tag{12.27}$$

$\Delta^{F/N}$ represents the effect of the uncertainty in the Far/Near ratio, which contributes $N^{\rm exp}$ linearly. For Δ^{ϕ} and $\Delta^{\mathcal{I}}$, on the other hand, contributions from SK and 1KT are partly canceled out each other. Cancellations are not perfect due to:

- The difference of the energy spectrum times the efficiency curve ($\Phi_{\rm SK(1KT)} \cdot \epsilon^{\mathcal{I}}_{\rm SK(1KT)}$) between SK and 1KT.
- The difference of the detection efficiency for each interaction channel between SK and 1KT.
- The oscillation parameter set (Δm^2, $\sin^2 2\theta$) because of the distortion of $\Phi_{\rm SK}$.

Consequently, uncertainties in $N^{\rm exp}$ are properly taken into account including the complicated error cancellation. Since the detector response of 1KT is the most similar to SK among near detectors, the error cancellation effect is maximized by using 1KT data for the $N^{\rm exp}$ estimation.

Systematic errors on the number of events

We first evaluate the systematic error on $f^{\rm norm}_{\rm K2K\text{-}Ia}$. Since the systematic parameters for the ND spectrum (f^{ϕ}) and the Far/Near flux ratio ($f^{F/N}$) are not implemented in $N^{\rm exp}_{\rm K2K\text{-}Ia}$, the systematic uncertainties from f^{ϕ} and $f^{F/N}$ are put into the error on $f^{\rm norm}_{\rm K2K\text{-}Ia}$. The systematic error on each source is summarized in Table 12.1. The statistical error on the 1KT measurement is $\pm 1.5\%$. The systematic uncertainties in the event selections of 1KT and SK are already described in Section 9.4 and 11.2, respectively. The uncertainty in $N^{\rm exp}_{\rm K2K\text{-}Ia}$ from the neutrino energy spectrum is estimated to be 9.3%. The systematic errors due to CC-nonQE/CC-QE and NC/CC cross-section ratios are $+1.6\%$ -2.4% and $\pm 0.2\%$, respectively. The error on the POT correction comes from the spills when SK is alive but 1KT is not taking data. This error is written as

$$\frac{\rm POT_{SK} - POT_{1KT}}{\rm POT_{1KT}} \cdot \Delta S, \tag{12.28}$$

where ΔS is the stability of the 1KT event rate. Since the fluctuation of the event rate is within 6%, we use this value as ΔS. In total, the systematic error on $N^{\rm exp}_{\rm K2K\text{-}Ia}$ is obtained to be +17.6% –14.9%.

By using Equation (12.12), the central value and the error of $N^{\rm exp}_{\rm K2K\text{-}Ia}$ are calculated to be 4.57 +0.80 –0.68 events in case of null oscillation. Although $N^{\rm exp}_{\rm K2K\text{-}Ia}$ depends on ($\Delta m^2, \sin^2 2\theta$), the error on $N^{\rm exp}_{\rm K2K\text{-}Ia}$ stays at +0.80 –0.68 event during the fit because the error cancellation is not considered.

For the errors on $f^{\rm norm}_{\rm K2K\text{-}Ib}$ and $f^{\rm norm}_{\rm K2K\text{-}II}$, the uncertainties in the Far/Near flux ratio, the neutrino energy spectrum, and the cross-section for each interaction channel are treated in Equation (12.12). Therefore, the errors on $f^{\rm norm}_{\rm K2K\text{-}Ib}$ and $f^{\rm norm}_{\rm K2K\text{-}II}$ are the quadratic sum of the other uncertainties, which are the 1KT event selection, the SK event selection, the POT normalization, and the statistics. Errors on $f^{\rm norm}_{\rm K2K\text{-}Ib}$ and $f^{\rm norm}_{\rm K2K\text{-}II}$ are summarized in Table 12.2.

We then evaluate the central value of $N^{\rm exp}$, its total error, and the contribution from each systematic parameters in case of null oscillation. The systematic parameters ($\boldsymbol{f}$) are randomly generated many times within their systematic errors, and $N^{\rm exp}$ for each parameter set is computed. The distribution of $N^{\rm exp}$ is shown in Figure 12.3. The mean value of the $N^{\rm exp}$ distribution is 150.9, and the standard deviation of the asymmetric Gaussian fitted to the distribution is +11.5 −10.1. The mean and the standard deviation for either of K2K-I or K2K-II are summarized in Table 12.3. The contribution from each systematic error source is obtained by varying

Table 12.1: Errors on the number of expected events in K2K-Ia.

1KT statistics	±1.5%
1KT event selection	±4.9%
SK event selection	±3.0%
Energy spectrum	±9.3%
Far/Near ratio	+13.6% –9.9%
CC-nonQE/CC-QE ratio	+1.6% –2.4%
NC/CC-QE ratio	±0.2%
POT correction	±0.9%
Total	+17.6% –14.9%

Table 12.2: Errors on $f^{\rm norm}_{\rm K2K\text{-}Ib}$ and $f^{\rm norm}_{\rm K2K\text{-}II}$.

	K2K-Ib ($f^{\rm norm}_{\rm K2K\text{-}Ib}$)	K2K-II ($f^{\rm norm}_{\rm K2K\text{-}II}$)
1KT statistics	±0.4%	±0.4%
1KT event selection	±4.7%	±4.7%
SK event selection	±3.0%	±3.0%
POT correction	±0.6%	±0.3%
Total	±5.6%	±5.6%

each systematic parameter one by one, and summarized in Table 12.4. Owing to the error cancellation, uncertainties from the neutrino energy spectrum (f_i^{ϕ}) and the cross-section for each interaction channel ($f^{\rm nonQE}, f^{\rm NC}$) are much smaller than the other parameters.

12.1.4 Constraint term for systematic parameters

Each systematic parameter is supposed to distribute as a Gaussian with the standard deviation of the error. Therefore, the constraint term ($\mathcal{L}_{\rm syst}$) for the systematic parameters is given by

$$\begin{aligned}\mathcal{L}_{\rm syst} \equiv & \exp\left[-{}^t\Delta\boldsymbol{f}^{\phi,\rm nonQE}\cdot(M^{\phi,\rm nonQE})^{-1}\cdot\Delta\boldsymbol{f}^{\phi,\rm nonQE}-\frac{(\Delta f^{\rm NC})^2}{2(\sigma^{\rm NC})^2}\right]\\ & \times\exp\left[-{}^t\Delta\boldsymbol{f}^{F/N}\cdot(M^{F/N})^{-1}\cdot\Delta\boldsymbol{f}^{F/N}\right]\\ & \times\exp\left[-\sum\frac{(\Delta f_i^{\epsilon_{\rm SK\text{-}X}})^2}{2(\sigma_i^{\epsilon_{\rm SK\text{-}X}})^2}-\sum\frac{(\Delta f^{E\text{-scale}}_{\rm SK\text{-}X})^2}{2(\sigma^{E\text{-scale}}_{\rm SK\text{-}X})^2}-\sum\frac{(\Delta f^{\rm norm}_{\rm K2K\text{-}X})^2}{2(\sigma^{\rm norm}_{\rm K2K\text{-}X})^2}\right],\end{aligned} \tag{12.29}$$

where Δf is defined as

$$\Delta f \equiv f - \langle f\rangle, \tag{12.30}$$

which is the deviation of f from its central value $\langle f\rangle$. For $\boldsymbol{f}^{\phi,\rm nonQE}$ and $\boldsymbol{f}^{F/N}$, the correlations between parameters are taken into account by using the error matrices[3], $M^{\phi,\rm nonQE}$ and $M^{F/N}$. The central values and the errors for the systematic parameters are summarized in Table 12.5.

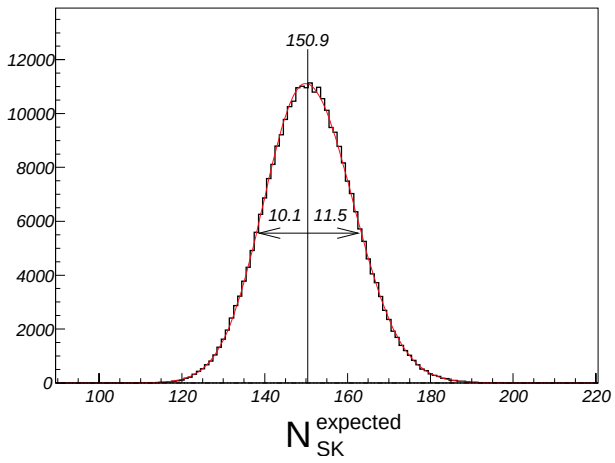

Figure 12.3: Distribution of $N^{\rm exp}$ in case of null oscillation, when the systematic parameters are randomly generated within their errors. The distribution is fitted with an asymmetric Gaussian.

Table 12.3: The number of expected events in SK assuming the null oscillation. The definition of the error is the standard deviation from the fit with an asymmetric Gaussian to a $N^{\rm exp}$ distribution.

	$N^{\rm exp}$	Error		$N^{\rm obs}$
Total	**150.9**	**+11.5** (+7.7%)	**−10.1** (−6.7%)	**107**
K2K-I	79.1	+6.1 (+7.7%)	−5.4 (−6.8%)	55
K2K-II	71.8	+5.9 (+8.2%)	−5.1 (−7.1%)	52

Table 12.4: Contribution from each systematic error source to the expected number of events in SK assuming null oscillation.

	Error	
Far/Near flux ratio ($f_i^{F/N}$)	+7.7 (+5.1%)	−7.5 (−5.0%)
Neutrino energy spectrum (f_i^{ϕ})	+1.0 (+0.7%)	−0.9 (−0.6%)
CC-nonQE/CC-QE and NC/CC-QE ($f^{\rm nonQE}$, $f^{\rm NC}$)	+0.7 (+0.5%)	−0.8 (−0.5%)
Others ($f^{\rm norm}_{\rm K2K\text{-}X}$)	+7.6 (+5.0%)	−7.7 (−5.1%)
Total	+11.5 (+7.7%)	−10.1 (−6.7%)

Table 12.5: Summary of the central values and the errors for the systematic parameters. If a parameter is correlated with another, the square root of the diagonal element is written as the error.

	Center	Error		Center	Error
f_1^{ϕ} (0.0–0.5 GeV)	0.784	$\pm$0.366	$f_1^{\text{SK-I}}$ (0.0–0.5 GeV)	1.000	$\pm$0.037
f_2^{ϕ} (0.5–0.75 GeV)	1.012	$\pm$0.098	$f_2^{\text{SK-I}}$ (0.5–1.0 GeV)	1.000	$\pm$0.030
f_3^{ϕ} (0.75–1.0 GeV)	1.119	$\pm$0.067	$f_3^{\text{SK-I}}$ (1.0–1.5 GeV)	1.000	$\pm$0.034
f_4^{ϕ} (1.0–1.5 GeV)	1.000	$\pm$0.000	$f_4^{\text{SK-I}}$ (1.5–2.0 GeV)	1.000	$\pm$0.049
f_5^{ϕ} (1.5–2.0 GeV)	0.901	$\pm$0.044	$f_5^{\text{SK-I}}$ (2.0–2.5 GeV)	1.000	$\pm$0.049
f_6^{ϕ} (2.0–2.5 GeV)	1.069	$\pm$0.065	$f_6^{\text{SK-I}}$ (2.5 GeV –)	1.000	$\pm$0.049
f_7^{ϕ} (2.5–3.0 GeV)	1.334	$\pm$0.171	$f_{\text{SK-I}}^{E\text{-scale}}$	1.000	$\pm$0.020
f_8^{ϕ} (3.0 GeV –)	1.041	$\pm$0.179	$f_1^{\text{SK-II}}$ (0.0–0.5 GeV)	1.000	$\pm$0.045
f^{nonQE}	1.020	$\pm$0.109	$f_2^{\text{SK-II}}$ (0.5–1.0 GeV)	1.000	$\pm$0.032
f^{NC}	1.000	$\pm$0.153	$f_3^{\text{SK-II}}$ (1.0–1.5 GeV)	1.000	$\pm$0.082
$f_1^{F/N}$ (0.0–0.5 GeV)	1.000	$\pm$0.026	$f_4^{\text{SK-II}}$ (1.5–2.0 GeV)	1.000	$\pm$0.078
$f_2^{F/N}$ (0.5–1.0 GeV)	1.000	$\pm$0.043	$f_5^{\text{SK-II}}$ (2.0–2.5 GeV)	1.000	$\pm$0.074
$f_3^{F/N}$ (1.0–1.5 GeV)	1.000	$\pm$0.065	$f_6^{\text{SK-II}}$ (2.5 GeV –)	1.000	$\pm$0.074
$f_4^{F/N}$ (1.5–2.0 GeV)	1.000	$\pm$0.104	$f_{\text{SK-II}}^{E\text{-scale}}$	1.000	$\pm$0.021
$f_5^{F/N}$ (2.0–2.5 GeV)	1.000	$\pm$0.111			
$f_6^{F/N}$ (2.5 GeV –)	1.000	$\pm$0.122			
$f_{\text{K2K-Ia}}^{\text{norm}}$	1.000	$^{+0.80}_{-0.68} \cdot (\frac{1}{N_{\text{K2K-Ia}}^{\text{exp}}})$			
$f_{\text{K2K-Ib}}^{\text{norm}}$	1.000	$\pm$0.056			
$f_{\text{K2K-II}}^{\text{norm}}$	1.000	$\pm$0.056			

12.2 Fit results

12.2.1 Best fit parameters

The maximum of the likelihood $\mathcal{L}$ is searched for, and the best fit parameters are obtained to be

$$(\Delta m^2,\ \sin^2 2\theta) = (2.2\times10^{-3}\ [\text{eV}^2],\ 1.5). \tag{12.31}$$

The best $\sin^2 2\theta$ value is higher than the upper limit of the physical condition ($0 \le \sin^2 2\theta \le 1$). If $\sin^2 2\theta$ is restricted within the physical region, the best fit parameters are

$$(\Delta m^2,\ \sin^2 2\theta) = (2.8\times10^{-3}\ [\text{eV}^2],\ 1.0). \tag{12.32}$$

The best fit parameters are summarized in Table 12.6 together with the best fit parameters for only the E_ν^{rec} shape. In addition, the best parameters for either of only K2K-I or K2K-II data are determined and summarized in the same table. For the fit results in the physical region, the best fit values are almost independent of fitting conditions. Since the normalization term $\mathcal{L}_{\text{norm}}$ is a single Poisson probability, the fit result using only the normalization cannot determine two parameters simultaneously. The consistency of the fit with only the normalization term is discussed later.

[3] $M^{\phi,\text{nonQE}}$ is obtained from the ND spectrum analysis (Table 8.14), and $M^{F/N}$ is evaluated from the PIMON measurement and the Beam-MC simulation (Table 10.2).

12.2.2 Basic distributions and quantities

Figure 12.4 shows $E_\nu^{\rm rec}$ distributions at the best fit point in the physical region for the K2K-I+II data set [Equation (12.32)]. In addition to the best fit case, the spectra in case of null oscillation $[(\Delta m^2, \sin^2 2\theta) = (0, 0)]$ are overlaid. The data looks consistent with the best fit oscillation case. A dip around 0.6 GeV is seen in data. A Kolmogorov-Smirnov test (KS-test)[93] is performed to examine whether data is consistent with the best fit spectrum. The confidence probabilities from KS-test are summarized in Table 12.7. The KS-test results for null oscillation spectra are also listed. The KS-probability for the best fit spectrum is 36%, whereas that for the null oscillation case is less than 0.1%. Each sub-sample also favors the best fit point. Thus, the $E_\nu^{\rm rec}$ spectrum at the best fit point is consistent with data.

The expected number of events ($N^{\rm exp}$) at the best fit point is summarized in Table 12.8. The best fit values are consistent with the observation within the statistical uncertainty.

The systematic parameters at the best fit point are shown in Figure 12.5. All systematic parameters stay within their errors.

Consequently, the fit result appropriately reproduces data.

12.2.3 Toy-MC test for large $\sin^2 2\theta$

Since the best fit point in the whole region is out of the physical boundary, we test whether this result is statistically obtained or not by using a toy-MC technique. Assuming the true oscillation parameter set is Equation (12.32), many virtual experiments are performed by generating neutrino events randomly. The fit result of each experiment is plotted in Figure 12.6. The probability that $\sin^2 2\theta$ exceeds 1.5 is 12.6%. Therefore, we conclude that our fit result ($\sin^2 2\theta = 1.5$) is within the statistical fluctuation.

12.3 Null oscillation probability

12.3.1 Likelihood ratio method

The null oscillation hypothesis is tested by the likelihood ratio between the null oscillation and the best fit oscillation. Here, we define the maximum likelihood in the physical region as $\mathcal{L}_{\rm max}^{\rm phys}$, and that for the null oscillation case as $\mathcal{L}_{\rm null}$. By using the logarithm of the ratio between $\mathcal{L}_{\rm max}^{\rm phys}$ and $\mathcal{L}_{\rm null}$:

$$\Delta\ln\mathcal{L}_{\rm null} \equiv \ln\left(\frac{\mathcal{L}_{\rm max}^{\rm phys}}{\mathcal{L}_{\rm null}}\right) = \ln\mathcal{L}_{\rm max}^{\rm phys} - \ln\mathcal{L}_{\rm null}, \tag{12.33}$$

we obtain the probability that data is observed due to the statistical fluctuation in case of null oscillation, assuming the likelihood $\mathcal{L}$ follows a two-dimensional Gaussian of $(\Delta m^2, \sin^2 2\theta)$. From the logarithm of the likelihood ratio $\Delta\ln\mathcal{L}_{\rm null} = 9.90$, the null oscillation probability is evaluated to be 0.0050%, corresponding to 4.0 standard deviations. The null oscillation hypothesis is excluded with 99.995% confidence level (C.L.). The null oscillation probability for each sub-sample or for each likelihood term is summarized in Table 12.9. Either shape or normalization rejects the null oscillation hypothesis with 99% C.L. This strong rejection power of the $E_\nu^{\rm rec}$ shape term is an indication of the E_ν dependence of the oscillation probability.

12.3.2 Toy-MC test for normalization

For the crosscheck, we evaluate the probability that the number of events is less than or equal to $N^{\rm obs}(= 107)$ in case of null oscillation. We generate random numbers following the convolution of Poisson statistics and the systematic fluctuation of $N^{\rm exp}$. The distribution of the generated

Table 12.6: Summary of the oscillation parameters at the best fit point for each fitting condition. If the best fit point is unphysical, the best point within the physical region is also listed.

		all region		physical region	
		Δm^2 [eV^2]	$\sin^2 2\theta$	Δm^2 [eV^2]	$\sin^2 2\theta$
K2K-I+II	shape + norm.	2.2×10^{-3}	1.5	$\mathbf{2.8\times10^{-3}}$	**1.0**
	shape only	2.5×10^{-3}	1.4	3.0×10^{-3}	1.0
K2K-I only	shape + norm.	2.7×10^{-3}	1.1	2.9×10^{-3}	1.0
K2K-II only	shape + norm.	1.9×10^{-3}	2.13	2.7×10^{-3}	1.0

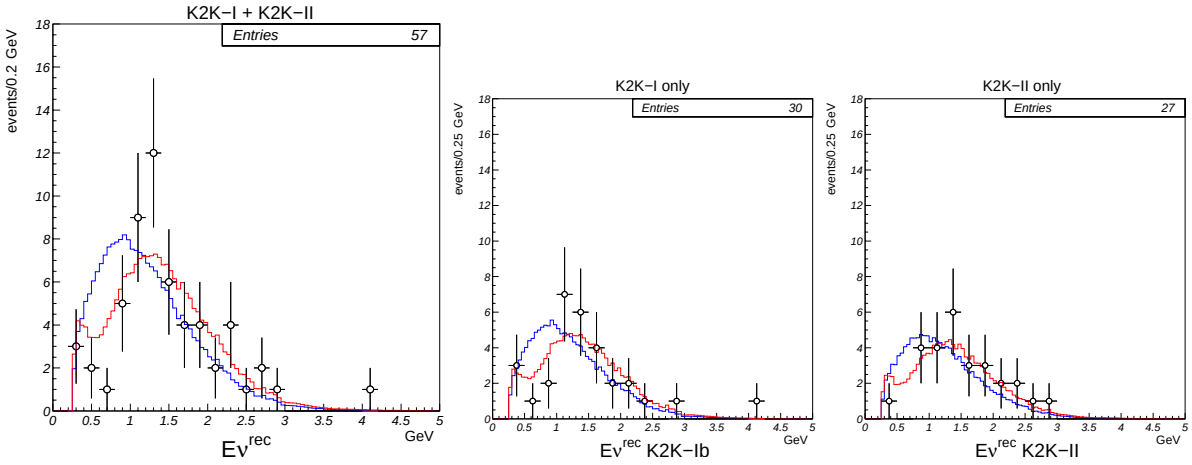

Figure 12.4: $E_\nu^{\rm rec}$ distributions of 1Rμ samples at the best fit point in the physical region. K2K-I+II data is plotted in the left figure. Center and right figures show K2K-I and K2K-II sub-samples, respectively. Open circles with error bars are data, and the red lines are the best fit spectra. Blue lines show the spectra in case of null oscillation.

Table 12.7: Summary of the KS-probability for each $E_\nu^{\rm rec}$ distribution. This test is performed at the best fit point in the physical region and in the null oscillation case for the K2K-I+II data set.

	Best fit	Null oscillation
(Δm^2 [eV^2], $\sin^2 2\theta$)	$(2.8\times10^{-3}, 1.0)$	$(0, 0)$
K2K-I+II	**36%**	0.080%
K2K-I only	63%	3.3%
K2K-II only	33%	1.3%

Table 12.8: Summary of the expected number of events at the best fit point. For reference, the number of observed events and the expected number in the null oscillation case are also listed.

	Best fit	Observation	Null oscillation
(Δm^2 [eV^2], $\sin^2 2\theta$)	$(2.8\times10^{-3}, 1.0)$	—	$(0, 0)$
K2K-I+II	**103.8**	107	$150.9^{+11.5}_{-10.1}$
K2K-I only	54.4	55	$79.1^{+6.1}_{-5.4}$
K2K-II only	49.4	52	$71.8^{+5.9}_{-5.1}$

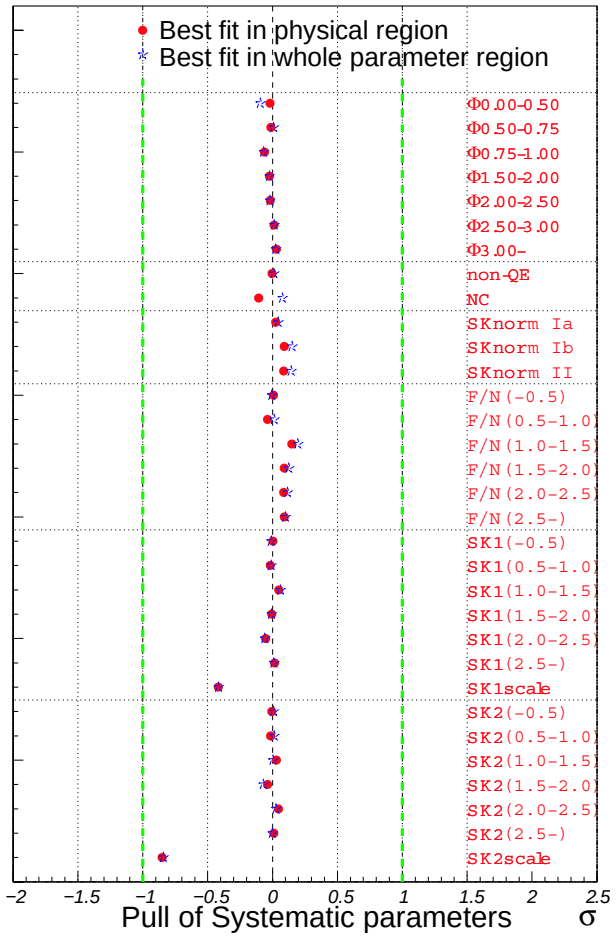

Figure 12.5: Deviation of systematic parameters at each best fit point. The horizontal axis shows the ratio of the deviation to its error. Closed circles are the parameters at the best fit point in the physical region, and stars are those at the best point in the whole parameter region.

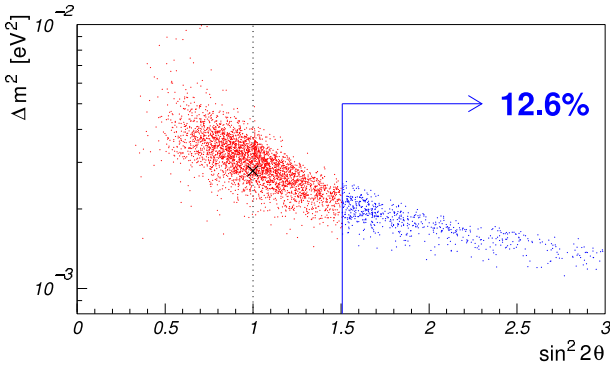

Figure 12.6: Fit results from many toy-MC virtual experiments generated at $(\Delta m^2,\ \sin^2 2\theta) = (2.8{\times}10^{-3}\ [\mathrm{eV}^2],\ 1.0)$. Each dot shows the best fit point in the whole region for each experiment. The true oscillation parameter is specified by '×'. The fraction of $\sin^2 2\theta > 1.5$ is 12.6%.

Table 12.9: Summary of the null oscillation probability. Each row is classified by used likelihood, and each column represents the data set.

	K2K-I+II	K2K-I only	K2K-II only
Shape + Norm.	**0.0050%**	0.58%	0.56%
Shape only	0.74%	12%	5.8%
Norm. only	0.26%	1.4%	3.7%

numbers is shown in Figure 12.7. In this figure, the fraction of the area less than or equal to 107 is 0.28%. This result is consistent with the likelihood ratio method of 0.26%.

12.4 Allowed region for oscillation parameters

We evaluate the allowed region for the oscillation parameters by using the logarithm of the likelihood ratio:

$$\Delta\ln\mathcal{L}(\Delta m^2,\sin^2 2\theta) \equiv \ln\left(\frac{\mathcal{L}^{\rm phys}_{\rm max}}{\mathcal{L}(\Delta m^2,\sin^2 2\theta)}\right) = \ln\mathcal{L}^{\rm phys}_{\rm max} - \ln\mathcal{L}(\Delta m^2,\sin^2 2\theta), \tag{12.34}$$

where $\mathcal{L}(\Delta m^2,\sin^2 2\theta)$ is the likelihood at $(\Delta m^2,\sin^2 2\theta)$. In the large sample limit, the parameter region

$$\Delta\ln\mathcal{L}(\Delta m^2,\sin^2 2\theta) \leq C \tag{12.35}$$

covers the true value with a certain probability corresponding to the $\Delta\ln\mathcal{L}$ threshold C.

Since the best fit parameter set [Equation (12.31)] is out of the physical region:

$$0 \leq \sin^2 2\theta \leq 1, \tag{12.36}$$

the coverage probability within the physical region is different from the case that $\sin^2 2\theta$ can take all real numbers. Therefore, we compute the C value for each coverage probability within the physical region. Assuming that $\mathcal{L}(\Delta m^2,\sin^2 2\theta)$ follows the two-dimensional Gaussian which peaks at Equation (12.31), we calculate two probabilities defined as:

- $P^0_{\rm phys}$: The probability that $\sin^2 2\theta$ satisfies Equation (12.36).
- $P^{\Delta\ln\mathcal{L}}_{\rm phys}$: The probability to satisfy both Equation (12.35) and (12.36).

In this case, the coverage probability for C is obtained to be $P^{\Delta\ln\mathcal{L}}_{\rm phys}/P^0_{\rm phys}$.

Figure 12.8 shows the allowed region for oscillation parameters by using the appropriate value of C. Figure 12.9 shows the behavior of the log-likelihood along the axes of $\sin^2 2\theta = 1$ and $\Delta m^2 = 2.8\times10^{-3}$ [eV^2]. The 90% confidence interval for Δm^2 on the axis of $\sin^2 2\theta = 1$ is

$$1.9\times10^{-3} \leq \Delta m^2 \leq 3.6\times10^{-3}\ [\text{eV}^2] \qquad 90\%\ \text{C.L.} \tag{12.37}$$

Figure 12.10 shows the comparison of the confidence regions between the shape-only and the normalization-only analyses. Since the normalization term of the likelihood is a single Poisson probability, it cannot restrict both $\sin^2 2\theta$ and Δm^2 at the same time, and the allowed region for the normalization-only analysis looks like a band. The best fit point $(\Delta m^2,\sin^2 2\theta) = (2.8\times10^{-3}\ [\text{eV}^2], 1.0)$ lies within the 68% C.L. allowed regions for both cases. The allowed region of the shape-only analysis overlaps with that of the normalization-only analysis. Consequently, the results from the $E^{\rm rec}_\nu$ shape and the normalization are consistent with each other.

Figure 12.11 shows the allowed region for either K2K-I or K2K-II data set. Each contour covers almost the same region. Thus, the results from K2K-I and K2K-II are consistent each other.

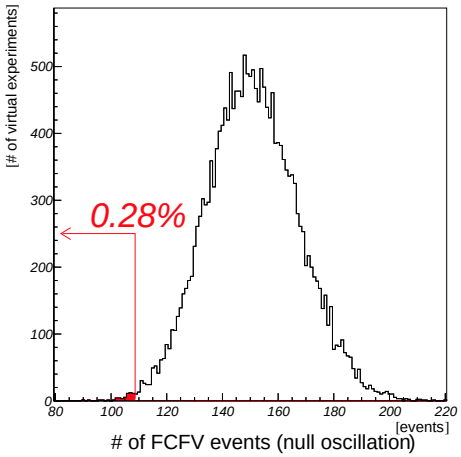

Figure 12.7: Convolution of Poisson statistics and the $N^{\rm exp}$ fluctuation in case of null oscillation. The fraction of the area below or equal to $N^{\rm obs}(= 107)$ is also shown.

12.5 Comparison between low-q^2 correction models

In Section 8.8, there are two candidate models for the correction of the low-q^2 deficit: CC resonance production mode and CC coherent pion production mode. We have studied neutrino oscillation with the correction of the CC resonance production mode by default. To compare the results between the two models, we perform the same analysis with the suppression of the CC coherent pion production mode.

The results from the two models are summarized in Table 12.10. The best fit points are very close each other. Figure 12.12 shows the $E_\nu^{\rm rec}$ spectrum at the best fit point in the physical region. The best fit $E_\nu^{\rm rec}$ spectrum agrees with data well, and the KS-probability is evaluated to be 35%. The expected number of events at the best fit point is 103.9, which is also close to that for the suppression of the resonance production channel. Figure 12.13 shows the allowed region of oscillation parameters. The contours are almost same each other. Thus, the results are not changed by the choice of the low-q^2 correction.

12.6 Conclusion

We have examined the $\nu_\mu \to \nu_x$ neutrino oscillation with a maximum likelihood method. In the likelihood function, uncertainties in ND measurements, the Far/Near flux ratio and SK systematics are properly taken into account, including the error cancellation in the normalization term.

The fit results represent data very well. The KS-probability for the $E_\nu^{\rm rec}$ spectrum is 36% at the best fit point in the physical region, and the expected number of events (103.9) agrees with data (107) within the statistical error. Consequently, observation is consistent with neutrino oscillation.

On the other hand, observation does not agree with the null oscillation hypothesis. The null oscillation hypothesis is excluded with 99.995% C.L. (4.0 standard deviations) by using the likelihood ratio method. Even if we use either the $E_\nu^{\rm rec}$ shape or the number of events, the null oscillation probability is less than 1%. The fact that the $E_\nu^{\rm rec}$ shape excludes the null oscillation hypothesis indicates the E_ν dependence of the oscillation probability.

Finally, we compare the results with an atmospheric neutrino experiment. According to recent atmospheric neutrino results from SK [11], the 90% C.L. allowed parameter region has been

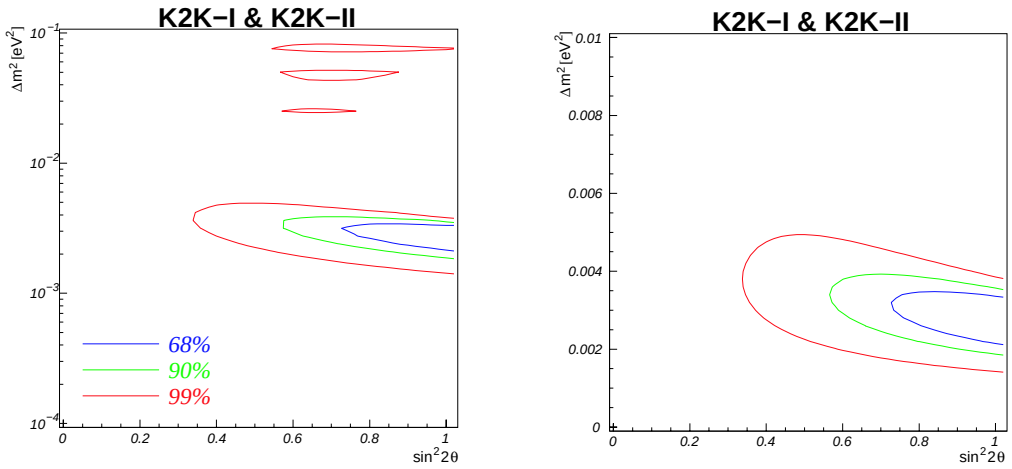

Figure 12.8: Allowed region for oscillation parameters. The difference of these two figures is only the scale of vertical axes: log scale (left) and linear scale (right). Blue, green, and red lines show 68%, 90%, and 99% C.L. contours, respectively.

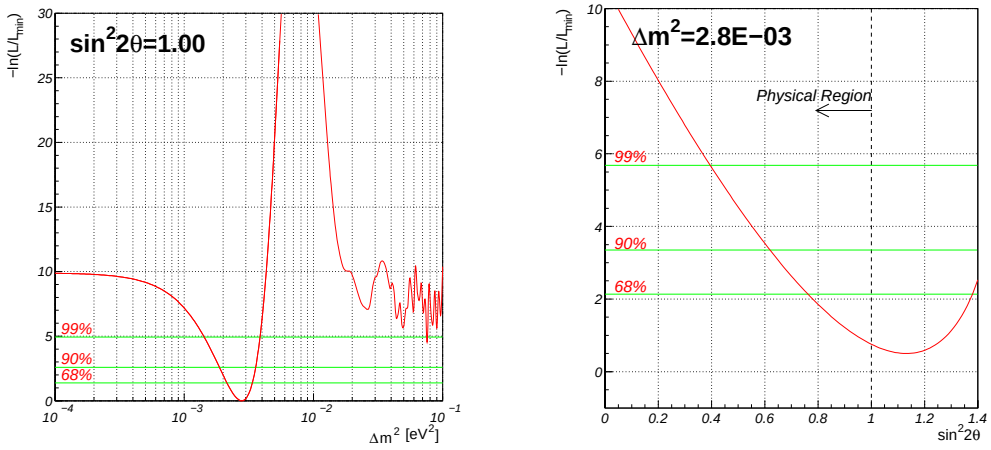

Figure 12.9: Log-likelihood curve as a function of Δm^2 along the axis of $\sin^2 2\theta = 1$ (left), and as a function of $\sin^2 2\theta$ along the axis of $\Delta m^2 = 2.8 \times 10^{-3}$ [eV^2] (right). The vertical axis shows the minus of the log-likelihood difference. The $\Delta \ln \mathcal{L}$ threshold for each confidence level is shown by a green line.

obtained as ($1.9{\times}10^{-3} < \Delta m^2 < 3.1{\times}10^{-3}$ [eV^2], $\sin^2 2\theta > 0.90$). This region is consistent with our result (Figure 12.8). Thus, our measurement has confirmed neutrino oscillation observed by atmospheric neutrino experiments.

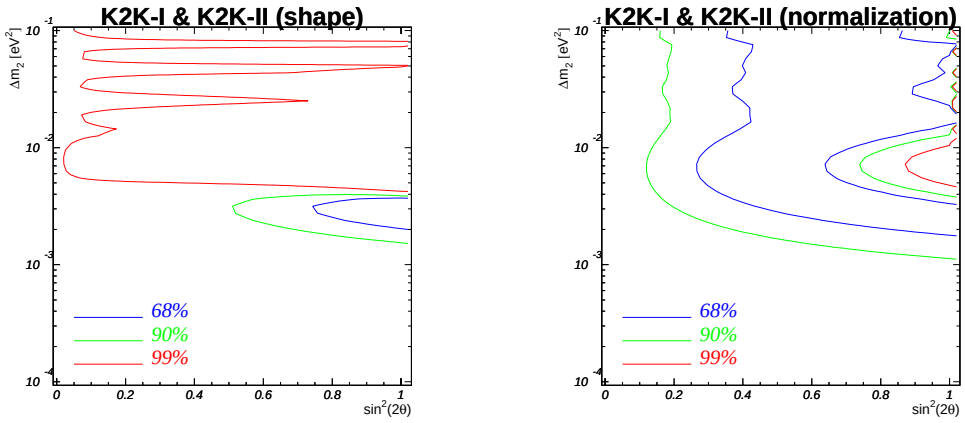

Figure 12.10: Comparison of the allowed regions for oscillation parameters between the shape-only (left) and the normalization-only (right) analyses.

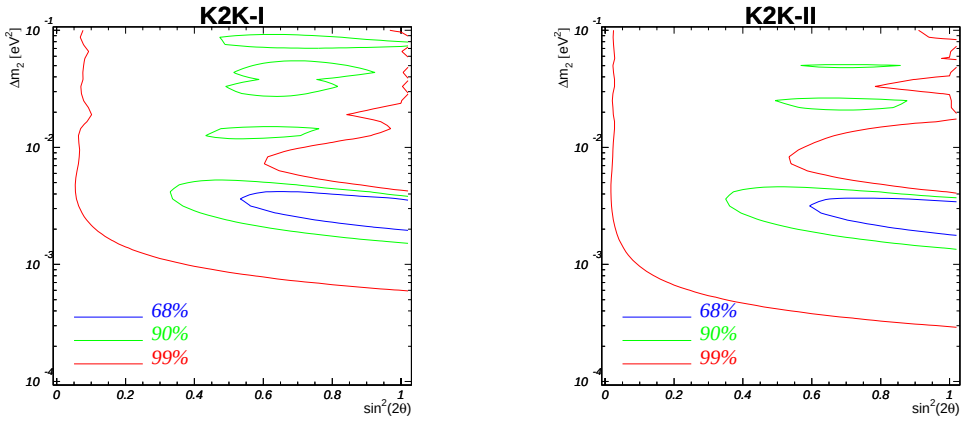

Figure 12.11: Comparison of the allowed regions for oscillation parameters between K2K-I (left) and K2K-II (right).

Table 12.10: Oscillation analysis results with the removal of the coherent pion scattering channel. The results from the suppression of the resonance production channel are also listed for reference.

Suppressed channel	Coherent pion	Resonance production
Best fit (all region) $(\Delta m^2\ [\mathrm{eV}^2], \sin^2 2\theta)$	$(2.2\times10^{-3}, 1.6)$	$(2.2\times10^{-3}, 1.5)$
Best fit (physical region)	$(2.8\times10^{-3}, 1.0)$	$(2.8\times10^{-3}, 1.0)$
KS-probability for E_ν^{rec} shape	35%	36%
N^{exp} in total	103.9	103.8
Null oscillation probability	0.0044%	0.0050%

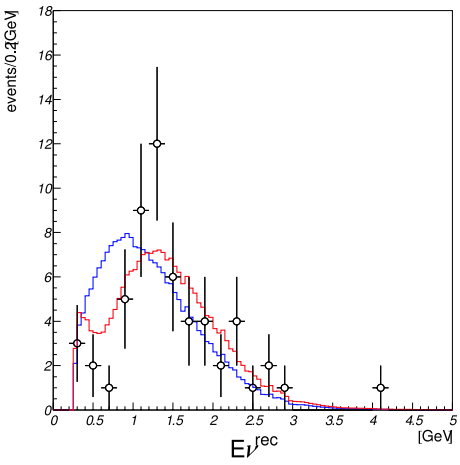

Figure 12.12: The best fit $E_\nu^{\rm rec}$ spectrum for the removal of the CC coherent pion scattering channel. Open circles with error bars are data, and the red line is the best fit spectrum. The blue line is the spectrum in case of null oscillation.

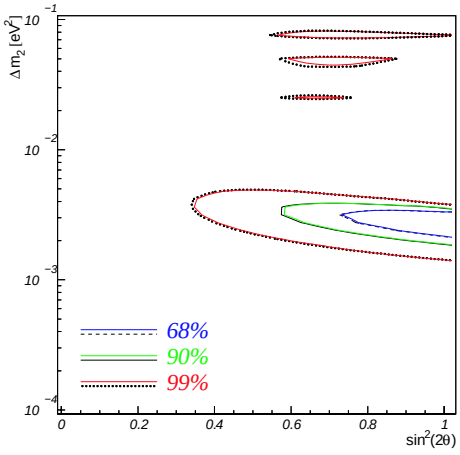

Figure 12.13: Comparison of the allowed regions for oscillation parameters between the low-q^2 suppression of the CC resonance production channel and the removal of the CC coherent pion scattering channel. Colored lines show allowed regions for the removal of the coherent pion scattering channel. The 68%, 90%, and 99% C.L. regions are shown by blue, green and red lines, respectively. Black lines represent arrowed regions for the suppression of the resonance production channel. Dashed, solid, and dotted lines show 68%, 90%, and 99% C.L. regions, respectively. Since these regions are almost same, it is difficult to distinguish between them.

Chapter 13

Summary

The K2K long baseline neutrino oscillation experiment has been conducted to study neutrino oscillation. We started taking data in June 1999, and we have accumulated data corresponding to 8.9×10^{19} protons on target so far.

The SciBar detector was newly installed in summer 2003. The basic performance is sufficient up to our expectation. The light yield is 9 photo-electrons/MeV without attenuation, and its stability is within 1% after the PMT gain correction. CC events for the neutrino energy spectrum analysis are properly selected. Thus, the characteristics of SciBar is properly understood.

To study the neutrino energy spectrum at the near site, we selected CC events from SciBar, SciFi, and 1KT data. We have encountered the disagreement of the low-q^2 region between data and the MC simulation. Therefore, the spectrum is obtained without using forward going events. The cause of the low-q^2 deficit is investigated with SciBar data, and it is found to be either the CC resonance production mode or the CC coherent pion production mode. In the meanwhile, the number of neutrino events is obtained from 1KT data to estimate the expected number of SK events.

Neutrino events in SK are properly selected by GPS information and by the event selection procedure based on the atmospheric neutrino analysis. In total, 107 fully-contained events are observed in the 22.5 kton fiducial volume, and 57 events are classified as single-ring μ-like for the energy spectrum analysis. In addition, the performance of both SK-I and SK-II are confirmed to be sufficient for the oscillation analysis.

A maximum likelihood fit has been performed to study the existence of the neutrino oscillation and to determine the oscillation parameters. Both the energy spectrum and the number of events are used in this analysis. Before the fit, the expected number of events in the case of null oscillation is estimated to be $150.9^{+11.5}_{-10.1}$ events. The best fit parameters are obtained to be

$$(\Delta m^2,\ \sin^2 2\theta) = (2.8 \times 10^{-3}\ [\mathrm{eV}^2],\ 1.0). \tag{13.1}$$

By using the likelihood ratio method, the null oscillation hypothesis is excluded with 99.995% C.L., corresponding to 4.0 standard deviations. Even if the analysis is performed with only the energy spectrum, the null oscillation is rejected with more than 99% C.L. It indicates the neutrino energy dependence of the oscillation probability. Allowed regions for the oscillation parameters are determined, and the 90% confidence interval of Δm^2 on the axis of $\sin^2 2\theta = 1$ is found to be

$$1.9 \times 10^{-3} \leq \Delta m^2 \leq 3.6 \times 10^{-3}\ [\mathrm{eV}^2]). \tag{13.2}$$

These results are consistent with atmospheric neutrino observations.

We conclude that we have obtained the evidence of the muon neutrino oscillation by using the well-understood neutrino beam, and that we have confirmed the atmospheric neutrino oscillation results. We have established the fact that a muon neutrino is a superposition of several mass eigenstates, and that at least one of the eigenstates have finite masses.

Appendix A

Cellular Automaton Tracking

We describe the track finding procedure of SciBar. In Section A.1, two-dimensional (2D) tracks are looked for by using the cellular automaton tracking algorithm. In Section A.2, a couple of 2D tracks are combined into a three-dimensional (3D) track.

A.1 Two-dimensional track search

The reconstruction of 2D tracks in SciBar is based on a cellular automaton algorithm. In this section, we introduce an overview of a cellular automaton. Then, we describe the application to the track finding.

A.1.1 Overview of a cellular automaton

A cellular automaton is a dynamical systems that evolve in discrete steps. Space, time, and the states of the system are discrete. Each cell has a finite number of states. The states of the cells are updated according to a local rule. The state of a cell at a given time depends only on its own state and the states of its nearby neighbors at the previous time step. All cells are updated synchronously. For example, Conway's game of life[95] is a familiar cellular automaton. The applications of cellular automata are already used in some high energy physics experiments[96].

A.1.2 Cellular automaton tracking

Before applying the cellular automaton tracking (CAT) algorithm, we make clusters of adjacent hits in each layer, because a slanting track may hit more than one strips in a layer. Here, a layer is comprised of a X readout plane and a Y readout plane vertical to the beam axis. In the CAT algorithm, we look for a continuous sequence of clusters.

We define cells, neighbors, and rules of evolution for the cellular automaton. To avoid confusion, we describe these three terms as "CAT cell", "CAT neighbor", and "CAT rule", respectively. The definition of these terms are:

- **CAT cell:** A straight line segment connecting two clusters in adjacent layers. The CAT cell is neither a hit nor a cluster. To take into account detector inefficiency and geometrical acceptance due to reflective coating, the line segment is allowed to skip over one layer. Each CAT cell has a state value to represent the position in a track.

- **CAT neighbor:** Only CAT cells with a common cluster are considered as CAT neighbors. To take into account multiple scattering and the detector segmentation, an upper limit on the χ^2 is imposed. The χ^2 is computed from a linear least square fit to the three clusters belonging to two neighboring CAT cells.

- **CAT rule:** The CAT cells are initialized with a state value equal to one. At each time step, the CAT algorithm look at the upstream neighbor CAT cells of the current one and increment the state value by one unit if there is a CAT neighbor with the same state value. The evolution stops when there are no more neighboring CAT cells with the same state value.

According to the above CAT rules, the state value of each CAT cell is updated. Figure A.1 shows each step of the cellular automaton tracking algorithm. The track candidates are collected by starting from a CAT cell with the lowest state value and adding the CAT neighbor with the consecutive state value like 1, 2, 3, $\cdots$. The procedure travels along the tree until all combinations are considered. At this level, tracks with splitting branches are considered. Finally, each set of clusters is fitted to a straight line by a least square method.

A.2 Three-dimensional track search

The 2D track in XZ-plane (X-track) and that in YZ-plane (Y-track)[1] are combined into a three-dimensional (3D) track, according to two rules. One is that the average of hit timing for each 2D track is within 50 nsec. The other is the condition of the Z positions of track edges.

The track finder looks at the Z positions of the track edges of an X-track and a Y-track, and favors smaller difference in the Z positions. Here, we introduce N^Z, which is a serial number of X-planes and Y-planes. The most upsteam X-plane is defined as $N^Z = 1$, and the most upstream Y-plane is defined as $N^Z = 2$. Therefore, N^Z of an X-plane takes an odd number, and that of a Y-plane takes an even number. We define $\Delta N^Z_{\rm up}$ and $\Delta N^Z_{\rm down}$ as

$$\begin{aligned} \Delta N^Z_{\rm up} &\equiv |N^Z_{X\text{-up}} - N^Z_{Y\text{-up}}|, \\ \Delta N^Z_{\rm down} &\equiv |N^Z_{X\text{-down}} - N^Z_{Y\text{-down}}|, \end{aligned} \tag{A.1}$$

where $N^Z_{X\text{-up}}$ and $N^Z_{X\text{-down}}$ are N^Z at the upstream edge and the downstream edge of an X-track, respectively, and the same is true for a Y-track. The track finder looks for the pair of an X-track and a Y-track, which satisfies the following criteria:

$$\Delta N^Z_{\rm up} < 6 \qquad \text{and} \qquad \Delta N^Z_{\rm down} < 6. \tag{A.2}$$

After all the combinations are tried, the track finder again looks for the pair which satisfies the condition:

$$\Delta N^Z_{\rm up} < 4 \qquad \text{or} \qquad \Delta N^Z_{\rm down} < 4, \tag{A.3}$$

from remaining 2D tracks. In this way, the matched pairs are combined into 3D tracks.

If more than one 2D tracks are matching to one 2D track, the pair with smaller $\Delta N^Z_{\rm up}$ and $\Delta N^Z_{\rm down}$ has a priority. If $\Delta N^Z_{\rm up}$ and $\Delta N^Z_{\rm down}$ are the same, ADC information of each plane is used to select the best combination. Once a pair of 2D tracks is found, we correct the attenuation of the WLS fiber, and we obtain the path length in each plane. In addition, the energy deposit of a proton around 1 GeV/c is larger than that of a muon and a charged pion. If the combination is wrong, therefore, the ADC values per unit length of the 2D tracks are different from each other. The track finder calculates the χ^2 of the ADC values per unit length between an X-track and a Y-track, and the smaller χ^2 is favored.

[1] The coordinate system of SciBar is shown in Figure 4.2.

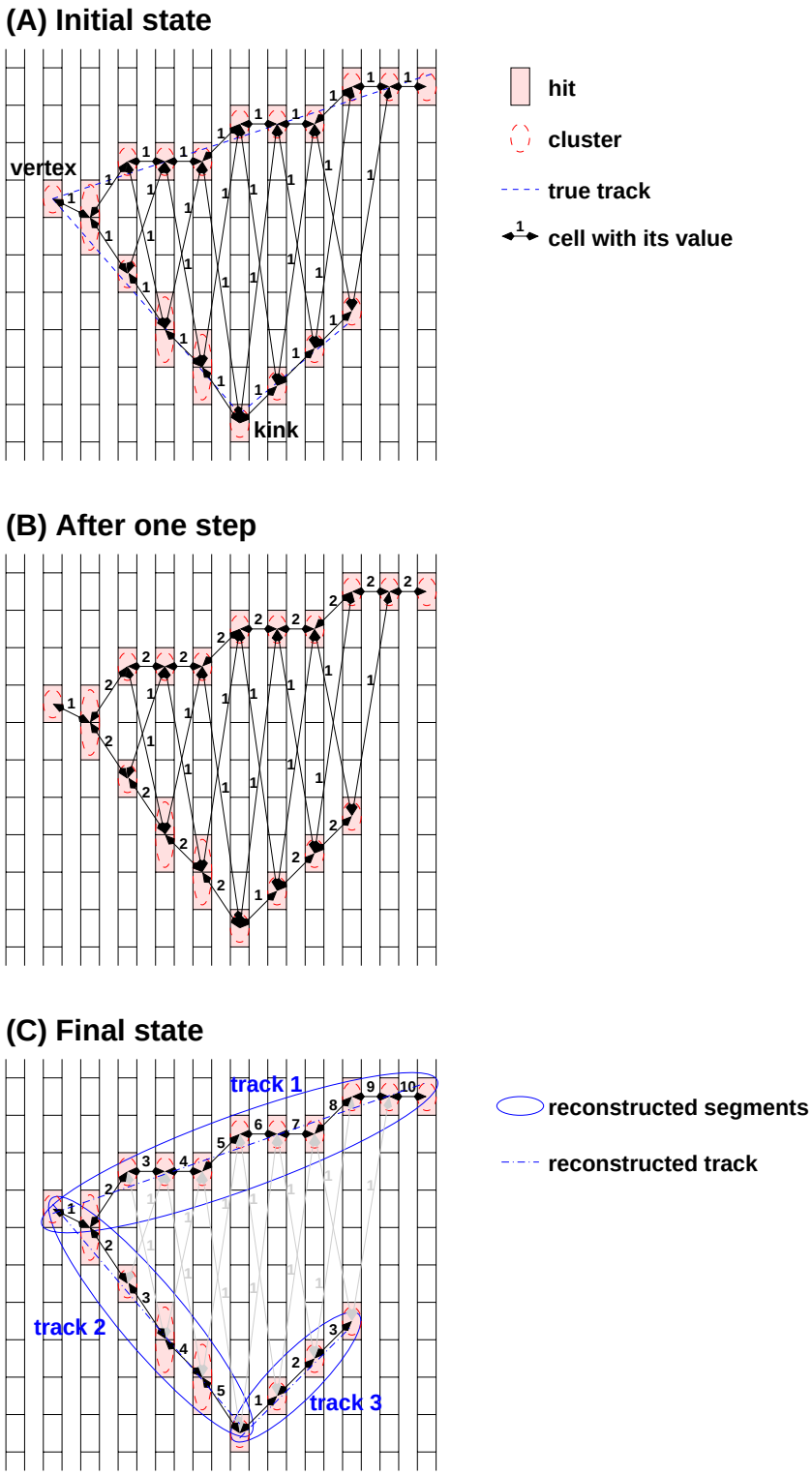

Figure A.1: Schematic figure of the cellular automaton tracking for each step. Hits and clusters are shown by filled boxes and dashed circles, respectively. CAT cells and their state values are shown by arrows. (A), (B) and (C) show the initial state, the snapshot after one step, and the final state of the cellular automaton, respectively. The true tracks are drawn in figure (A). In figure (C), the reconstructed combinations of CAT cells are shown by solid circles, and fitted tracks are shown by dash-dotted lines.

Appendix B

Neutrino Beam Stability

The stability of the neutrino beam is monitored by the muon monitor (MUMON) at the end of the decay volume and the muon range detector (MRD) at the near detector hall. MUMON measures the profile and the yield of the muons from pion decays on spill-by-spill basis. MRD monitors the beam profile and the the neutrino event rate every a few days. Since MRD can measure the energy (E_μ) and the angle (θ_μ) of the muon from a neutrino interaction, the E_ν spectrum is indirectly monitored. Here, θ_μ is the muon angle with respect to the neutrino beam. The stability of the E_ν spectrum is important for the E_ν spectrum determination.

B.1 MUMON measurement

ICH and SPD of MUMON provide the beam profile and the muon yield, respectively, for each beam spill. Figure B.1 shows the stability of the beam center measured by ICH. The beam direction has been stable within 1 mrad from the SK direction. Figure B.2 shows the stability of the sum of SPD signals normalized by POT, which is proportional to the muon yield. The yield in June 1999 is lower due to the smaller horn current. The RMS of the muon yield since November 1999 is 2.5% of the mean value.

B.2 MRD measurement

Since MRD is a massive detector among the near detectors, MRD is suitable to monitor the neutrino beam itself. MRD monitors the beam profile, the neutrino event rate, the E_μ distribution, and the θ_μ distribution. The outline of the event selection criteria is:

1. A contained track within MRD.
2. The number of penetrated iron plate is more than or equal to two.
3. The neutrino interaction vertex is defined as the upstream edge of the track, and it is required to be within a certain fiducial volume. We use two types of fiducial volumes. One is 6×6 m^2 transverse area and from first to ninth iron plates, corresponding to 419 tons. The other is the cylinder of 6m-diameter along the beam and from first to ninth iron plates longitudinally, corresponding to 329 tons. The former is employed by the beam profile measurement. The latter is used by the measurements of the event rate, the E_μ distribution, and the θ_μ distribution.

The detail of the criteria is described in [29].

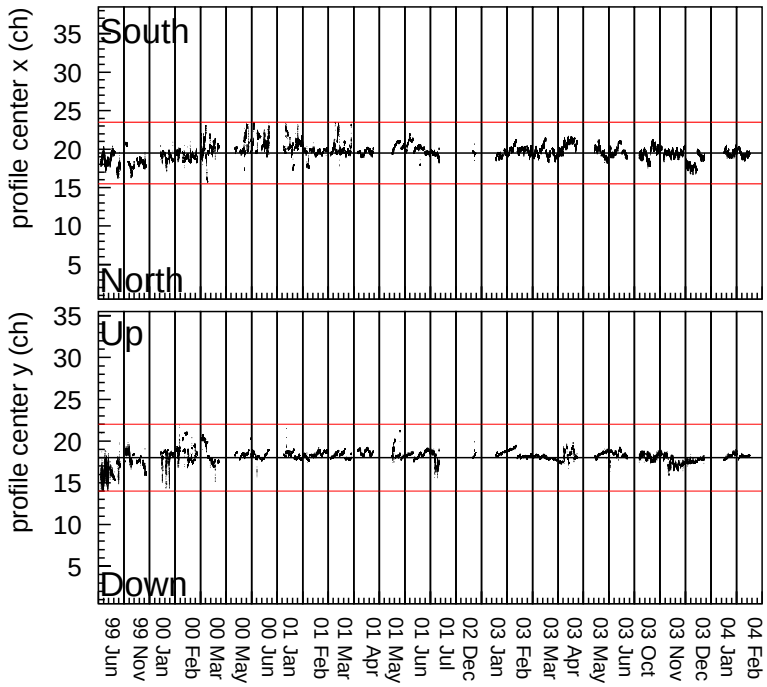

Figure B.1: Stability of beam center measured by MUMON-ICH. Horizontal black lines show the SK direction, and red lines show the ±1mrad off the center.

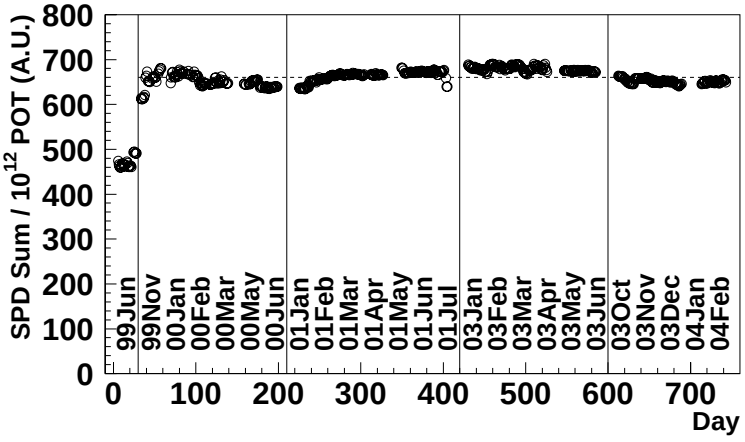

Figure B.2: Stability of secondary muon yield from pion decay measured by MUMON-SPD. The vertical axis shows the sum of ADC outputs from SPD normalized by POT.

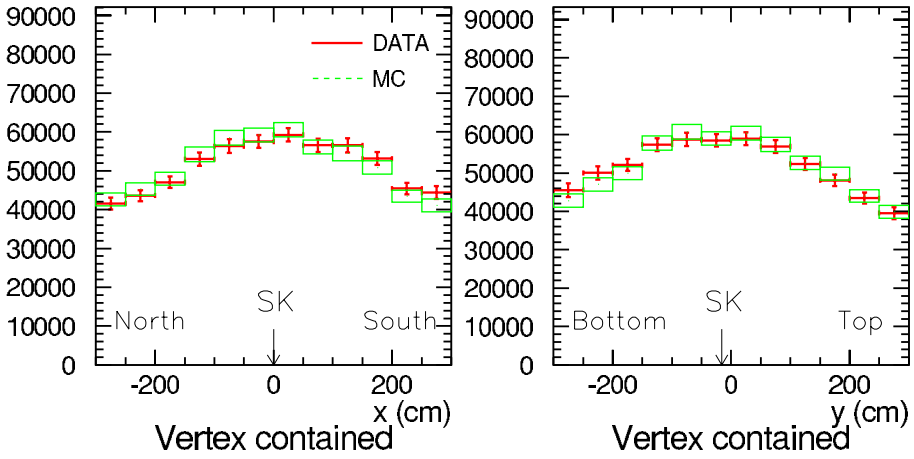

Figure B.3: Neutrino beam profile measured by MRD. The left figure shows the horizontal profile, and the right one shows the vertical profile. Crosses are data, and boxes are the MC simulation. The SK direction is specified by arrows. If the beam is 1 mrad off the SK direction, the profile is shifted by 30 cm.

B.2.1 Beam profile

Figure B.3 shows the neutrino beam profile for K2K-Ib after acceptance correction. The acceptance is estimated by the MC simulation as a function of vertex position and muon energy. Although the data looks slightly shifted from the MC simulation in Figure B.3, the deviation of the beam direction from SK is less than 1 mrad. The beam center is determined by fitting the profile distribution with Gaussian. The long-term stability of the beam center is shown in Figure B.4. Almost all of the data points are within the 1 mrad from the SK direction.

B.2.2 Event rate

Figure B.5 shows the stability of the neutrino event rate normalized by POT. The standard deviation of the data points is 2.6% of the mean value. If the event rate is normalized by the MUMON-SPD data, the standard deviation becomes 2.2%. In both cases, the event rate is stable within a few % level.

B.2.3 Muon energy and angle

Figure B.6 shows the comparison of muon energy and angle distributions for each year. All the histograms are almost identical, and hence it is hard to distinguish each histogram. The monthly stability of each E_μ bin is shown in Figure B.7, and that of each θ_μ bin is shown in Figure B.8. The vertical axis represents the ratio of the bin content to that of November 1999. The deviation of each plot is consistent with the statistical fluctuation. Consequently, the E_ν spectrum is stable within the sensitivity.

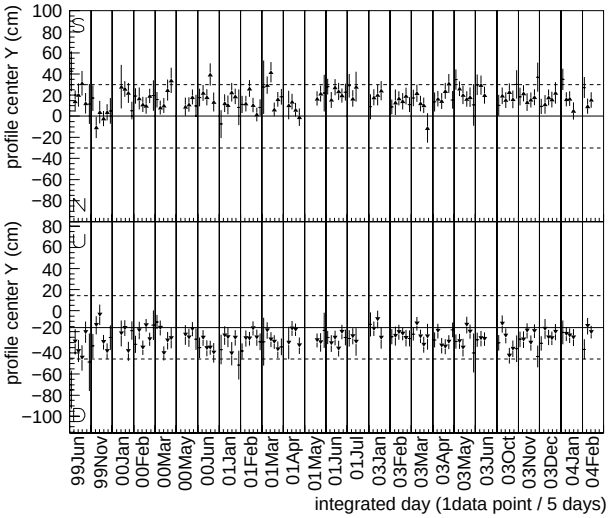

Figure B.4: Stability of the beam center measured by MRD. The upper figure shows the vertical position, and the lower figure shows the horizontal position. Horizontal solid lines illustrate the SK direction, and dashed lines indicate the 1mrad off the SK direction.

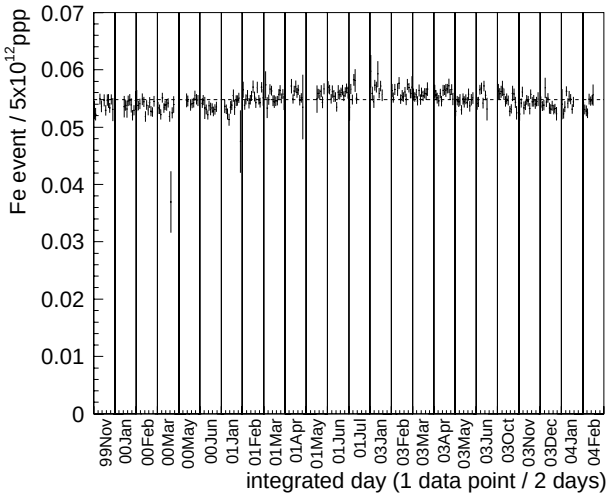

Figure B.5: Stability of the neutrino event rate measured by MRD. The vertical axis shows the number of events per 5×10^{12} POT.

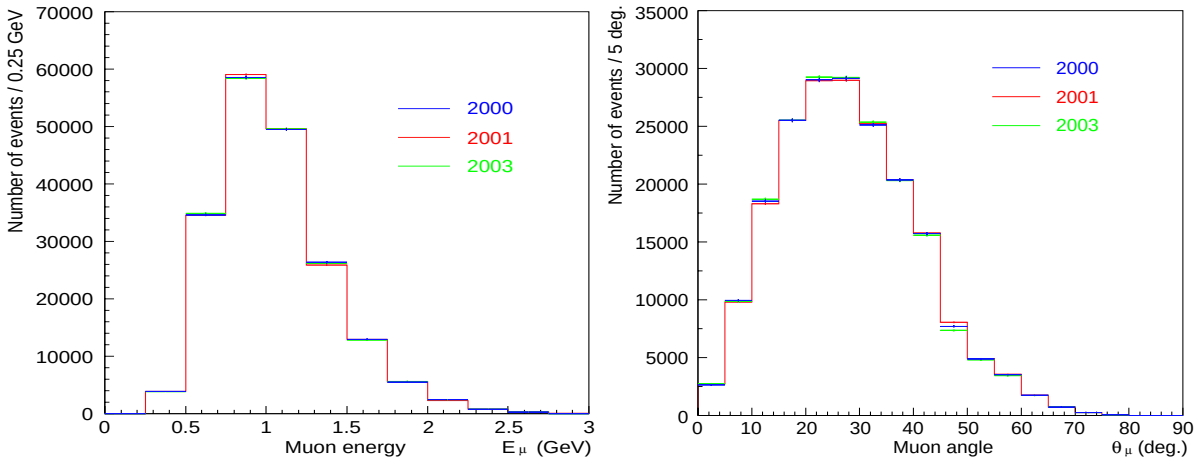

Figure B.6: Comparison of the MRD muon energy spectrum (left) and the angle distribution (right) for each year. Blue, red, and green lines represent the data taken in 2000, 2001, and 2003, respectively. These histograms are almost the same.

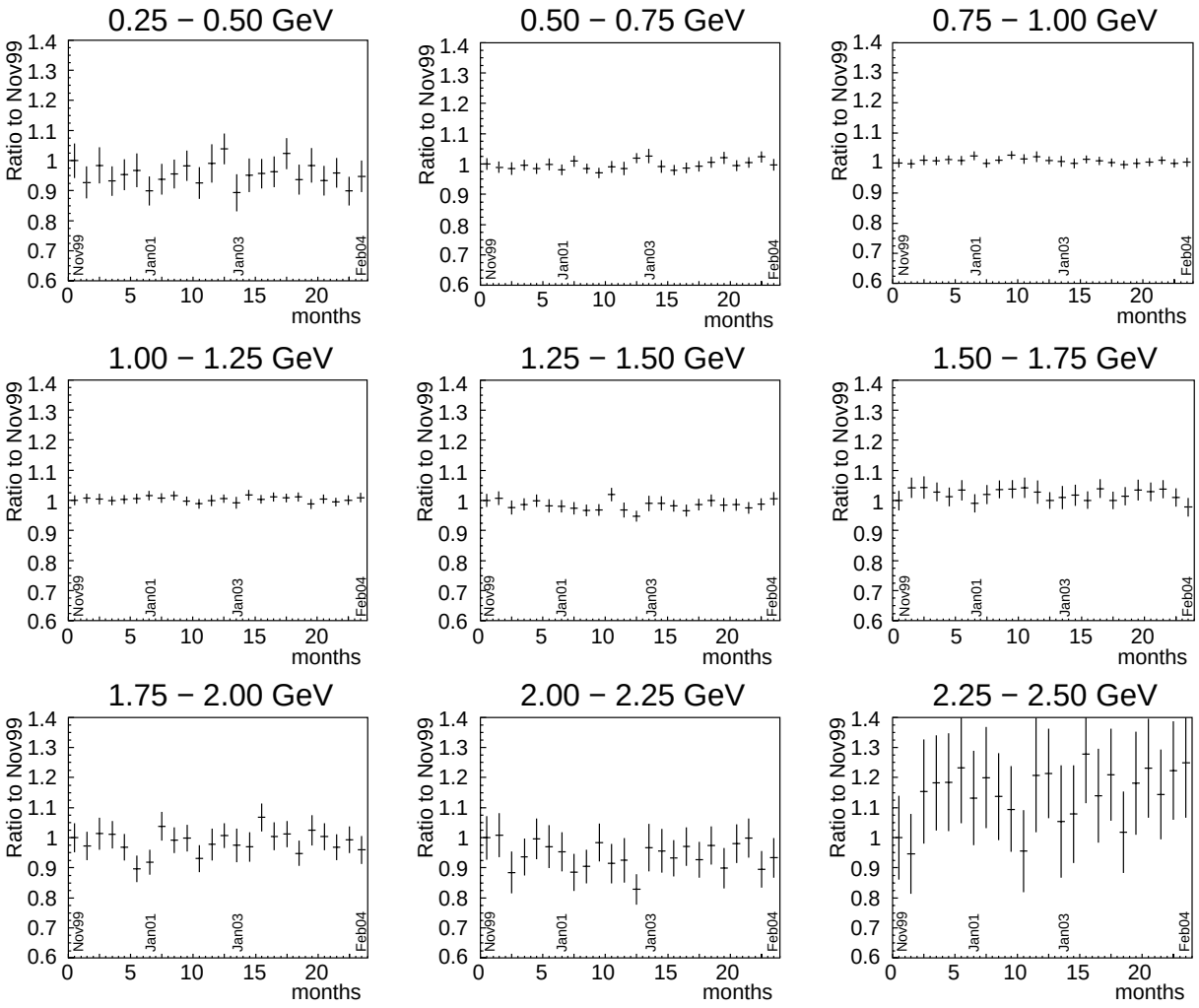

Figure B.7: Monthly stability of each E_μ bin for MRD events.

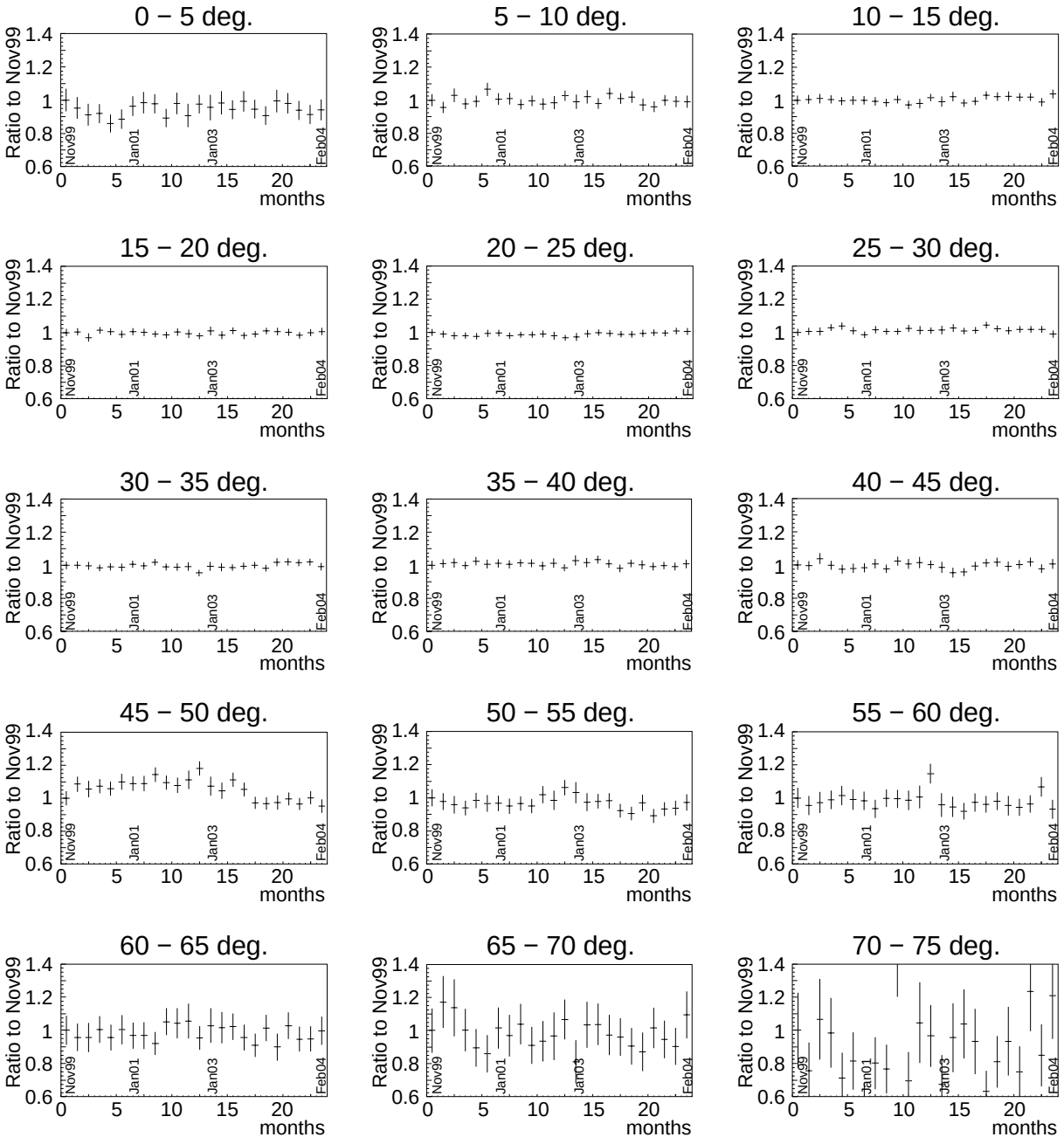

Figure B.8: Monthly stability of each θ_μ bin for MRD events.

Appendix C

Toy MC Study for ND Spectrum Fit

When we measure the neutrino energy spectrum at the near site by a chi-square fitting method, we cut forward scattering muons. We confirm the validity of the fit by using toy Monte Carlo technique. The SciBar and 1KT parts are investigated in this chapter.

C.1 SciBar part

The dummy data $N^{\rm dummy}(i,j)$ is created from the MC distribution $N^{\rm MC}(i,j)$ by the random number generator which follows the Poisson statistics. $N^{\rm dummy}(i,j)$ is written as

$$N^{\rm dummy}(i,j) = R(N^{\rm MC}(i,j)), \tag{C.1}$$

where $R(\mu)$ is the Poisson random number generator with the mean value μ. We fit the dummy data $N^{\rm dummy}(i,j)$ with the MC simulation $N^{\rm MC}(i,j)$. We perform such a virtual experiment many times and understand the characteristics of the fitting method.

Using default $N^{\rm MC}$ as a dummy data generator, we confirm whether the fitting parameters sit near the central values or not. We perform the fit 1000 times and plotted each fitting parameter, as shown in Figure C.1. Since the present SciBar data is not sensitive to f_1^ϕ, it is fixed to unity. All free parameters distribute around unity, and the RMS of them are almost equal to the fitting errors. Thus, there is no bias in the fitting method itself. Since the sensitivity to f_8^ϕ is poor[1], we fix f_8^ϕ to unity hereafter.

We carry out the toy MC again with fixed f_8^ϕ. The mean and RMS of each parameter are illustrated in Figure C.2. If f_8^ϕ is fixed, f_7^ϕ is biased by 5%. When all the three detectors are analyzed simultaneously, however, f_8^ϕ is released and hence the bias in f_7^ϕ is expected to disappear.

The systematic error on the angle measurement is a source of a bias, and the requirement of $\theta_\mu > 10$ degrees may enlarge the effect. Therefore, we shift or smear the angle of a muon track, and investigate the bias. Since the systematic uncertainty in θ_μ is 0.2 degree as discussed in Section 6.2.6, we shift a two-dimensional angle (θ_x) or the angle with respect to the beam (θ_μ) by 0.2 degree. In addition, we smear θ_μ by 1.5 degrees so that the θ_μ resolution becomes twice as poor as the actual value. The results from the toy MC study are shown in Figure C.3. If θ_μ is shifted, f_2^ϕ moves systematically by 10%. However, this bin is mainly determined by 1KT in the combined analysis. Actually, the fitting error on f_2^ϕ is 10% in the 1KT result[2], while the SciBar result has the error of 25%. The contribution of the bias from SciBar is estimated to be:

$$\frac{\frac{10}{25}}{\frac{1}{25}+\frac{1}{10}} \simeq 2.9\%, \tag{C.2}$$

[1] If the entire θ_μ region is used, f_8^ϕ distributes from 0 to 2.

[2] The 1KT result is shown in Table 8.8.

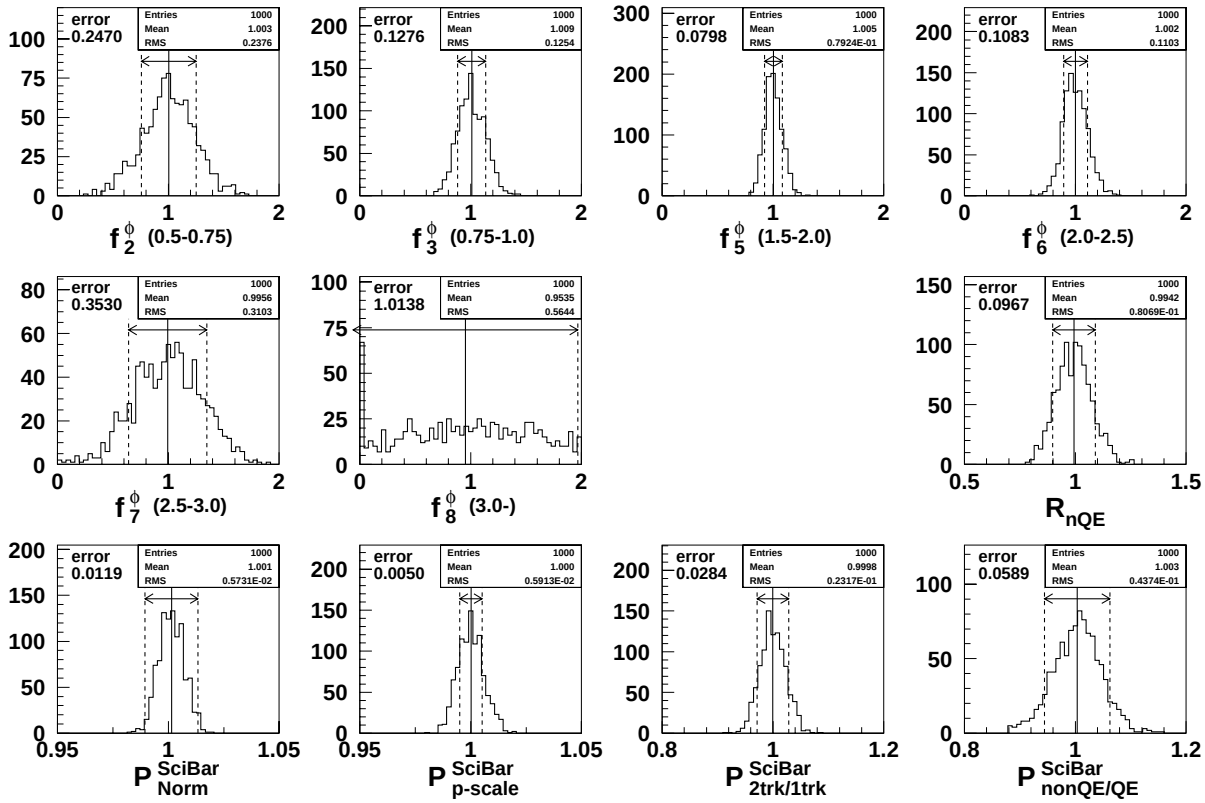

Figure C.1: The distribution of each fitting parameter from Toy MC in the default case. One entry corresponds to one virtual experiment. Arrows show the fitting errors.

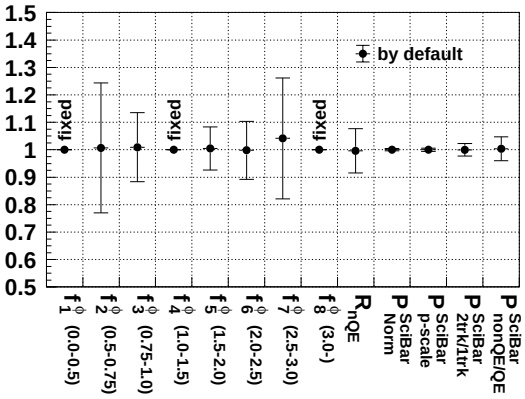

Figure C.2: Fitting results from Toy MC in the default case. The central values and error bars represent, respectively, the mean and RMS of the distributions of fitting parameters.

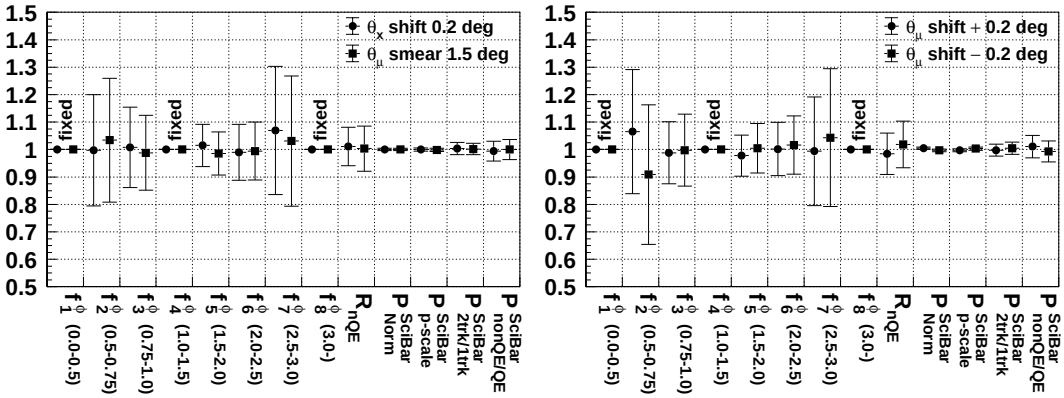

Figure C.3: Fit results from toy MC in the case of θ_μ shift or smearing.

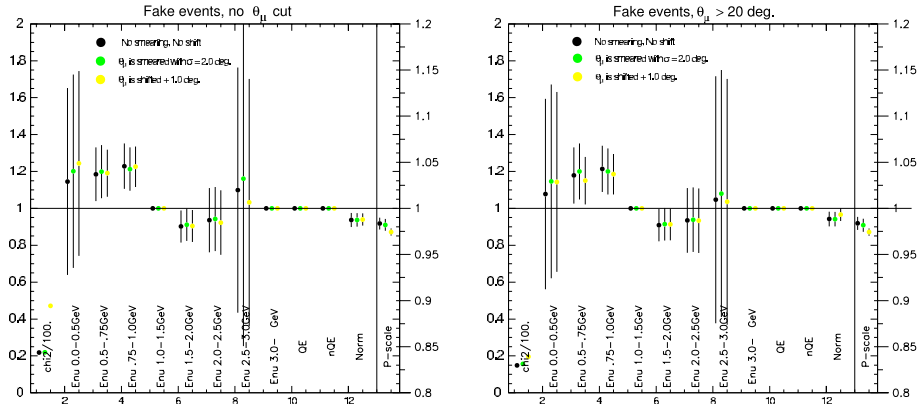

Figure C.4: Fit results from toy MC of 1KT in the cases of θ_μ shift and smearing. The left figure is the results without θ_μ cut, and the other is those with the requirement of $\theta_\mu > 20$ degrees. The results from default dummy data is shown by black symbols. Green and yellow symbols represents, respectively, θ_μ smearing by 2 degrees and θ_μ shift by 1 degree. The error bar shows the fitting error.

assuming the chi-square follows a parabola. The influence on f_2^ϕ is only 3% level. Therefore, we ignore it for the oscillation analysis.

C.2 1KT part

We perform a virtual experiment by generating events randomly, and we fit the dummy data with the MC simulation. We compare the fit results between with and without θ_μ cut. In each case, θ_μ is intentionally smeared by 2 degrees or shifted 1 degree. These values correspond to the uncertainties in the θ_μ measurement of 1KT. On the contrary to the SciBar toy MC study, the number of virtual experiments is one. However, the same data set is used in all the fit conditions. Therefore, the best fit value is allowed deviating from unity. Figure C.4 shows the fit results from a virtual experiment of 1KT. The fit results are independent of θ_μ cut, θ_μ shift, and θ_μ smearing. Thus, the validity of θ_μ cut in the fit is confirmed.

Bibliography

[1] S. Eidelman *et al.*, Phys. Lett. B **592**, 1 (2004).

[2] C. Weinheimer *et al.*, Phys. Lett. B **460**, 219 (1999);
V. M. Lobashev *et al.*, Phys. Lett. B **460**, 227 (1999).

[3] K. Assamagan *et al.*, Phys. Rev. D **53**, 6065 (1996).

[4] R. Barate *et al.*, Eur. Phys. J. C **2**, 395 (1998).

[5] Y. Fukuda *et al.*, Phys. Rev. Lett. **81**, 1562 (1998).

[6] S. Fukuda *et al.*, Phys. Lett. B **539**, 179 (2002).

[7] Q. R. Ahmad *et al.*, Phys. Rev. Lett. **89**, 011301 (2002).

[8] K. Eguchi *et al.*, Phys. Rev. Lett. **90**, 021802 (2003).

[9] M. H. Ahn *et al.*, Phys. Rev. Lett. **90**, 041801 (2003).

[10] Z. Maki, M. Nakagawa and S. Sakata, Prog. Theor. Phys. **28**, 870 (1962).

[11] Y. Ashie *et al.*, Phys. Rev. Lett. **93**, 101801 (2004);
M. Ishitsuka, Ph.D thesis, Tokyo University (2004).

[12] K. Nishikawa *et al.*, KEK-PS proposal (1995).

[13] S. P. Mikheev and A. Y. Smirnov, Sov. J. Nucl. Phys. **42**, 913 (1985) [Yad. Fiz. **42**, 1441 (1985)];
L. Wolfenstein, Phys. Rev. D **17**, 2369 (1978).

[14] T. Araki *et al.*, arXiv:hep-ex/0406035.

[15] M. Apollonio *et al.*, Eur. Phys. J. C **27**, 331 (2003);
F. Boehm *et al.*, Phys. Rev. D **64**, 112001 (2001).

[16] M. H. Ahn *et al.*, Phys. Rev. Lett. **93**, 051801 (2004).

[17] S. H. Ahn *et al.*, Phys. Lett. B **511**, 178 (2001).

[18] H. Sato, Proc. Particle Accelerator Conference, (1999);
K. Takayama, ICFA Beam Dynamics Newsletter **20**, (1999)

[19] K. H. Tanaka *et al.*, KEK-preprint 91-27 (1991).

[20] Y. Yamanoi *et al.*, IEEE Trans. on Applied Superconductivity **10**, 252 (2000);
M. Kohama, Master thesis, Kobe University (1997), *in Japanese*;
Y. Yamanoi *et al.*, KEK-preprint 97-225 (1997);
Y. Yamanoi *et al.*, KEK-preprint 99-178 (1999).

[21] T. Maruyama, Ph.D thesis, Tohoku University (2000).

[22] I. Kato, Ph.D thesis, Kyoto University (2004).

[23] S. Nakayama, Master thesis, University of Tokyo (1999), *in Japanese*.

[24] A. Suzuki *et al.*, Nucl. Instrum. Meth. A **453**, 165 (2000);
B. J. Kim *et al.*, Nucl. Instrum. Meth. A **497**, 450 (2003).

[25] T. Iwashita, Ph.D thesis, Kobe University (2003).

[26] M. Yoshida, Ph.D thesis, Osaka University (2001).

[27] S. Kawabata *et al.*, Nucl. Instrum. Meth. A **270**, 11 (1988).

[28] T. Ishii *et al.*, Nucl. Instrum. Meth. A **482**, 244 (2002) [Erratum-ibid. A **488**, 673 (2002)].

[29] T. Inagaki, Ph.D thesis, Kyoto University (2001).

[30] Y. Asano *et al.*, Nucl. Instrum. Meth. A **259**, 430 (1987);
Y. Ikegami *et al.*, IEEE Trans. Nucl. Sci. **36**, 665 (1989).

[31] Y. Fukuda *et al.*, Nucl. Instrum. Meth. A **501**, 418 (2003).

[32] H. G. Berns and R. J. Wilkes, IEEE Trans. Nucl. Sci. **47**, 340 (2000);
S. Yamada, Ph.D thesis, University of Tokyo (2003).

[33] The MINOS Collaboration, "Technical Design Report" NuMI-L-337 (1998).

[34] A. Pla-Dalmau, FERMILAB-Conf-00/343 (2001).

[35] T. Morita, Master thesis, Kyoto University (2004) *in Japanese*;
T. Morita, Proc. Scintillating crystals, KEK Proceedings 2004-4 H, 227 (2004).

[36] T. Sasaki, Master thesis, Kyoto University (2004) *in Japanese*.

[37] M. Hasegawa, Master thesis, Kyoto University (2003) *in Japanese*;
M. Hasegawa, Proc. Scintillating crystals, KEK Proceedings 2004-4 H, 243 (2004).

[38] S. Yamamoto, Master thesis, Kyoto University (2003) *in Japanese*;
S. Yamamoto, Proc. Scintillating crystals, KEK Proceedings 2004-4 H, 257 (2004).

[39] Y. Arai, M. Ikeno, S. Iri, T. Sofue, M. Sagara and M. Ohta, IEEE Trans. Nucl. Sci. **49**, 1164 (2002).

[40] Y. Takubo, Proc. Scintillating crystals, KEK Proceedings 2004-4 H, 263 (2004).

[41] S. Buontempo *et al.*, Nucl. Instrum. Meth. A **349**, 70 (1994).

[42] N. Armenise *et al.*, CERN-SPSC/90-42;
M. de Jong *et al.*, CERN-PPE/93-134.

[43] T. A. Gabriel, J. D. Amburgey, and B. L. Bishop (1977), ORNL/TM-5619.

[44] C. Zeitnitz and T. A. Gabriel, Nucl. Instrum. Meth. A **349**, 106 (1994).

[45] A. Fasso, A. Ferrari, J. Ranft, and P. R. Sala, *FLUKA: Present status and future developments* (1993), given at 4th International Conference on Calorimetry in High-energy Physics, La Biodola, Italy, 19–25 Sep. 1993.

[46] *GEANT – Detector Description and Simulation Tool*, Application Software Group, Computing and Networks Division, CERN (1993), CERN Program Library Long Writeup W5013.

[47] J. R. Sanford and C. L. Wang, Brookhaven National Laboratory, AGS internal report, (1967), unpublished;
C. L. Wang, Phys. Rev. Lett. **25** 1068 (1970);
C. L. Wang, Phys. Rev. D **16**, 2196 (1977).

[48] R. A. Lundy *et al.*, Phys. Rev. Lett. **14** 504 (1966).

[49] D. Dekkers *et al.*, Phys. Rev. **137** B962 (1965).

[50] W. F. Baker *et al.*, Phys. Rev. Lett. **7** 101 (1961).

[51] A. Yamamoto, KEK Report 81-13 (1981).

[52] Y. Cho *et al.*, Phys. Rev. D **4** 1967 (1971).

[53] Private communication with W. Gajewski, a K2K collaborator;
J. Hill, K2K internal note BEAM/BMMC/00-001 (2000).

[54] G. J. Marmer *et al.*, Phys. Rev. **179** 1294 (1969);
G. J. Marmer and D. E. Lundquist, Phys. Rev. D **3** 1089 (1971).

[55] J. G. Asbury *et al.*, Phys. Rev. **178** 2086 (1969).

[56] J. V. Allaby *et al.*, CERN Report No. CERN-TH-70-12 (1970), unpublished.

[57] Y. Hayato, Nucl. Phys. Proc. Suppl. **112**, 171 (2002).

[58] K. Okumura, Ph.D thesis, University of Tokyo (1999);
M. Shiozawa, Ph.D thesis, University of Tokyo (1999);
K. Ishihara, Ph.D thesis, University of Tokyo (1999);
S. Yamada, Ph.D thesis, University of Tokyo (2003).

[59] C. H. L. Smith, Phys. Rept. **3**, 261 (1972).

[60] V. Bernard, L. Elouadrhiri and U. G. Meissner, J. Phys. G **28**, R1 (2002).

[61] S. J. Barish *et al.*, Phys. Rev. D **16**, 3103 (1977).

[62] N. J. Baker *et al.*, Phys. Rev. D **23**, 2499 (1981).

[63] S. Bonetti *et al.*, Nuovo Cim. A **38**, 260 (1977).

[64] S. V. Belikov *et al.*, Z. Phys. A **320**, 625 (1985).

[65] L. A. Ahrens *et al.*, Phys. Rev. Lett. **56**, 1107 (1986) [Erratum-ibid. **56**, 1883 (1986)];
C. H. Albright, C. Quigg, R. E. Shrock and J. Smith, Phys. Rev. D **14**, 1780 (1976).

[66] F. A. Brieva and A. Dellafiore, Nucl. Phys. A **292**, 445 (1977).

[67] D. Rein and L. M. Sehgal, Annals Phys. **133**, 79 (1981);
D. Rein, Z. Phys. C **35**, 43 (1987).

[68] R. P. Feynman, M. Kislinger and F. Ravndal, Phys. Rev. D **3**, 2706 (1971).

[69] G. M. Radecky *et al.*, Phys. Rev. D **25**, 1161 (1982) [Erratum-ibid. D **26**, 3297 (1982)].

[70] T. Kitagaki *et al.*, Phys. Rev. D **34**, 2554 (1986).

[71] M. Pohl *et al.*, Lett. Nuovo Cim. **24**, 540 (1979).

[72] D. Rein and L. M. Sehgal, Nucl. Phys. B **223**, 29 (1983);
P. Marage *et al.*, Z. Phys. C **31** (1986) 191.

[73] J. Marteau, Eur. Phys. J. A **5**, 183 (1999);
J. Marteau, J. Delorme and M. Ericson, Nucl. Instrum. Meth. A **451**, 76 (2000).

[74] C. H. Albright and C. Jarlskog, Nucl. Phys. B **84**, 467 (1975).

[75] M. Gluck, E. Reya and A. Vogt, Z. Phys. C **67**, 433 (1995).

[76] A. Bodek and U. K. Yang, Nucl. Phys. Proc. Suppl. **112**, 70 (2002).

[77] M. Derrick *et al.*, Phys. Rev. D **17**, 1 (1978).

[78] H. Sarikko, Proc. of NEUTRINO'79, 507 (1979).

[79] S. Barlag *et al.*, Z. Phys. C **11**, 283 (1982) [Erratum-ibid. C **14**, 281 (1982)].

[80] T. Sjostrand, CERN Report No. CERN-TH-7112-93 (1994), hep-th/9508391.

[81] P. Musset and J. P. Vialle, Phys. Rept. **39**, 1 (1978);
J. E. Kim, P. Langacker, M. Levine and H. H. Williams, Rev. Mod. Phys. **53**, 211 (1981).

[82] L. L. Salcedo, E. Oset, M. J. Vicente-Vacas and C. Garcia-Recio, Nucl. Phys. A **484**, 557 (1988).

[83] C. H. Q. Ingram *et al.*, Phys. Rev. C **27**, 1578 (1983).

[84] H. W. Bertini, Phys. Rev. C **6**, 631 (1972).

[85] S. J. Lindenbaum *et al.*, Phys. Rev. **105**, 1874 (1957).

[86] K. V. Alanakian *et al.*, Phys. Atom. Nucl. **61**, 207 (1998) [Yad. Fiz. **61**, 256 (1998)].

[87] T. S. Kosmas and E. Oset, Phys. Rev. C **53**, 1409 (1996).

[88] H. Maesaka, Master thesis, Kyoto University (2002) *in Japanese.*

[89] H. Yokoyama, Ph.D thesis, Tokyo University of Science (2004).

[90] A. Shima, Master thesis, Kyoto University (2001) *in Japanese.*

[91] S. Eidelman *et al.*, Phys. Lett. B **592**, 279 (2004);
S. Baker and R. D. Cousins, Nucl. Instrum. Meth. A **221**, 437 (1984).

[92] F. James, *MINUIT — Function Minimization and Error Analysis — Reference Manual,* Computing and Networks Division, CERN (1994), CERN Program Library Long Writeup D506.

[93] W.H. Press *et al.* Numerical Recipes in C, Second edition, 620 (1992), Cambridge University Press.

[94] S. Nakayama *et al.* arXiv:hep-ex/0408134.

[95] M. Gardner, "Mathematical Games", Scientific American 223(4) (1970) 120.

[96] I. Abt, I. Kisel, S. Masciocchi and D. Emelyanov, Nucl. Instrum. Meth. A **489**, 389 (2002); I. Kisel *et al.*, Nucl. Instrum. Meth. A **387**, 433 (1997).

List of Tables

List of Figures